Titre: Title:	Polyolefin/Clay Nanocomposite Peelable Sealants: Microstructure and Performance
Auteur: Author:	Seyedeh Raziyeh Mohammadi
Date:	2017
Type:	Mémoire ou thèse / Dissertation or Thesis
Référence: Citation:	Mohammadi, S. R. (2017). Polyolefin/Clay Nanocomposite Peelable Sealants: Microstructure and Performance [Ph.D. thesis, École Polytechnique de Montréal]. PolyPublie. https://publications.polymtl.ca/2902/

UNIVERSITÉ DE MONTRÉAL

POLYOLEFIN/CLAY NANOCOMPOSITE PEELABLE SEALANTS: MICROSTRUCTURE AND PERFORMANCE

SEYEDEH RAZIYEH MOHAMMADI

DÉPARTEMENT DE GÉNIE CHIMIQUE

ÉCOLE POLYTECHNIQUE DE MONTRÉAL

THÈSE PRÉSENTÉE EN VUE DE L'OBTENTION

DU DIPLÔME DE PHILOSOPHIAE DOCTOR

(GÉNIE CHIMIQUE)

DÉCEMBRE 2017

UNIVERSITÉ DE MONTRÉAL

ÉCOLE POLYTECHNIQUE DE MONTRÉAL

Cette thèse intitulée :

POLYOLEFIN/CLAY NANOCOMPOSITE PEELABLE SEALANTS:

MICROSTRUCTURE AND PERFORMANCE

présentée par : MOHAMMADI Seyedeh Raziyeh

en vue de l'obtention du diplôme de : Philosophiae Doctor

a été dûment acceptée par le jury d'examen constitué de:

M. CICOIRA Fabio, Ph. D., président

M. AJJI Abdellah, Ph. D., membre et directeur de recherche

Mme HEUZEY Marie-Claude, Ph. D., membre

M. PARK Chul B., Ph. D., membre

DEDICATION

I dedicate this thesis to Ali, my parents and my beloved sons Parsa and Borna for their unconditional support and love.

ACKNOWLEDGEMENTS

First, I wish to express my best appreciations to my dear advisor and mentor, Professor Abdellah Ajji, for his continuous support during my PhD study and writing this thesis. I sincerely thank his insight, encouragement, patience and guidance during development of this research. I am very honored that I did my PhD under his supervision. I highly appreciate his honesty, discipline and very supportive behavior with his research group. Also, I greatly thank him for the time he spent to precisely revise the articles of this research.

I am very grateful to my co-advisor Dr. Seyed Hesamoddin Tabatabaei for his valuable advices during the development of this research project. I highly appreciate our fruitful discussions and his scientific attitude during our meetings. I am very honored that I have had the opportunity to work with him.

Thanks to Prof. Chul B. Park, Prof. Marie-Claude Heuzey, and Prof. Fabio Cicoira for accepting to evaluate my thesis and to be a part of the jury in my thesis defense.

I would like to thank my friends and members of our research group in the Department of Chemical Engineering. I greatly value our friendship and I will keep in my mind our sweet memories in the group.

I also would like to thank the technical and administrative staff of the Department of Chemical Engineering at Polytechnique Montréal.

Most importantly, I would like to thank my beloved family. I would like to thank my parents for their unconditional love, presence, patience and support throughout the time I've been writing my thesis. Their encouragement had great influence on me to continue my study and doing my PhD. I warmly thank my parents in law for their encouragement. My most thanks go to my dear husband Ali who is my best friend ever. This journey would not have been possible without his valuable supports. I gratefully thank Ali for encouraging and inspiring me to pursue and follow all my dreams.

RÉSUMÉ

De nos jours, l'emballage facile à ouvrir pour une grande variété d'applications telles que les marchandises, l'électricité, l'agriculture, les aliments cosmétiques et les emballages médicaux est d'une grande importance en raison des demandes de plus en plus nombreuses des consommateurs. Les polymères à base de polyoléfines ont été largement utilisés comme matériaux d'étanchéité en raison de leurs propriétés mécaniques, rhéologiques et thermiques acceptables ainsi que de leur faible coût. Néanmoins, un grand nombre de formulations d'étanchéité constituées de mélanges à base de polyoléfine souffrent d'une fenêtre de température thermocollante pelable étroite (ΔT_p). L'incorporation de l'argile organo-modifiée (organoargile) aux couches de scellement est une nouvelle approche pour réaliser des scellants pelables avec un large ΔT_p. Cependant, les produits d'étanchéité pelables fabriqués à partir de nanocomposites d'argile sont à leur début et les facteurs clés contrôlant la performance de décollement des scellants nanocomposites n'ont pas encore été établis.

Dans la première partie de ce travail, nous discutons de l'effet de l'incorporation de divers types d'organoargiles sur la performance de pelage du scellant polyéthylène à faible densité (LDPE). Le mélange LDPE/organoargile non modifié représente une performance de joint d'étanchéité de verrouillage semblable au scellant de LDPE pur. L'augmentation de la quantité de modificateur de surface de l'argile entraîne une amélioration des performances de décollement. L'étude de diverses teneurs en organoargiles de 2 à 10% en poids indique qu'au moins 6% en poids d'organoargile sont nécessaires pour obtenir un ΔT_p d'environ 12-15 °C à partir du scellant LDPE sans l'utilisation d'agent compatibilisant. Les résultats de la diffraction des rayons X (WAXD) et de la microscopie électronique à transmission (TEM) indiquent qu'une amélioration substantielle de la dispersion et de la distribution des argiles dans la couche de scellement est obtenue en rendant l'organoargile compatible avec l'anhydride maléique greffé PE (PE-g-MA). En conséquence, le ΔT_p augmente à 45 °C avec le même niveau de la teneur en organoargile (6% en poids). En augmentant le rapport pondéral PE-g-MA/organoargile de 2 à 5, une dispersion semi-exfoliante des argiles organo-modifiée dans la couche de scellement est obtenue et un ΔT_p ultra-large de plus de 100 °C est atteint. L'analyse des résultats du test de pelage en T et de la microscopie électronique à balayage (MEB) de la surface de scellement des scellants indique que la dispersion et la distribution des particules d'argile dans la zone du joint sont les principaux facteurs contrôlant la performance de pelage du PE/argile les scellants nanocomposites.

Dans la seconde partie de cette étude, nous examinons l'effet de la localisation de l'argile dans deux mélanges à base de LDPE, à savoir le LDPE/copolymère d'éthylène-acrylate de méthyle (EMA) et le LDPE/terpolymère éthylène-acrylate de méthyle-méthacrylate de glycidyle (EMA-GMA). Les résultats WAXD et TEM sont en accord avec les prédictions thermodynamiques qui montrent la localisation de l'argile à l'interface de LDPE/EMA et dans la phase dispersée EMA-GMA dans le mélange LDPE/EMA-GMA. La localisation de l'argile organo-modifiée est également confirmée par des analyses rhéologiques et mécaniques. L'incorporation de l'argile de 4 phr au système LDPE/EMA convertit son comportement de scellement de verrouillage en un comportement pelable avec un ΔT_p large de plus de 35 °C. En revanche, l'aptitude au pelage du scellant nanocomposite à base de LDPE/EMA-GMA/organoargile a légèrement changé par rapport au scellant de mélange LDPE/EM-GMA. La localisation des particules d'argile à l'interface du mélange LDPE/EMA se traduit par une réduction de la taille des particules et de la distance interparticulaire, ce qui facilite le pontage de la fissure lors du pelage. Cependant, l'encapsulation d'organoargiles dans la phase dispersée EMA-GMA agit contre la pelabilité.

Dans la troisième partie de ce travail, l'effet de la nanoargile sur la performance de pelage et le vieillissement des scellants de mélange LDPE/PB-1 sont étudiés. En utilisant l'analyse WAXD et l'imagerie TEM, on a démontré que lorsque l'argile est ajouté au mélange LDPE/PB-1, il a tendance à se localiser à l'interface des composants du mélange. Le mélange LDPE / PB-1 contenant 5% en poids d'agent d'étanchéité PB-1 et LDPE/organoargile contenant 1 phr d'argile organo-modifiée présentent tous les deux un comportement d'étanchéité semblable à celui du scellant LDPE pur. En revanche, le scellant LDPE/PB-1/organoargile contenant 5% en poids de PB-1 et 1 phr d'argile présente une performance de pelage polyvalente sur un large ΔT_p d'environ 100 °C. L'efficacité de 1 phr organoargile dans l'amélioration de la pelabilité est réduite en augmentant la teneur en PB-1 dans les mélanges. Cela pourrait être dû à la plus faible couverture interfaciale des particules d'argile à l'interface des mélanges de LDPE/PB-1 en raison de l'augmentation de la teneur en PB-1. La force d'arrachement des scellants LDPE/PB-1 contenant 5 à 20% en poids de PB-1 est diminuée au cours du vieillissement en raison de la formation de cristaux de PB-1 instables après le thermoscellage, tel que démontré par les analyses par WAXD. Aucune trace de la forme cristalline métastable II n'est détectée après thermoscellage des scellants nanocomposites LDPE/PB-1/organoargile, ce qui correspond à la performance de pelage constante observée pour les scellants nanocomposites.

Dans la quatrième partie de cette étude, le mécanisme sous-jacent du polymorphisme PB-1 après thermoscellage du mélange LDPE/PB-1 et des scellants nanocomposites est étudié. Les images SEM indiquent que PB-1 forme des structures nanofibrillaires dans les mélanges de LDPE/PB-1 contenant 5 à 20% en poids de PB-1. L'épaisseur moyenne des nanofibrilles de PB-1 a diminué significativement de 100 à 60 nanomètres lors de l'incorporation de 1 phr organoargile à l'agent d'étanchéité contenant 5% en poids de PB-1. L'épaisseur des nanofibrilles PB-1 a légèrement diminué de 190 à 170 nm et de 200 à 190 nm dans les scellants contenant respectivement 10 et 20% en poids de PB-1. Les résultats du FTIR et du WAXD ont révélé la présence de la forme stable I et possiblement la formation directe de la forme 1. Ceci peut être attribué à l'effet mémoire de la fusion et à la ségrégation des cristaux dans le procédé de thermoscellage rapide plutôt qu'à la fusion complète des cristaux. En plus des formes I/I′, la forme métastable II est détectée juste après le thermoscellage qui est responsable du vieillissement des agents d'étanchéité LDPE/PB-1. Aucune trace de la forme II n'est observée après le thermoscellage du nanocomposite LDPE/PB-1/organoargile, alors que les cristaux avec les formes I et III sont détectés avec les caractérisations par FTIR et WAXD juste après le thermoscellage. Ceci est attribué à la cristallisation confinée des nanofibrilles PB-1 comme confirmé par les résultats de la caractérisation par FTIR polarisée qui indiquent l'orientation anisotrope des cristaux PB-1 dans les matériaux d'étanchéité nanocomposites. Ce confinement est imposé en raison de la solidification antérieure de la matrice de LDPE avec une température de cristallisation plus élevée à 95 °C comparée à celle de PB-1 à 75 °C. La cristallisation des nanofibrilles PB-1 dans du LDPE solidifié est encore confinée en présence d’organoargiles à l'interface et possiblement dans la phase PB-1.

Les résultats de cette étude établissent une stratégie pour produire des produits d'étanchéité pelables avec des performances de pelage souples et constantes sur une large gamme de températures de thermoscellage.

ABSTRACT

Nowadays, easy to open packaging for vast variety of applications such as merchandise, electrical, agricultural, cosmetic food and medical packaging is of great importance due to increasingly consumer demands. Polyolefin-based polymers have been extensively used as seal materials due to their acceptable mechanical, rheological and thermal properties as well as low cost. Nonetheless, many seal formulations made of polyolefin based blends suffer from narrow peelable heat seal temperature window (ΔT_p). The incorporation of organoclay to seal layers is a novel approach to achieve peelable sealants with broad ΔT_p. However, peelable sealants made of clay nanocomposites are in their infancy and this dissertation reports on the key factors controlling the peel performance of the nanocomposites sealants containing nanoclay.

In the first part of this work, we discuss the effect of incorporation of various types of organoclays on the peel performance of low density PE (LDPE) sealant. PE/unmodified clay sealant represents a lock seal performance similar to neat LDPE sealant. Increasing the amount of clay surface modifier results in enhanced peel performance. Investigating various contents of organoclays from 2 to 10 wt% indicates that at least 6 wt% of organoclay is needed to achieve a ΔT_p of about 12-15 °C from LDPE sealant without the use of any compatibilizer. Wide angle X-ray diffraction (WAXD) results and transmission electron microscopy (TEM) images indicate that a substantial enhancement in the dispersion and distribution of the organoclays in the seal layer is achieved upon compatibilizing the organoclay with PE-grafted maleic anhydride (PE-g-MA) copolymer. As a result, the ΔT_p enhances to 45 °C with the same level of the organoclay content (6 wt%). By increasing PE-g-MA/organoclay weight ratio from 2 to 5, a semi-exfoliate dispersion of the organoclays in the seal layer is achieved and results is an ultra-wide ΔT_p of over 100 °C. Analyzing the T-peel test results and scanning electron microscopy (SEM) of the peel fractured surface of the sealants indicated that the dispersion and distribution of the clay particles in the seal area are the main factors which control the peel performance of the PE/clay nanocomposite sealants.

In the second part of this study, we examine the effect of organoclay localization in two PE based blends i.e. LDPE/ethylene-methyl acrylate copolymer (EMA) and LDPE/ethylene-methyl acrylate-glycidyl methacrylate terpolymer (EMA-GMA). The WAXD and TEM results are in agreement with the thermodynamic predictions which show the localization of organoclay at the interface of LDPE/EMA and within the EMA-GMA dispersed phase in the LDPE/EMA-GMA blend. The

localization of organoclay is also confirmed through rheological and mechanical analyses. The incorporation of 4 phr organoclay to the LDPE/EMA system converts its lock seal behavior to a peelable one with a wide ΔT_p of over 35 °C. In contrast, the peelability of the LDPE/EMA-GMA/organoclay nanocomposite sealant marginally changed when compared to the LDPE/EM-GMA blend sealant. The localization of clay particles at the interface of LDPE/EMA blend results in a reduced particle size and interparticle distance, which facilitate the crack bridging upon peeling. However, the encapsulation of organoclays within the EMA-GMA dispersed phase works against peelability.

In the third part of this work, the effect of nanoclay on the peel performance and aging of the LDPE/PB-1 blend sealants are investigated. Using WAXD analysis and TEM imaging, it is shown that when organoclay is added to the LDPE/PB-1 blend, it tends to localize at the interface of the blend components. The LDPE/PB-1 blend containing 5 wt% of PB-1 and LDPE/organoclay sealant containing 1 phr organoclay both exhibit lock seal behavior similar to the neat LDPE sealant. In contrast, LDPE/PB-1/organoclay sealant containing 5 wt% of PB-1 and 1 phr organoclay shows a versatile peel performance over a wide ΔT_p of about 100 °C. The effectiveness of 1 phr organoclay in enhancing peelability is reduced by increasing PB-1 content in the blends. This might be due to the lower interfacial coverage of the clay particles at the interface of LDPE/PB-1 blends due to increase in the PB-1 content. The peel force of the LDPE/PB-1 sealants containing 5 to 20 wt% of PB-1 is decreased upon aging due to the formation of unstable form II crystals of PB-1 after heat sealing as approved through WAXD experiments. No trace of the metastable crystal form II is detected after heat sealing of the LDPE/PB-1/organoclay nanocomposites sealants which is in line with the consistent peel performance observed for the nanocomposite sealants.

In the fourth part of this study, the underlying mechanism of PB-1 polymorphism after heat sealing of the LDPE/PB-1 blend and nanocomposite sealants is investigated. SEM images indicate that PB-1 forms nanofibrillar structures in the LDPE/PB-1 blends containing 5 to 20 wt% PB-1. The average thickness of PB-1 nanofibrils significantly decreased from 100 to 60 nanometers upon the incorporation of 1 phr organoclay to the sealant containing 5 wt% of the PB-1. The thickness of PB-1 nanofibrils moderately decreased from 190 to 170 nm and from 200 to 190 nm in the sealants containing 10 and 20 wt% of PB-1, respectively. FTIR and WAXD results revealed the presence of the stable form I and possibly direct formation of form I′. The presence of form I and direct formation of form I′ can be attributed to melt memory effect and crystal segregation in the fast heat

sealing process rather than complete melting of the crystals. In addition to the forms I/I′, the metastable form II is detected right after the heat sealing which is responsible for the aging of the LDPE/PB-1 sealants. No trace of form II is observed after the heat sealing of the LDPE/PB-1/organoclay nanocomposite, while the crystals form I′ and form III are detected trough FTIR and WAXD patterns right after heat sealing. This is attributed to the confined crystallization of the PB-1 nanofibrils as confirmed by the results of polarized FTIR experiment which indicate anisotropic orientation of the PB-1 crystals in the nanocomposite sealants. This confinement is imposed due to the earlier solidification of the LDPE matrix with a higher crystallization temperature at 95 °C compared to that of the PB-1 at 75 °C. The crystallization of PB-1 nanofibrils in solidified LDPE is further confined in the presence of organoclays at the interface and possibility within the PB-1 phase.

The results of this study establish a strategy to produce peelable sealants with versatile and consistent peel performance over a wide range of heat seal temperatures.

TABLE OF CONTENTS

LIST OF TABLES

LIST OF FIGURES

LIST OF SYMBOLS AND ABBREVIATIONS

Symbols:

G^*	complex modulus
CA	contact angle
ρ	density of polymers
σ_i^d	dispersive component of surface tension
ω	wettability parameter
G	Gibbs free energy
σ_{ij}	interfacial tension
G''	loss modulus
M_w	molecular weight of the polymers
σ_i^p	polar component of surface tension
$\dot{\gamma}$	shear rate
G'	storage modulus
σ	surface/interfacial tension
η	viscosity
$\eta *$	complex viscosity
η_0	zero shear viscosity
λ	x-ray wavelength
θ	the angle of the x-ray incident of reflected beam
d	crystal plane distance
ΔH_m	heat of fusion
$\Delta H_{m,100}$	enthalpy of 100% crystal
X_c	degree of crystallinity

T_i	heat seal initiation temperature
T_m	melting temperature
T_c	crystallization temperature
ΔT_p	peelable heat seal temperature range
E_p	plastic dissipated energy
E_a	adhesive fracture energy
$E_{d,p}$	dissipated energy in the peel arm
$E_{d,s}$	deformation energy of the peeled seal area
W	width of the seal
L	length of the seal

Abbreviations:

LDPE	low density polyethylene
HDPE	high density polyethylene
LLDPE	linear low density polyethylene
PP	polypropylene
PE	polyethylene
mPE	metallocene polyethylene
EMA	ethylene-methyl acrylate copolymer
EVA	ethylene-vinyl acetate copolymer
EMA-GMA	ethylene-methyl acrylate-glycidyl methacrylate terpolymer
PB-1	polybutene-1
OC	organoclay
Organoclay	surface modified clay

NC	nanoclay
CPN	clay polymer nanocomposite
C15	Cloisite15
C20	Cloisite20
Na^+	unmodified sodium montmorillonite
MMT	montmorillonite
OMt	organomodified montmorillonite
CEC	cation exchange capacity
TD	transverse direction
MD	machine direction
ND	normal direction
wt	weight
PE-g-MA	polyethylene grafted maleic anhydride
WAXD	wide angle x-ray diffraction
TEM	transmission electron microscopy
SEM	scanning electron microscopy
DSC	differential scanning calorimetry
FTIR	Fourier transform infrared
POFTIR	polarized Fourier transform infrared
ATR-FTIR	attenuated transmission reflectance-Fourier transform infrared
TSE	twin screw extruder

LIST OF APPENDICES

CHAPTER 1 INTRODUCTION

1.1 Introduction

An effective packaging with appropriate barrier and mechanical properties, must be sealed tightly with the container to efficiently protect the product inside. In many cases, both sides of the seal are welded together so that the opening of the packaging is not possible unless by cutting instruments. Opening the packaging by this way is associated with many risks and is not convenient regarding to the modern life style. The high cost of compensations that is paid for the injuries related to packaging (Winder, Ridgway, Nelson, & Baldwin, 2002) along with increasing demands of consumers for convenient packaging, encourage film packaging manufacturers to produce user-friendly packaging with safe and effective seal performance (Gómez, Martín-Consuegra, & Molina, 2015). Easy opening packaging includes a wide variety of packaging with peelable sealant that requires a low peel force (about less than 650 N/m) to be opened (Manias et al., 2009).

Basically, three rupture mechanisms or failures describe the peeling process: adhesive or interfacial failure (M. Nase, Großmann, Rennert, Langer, & Grellmann, 2014a), cohesive failure (Michael Nase, Langer, & Grellmann, 2008), and their combination (Martínez-García et al., 2008). In adhesive failure, the separation takes place either at the interface of the sealant and substrate or at the interface of the sealant layer and its adjacent layer in a multilayer film. No residue is left on the surface of the substrate after opening an adhesive film, therefore, these types of films are not recommended for perishable products. In the cohesive peeling mechanism, the separation takes place from inside of sealant layer and the residue of the seal remains on the substrate. Thus, this failure mechanism results in a more functional and reliable packaging performance. Furthermore, cohesive peels are less sensitive to the seal parameters i.e. heat seal temperature, pressure and dwell time (M. Nase et al., 2014a).

Cohesive peelable films are usually produced by blending two or more immiscible polymers and generally are thicker than the adhesive sealants to have enough room for separation from inside the seal layer (Hwo, 1987). Since the interface of the blend components is known to be the weakest point in an immiscible blend, therefore, cracks initiate at the interface of phases and develop throughout the inside of the seal layer upon peeling process. For this to happen, the yield strength of the sealant must be higher than the interfacial adhesions inside the seal layer, otherwise the

sealant will be elongated prior to peeling. If the yield strength of the sealant is equal to the interfacial adhesions in seal, the peeling is accompanied with elongation and yielding.

Among various polyolefins, PE and its counterparts are mainly used for seal applications owing to their fair mechanical properties and particularly their low cost (Coles, McDowell, & Kirwan, 2003; Han, 2005; Robertson, 2013). Many of these sealants suffer from narrow peelable heat seal temperature window, ΔT_p, possibly due to their insufficient incompatibility on one hand and their low yield strength on the other (Liebmann, Schreib, E. Schlözer, & Majschak, 2012). Thus, the sealants yield upon peeling prior to be peeled. Blending at least 10 wt% of PB-1 with PE based materials is known as an effective approach to achieve peelable sealants with wide ΔT_p (Hwo, 1987). However, PB-1 exhibits unstable and complex polymorphism after heat treatment (Kalay & Kalay, 2002; Qiao, Wang, & Men, 2016; Yamashita, Kato, K., A., & H., 2007). After melting and during cooling at ambient pressure, PB-1 crystallizes into the kinetically favored metastable form II. The metastable form II spontaneously converts to thermodynamically favored stable form I crystal with time. This conversion is very slow and, depending on the physical conditions, may last several weeks. Since the density and thermal properties of forms II and I are very different, form II to form I conversion is accompanied by shrinkage and failure of the sealant (Azzurri, Flores, Alfonso, & Baltá Calleja, 2002; Michael Nase, Androsch, Langer, Baumann, & Grellmann, 2008). Thanks to the extensive research efforts, crystal from II to form I conversion might be accelerated with various approaches such as pressure (Nakafuku & Miyaki, 1983), orientation (Liu et al., 2012; Samon, Schultz, Hsiao, Wu, & Khot, 2000), copolymerization (Kaszonyiova, Rybnikar, Lapcik, & Manas, 2012; Shieh, Lee, & Chen, 2001; Stolte & Androsch, 2013) and incorporation of additive (Yamashita et al., 2007; X. Zhang, Zhang, & Shi, 1992) but, the metastable polymorphism of PB-1 still remains challenging, which restricts the fair use of this commercially interesting polymer in a variety of applications as well as packaging.

In addition to polymer blending, peelable seals with cohesive failure can be generated by incorporation of nanoclay in the seal layer (J. Zhang et al., 2009). Nanocomposite sealants can open a new window towards packaging industry since, taking advantage of the high barrier and mechanical performances of the nanoclays, monolayer films with lower thickness and less material as well as easier and faster melt processing can be produced instead of multilayer films with the same level of seal properties. It is known that the microstructure of nanocomposites, i.e. dispersion and distribution of nanoparticles, are the main parameters to control their final properties (Sinha

Ray & Okamoto, 2003b) while, there is lack of information on the effects of these key parameters on the peel and seal properties.

Furthermore, blending PE with its counterparts with lower softening point such as PE copolymers and terpolymers is a common approach to reduce the heat seal initiation temperature and optimize the seal properties of sealant. It is also reported that blending PE with its copolymers containing polar groups in the polymer backbone such as ethylene vinyl acetate copolymer (EVA) is effective to achieve peelable sealants with promoted peelability from PE/clay nanocomposite based sealants (Manias et al., 2009). In this regard, investigating the organoclay localization in the sealants composed of PE based blends is of great importance. In such a case, the preferred localization of the clay particles may profoundly affect the final properties of the sealant. To our knowledge, there is no literature to discuss the effect of organoclay localization on the peel performance of the sealants made of polymer blends.

CHAPTER 2 LITERATURE REVIEW

2.1 Film casting

Cast extrusion is one of the most important techniques that is used to produce thousands of tons of polymer films and coatings. In the film casting process, a molten polymer is extruded through a flat die to form continuous thin sheet that is also called “web”. The extruded polymer is stretched in machine direction (MD) and rapidly cooled using air knifes and wound on calendar rolls, which are chilled with cold water (Figure 2.1). Although the thickness of the film near the die exit is increased due to die swell (because of molecular stress relaxation), the monotonic thickness reduction of the film takes place along the take-up length. The take-up length is defined as the distance between the die and chill roll. The amount of the stretch of the film along take-up length is called “draw ratio” which is defined as the ratio of the tangential velocity of the chill roll per linear velocity of the extruded polymer near the die. Necking and edge beading are respectively the inhomogeneity reduction in width and thickness of the film and are the two defects that usually take place during cast extrusion (Acierno, Di Maio, & Ammirati, 2000; Pol et al., 2014). Temperature variations from the die to chill roll as well as molecular weight, molecular weight distribution and presence of long chain branches are the parameters that affect necking and the edge breading defects (Barborik & Zatloukal, 2015; Chikhalikar et al., 2015; Rokade et al., 2017). The presence of long chain branches leads to a stress hardening and increases the deformation resistance of the film and consequently results in further and earlier necking near the die exit. The cooling rate of the extruded polymer is an important factor that affects polymer crystallinity after extrusion. A high cooling rate considerably decreases the degree of crystallinity of polymer (Mueller, Capaccio, Hiltner, & Baer, 1998).

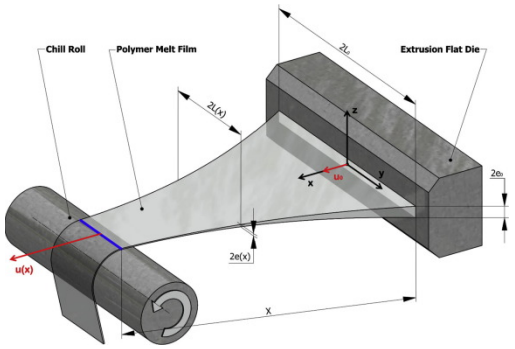

Figure 2.1. A schematic of the film casting (Barborik & Zatloukal, 2015).

2.2 Heat sealing process

Heat sealing is a process in which, two structures containing at least one thermoplastic layer are sealed over a time so called dwell time under specific heat and pressure (Figure 2.2). The seal pressure is defined as the minimum platen pressure that is required to bring the seal surfaces into an intimate contact as low as 5 Å. During sealing time, the applied pressure holds the two surfaces in a close contact and heat is transferred to the seal layer through conduction or radiation. The heat must be sufficient to make the seal structures molten and allow the seal surfaces to fuse together and make a homogenous interphase (Meka & Stehling, 1994; Theller, 1989).

The sealant characteristics are associated to material functions such as molecular weight, molecular weight distribution and crystallinity (Moreira, Dartora, & Paulo dos Santos, 2017; Planes, Marouani, & Flandin, 2011). Once the pressure is removed at the end of dwell time, the seal materials are still molten and soft. The molecular interactions in the seal layer must be high enough to maintain the seal layer against external forces that may act to pull them apart and withstand the strain while it is molten. The strength of the seal against external forces in a molten state to maintain its integrity is known as hot tack strength. In contrast to hot tack, which is the strength of the seal in molten or soft state right after sealing, the seal strength is defined as the strength of the seal after cooling to the ambient temperature. The maximum load required to pull the seal apart at ambient temperature is reported as seal strength (Aithani, Lockhart, Auras, & Tanprasert, 2006). The seal conditions including sealing pressure, dwell time and heat seal temperature significantly affect the seal properties as well as the mechanisms of failure upon peeling the seal (Iwasaki, Takarada, & Kikutani, 2016; Planes et al., 2011; Yuan & Hassan, 2007).

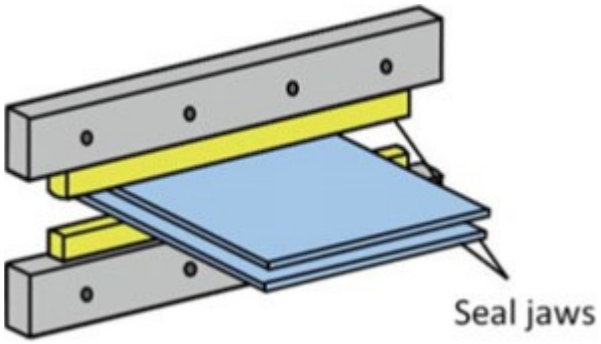

Figure 2.2. Schematic of the heat seal process (M. Nase et al., 2017).

2.2.1 Platen pressure

It has been reported that a minimum pressure is required to bring the seal surfaces into a close and intimate contact and an increase in the platen pressure does not have considerable influence on the seal strength. Aithani et al. (Aithani et al., 2006) investigated the effect of seal parameters on the failure mechanisms of five different films including LDPE, LLDPE, LDPE-black, HDPE and cast PP (CPP). Their results revealed that a minimum pressure was required to initiate sealing. After sealing was initiated, increasing the pressure did not have notable effect on the seal strength of the sealants. The findings of another work by Yuan and Hassan (Yuan & Hassan, 2007) showed the same behavior for the effect of the platen pressure on the seal strength of an oriented polypropylene (OPP)/metallic cast polypropylene (MCPP). They observed that a minimum pressure (about 1.25 bars) was required to form a sealing layer and no seal was produced below that pressure. Further increasing the pressure during sealing did not affect the seal strength of the sealants.

2.2.2 Dwell time

The results of several studies revealed that increasing dwell time after the seal strength reaches a plateau does not have significant effect on seal strength. In fact, increasing dwell time below the seal strength plateau results in higher seal strength while increasing dwell time after reaching seal strength plateau does not have significant effect on it. By increasing the seal temperature, a lower dwell time is needed to achieve equivalent seal strength. Usually, lowering dwell time is more favorable in industry to increase the production rate. It is known that at temperatures under the melting point of seal material, dwell time does not have any influence on the seal strength while the required dwell time becomes shorter by increasing sealing temperature above the heat seal initiation temperature

2.2.3 Heat seal temperature

The effect of the heat seal temperature is predominant over the effect of the dwell time and platen pressure. Aithani et al. (Aithani et al., 2006) observed that increasing the heat seal temperature enhances the seal strength of the samples. Their results also revealed a predominant effect of the heat seal temperature on the seal strength over the effects of dwell time and pressure. Mazzola et al. (Mazzola, Cáceres, França, & Canevarolo, 2012) studied the correlation between the seal properties and heat sealing of polyolefin films. According to their results, the seal strength of

various polyolefins including propylene-ethylene plastomer (PEP) and terpolymer of propylene-ethylene-butene (TERP) increased by increasing the seal temperature. Tetsuya et al. (Tetsuya, Ishiaku, Mizoguchi, & Hamada, 2005) studied the effect of heat seal temperature on the mechanical properties of OPP/CPP films. They indicated that below the heat seal initiation temperature a weak seal is achieved while, increasing temperature beyond the heat seal initiation results in a hermetic seal. Similar results were earlier reported by Mueller et al. (Mueller et al., 1998). Figure 2.3 shows more fibril and membrane-like structures by increasing the seal temperature in the morphology of the peeled surfaces. An increase in the density of the interconnected structure by increasing temperature was attributed to the more diffusion of the molecular entanglements across the interface.

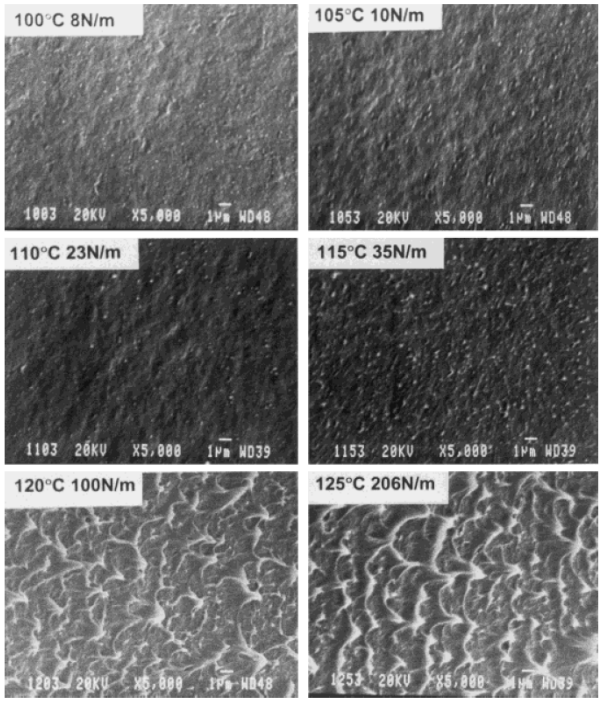

Figure 2.3. SEM images of the peeled surfaces of LLDPE films sealed for 1 sec. Temperatures and corresponding seal strengths are indicated (Mueller et al., 1998)

It was reported that heat sealing temperature must be higher than the melting point of seal materials to allow movement of the polymer chains across the interface (Lamnawar, Vion-Loisel, & Maazouz, 2010). By increasing the heat seal temperature, the seal strength enhances to reach a plateau. The temperature at which the plateau is started is called plateau initiation temperature (T_{pi}) and the temperature at the end of the plateau is named plateau final temperature (T_{fi}). After the

plateau, the seal strength gradually decreases by increasing the heat seal temperature, which is attributed to thinning out and failing the seal under the seal jaw pressure at elevated heat sealing temperatures. Figure 2.4 illustrates the correlation between the heat seal temperature and seal strength. The width of the plateau in this curve is very important. The wider the heat seal plateau, the lower the heat sealing complexity and so one can increase the heat seal temperature to decrease the dwell time and increase the rate of the sealing process. The width of the plateau is dependent on the molecular characteristics of seal materials (Farley & Meka, 1994).

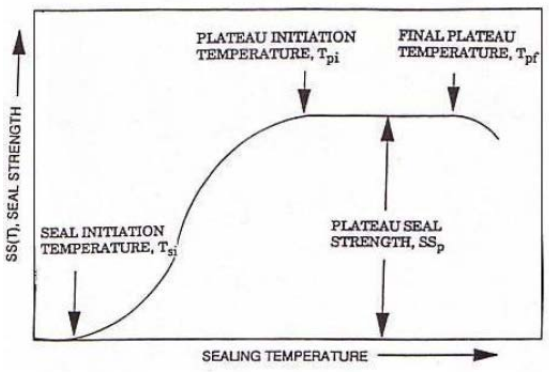

Figure 2.4. Correlation between sealing temperature and seal strength of the semi-crystalline materials (Farley & Meka, 1994).

2.2.4 Effect of molecular architecture and crystallinity on heat seal properties

It has been reported that the seal properties are strongly influenced by the molecular structures and rheological properties of seal materials. In order to attain a reliable seal, it is very important for the seal materials to be completely melted under the defined seal process conditions and defuse across the interface to make a strong bridge. For crystalline polymers, a good seal is obtained when all the crystals are melted, diffuse across the interface and form entanglements. More crystalline lamellas and tie chains are produced by increasing the molecular weight. Well-ordered crystalline structures are produced in long and linear chains which provide strong connected anchors to the tie chains (Farley & Meka, 1994; Moreira et al., 2017). It has been shown that low molecular weight chains with short chain branches (SCB) contain a small fraction of crystallinity and easily melt and fuse to the interface in heat sealing process. After the heat sealing, during the cooling, crystalline structures are formed again and strengthen the seal area. The crystalline structure produced by low molecular weight chains with SCB makes weak anchors and so are not responsible of the high seal

strength. Chains with low content of SCB have higher molecular weights and more crystalline structures with strong interconnecting anchors. These high molecular weight segments need more time and temperature to be molted in order to result in a fully sealed area (Mueller et al., 1998).

Blending conventional polyethylene (PE which produced by the Ziegler-Natta catalysts) with metallocene polyethylene (mPE) results in a sealant with higher mechanical properties and seal strength, which is due to the narrower weight distribution of mPE. This improvement in mechanical and seal strength is accompanied with more difficulties in process-ability and heat sealing (Jordens, Wilkes, Janzen, Rohlfing, & Welch, 2000; Majumdar & Kale, 2001). It can be concluded that although increasing the molecular weight and molecular weight distribution of the seal material is accompanied with more difficulties in melt processing, but such materials have higher mechanical properties as well as stronger seal strengths.

Najerzadeh and Ajji (Najarzadeh, 2014) indicated that increasing the long chain branches (LCB) of PE results in lower adhesion strength across the seal while higher seal strength is achieved for sealants with more linear structure such as mPE.

2.3 Peelable sealants

The material selection is the first criterion to produce an appropriate sealant for different applications. The selected materials for easy to open films should be sealable through one of the following sealing methods: heat seal, radiofrequency, high frequency, high pressure and ultrasonic (Selke & Culter, 2016) and also should be easily peeled after sealing with low peel force (lower than 650 N/m) (Manias et al., 2009). During heat sealing, the hot jaws come to the direct contact with the outer layer and so first the heat transfers to the outer layer and then transfers to the inner seal layer. In order to prevent the adhesion of the outer layer to the seal jaw, the outer layer should not melt during the sealing process. Therefore, the melting temperature of the outer layer must be higher than that of the inner seal layer. The seal materials as well as the peelable seal materials are preferred to have a low heat seal initiation temperature to ensure a fast production line speed and also, to prevent the melting of the outer layers.

A low heat seal initiation temperature and a wider heat seal temperature window are in favor of a heat seal process with lowest possible complications especially for heat sensitive materials. The seal materials also need to have good hot tack strength that is the strength of the sealant against

external forces after heat sealing while the sealant layer is still molten. The peelable seal materials should have good resistance to withstand tears and punctures that may happen because of the irregularly and rigid shapes of the packed products. Low shear thinning to facilitate melt processing should also be considered in selection of the materials for easy opening seal films (Julie W. Gibbons, Alveda J. Williams, Rajen M. Patel, Jeffrey J. Wooster, Enrique Torres, Miguel A. Prieto Goubert, 2006).

Polyolefins are reported to have most of the required properties by the peelable sealants and are the best candidates for the seal layer due to their superior ability to be extruded, molded or blown into different shapes (Wagner Jr., 2009). Low cost, low heat seal initiation temperature and good rheological properties are among the advantages of polyolefins (Coles et al., 2003). Generally, polyolefins are thermoplastic materials derived from polyethylene (PE) or polypropylene (PP) (Wagner Jr., 2009).

Usually, two or more immiscible polymers are melt blended to produce peelable seals. Some examples of immiscible polymer blends that are used for peelable sealants are ionomer/ethylene vinyl acetate (EVA), EVA/polybutene-1 (PB-1), metallocene polyethylene (mPE)/propylene (PP), ethylene acrylic acid (EAA) copolymer/EVA and EAA/PB-1 (Liebmann et al., 2012). PB-1 is used as the minor phase in most of the peelable seal systems (Bai & Wang, 2003, US7055683 B2, 2003, US6630237 B2, 2003; Hwo, 1987; Mohammdi, Ajji, & Tabatabaei, 2015). PB-1 considerably reduces the heat seal initiation temperature and results in a wide range of peelable heat seal temperature. Although blending PB-1 with many polyolefins results in cohesive peelable film, but PB-1 is a polymorphic resin with different crystalline forms. PB-1 exhibits five different crystalline forms in which hexagonal crystalline form I and tetragonal crystal form II are of more interest. During melt crystallization in ambient pressure, crystals form II appear and then spontaneously transfer to thermodynamically stable crystalline phase I at room temperature (Holland & Miller, 1964; Kalay & Kalay, 2002; Qiao & Men, 2017; Stolte, Androsch, & Di Lorenzo, 2014). This phase transition is very slow and may be completed after several weeks. Different crystalline forms of PB-1 exhibit different physical, mechanical and thermal properties, therefore its crystal transformation lead to profound changes in its properties after melt processing (Azzurri et al., 2002; Kaszonyiova M, Rybnikar F, 2005). Nase et al., investigated the peel strength of films blends of LDPE/PB-1 (Michael Nase, Androsch, et al., 2008). Their results showed that after sealing at 413 K crystal-crystal transformation from meta-stable tetragonal form II to stable hexagonal form I,

significantly reduced the peel strength of the sealant as it is illustrated in Figure 2.5. This figure also illustrates the wide angle X-ray scattering (WAXS) of the LDPE/iPB-1 containing 20 m% iPB-1 after 2 and 240 hours after sealing at 413 K. As it can be seen in this figure, by increasing the time from 2 hours to 240 hours the intensity of the peaks related to crystals form II at 11.9^{o} decreased while the intensity of the peaks related to crystals form I at 9.9^{o} increased.

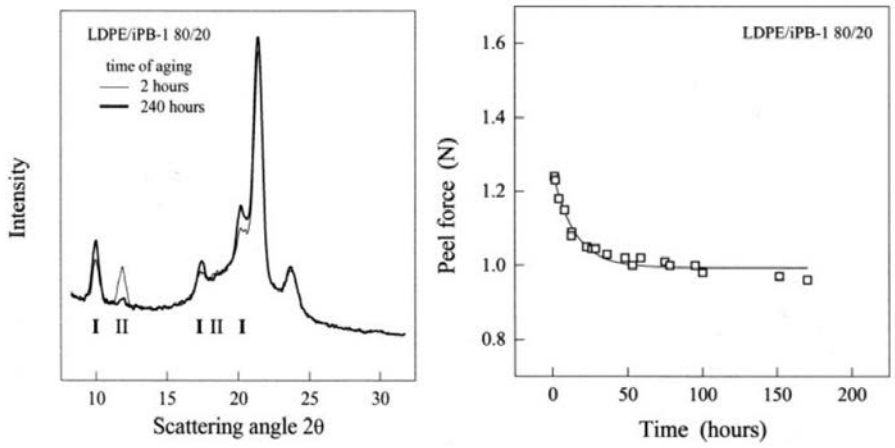

Figure 2.5. WAXS of LDPE/iPB-1 containing 20 m% iPB-1 after 2 and 240h after sealing at 413 K (left side), Peel force of the blend of LDPE/iPB-1 containing 20 m% iPB-1 as a function of time after sealing at 413 K (right side) (Kaszonyiova M, Rybnikar F, 2005).

In addition to PB-1, although the blending of different thermoplastics with ionomers are also suggested in the literature, but peelable seal containing ionomers usually show stringiness upon peeling. In the packaging of the dry goods, ionomers may also cause static charge because of the ionic sites in their structure and so statically attract the seal contaminations. Ionomers have undesired odor and are expensive as well (Julie W. Gibbons, Alveda J. Williams, Rajen M. Patel, Jeffrey J. Wooster, Enrique Torres, Miguel A. Prieto Goubert, 2006, US 20050266257 A1, 2005). Application of nanoparticles to achieve easy opening packaging was reported in a few literatures. Kinigakis et al. (US9309027 B2, 2016) produced peelable sealant layer consisting of linear low density (LLDPE) as matrix with EVA resin and nanoparticles as minor phases. A similar formulation for sealant layer was also investigated by Manias et al. (Manias et al., 2009). The synergistic effect of the EVA resin and nanoparticles results in an interface which is strong enough to maintain the integrity of the sealant and is weak enough to dictate peel ability with cohesive failure in a broad range of heat seal temperatures with at least 30 ^{o}C heat seal temperature window.

2.4 Fracture Mechanisms upon peeling

When a sealant is subjected to peeling load, various mechanisms may occur based on the seal integrity and interfaces in seal area. If polymer A is sealed against polymer A, a symmetric interface (A/A) is formed. In this case, a lock seal performance is achieved if the sealing temperature and dwell time are high enough to let the polymer chains melt and move across the interface and then, recrystallize upon cooling (Najarzadeh, 2014). Asymmetric interface (A/B) is formed either when, polymer A is sealed against polymer B or when, the sealant is heterogenous and made with polymer blends and nanocomposites (Manias et al., 2009; Michael Nase, Zankel, et al., 2008). In general, there are three types of peeling mechanisms in heterogenous systems including adhesive peel, cohesive peel and combination of them (M. Nase et al., 2017). In an adhesive peel fracture, the two interfaces are adhesively connected and cracks propagate exactly from the interface of the two adhered components during the peeling. Thus, no residue is left on the substrate after peeling (Ernesto Mendoza-Navarro, Diaz-Diaz, Castañeda-Balderas, Hunkeler, & Noret, 2013; M. Nase, Großmann, Rennert, Langer, & Grellmann, 2014b; Santos, Ribeiro, Portela, & Bordado, 2001). In a cohesive peel, the two sides of the seal are welded together while, the sealant is peeled from the weak interfaces inside the seal. Cracks are initiated at the interface of the blend components then, propagate in the seal in a zig-zag pass way upon further loading. In the cohesive peel fracture, some residue are left on the substrate and the peeled surface looks white because of the light scattering from the remained microdomains on the peeled surface (Michael Nase, Zankel, et al., 2008). These peeling mechanisms are illustrated in Figure 2.6.

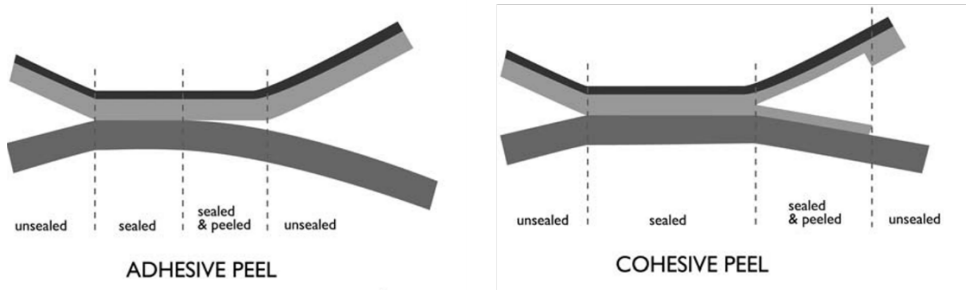

Figure 2.6. Schematic of adhesive and cohesive peeling.

For a sealant to be cohesively peeled, the yield strength of the sealant plays a crucial role (Tetsuya et al., 2005). If the yield strength of the sealant is much lower than the adhesion forces in the seal structure, the sealant yields prior to be peeled. If the yield strength is equal to the adhesion forces

in the seal area, the sealant is yielded and elongated upon peeling. If the yield strength is higher than the adhesion forces inside the seal, the sealant is cohesively peeled. To better understand the fracture mechanisms, usually force-displacement data during the peeling process is necessary. Figure 2.7 indicates an example of the force-displacement diagram upon peeling. The average of the plateau zone is considered as the peel force. The total peel energy, E_G, is defined as the whole area under the force-displacement diagram. $E_{d,P}$ and $E_{d,S}$ are the energy dissipated in peel arm and the energy dissipated due to the seal deformation respectively.

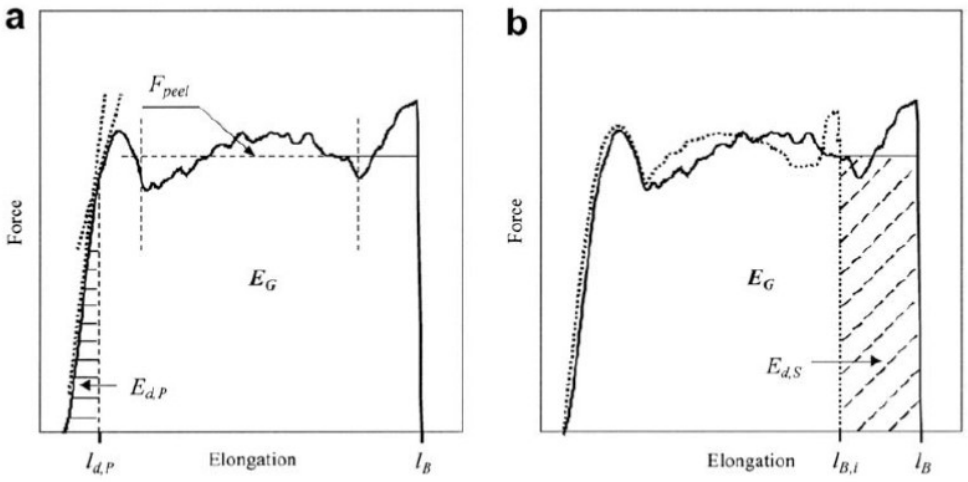

Figure 2.7. A typical force-displacement diagram obtained in a peel test: the continuous curve indicates a real peel curve (a) and the dotted curve is an ideal peel curve without deformation of the seal (b).

If the yield strength is lower than the adhesion forces in the seal layer, $E_{d,P}$ significantly increased without having a plateau upon peeling until the breakage of the sealant. If the yield strength of the seal is comparable to the adhesion forces in the seal area, a very small plateau is observed while, the portion of the $E_{d,S}$ significantly increased. Finally, a wide plateau is achieved when, the yield strength is higher than the adhesion forces in the seal area (M. Nase et al., 2017; Michael Nase, Langer, et al., 2008).

2.5 Layered silicates nanoparticles for easy opening packaging

Nanoparticles are a big category of particles which at least in one of their dimensions are smaller than 100 nanometers. According to their shape, size and principles of their precursors, nano-

particles exhibit enhanced electronic, optic, magnetic, barrier, thermal and mechanical properties (Arora & Padua, 2010; Kango et al., 2013).

Among various types of nanoparticles which can be used in food packaging applications, layered clay and silicate nanoparticles due to their better availability, superior reinforcements, low cost and simple processability are appropriate candidates for food packaging applications as well as for the use in seal layer (Arora & Padua, 2010). The most common type of layered nanoclays is montmorillonite (MMT) that is a hydrated alumina-silicate layered clay and are consisting of an edge-shared octahedral sheet of aluminum hydroxide between two silica tetrahedral layers (Azeredo, 2009). A very high surface to volume ratio and presence of unbounded atoms in their surface, make them unstable resulting in a high surface energy. To reduce energy and become stable, nanoparticles highly intend to agglomerate that results in inverse effects on their properties. Nanoclays also have high surface area (750 m^2/g) and high aspect ratio (100-500) (Arora & Padua, 2010; Sinha Ray & Okamoto, 2003a). To take advantage from high surface area of the layered nanoclays, it is very important to disaggregate and disperse them in the polymer matrix. Depending on the dispersion state of the nanoclays in polymer matrix, three main types of polymer-clay nanocomposites morphologies are reported; tactoids, intercalated and exfoliated (LeBaron, 1999). These structures are illustrated in Figure 2.8.

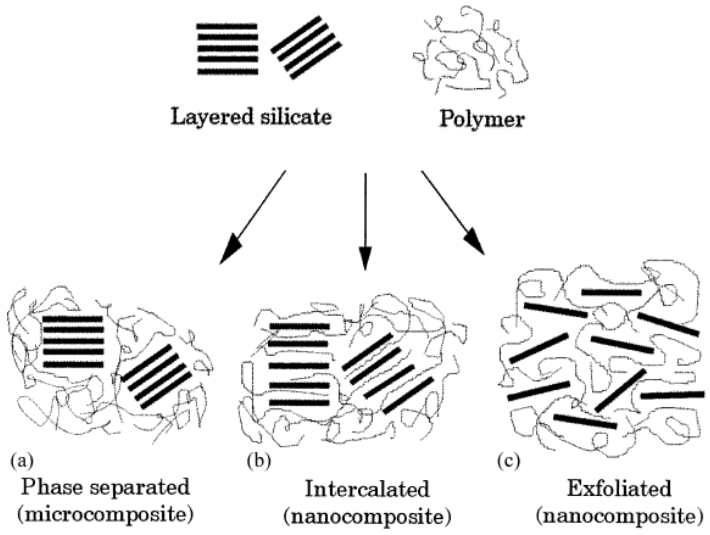

Figure 2.8. Schematic picture of three main structures of polymer-nanoclays hybrids (LeBaron, 1999).

When polymer chains are unable to penetrate and intercalate into the layers of nanoclays, tactoids or phase separation occurs. Diffusion of a single or more than one polymer chain into the layers of the nanoclays results in intercalated nanocomposites. The structure in which layered nanoclays are completely separated and dispersed in polymer matrix is known as exfoliated. X ray diffraction (XRD) and transmission electron microscopy (TEM) are usually used to study nanoclay dispersion in the polymer matrix. According to the Bragg's law ($\lambda=2d \sin\theta$), λ is intensity of diffraction peak, d is distance between nanoclays and θ is diffraction angle, by increasing the distances between layers of nanoclays, diffraction peak is shifted to a smaller diffraction angle. In an exfoliated structure, no peak is observed in XRD patterns due to the large space between the layers. In an exfoliated structure, TEM technique is used to study the morphology of the nanocomposites. Appearance of a broad peak at a very low diffraction angle (less than $2\theta = 10^{o}$) may be due to coexsiting exfoliated and intercalated structures. In this case, XRD is not sufficient to characterize the morphology of the nanocomposites and TEM should be exploited as well (Alexandre & Dubois, 2000; Krishnamoorti, Vaia, & Giannelis, 1996). Figure 2.9 and Figure 2.10 illustrate the examples of the XRD patterns and TEM images to characterize morphology of nanocomposites.

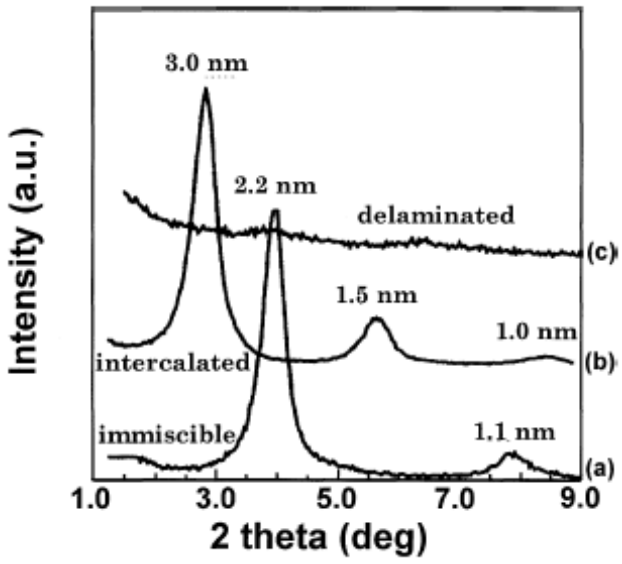

Figure 2.9. Phase separation in nanoclay/HDPE nanocomposites (a), exfoliated structure in the same nanoclay/PS nanocomposites (b), and exfoliated structure for the same nanoclay/silicone rubber nanocomposites (Alexandre & Dubois, 2000).

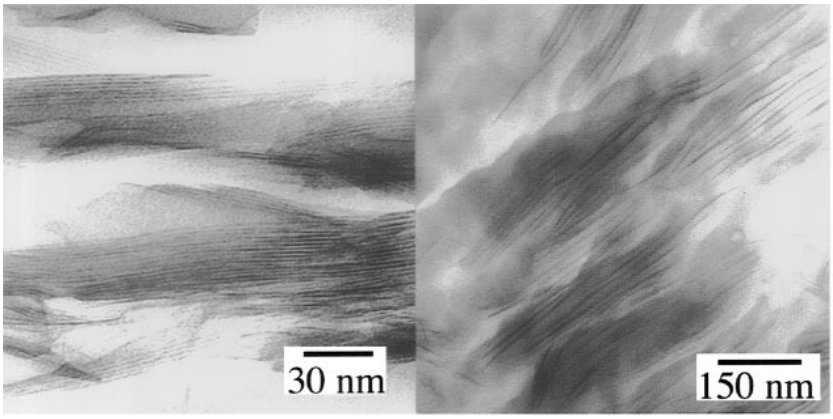

Figure 2.10. TEM images of styrene based nanocomposites. Intercalated microstructure of octadecylammonium-exchanged fluorohectorite/PS nanocomposites (left side) and exfoliated microstructure of bis(2-hydroxyethyl) methyltallow-exchanged montmorillonite/epoxy nanocomposites (right side) (Krishnamoorti et al., 1996).

It is well-known that dispersion and distribution of nanoclays (exfoliated or intercalated) are the key factors controlling the final properties of nanocomposites such as mechanical (Fu & Naguib, 2006; Rhim, Hong, & Ha, 2009; Shah, Shukla, Shah, & Imae, 2016), thermal (Fukushima, Tabuani, Arena, Gennari, & Camino, 2013; S. W. Kim & Cha, 2014; Krump, Luyt, & Hudec, 2006; Modesti, Lorenzetti, Bon, & Besco, 2006; Molinaro et al., 2013; Sharma & Nayak, 2009; Yourdkhani, Mousavand, Chapleau, & Hubert, 2013), optical (Munhoz et al., 2017), electrical (Jlassi et al., 2016; Ma et al., 2014), barrier (Fereydoon, Tabatabaei, & Ajji, 2014; J.-K. Kim, Hu, Woo, & Sham, 2005; S. W. Kim & Cha, 2014) and rheological properties (Hajir Bahrami & Mirzaie, 2011). In melt processed polymer/clay nanocomposites, surface modification of clay nanoparticles and incorporation of compatibilizer are the most common approaches to increase the polymer/clay interactions and thus, enhance the dispersion and distribution of nanoclays in polymer matrix (Arora & Padua, 2010; Kiliaris & Papaspyrides, 2010; Pavlidou & Papaspyrides, 2008; Sinha Ray & Okamoto, 2003b).

Despite significant breakthroughs in polymer nanocomposite in vast variety of applications, very limited studies have been conducted on the clay/nanocomposites for seal applications. Manias et al. (Manias et al., 2009) investigated the effect of incorporation of dioctadecyldimethyl ammonium-modified montmorillonite on peel behavior of PE/EVA/clay nanocomposites sealants. Their results showed that the presence of the EVA helped for a better dispersion of the nanoclays

in the matrix and also reduced the melting temperature of the PE. Samples without nanoparticles showed a peelable seal in a narrow heat sealing temperature window (about 5 ^{0}C wide). The samples with both the nanoparticles and EVA in their formulations revealed a peel behavior in a broad temperature window (25-30 ^{o}C wide) with almost consistent peel strengths as depicted in Figure 2.11.

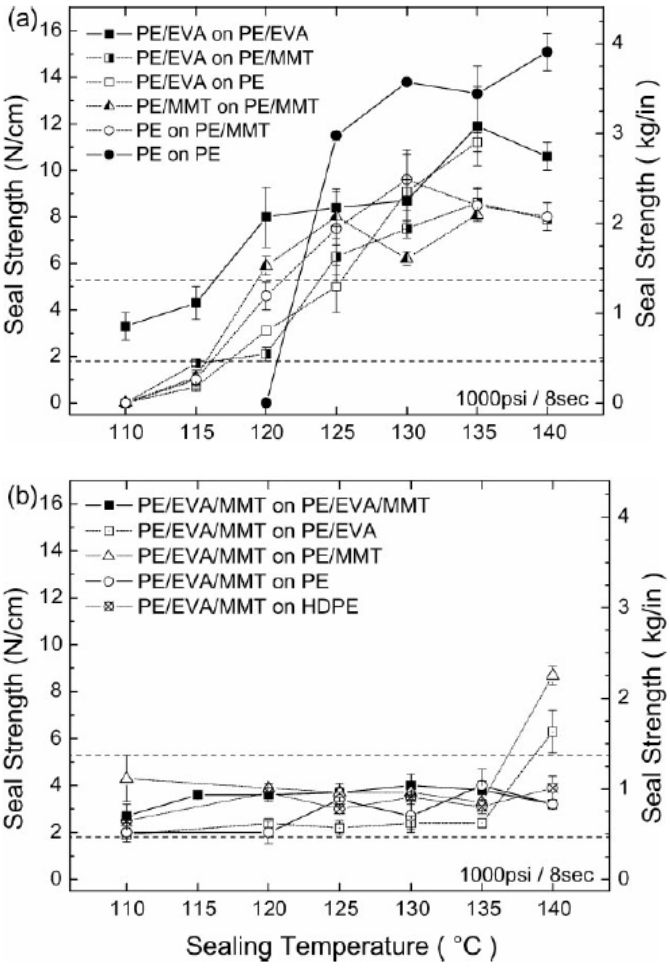

Figure 2.11. Seal strength of 24.5 mm flat sealants, seals at 1000 psi pressure and 8 s dwell time to fully equilibrate the seal interface (Manias et al., 2009).

The seal strength consistency of the PE/EVA/MMT nanocomposite sealants, clearly indicated that this behavior was the inherent property of the nanocomposite sealant and did not arise from sealing interface or sealing process. The traces of the EVA and MMT on the peeled surfaces were observed by ATR-FTIR and ESEM. The peel behavior of the PE/EVA/MMT nanocomposite seals were

cohesive, but the peel behavior of the PE/EVA sealants were adhesive as no traces of EVA observed by ATR-FTIR and their ESEM images showed smooth peeled surfaces.

Idiyatullina et al. (Idiyatullina, Vol'fson, Sabirov, & Yarullin, 2012) clearly showed that how montmorillonite clay nanoparticles increase the mechanical and thermal properties of PB-1. They indicated that adding 5 wt % of Cloisite15A into PB-1 accelerated its crystal transformations from the meta-stable form II to the stable form I. In the pure PB-1 resins, the phase transition from the form II to the form I occurred after 13.5 h and after 8 days the content of the form II in the resin was 6 %. While in montmorillonite containing PB-1, the phase transition occurred after 2.2 h and after 72 h the content of the crystal form II in the matrix was only 3 %.

Aithani and Brigges (Aithani & Briggs, 2009) invented different peelable films containing clay nanoparticles and showed incorporation of nanoparticles resulted in peelable sealant films with a wide range of heat seal temperatures. They also showed that incorporation of nanoclay in the seal layer significantly decreased the peel force as well as the aging of the films.

2.6 Morphology of immiscible polymer blends

Polymer blending is usually used to develop new materials with tailored properties (Rizvi & Park, 2014; Rizvi, Park, & Favis, 2015). Melt processing is typically employed to produce polymer blends with variety of morphologies for different applications. It is well-known that morphology of a blend significantly affects the rheological (García-Morales, Partal, Navarro, & Gallegos, 2006; McNally et al., 2002; Souheng Wu, 1987), mechanical (Heshmati, Zolali, & Favis, 2017; Meincke et al., 2004; Sepehr Ravati, Beaulieu, Zolali, & Favis, 2014; Zolali, Heshmati, & Favis, 2017) and thermal (Dell'Erba, Groeninckx, Maglio, Malinconico, & Migliozzi, 2001; Kubo & Kadla, 2004) properties of the blends. For binary immiscible polymer blends, there are four basic morphologies as illustrated in Figure 2.12; matrix/disperse, matrix/fiber, lamellar structure and co-continuous morphologies (Pötschke & Paul, 2003).

Material parameters such as viscosity ratio (Everaert et al., 2000; Favis & Chalifoux, 1987; Heino, Hietaoja, Vainio, & Seppälä, 1994), blend composition (Favis, 2000; Michael Nase et al., 2009; Sundararaj & Macosko, 1995; Tokita, 1977), elasticity (Levitt, Macosko, & Pearson, 1996), interfacial modification (Favis, 2000; Sundararaj & Macosko, 1995) and process conditions such as shear rate (Favis, 1990; M. Nase, Langer, & Grellmann, 2009; Xi, Jun, & Guo, 2006; Zeng,

Aoyama, & Takahashi, 2003), melt temperature (M. Nase et al., 2009; Potente, Bastian, Gehring, Stephan, & Pötschke, 2000; Xi et al., 2006) and mixing time (Bourry & Favis, 1998b; Xi et al., 2006) significantly affect the final morphology. However, the effect of the morphology of the seal on peel performance is not well understood and very limited literature addressed this effect.

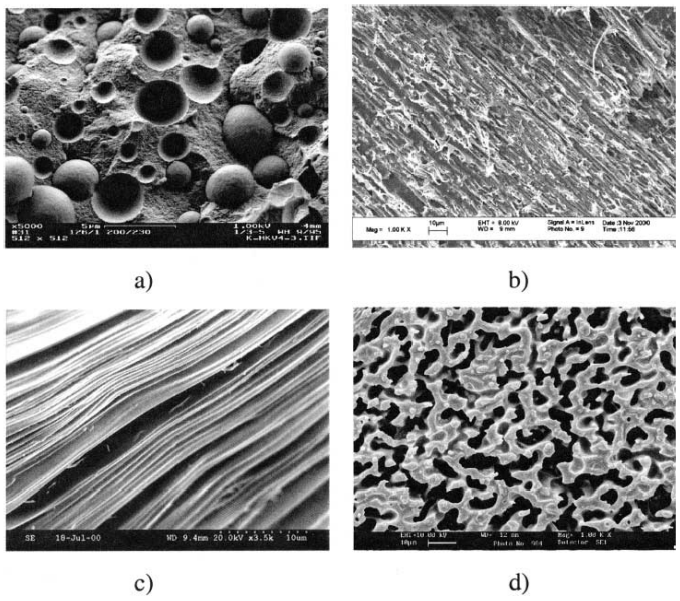

Figure 2.12. Different morphologies for binary immiscible blends. a) Dispersed structure (TPU/PP 80/20); b) Fibrillar structure (PA6/SAN 30/70); c) Lamellar structure (PP/EPDM 80/20) and d) Co-continuous morphology (PE/PS) (Pötschke & Paul, 2003; Zumbrunnen & Inamdar, 2001).

Since, the majority of the sealants of this research have been made of immiscible polymer blends with and without nanoclay, the following sections of this literature review are paid on the main parameters which control the morphology of binary polymer blends, the effect of organoclay on the morphology of binary blends and nanoclay localization in binary polymer blends.

2.6.1 Effective parameters on morphology of polymer blends

2.6.1.1 Effect of interfacial tension

According to the equation (2.1), the reversible work that is required to create a unit surface area is defined as the surface tension where, γ is the surface tension, G is Gibbs free energy, A is interfacial (surface) area, T is temperature, p is pressure and n is the total number of moles of matter (S Wu, 1982).

$$\sigma = \left.\frac{\partial G}{\partial A}\right|_{T,p,n} \qquad 2.1$$

Generally, for homologous series under the infinite molecular weight, the surface tension tends to increase by increasing the molecular weight. At infinite molecular weight, surface tension is independent of the molecular weight (S Wu, 1982). The dependence of a polymer surface tension to the molecular weight (under the infinite molecular weight) is expressed by either one of the equations (2.2) or (2.3) (S Wu, 1982):

$$\sigma^{1/4} = \sigma_{\infty}^{1/4} - k_1/M_n \qquad 2.2$$

$$\sigma = \sigma_{\infty} - k_2/M_n^{2/3} \qquad 2.3$$

σ_{∞} is the surface tension at the infinite molecular weight, k_1 and k_2 are semi-empirical parameters and M_n is the number average molecular weight. For molecular weights less than the infinite molecular weight, Eq. (2.3) is more accurate than Eq. 2 (Jalbert et al., 1993) for polymers. Wu also proposed:

$$k_2 = (\sigma_{\infty} - \sigma_e)(2m)^{2/3} \qquad 2.4$$

in which σ_e is surface tension of the endgroups and m is formula weigh of a repeat unit (S Wu, 1982) According to Eq. (2.4), in low molecular weights, the surface tension depends on the sign of $(\sigma_{\infty} - \sigma_e)$. If the surface tension of the end groups is less than that of polymer backbone, it is predicted that the surface tension of polymer increases by increasing the molecular weight, same as homologous polymer. Jelbert and Kobelstein (Jalbert et al., 1993) investigated the correlation between the molecular weight and the surface tension of poly(dimethylsiloxane) (PDMS) with three different end groups of methyl, amine and hydroxyl. Their results showed that for amine terminated PDMS, the surface tension decreased by increasing the molecular weight. The surface tension of methyl terminated PDMS increased by increasing the molecular weight and surface tension of hydroxyl terminated PDMS was independent of the molecular weight (Figure 2.13). They attributed this effect to the difference between surface tension of polymer backbone and the end groups.

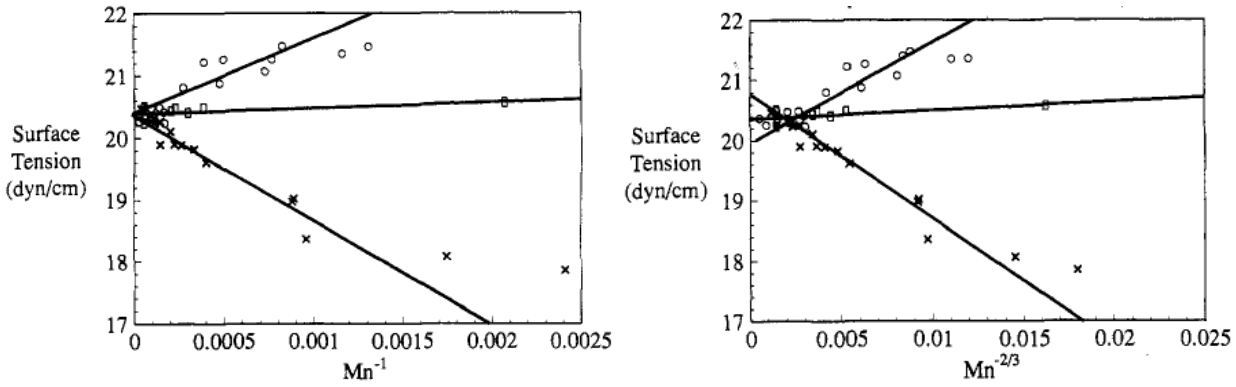

Figure 2.13**.** The surface tension of PDMS terminated with amine group (crosses), terminated with hydroxyl group (open circle) and terminated with methyl group (open Square) as a function of number average molecular weight (M_n) (Jalbert et al., 1993).

They showed that the surface tension of all functionalized PDMS converged to a similar value at very high molecular weight because of vanishing the effect of end groups at infinite molecular weight. Since the surface tension of small-molecule liquids decreases linearly with temperature, Wu (S Wu, 1982) concluded that below the critical temperature (T_c= 600-900 °C), surface tension of polymers also vary linearly with temperature. Wu also reported Guggenheim equation for small-molecule liquids (Guggenheim, 1945) that can be applied for polymers:

$$\sigma = \sigma_0(1 - T/T_c)^{11/9} \qquad 2.5$$

where σ_0 is surface tension at $0K$ and T_c is critical temperatures. According to this equation, the surface tension linearly decreases by increasing the temperature. The slop of the plot of σ versus T, $-(d\sigma/dT)$, increases by decreasing the molecular weight. $-(d\sigma/dT)$ is the surface entropy, therefore, for a polymer smaller $-(d\sigma/dT)$ is attributed to conformational restrictions of long chain molecules and lower thermal expansion coefficient. Sauer and Dee (Sauer and Dee, 1992) indicated that surface tension of poly(dimethylsiloxane) decreased by increasing the temperature. This variation was more significant for low molecular weight polymers such as oligomers. They attributed this effect to lower thermal expansion coefficient of polymer in compare to that of oligomers.

Molecular weight and nature of the components are two main parameter that influence the interfacial tension of a blend. The way that the molecular weight affects the interfacial tension is

similar to its effect on the surface tension. Using the theory of Girifalco and Good (Girifalco and Good, 1957), Wu derived the following equation to estimate the interfacial tension:

$$\sigma = k_0 - k_1/M_{n1}^{\frac{2}{3}} - k_2/M_{n2}^{2/3} \qquad 2.6$$

Thus, if the molecular weight of one phase is kept constant, the interfacial tension will be a function of the molecular weight of the second component and will change linearly with $M_{n2}^{2/3}$.

The surface tension can be separated into two terms of dispersion and polar interactions:

$$\sigma = \sigma^d + \sigma^p \qquad 2.7$$

in which polar component consists of dipole, induction and hydrogen-bonding interactions. The interfacial tension is determined primarily by the difference between the polarities of the two phases and the dispersion interaction plays a minor role. The interfacial tension of a blend of two polymers can be calculated by:

$$\sigma_{12} = \sigma_1 + \sigma_2 - W_a \qquad 2.8$$

where σ_{12} is the interfacial tension of the blend, σ_1 and σ_2 are surface tensions of polymers and W_a is work of adhesion that is the required work to separate interface of two bulks. The value of the work of adhesion is mainly estimated by two well-known equations of the harmonic-mean and geometric-mean as the followings, respectively (S Wu, 1982):

$$\sigma_{12} = \sigma_1 + \sigma_2 - \frac{4\sigma_1^d\sigma_2^d}{\sigma_1^d + \sigma_2^d} - \frac{4\sigma_1^p\sigma_2^p}{\sigma_1^p + \sigma_2^p} \qquad 2.9$$

and

$$\sigma_{12} = \sigma_1 + \sigma_2 - 2\left(\sigma_1^d\sigma_2^d\right)^{1/2} - 2\left(\sigma_1^p\sigma_2^p\right)^{1/2} \qquad 2.10$$

The harmonic-mean equation is valid for polymers and low energy materials while the geometric-mean equation is shown to be more suitable for estimating the interfacial tension between a low energy material and a high energy material. Also, the following equation can be used to predict the

interfacial tension of two immiscible polymers with infinite molecular weight and zero isothermal compressibility (Anastasiadis, Chen, Koberstein, Sohn, & Emerson, 1986):

$$\sigma = (\chi/6)^{1/2} b\rho kT \qquad 2.11$$

where, χ is Florry-Huggins interraction parameter, ρ is density, *k* is Boltzman constant, and *b* and *T* are the lattice parameter and absolute temperature, respectively. We can see that interactions between two components significantly affects the interfacial tensions between phases. Since more interactions mean lower χ, therefore, the greater the interactions, the lowere the interfacial tension will be.

The major effects of interfacial tension are on shape relaxation, coalescence and breakup. The final morphology will be a balance between deformation – disintegration and coalescence phenomena. For breakup of dispersed phase, Taylor defined Capillary number (*Ca*) as the ratio of deforming stress ($\eta_m \dot{\gamma}$) per interfacial forces (σ /R).

$$Ca = \eta_m R\dot{\gamma}/\sigma \qquad 2.12$$

where η_m is the viscosity of the matrix, $\dot{\gamma}$ is the shear rate, *R* is the droplet radius and σ is the interfacial tension. When the *Ca* number is low, the interfacial forces are dominant compared to the viscous forces imposed by flow and stable drop shapes are formed. While the *Ca* is higher than its critical capillary number, the deforming stress is dominant and droplets finally disintegrate through breakup phenomenon. The critical capillary number is different for each system and is defined as the point in which the viscose forces are dominant and droplets disintegrate through breakup. Equation (2.12) was developed for the Newtonian fluids, hence does not take into account the coalescence of viscoelastic dispersed phases. It has been reported that the mobility of interface is a determinant factor for the coalescence phenomenon. When viscosity ratio is high, a fully immobile interface (FII) is expected and for a very low viscosity ratio ($p << 1$), a fully mobile interface is expected (Gabriele, Pasquino, & Grizzuti, 2011) . Coalescence takes place by three mechanisms; collision of dispersed particles, particle deformations and expelling matrix from regions between two particles (Favis, 2000). As it can be seen in Figure 2.14, it has been shown that elongational flow is much more effective than the simple shear flow in which the limitation of the viscosity ratio in the elongation flow is much less than that of the simple shear flow.

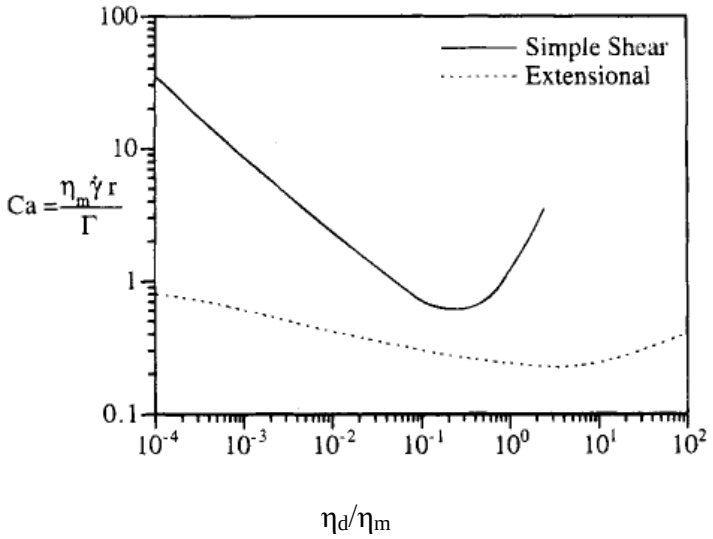

Figure 2.14. Critical Capillary number versus viscosity ration in simple shear flow and elongation flow (Grace, 1982).

2.6.1.2 Viscosity ratio

Viscosity ratio, $P = \eta_d / \eta_m$, is defined as the ratio of the dispersed phase viscosity per matrix viscosity. Generally, if the viscosity of the minor phase is lower than that of the matrix, a fine and uniform dispersion is achieved. If the minor phase has a higher viscosity than that of the matrix, a coarse dispersion is obtained and the size of the dispersed phase increases by increasing its viscosity (Everaert, Aerts, & Groeninckx, 1999; Favis, 2000; Favis & Chalifoux, 1987; Heino et al., 1994).

2.6.1.3 Blend composition

For a blend of polymers A and B, depending on the blend composition, three morphological states could be achieved; A is continuous and B is dispersed phase, B is continuous and A is dispersed phase, A and B are both continuous phases. Since the final morphology is a balance of the breakup and coalescence phenomena, increasing the amount of dispersed phase enhances the coalescence (Favis, 2000). It was reported that the drop breakup is not affected by changing the volume fraction of the dispersed phase whereas the drop coalescence is significantly influenced by increasing the volume fraction (Sundararaj & Macosko, 1995). Figure 2.15 illustrates a schematic picture of the revolutions of different morphologies in a binary immiscible polymer blend.

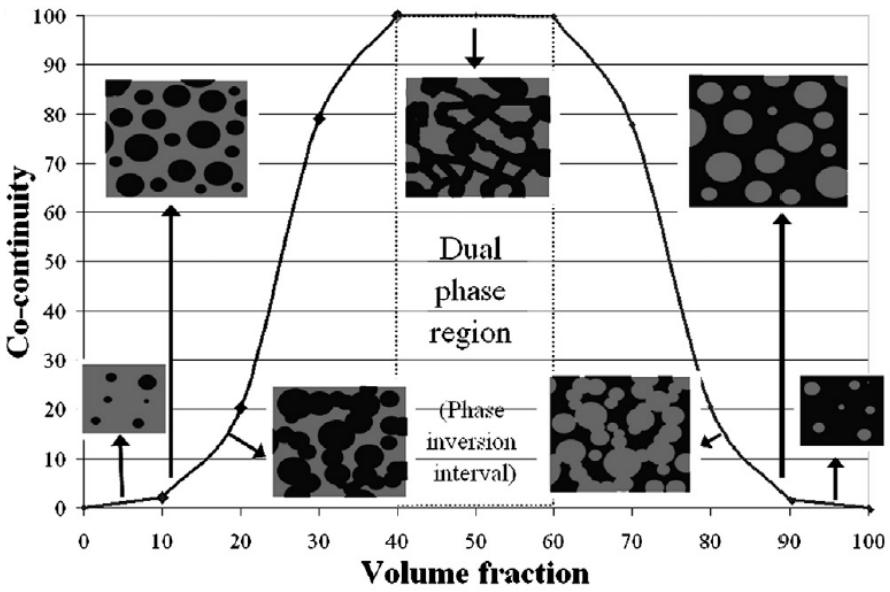

Figure 2.15. Schematic picture of the evolutions of different morphologies by changing the volume fraction of the components (S Ravati & Favis, 2010).

There are several theories such as equations expressed by Taylor (Taylor, 1934), Wu (Souheng Wu, 1987), Fortelny (Fortelný, Černá, Binko, & Kovář, 1993a)and Tokita (Tokita, 1977). Although the results of these equations for a unique system is different, but all of these theories confirm the important correlation between particle size and volume fraction.

The effect of blend composition on the morphology and properties of the LDPE/iPB-1 films was studied (Michael Nase et al., 2009). The results revealed an obvious effect of the blend composition on the morphology and consequently on the peel properties of the films. It was concluded that matrix/belt-like morphology results in peelability of the films and this kind of morphology is obtained with a dispersed phase content of at least 6 mol%. The TEM images depicted in Figure 2.16 clearly show that the thickness of the belt-like structures significantly enhanced by increasing the dispersed phase content.

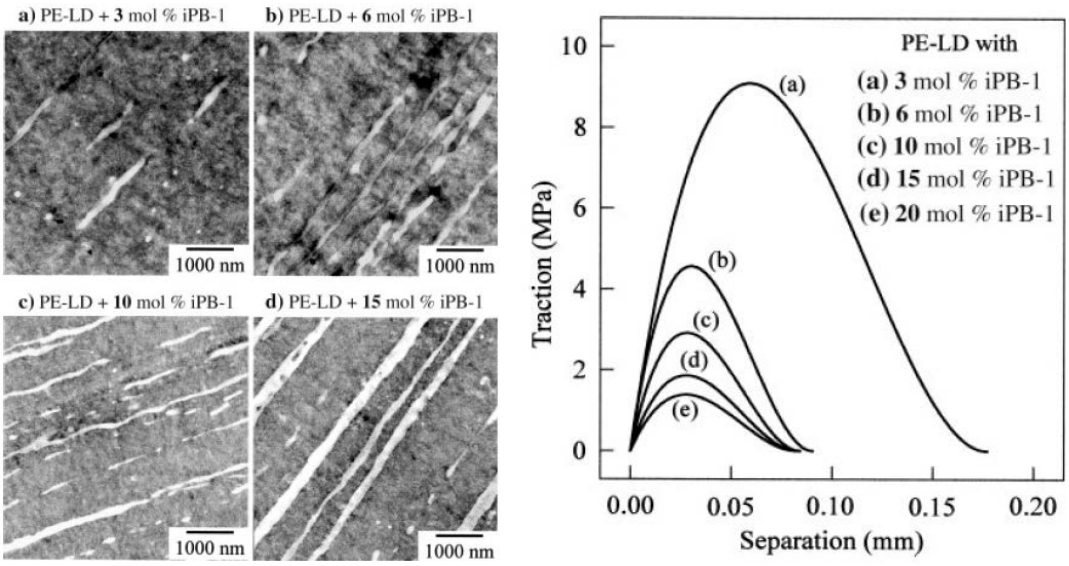

Figure 2.16. TEM images (left side) and traction-separation relationship (right side) for LDPE/iPB-1 blends with different contents of iPB-1 (Michael Nase et al., 2009).

2.6.1.4 Processing conditions

Melt processing is extensively used to prepare different polymer blends. For this aim, internal mixing, single and twin screw extruder are exploited to prepare polymer blends in melt state. It is well known that twin screw extruder (TSE), because of the generation of both intensive shear and elongation flow fields, is the most efficient equipment to prepare polymer blends and nowadays, most of the polymer blends are produced by TSEs. In screws of TSE, kneading blocks are responsible to generate both shear and elongation flow fields and consequently provide an intensive mixing zone to make polymer blends. Depending on the requirements, there could be different screw configurations consisting of numerous kneading blocks and shear elements (Favis, 2000). There are many literatures which investigated the morphology evolution in twin screw extruder and reported the effect of extrusion process conditions such as screw speed, melt temperature and mixing time on the morphology of the blends (Bourry & Favis, 1998b; J. Lee & Han, 2000; Potente et al., 2000; Sau & Jana, 2004).

For morphology evolution of two immiscible polymers during chaotic mixing as well as in twin screw extruder, three main morphologies are formed gradually; lamella/layers, thread/fibril and droplet. These three developing stages are illustrated in Figure 2.17.

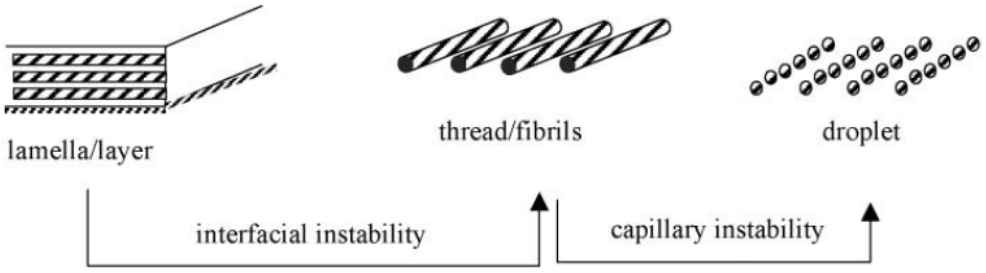

Figure 2.17. Schematic picture of three general developing stages for morphology evolution in chaotic mixing (Sau & Jana, 2004).

Lamella morphology is generated at the earlier stages of blending in the extruder. By decreasing the striation thickness, lamellas then undergo the interfacial instabilities beyond the critical striation thickness and periodic distortions are produced at the surface of the lamellas until breakup to the threads. Threads undergo the capillary instability and form droplets. Due to the coalescence probability, droplets may deform to threads or lamellas and then break up to the droplets to repeat the stages. Finally, a semi-stable morphology is formed at a balance between coalescence and breakup (Lyngaae-Jørgensen, 1996). Morphological evolution is affected by various parameters such as shear rate, process temperature and mixing time, which are discussed in the following sections.

2.6.1.4.1 Shear rate

Although the theories proposed by Taylor (Taylor, 1934), Wu (Souheng Wu, 1987), Fortelny (Fortelný, Černá, Binko, & Kovář, 1993b)and Tokita (Tokita, 1977) indicate the inverse effect of shear rate on the dispersed phase size, however, the experimental results revealed different impacts of shear rate on the blend morphology. Favis (Favis, 1990) reported that shear rate did not affect the size of the dispersed phase in the PP/PC blends. Nase et al. (M. Nase et al., 2009) reported that increasing the shear rate did not have influence on the morphology of the blends. They attributed this result to the inverse effect of the shear rare and residence time. Fortelny et al. (Fortelný et al., 1993b) showed that in the polyamide/(polyphenylene oxide/polystyrene) blends, the size of the dispersed phase first increased by increasing the shear rate and then decreased. Minale et al. (Minale, Moldenaers, & Mewis, 1997) indicated that there is a critical shear rate that above which, a stable morphology is attained in a balance of coalescence and break. Below the critical shear rate,

there are multiple steady state morphologies and a stable morphology resulted from the balance of the coalescence and breakup is generated above the critical shear rate.

2.6.1.4.2 Melt temperature

Different possibilities on the role of temperature on the blends morphology have been reported. Increasing temperature can either enhance the coalescence or breakup depending on the variation of the viscosity ratio through changing temperature (Potente et al., 2000; Xi et al., 2006). By increasing temperature, if the viscosity of the matrix decreases more than that of the dispersed phase, a lower capillary number is obtained, which consequently enhances the size of the dispersed phase. Increasing the extrusion temperature for the blends of the LDPE/iPB-1 revealed finer and thinner belt-like structures in the TEM images of the films. This effect was attributed to more interactions of the blend components due to increasing temperature (M. Nase et al., 2009).

2.6.1.4.3 Mixing time

There is no unique effect of mixing time on blends morphology. Bourry and Favis (Bourry & Favis, 1998a) studied the binary blends of the PS/HDPE blended in twin screw extrude and observed that the early stages of the mixing did not affect the final morphology of the blends. They emphasized that the later mixing time at which all the materials were molten determined the stable morphology of the blends. Chen et al. (Xi et al., 2006) studied the role of mixing time in internal mixing for the polyamide 12/poly(ethylene glycol) blends and observed significant changes in the morphology at the earlier stage of the mixing. Their results showed that by increasing the mixing time, a narrower size distribution was attained, however, mixing time did not have a significant impact on the average dispersed phase.

2.6.1.5 Effect of interfacial modification

The main impact of the interfacial modification is to reduce particle size through reducing both the interfacial tension and coalescence. Most of the interfacial modifications are carried out using graft or block copolymers, which are miscible with the blend components through physical or chemical interactions (Favis, 2000; Sundararaj & Macosko, 1995). Although a very small amount of compatibilizer (as low as 5 wt%) revealed a notable reduction of dynamic coalescence as well as reduction in the dispersed size, however much more compatibilizer is needed to prevent static coalescence (Macosko et al., 1996). Sundararaj and Macosko (Sundararaj & Macosko, 1995)

studied the effect of di-block copolymers on coalescence of the dispersed phase. They observed that by adding the compatibilizer in the blend, coalescence suppressed and the dispersed phase size was equal to that of uncompatibilized blends. Because the size of the dispersed phase did not decrease, they concluded that the main contribution of the di-block compatibilizer is suppression of the coalescence and not a reduction in the interfacial tension. From the thermodynamic point of view, the block segment of the matrix migrates to the interface and since it is not compatible with the dispersed phase, it produces steric effect and causes suppression of the coalescence. This effect is schematically illustrated in Figure 2.18. It is worth to mention that before the formation of the copolymers due to the reaction, the reactive blends revealed significantly finer dispersed phase compared to the nonreactive blends. After the formation of the copolymers, the phase size stabilized and did not change even by increasing the concentration.

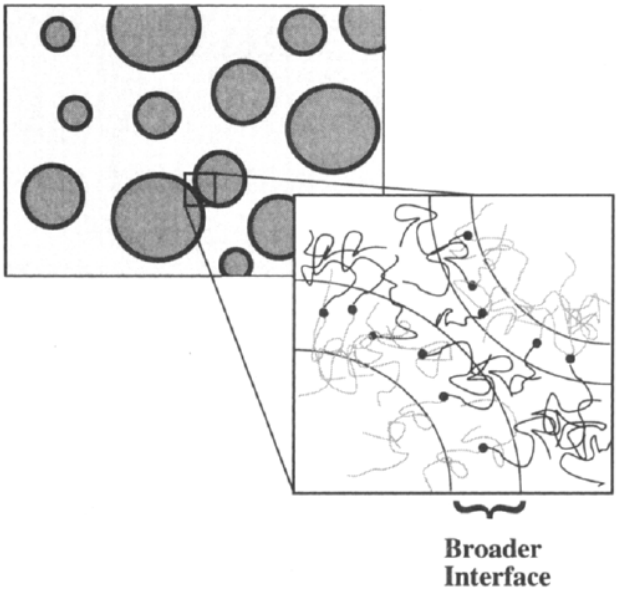

Figure 2.18. The schematic picture of the effect of the copolymer on the coalescence of the dispersed phase (J. Lee & Han, 2000).

2.6.1.6 Effect of elasticity

Due to the viscoelastic behavior of polymers, they show considerable discrepancy from many equations, which were developed for the Newtonian fluids that predict the morphology of the blends (Favis, 2000). Elasticity, as one of the important effective factors on the morphology of the blends, is the less understood aspect and there are very few publications that studied the role of

elasticity. Levitt and Macosko (Levitt et al., 1996) provided a simple shear flow field between two counter rotating parallel discs and followed the morphology of the PP/PS using situ optical microscopy. They found out in a high elastic matrix, the dispersed droplets stretched perpendicular to the flow direction and deformed into the sheets. Such morphology provided an effective gas barrier property. Under a small shear rate (~ 1 s^{-1}), they observed a remarkable widening of the droplets by decreasing the viscosity ratio from 4.4 to 2.2 and this effect was enhanced by decreasing the viscosity ratio. A reversible correlation between widening of the drops and elasticity ratio was attained. According to the authors, the normal stresses of the matrix on the droplets stretch them perpendicular to the flow direction. A higher elasticity of the matrix resulted in higher reduced width (reduced width = sheet width/initial drop diameter). The widening of the droplets due to the normal stresses of the matrix competes with the contractions caused by the interfacial tensions on the opposite direction. On the other words, in such conditions, the normal stresses of the matrix exerted on the droplets compete with the interfacial forces in the opposite direction. They defined a critical strain, which is a transition point from widening to contraction.

In another study, Sundararaj and Macosko (Sundararaj & Macosko, 1995) investigated the morphology of the PP/PS blends. They observed that breakup took place for the PP/PS blends with η_r= 8.6 as well as for the PS/PP with η_r=10.5. This phenomenon was not in agreement with Taylor and other researcher's predictions and observations that say for the Newtonian fluids in simple shear flow, there is no breakup at viscosity ratio above η_r = 4. They attributed this discrepancy to the viscoelastic behavior of the polymers. They indicated that there is a critical shear rate below which by increasing the shear rate, the dispersed phase size first decreased and then increased by increasing the shear rate beyond critical shear rate. They attributed the increase in the dispersed phase size beyond the critical shear rate to the coalescence as well as viscoelastic effects. At higher shear rates, due to the shear thinning of polymers, droplets have higher approach velocity and thus the possibility of the coalescence increases. During the deformation of a droplet, the viscous forces exerted by the matrix on the droplet compete with the droplet elasticity and interfacial tension.

2.6.1.7 Effect of incorporation of nanoparticle on the morphology of a blend

The incorporation of nanoparticles to a polymer blend can affect the morphology by affecting both kinetics and thermodynamics of the blend (Fenouillot, Cassagnau, & Majesté, 2009c). Several possible phenomena are proposed in the literature that explain the morphology changes in these

systems: i) a reduction of the interfacial energy, ii) the inhibition of coalescence by the presence of a solid barrier around the minor polymer drops, iii) the changes of the viscosity of the phases due to the uneven distribution of the filler, iv) the immobilization of the dispersed drops (or of the matrix) by the creation of a physical network of particles when the concentration of solid is above the percolation threshold and v) the strong interaction of polymer chains with the solid particles inducing steric hindrance.

Nanoparticles can stabilize the morphology of a blend by altering the interfacial properties and thus the size of the dispersed phase. Depending on the nature of the surface of the nanoparticles (hydrophone and hydrophilic), nanoparticles can change the interfacial energy (Sinha Ray, Pouliot, Bousmina, & Utracki, 2004). Localization of nanoparticles at the interface can act as rigid layers at the interface of the blend components and prevent the coalescence of dispersed phase. By reducing the rate of coalescence of the dispersed phases, the nanoparticles can decrease the size of the dispersed phase (Elias, Fenouillot, Majesté, Alcouffe, & Cassagnau, 2008). Partition of nanoparticles in a blend's components can influence the viscosity ratio and changes the size of the dispersed phase and dispersion quality. In this case, only the elasticity and viscosity ratio control the morphology evolution and the coalescence is not inhibited by these effects and only can cause a shift in the break-up/coalescence equilibrium. However, the localization of nanoparticles can be influenced due to these effects.

2.6.2 Quantitative method to predict localization of nanoparticles in a blend

The localization of solid particles in polymer blends can be predicted by thermodynamic effects while, the localization which is dictated by thermodynamic is not always achieved due to the kinetic effects. These effects are explained in more details in the following sections.

2.6.2.1 Thermodynamic effects

The localization of nanoparticles in a polymer blend can be linked to the balance of interactions between the surface of the particles and the polymer components in a quantitative manner by calculating the wettability parameter, ω_{12}, according to Young's equation (Fenouillot et al., 2009c):

$$\omega_{12} = \frac{\sigma_{s-2} - \sigma_{s-1}}{\sigma_{12}} \qquad 2.13$$

in which σ_{s-i} and σ_{12} are the interfacial tensions between solid inclusion-polymer and polymer-polymer, respectively. Base only on the thermodynamic criteria, there are three possible equilibrium configurations for nanoparticles in a binary polymer blend that are dictated by thermodynamic. If $-1 < \omega_{12} < 1$ nanoparticles will be localized at the interface of the blend components, for $\omega_{12} > 1$, nanoparticles will be localized in component 1 and for $\omega_{12} < -1$ nanoparticles will be localized in component 2. Interfacial tensions of the components can be calculated from there surface tensions using harmonic mean and geometric mean equations as discussed earlier. Since there is no direct method to measure the interfacial tension between a polymer and a nanoparticle, the interfacial tension between a polymer and nanoparticle pair can be estimated using the geometric-mean equation as it is suitable for pairs with high and low surface energies.

Calculation of the wettability parameter can help us to quantitatively predict the localization of particles in binary blend since it is of thermodynamic origin. Another thermodynamic approach to determine solid particle localization in a binary blend would be based on the spreading coefficient (Harkins, 1941; Virgilio, Desjardins, L'Esperance, & Favis, 2009) which is mainly used in case of ternary emulsion systems. Generally, the spreading coefficient represent the tendency of a component to form a continuous layer at the interface of two other components. For example, if phase *B* spread at the interface of the phase *A* and *C*, it means that phase *B* completely wets the *AC* interface and the corresponding spreading coefficient is positive. We can replace one phase with the solid microparticle and the only difference is that the shape of the solid phase is unchangeable. During the melt processing of polymer *A* and *B* with the third phase of *S* (solid microparticles), three different equilibrium configurations are possible and can be predicted based on this thermodynamic approach (Figure 2.19) (Harkins, 1941; Torza & Mason, 1970; Virgilio et al., 2009).Three spreading coefficients for such a ternary system can be written as follows:

$$\lambda_{ABS} = \sigma_{AS} - (\sigma_{AB} + \sigma_{BS}) \qquad 2.14$$

$$\lambda_{ASB} = \sigma_{AB} - (\sigma_{AS} + \sigma_{BS}) \qquad 2.15$$

$$\lambda_{BAS} = \sigma_{BS} - (\sigma_{AB} + \sigma_{AS}) \qquad 2.16$$

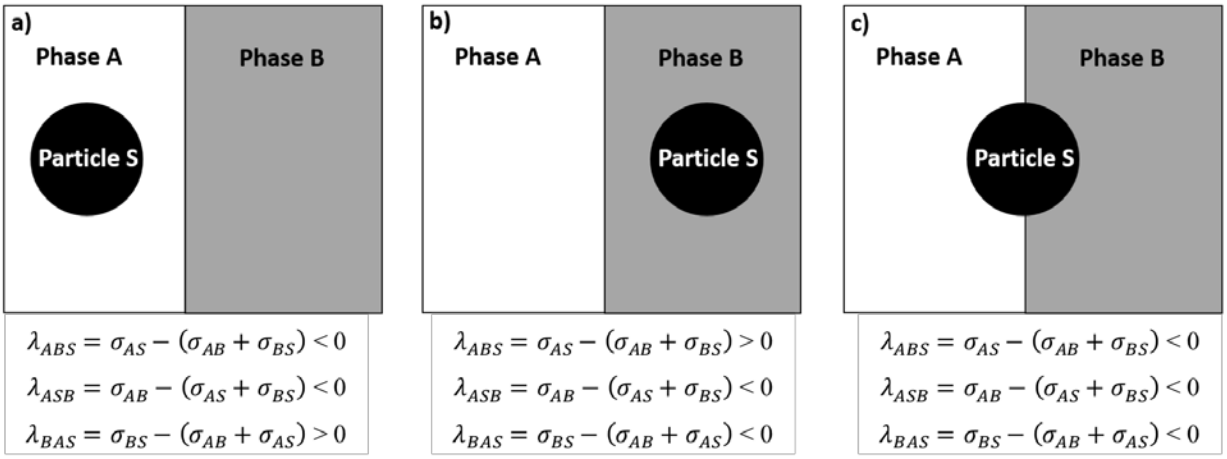

Figure 2.19**.** Possible localization of solid particle, *S,* in polymer *A* and *B.*

Since the surface of the clay is hydrophilic, generally we can say the nanoclays will localize in a phase with more hydrophilicity. If we suppose that A is hydrophilic and B is hydrophobic, nanoclay will be situated in the phase A. For such a case, the interfacial tensions of σ_{BS} is much higher than σ_{AS} and σ_{AB}, hence the spreading coefficient of λ_{BAS} will be positive and the case (a) in Figure 2.19 is most likely to happen. But for polymer components both hydrophilic or both hydrophobic, it is not possible to assess without having the interfacial tension values and therefore, all cases, particularly the partial wetting (Figure 2.19c) are possible.

The same conclusion can be obtained if we assess the system using the wettability parameter. For polymer A (hydrophilic) and polymer B (hydrophobic), since σ_{BS} is much higher than the two other interfacial tensions, therefore, the value of ω_{12} will be smaller than -1 which means the microparticle will be situated in the phase A.

2.6.2.2 Kinetic effects

At the end of melt processing, we will not always observe the thermodynamic predictions to be valid. First of all, during the melt processing, equilibrium morphology of the solid particles is not attained immediately due to high viscosity of polymer melts (Fenouillot et al., 2009c). Therefore, in addition to thermodynamic, kinetic is another important factor which significantly influence the localization of fine particles (i.e. nanoparticles and microparticles). Several investigations have been carried out on the effect of viscosity as the main kinetic parameter on localization of solid particles in binary blends (Clarke, Clarke, Freakley, & Sutherland, 2001; Fenouillot et al., 2009c;

Nofar, Heuzey, Carreau, & Kamal, 2016; Zhou et al., 2007a). As an example, during the melt mixing nanoparticles may incorporate to lower viscose component and interfacial energy may be effective only when the viscosity ratio is near one (Zhou et al., 2007b). It was reported that the sequence of mixing is also effective on the localization of solid inclusions. When the particle is added to the component with higher viscosity, despite the affinity of the microparticle to the other phase with lower viscosity, stay in the phase with higher viscosity since they aren't able to migrate to the other phase (Fenouillot, Cassagnau, & Majesté, 2009a; Taguet, Cassagnau, & Lopez-Cuesta, 2014). In a viscose liquid (such as polymer melt), diffusion coefficient ($D_0 = K_BT/6\pi\eta R$, K_B is Boltzmann constant, T is temperature, η is polymer melt viscosity and R is radius of the particles) of solid particles is extremely high. Motion of solid particles in low viscosity liquids is Brownian and the time is needed to diffuse on a distance is:

$$t_D = a^2/D_0 = 6\pi\eta R^3/K_BT \qquad 2.17$$

If we suppose that the motion of microparticles is Brownian, for example the time that microparticles with diameter of 50 μm need to diffuse in PP with η= 2500 Pa.s and T = 473 K is about $9 * 10^{11}$ sec. The order is very large and so the Brownian motion of the particles is impossible. Therefor the motion of the solid particles can be possible by shear and inconsequence collision of the particles and polymer phases (Fenouillot et al., 2009a). On the other hand, the stocks friction (~ $6\pi\eta R$) is exerted by polymer melt on the particles increases by increasing the viscosity of the melt and radius of the particles. As a consequence, when solid particles are trapped in a polymer with high viscosity, the thermodynamic predictions may never be reached even after high mixing time (Taguet et al., 2014).

Figure 2.20 shows schematically the effect of kinetic in localization of solid microparticles (S) in a blend of polymer A and B. We suppose that polymer A is more viscose rather than polymer B and we first mix the particles in polymer A in the first step. In the second step polymer B is added to the system. If particle S has more affinity to polymer B ($\gamma_{BS} < \gamma_{AS}$), thermodynamic predicts its localization in polymer B. But because of the high viscosity of polymer A, particles are trapped in polymer A and cannot localize in phase B.

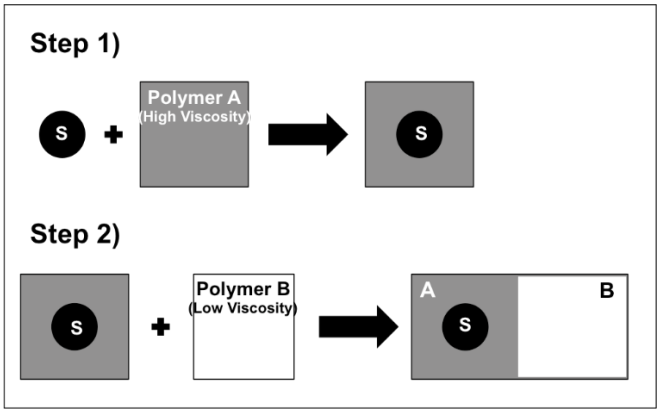

Figure 2.20. schematic of localization of solid particle S in high viscose polymer A due to the influence of the kinetic while S has affinity with polymer B and thermodynamic predicts its localization in polymer B.

However, due to unfavorable localization dictated by kinetic effects, solid particles migrate from one phase to another phase as soon as they collide with the interface through hydrodynamic forces (Elias, Fenouillot, Majesté, Martin, & Cassagnau, 2008).

2.7 Originality of the work

As discussed earlier, cohesive peelable sealants are produced through blending two or more immiscible polymers or incorporation of nanoclay in seal area. Based on the literature review, the morphology of blends and nanocomposites is the key factor influencing their final properties. However, the effect of this critical parameter on the peel performance of sealants made of polymer blends and nanocomposites is not well established and there is a lack of knowledge in this area.

Furthermore, majority of seal formulations are composed of at least two polymer components to optimize seal properties. As an example, PE sealants are blended with lower softening point polymer such as EMA or EVA to reduce the heat seal initiation temperature and enhance the seal properties. To our knowledge, there is no research to address the effect of nanoclay localization on their peel performance of sealants made of polymer blends.

Although polymer blending is a promising method to produce cohesive peelable sealants, but finding two immiscible polymer components with appropriate seal properties such as low shear thinning, low softening point and broad peelable heat seal temperature window remains a challenging issue. Among various seal formulations, blending PE with PB-1 is a promising

approach in generating peelable sealants with an acceptable peelable heat seal temperature window. High mechanical performance, low shear thinning, low melting point (compared to that of PE) and its incompatibility with PE and compatibility with polypropylene (PP) make PB-1 a good candidate for peelable seal applications. Blends of PE with less than 20 wt% of PB-1 are suitable for sealing of PE substrates, while blends of PE containing high PB-1 contents are suitable to be used in sealing of PP substrates. The main drawback of PB-1 which restricts its application is its unstable polymorphism after melt treatment. As a summary, PB-1 forms unstable crystal form II after cooling from melt at ambient conditions. The metastable form II spontaneously converts to stable form I over a long time of about several weeks. Due to significantly higher density of form I compared to that of form II, this bypass is accompanied with profound changes in mechanical and thermal properties and shrinkage of the heat sealed sealants containing PB-1. Although a significant body of literature reports acceleration of form II to form I or direct formation of form I of PB-1 in peculiar conditions, no effort to achieve peelable sealants containing PB-1 with consistent peel performance have been reported.

The main attempt of this work is to present a correlation between microstructure and peel performance of the sealants made of clay/polymer nanocomposites. Moreover, investigating the microstructure of peelable sealants containing PB-1 and presenting an approach to achieve consistent peel performance is of great value that can open new avenue toward broader application of PB-1 for many existing and immerging applications.

2.8 Objectives

The main objective of this research project is "*to investigate and establish a correlation between microstructure and peel performance of polyolefin-based blends/clay nanocomposite sealants*". Thus, the following sub-objectives are envisaged to achieve the main objective:

a) Investigate the effect of the dispersion and distribution of clay nanoparticles in LDPE (as the mostly used polyolefin for seal applications) based clay nanocomposite sealants on the peel performance of the nanocomposite sealants.

b) Determine the effect of the localization of nanoclay on the peel performance of sealants made of polyolefin-based blends.

c) Investigate the effect of seal microstructure on the peel performance and aging of the sealants made of LDPE/PB-1 blends and clay nanocomposites.

d) Develop a method to achieve peelable sealants containing PB-1 showing a consistent peel performance.

In this research project, the structure of the most relevant polyolefin based sealants are investigated. LDPE is used as the main seal material in the blends with various organoclays and different PE copolymers including EMA and EMA-GMA. The masterbatches and blends were prepared using twin screw extrusion followed by films casting of the blends and nanocomposites. Attempted are made to understand the effect of microstructure of various sealants on their peel performance.

CHAPTER 3 ORGANIZATION OF THE ARTICLES

The following chapters 4 to 7 represents the results of this research based on the specific objectives.

Chapter 4 dedicated to the first article in which the correlation between microstructure and peel properties of the PE nanocomposite sealants is discussed. The first article entitled: “Peelable PE/Clay Nanocomposite Seals with Ultra-wide Peelable Heat Seal Temperature Window”. The three-layer films composed of HDPE as the support layer, LLDPE as the core layer and the LDPE based seal layer were prepared through film casting. Various techniques including WAXD, TEM and SEM have been employed to analyze the microstructure of the nanocomposite sealants. The peel force measurements have been done by T-peel test and the peel fracture mechanism has been examined through ATR-FTIR, force-displacement diagram and SEM imaging. The peel performance is controlled through change in the organoclay microstructure in the seal layer. Ultimately, ultra-wide peelable heat seal temperature window was achieved followed by partially exfoliation of the organoclays in PE matrix.

The second article is presented in chapter 5 and is entitled “Effect of nanoclay localization on the peel performance of PE based blend nanocomposite sealants”. In this article, the effect of organoclay localization in two different blends i.e. LDPE/EMA and LDPE/EMA-GMA is investigated. The organoclay localization in the blends investigated based on the thermodynamic predictions and using WAXD and TEM results. The predicted localization was further confirmed through SEM imaging, rheological and mechanical tests. It has been shown that, the peel performance of the LDPE/EMA/organoclay sealants in which organoclays localized mainly at the interface of the LDPE/EMA, is significantly enhanced when compared to the neat LDPE/EMA blend sealant that exhibits lock seal performance. On the other hand, the LDPE/EMA-GMA/organoclay sealant in which organoclay localized inside the EMA-GMA phase exhibited lock seal performance similar to the LDPE/EMA-GMA sealant.

Chapter 6 presents the third article entitled “Novel Polyethylene/Polybutene-1/clay nanocomposite peelable sealants with versatile peel performance”. In this article, the effect of the incorporation of organoclay on the peel performance of the LDPE/PB-1 blends containing 5 to 20 wt% of the PB-1 is investigated. The microstructure of the organoclay and its localization at the interface of the LDPE/PB-1 revealed by WAXD, TEM and SEM results. The aging of the sealants was examined through T-peel test and WAXD right after and 10 days after the heat sealing. The results show that,

LDPE containing 1 phr organoclay or containing 5 wt% of the PB-1 is lock seal while, LDPE/PB-1/organoclay containing the same level of the organoclay and PB-1 is peelable in a very wide ΔT_p of over 100 °C. The effectiveness of 1 phr organoclay to enhance the peelability is reduced by increasing the PB-1 content that is attributed to reduced coverage of the interface of the blend components by organoclay. In contrast to the LDPE/PB-1 blends which aged after the heat sealing, the peel performance of the LDPE/PB-1/organoclay sealants are consistent.

The fourth article entitled “Confined Crystallization of Polybutene-1 Nanofibrils in Low Density Polyethylene/Polybutene-1/Organoclay Nanocomposite Films” is presented in chapter 7. In this article, it is shown that form I and I′ directly generated right after the heat sealing of the LDPE/PB-1 blend and their clay nanocomposite sealants. Existence of the metastable form II crystal of the PB-1 was revealed by WAXD and FTIR results right after the heat sealing of the LDPE/PB-1 sealants. In contrast, no trace of form II was detected after the heat sealing of the LDPE/PB-1/organoclay nanocomposite sealants. In the nanocomposite sealants, direct formation of form III was also confirmed through FTIR and WAXD results right after the heat sealing. In this article, effect of the melt memory as well as the effect of the confined crystallization on the direct formation of stable crystalline forms I, I′ and III and suppression of the form II formation of the PB-1 is discussed.

CHAPTER 4 ARTICLE 1: PEELABLE PE/CLAY NANOCOMPOSITE SEALS WITH ULTRA-WIDE PEELABLE HEAT SEAL TEMPERATURE WINDOW[1]

Raziyeh S. Mohammadi, Seyed H. Tabatabaei, Abdellah Ajji

3SPack NSERC-Industry Chair, CREPEC, Chemical Engineering Department, Polytechnique Montreal, C.P. 6079, Succ. Centre-ville, Montreal, QC, H3C 3A7, Canada

4.1 Abstract

It will be shown that the controlled dispersion and distribution of nanoclay in PE/clay nanocomposite result in peelable sealants with an ultra-wide peelable heat-seal temperature window (ΔT_p). Different nanoclays are examined for their capacity to generate peelable PE/clay nanocomposites in a melt-blending film extrusion process: unmodified montmorillonite (MMT) and organo-modified MMTs, i.e. Cloisite15 and 20. Polyethylene (PE) nanocomposite films containing 6 wt% organoclay exhibit a cohesive peel behavior with a ΔT_p of about 12 °C while PE film containing 6 wt% unmodified clay results in microcomposite with a lock seal performance. A much lower peel strength with a significantly broad ΔT_p of 45 °C is achieved mainly due to the fine dispersion of MMT when polyethylene-grafted-maleic anhydride (PE-g-MA) is used as a compatibilizer. WAXD and TEM results confirm that a substantial enhancement in the dispersion and distribution of intercalated nanoclays is achieved with PE-g-MA compatibilizer. Finally, an ultra-wide ΔT_p of over 100 °C is obtained for PE/PE-g-MA/3%Cloisite15 with partially exfoliated microstructure indicating that the exfoliation of nanoclay is in favor of peelability. The peel fracture mechanics of the nanocomposite sealants have been examined through T-peel test and SEM imaging. The results show that the dispersion and distribution of nanoclay along with the interfacial

[1] Submitted to *Industrial & Engineering Chemistry Research.*

adhesion between nanoclay and matrix are the key factors controlling the peel performance of the sealants.

4.2 Introduction

Packaging with peelable functionality is increasingly growing due to modern life style and is an important factor in consumer purchase behavior [1], [2]. Generally, a peelable sealant can be peeled either from the interface of the seal layer and its substrate [3], [4] or within the seal layer [5], [6] or a mixture of both [7]. In addition to their poor sealing, adhesive peels are more sensitive to seal parameters i.e. heat seal temperature, pressure and dwell time [4]. In contrast, in cohesive peels the sealant is completely welded to the substrate and ensures that the chance of leakage is prevented and the shelf life of the product inside the package is not affected [8]. Cohesive peelable sealants are mainly achieved through blending two or more immiscible polyolefins, such as blends of polyethylene (PE) or ionomer with Polybutene-1 (PB-1) and blends of poly(ethyl methyl acrylate) (PEMA) with propylene-ethylene copolymers [8]. Light weight, low cost, chemical resistance and low heat seal initiation temperature are among the key factors which make polyolefins and in particular PE, the best candidate for seal applications [9]. However, when used as seal materials, these blends mainly suffer from narrow peelable heat seal temperature window (ΔT_p). Increasing the heat seal temperature enhances co-crystallization and diffusion of long polymer chains across the interface of a seal area. Consequently, the seal strength increases up to a point where the peel functionality is lost and the sealant becomes a lock seal [10], [11]. Blending PE based matrices with PB-1 is known to results in peelable sealant with quite broad peelable heat seal temperature range [6]. But, long term aging of PB-1 after melt process [12]–[16] leads to inconsistent heat seal initiation temperature and peel strength thus, restricts the application of PB-1 for peelable seal applications [17].

Despite the significant breakthroughs of polymer/clay nanocomposites in a variety of applications [18], [19], there is still high potential to benefit from nanoclays in many emerging applications. Beside light weigh, low cost and easy processability, polymer/clay nanocomposites with only a small amount of nanoclay possess very unique properties mainly due to high aspect ratio of nanoclay [18], [20]–[23]. Packaging is an important global industry that has recently exploited nanotechnology to develop innovative products with novel characteristics which are absent from

pure polymers or composites [22], [24]–[26]. Montmorillonite (MMT) is the most common type of layered nanoclay [26] and is composed of hydrated alumina-silicate layered clay, which consists of an edge-shared octahedral sheet of aluminum hydroxide between two silica tetrahedral layers [27]. MMT possesses very high surface energy arising from very high surface to volume ratio of highly charged silicate layers, which form platen clusters [24]. It is known that a good dispersion of nanoclays is critical to take advantage of superior properties of nanoclays in polymer nanocomposites. However, the poor interactions between hydrophilic clay particles and hydrophobic polymers hinder the diffusion of polymer chains into clay galleries and its effective dispersion, thus, different methods are reported to enhance polymer-clay interactions in order to increase the aspect ratio of nanoclays in polymer nanocomposites [28]. Surface modification of nanoclay and the incorporation of a compatibilizer into the polymer matrix are amongst the most common ways to improve polymer-clay affinity in melt processed polymer nanocomposites [18], [28]. Numerous studies have investigated the effect of nanoclay surface chemistry on the affinity between the polymer and clay surface and its impact on properties such as thermal [29]–[35], mechanical [32], [33], [36]–[39] barrier [31], [32], [37], [40] and rheological [35], [39], [41] of the polymer/clay nanocomposites. In this approach, hydrated cations, such as Na^+, at the surface of the clay were replaced by organic cations, such as alkyl ammonia salts with various length of the alkyl group and various concentrations of the surfactants. Surface modification of nanoclay is usually adequate to improve dispersion of nanoclay in polar polymers such as nylon [42], [43] but, in the case of non-polar polymers such as polyethylene (PE) and polypropylene (PP) incorporation of an appropriate compatibilizer that is miscible with polymer matrix and whose polar groups are adequate to interact with clay surface, is necessary to achieve intercalated nanocomposites [30], [43]–[45]. The performance of polymer nanocomposites is usually enhanced by increasing the dispersion and distribution of nanoclays through compatibilizer addition [46], [47].

A massive study of polymer/clay nanocomposites suggests important benefit of nanoclays in achieving high performance materials. To date, controlling the dispersion and distribution of clay particles in polymer matrix have been shown to enhance various properties of polymer/clay nanocomposites such as thermal, electrical, mechanical, barrier and rheological. Nevertheless, it is not clear how the microstructure of nanoclay affects the seal and peel performance of polymer/clay nanocomposite sealants. This work reports on the effect of dispersion and distribution of nanoclays

on peel performance of PE (as the most common seal material)/clay nanocomposite sealants. For this aim, the impact of nanoclays surface modification as well as the effect of a PE-g-MA compatibilizer on the dispersion and distribution of nanoclays in the seal layer and its consequences on the seal and peel properties of the PE/nanoclay sealants are discussed. Finally, a mechanism of peeling correlating to the nanocomposite morphology is proposed.

4.3 Experimental

4.3.1 Materials

Low density polyethylene (LDPE, Novapol LF-0219-A) was obtained from Nova Chemicals and was used as the sealant layer in this study. Linear low density polyethylene (LLDPE, Exxon LL3003.32) and high density polyethylene (HDPE, SCLAIR 19A) were obtained from ExxonMobil and Nova Chemicals, respectively, and were used as support layers to eliminate yielding of the seal layer upon peeling. Unmodified sodium montmorillonite (Cloisite Na^+), organomodified clays Cloisite 20 and Cloisite15 were provided by Byk company. The two organomodified nanoclays have a similar organomodifier of dimethyl dihydrogenated tallow in which tallow is approximatly 65% C18, 30% C16, 5% C14 with cation exchange capacity (CEC) of 95 and 125 for Cloisite 20 and Cloisite15, respectively. A commercial grade of maleic anhydride (MAH) grafted low density polyethylene (PE-g-MA) with a trade name of Bynel 4288 containing 0.23 wt% of MAH was purchased from Dupont and used as compatibilizer.

4.3.2 Nanocomposite preparation

Highly concentrated (30 wt%) masterbatches of LDPE/nanoclay were prepared using a co-rotating twin-screw extruder (TSE), Leistritz ZSE 18HP, with an L/D ratio of 40. A screw speed of 110 rpm and a temperature profile of 150/160/170/180/180/190/190/190 °C from hopper to die were used for processing. The extrudates were quenched in a cold-water bath, pelletized and dried prior to the next step. In the next step, masterbatches were diluted with LDPE through the same TSE and the same processing conditions to obtain PE/clay nanocomposite containing 6 wt% of different types of nanoclays. For Cloisite15, other clay contents (2, 4 and 10 wt%) were also evaluated. Masterbatches containing the compatibilizer, with compatibilizer/nanoclay ratios of 5:1 and 2:1,

were prepared and then diluted with LDPE to obtain samples containing 3 and 6 wt% nanoclay using the TSE at the same processing conditions. PE/Na^+-6% and PE/C20-6% are used as nomenclatures for nanocomposites containing 6 wt% of Cloisite Na^+ and Cloisite 20 respectively and PE/C15-2% to 10% are nomenclatures of nanocomposites containing 2 to 10 wt% of Cloisite15. PE/PE-g-MA/C15-6% and PE/PE-g-MA/C15-3% are representative of the nanocomposites with PE-g-MA/nanoclay weight ratio of 2 containing 6 and 3 wt% of Cloisite15 respectively and PE/PE-g-MA/C15-3% (5:1) is the nanocomposite containing 3 wt% of Cloisite15 with PE-g-MA/nanoclay weight ratio of 5.

4.3.3 Film casting

Three layer films were co-extruded through cast line with single screw extruders, LE20-30 from Labtech, with 5 layer ABCDA 12 inches coat hanger cast film die with a die opening of about 500 microns on average. The films were composed of LDPE nanocomposites as the sealant layer, LLDPE in the middle and HDPE as the outer support layer. The processing conditions of each single screw extruder were as follow: the nanocomposite sealant was extruded with a screw speed of 40 rpm and a temperature profile of 180/190/195/200, LLDPE and HDPE layers were extruded at screw speeds of 20 and 60 rpm, respectively, and a temperature profile of 180/190/200/210. The polymer films were stretched in air and, then, cooled and collected on a calendar rolls chilled with cold water. The collection speed and the draw ratio were manipulated to achieve a uniform tri-layer film with a total thickness of 90 microns in which the thickness of the seal layer, LLDPE and HDPE were approximately 40, 20 and 30 microns, respectively.

4.3.4 Heat sealing

The cast films were cut to 25.4 mm wide bands and sealed using a heat sealing machine (hot tack/seal tester from LakoTool & Manufacturing Inc, USA). The two pieces of the films were sandwiched between acetate films to avoid sticking to the hot seal bars. The upper and lower seal bars were set at an identical temperature. A pressure of 0.5 N/mm^2 was applied to bring the bars into intimate contact to seal the films for a dwell time of 1 second. The seal and peel properties of each film were evaluated at a heat sealing temperature range from 110-210 °C, above the melting point of LDPE, with an interval of 5°C.

4.3.5 Mechanical test

The T-peel test was carried out per ASTM F88 at room temperature using a tensile testing machine (Instron E3000) to measure the peel force of sealants. The heat-sealed films were peeled at a peeling rate of 200 mm/min. The results were plotted in terms of the peel force as a function of displacement. The plateau part of the plot was reported as the peel force of the corresponding specimen. The average plateau force of at least 5 specimens is reported as the peel force of each film.

4.3.6 Thermal analysis

Conventional Differential Scanning Calorimetry (DSC) analysis was carried out using a DSC instrument Q2000 to evaluate the thermal properties of the film samples. Specimens of 10-15 mg in weight were placed in aluminum pans. Conventional DSC heating and cooling runs were performed from 25 to 150 °C under nitrogen atmosphere at a heating rate of 10 ^{o}C/min.

4.3.7 Morphology analysis

Wide angle X-ray diffraction (WAXD) measurements were performed using a Phillips X'pert apparatus to investigate dispersion of nanoclays in the seal area. The diffraction patterns were obtained from θ-2θ scans in the range of 2-10° at a scan rate of 0.02 °/s. The anode was copper (Cu) with a K_{α} wave length of 1.54 Å. The generator voltage and tube current were set at 50 kV and 40 mA, respectively, at room temperature. The distance between detector and sample was 20 cm. In order to maximize the diffraction intensity, 25 films were stacked to make approximately a 2 mm thick sample.

The dispersion and distribution of nanoclays of samples were further evaluated through transmission electron microscopy (TEM) using a TEM machine (JEOL JEM-2100F, Japan, operating at 200 kV). The observations were done on TD (transverse direction)-ND (normal direction) surface. For this aim, the film samples were embedded in epoxy mold and then, a Leica Microsystem EM-UC7 ultramicrotome unit equipped with EM FC7 cryochamber was used to cut sections of samples with a diamond knife to a thickness of about 100 nm at -120 ^{o} C. The average distances between clay stacks, were measured using SigmaScan Pro 5 software. For this aim, the

average of the side by side distance and also head to tail distance of at least 100 nanoclay stacks were measured.

Scanning electron microscopy (SEM) was used to observe and evaluate the morphology of the peeled surface of sealants. The specimens were first coated with gold/palladium through plasma vacuum deposition and then SEM observations were carried out using a Field Emission SEM machine (JSM 7600TFE, JEOL) operated at a voltage of 2 kV.

4.3.8 Fourier Transform Infrared (FTIR) Spectroscopy

FTIR spectroscopy was carried out using Perkin Elmer 65 FTIR-ATI instrument. The analysis has been done in a wavelength range of 4000-650 cm^{-1} with a total of 128 scans and 4 cm^{-1} resolution.

4.3.9 Rheological analysis

Discs of samples with 25 mm diameter and 1 mm thickness were prepared through compression molding at 190°C and 300 kPa under the nitrogen atmosphere. The rheological analysis was performed using a stress controlled rheometer and 25 mm parallel plate geometry (Physica MCR301 Anton Paar) with 1 mm gap between the plate at 190°C under the nitrogen atmosphere.

4.4 Results and discussion

4.4.1 Microstructure

Figure 4.1 shows the WAXD patterns of the nanocomposites sealants. The characteristic (001) plane peak corresponds to the basal spacing of the nanoclay platelets, shifts from a high 2θ of 9.5° in PE/Na^{+}-6% sealant containing unmodified nanoclay to a low 2θ of about 3.6 and 3.8° in PE/C15-6% and PE/C20-6% nanocomposite films, respectively. These results indicate the formation of an intercalated nanoclay morphology in these PE/organoclay films. The (001) plane peak of nanoclay in the compatibilized PE/PE-g-MA/C15-6% system is unchanged when compared with PE/C15-6% whereas the intensity of the peak is reduced significantly. This suggests a less regular structure of the nanoclay platelets while the periodic ordering of the clay stacks is still maintained [48]. By reducing the nanoclay content to 3wt% in PE/PE-g-MA/C15-3%, the (001) plane peak shifts to lower 2θ, which suggests an increased basal spacing of the nanoclay platelets. This result shows

that the dispersion of nanoclay is improved at lower nanoclay loadings due to the smaller size of the stacks with less numbers of clay layers [49]. The (001) peak at low 2θ disappears in WAXD pattern of PE/PE-g-MA/C15-3% (5:1), in which the PE-g-MA/nanoclay ratio is 5 to 1, that suggests the clay basal spacing exceeds 8.8 nm corresponding to 2θ = 1°, the limit of the WAXD machine. This is considered an exfoliated structure as the clay gallery spacing is too large with no layered structure [18], [50], [51]. Although the (001) peak at low 2θ disappears, there is still another characteristic peak at 2θ = 5.5° with very low intensity. This suggests that the morphology of PE/PE-g-MA/C15-6% is not fully exfoliated but is rather partially-exfoliated.

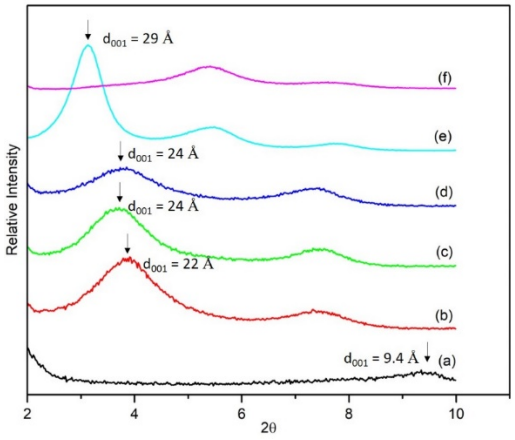

Figure 4.1. WAXD patterns of the nanocomposite films: PE/NC Na+-6% (a), PE/C20-6% (b), PE/C15-6% (c), PE/PE-g-MA/C15-6% (d), PE/PE-g-MA/C15-3% (e) and PE/PE-g-MA/C15-3% (5:1) (f). d_{001} indicates the clay gallery distance.

The TEM images presented in Figure 4.2 are in agreement with WAXD results. The big clusters in TEM image of PE/Na^{+}-6% indicates the formation of a microcomposite mainly due to a poor interaction between the organic polyolefin matrix and the inorganic clay. A significant reduction in the size and distance between the clay stacks are observed in TEM micrographs of the PE/C20-6% and PE/C15-6% nanocomposite films. According to the image analysis results, the ligament thickness between the stacks is 850 nm for PE/C15-6% system and 900 nm for PE/C20-6% system. This difference is attributed to the higher concentration of organic modifier used in the modification of Cloisite15, which results in the enhanced affinity of the clays with PE matrix. The TEM image of the PE/ PE-g-MA/C15-6% system shows marked dispersion and distribution of the clay stacks with average ligament thickness of 160 nm between the clay stacks. TEM micrographs also confirm

better dispersion of nanoclays with smaller clay stacks in PE/PE-g-MA/NC-3% rather than PE/PE-g-MA/NC-6% as it is suggested by WAXD patterns. But, the longer distance between the clay stacks, 415 nm, observed for PE/PE-g-MA/NC-3% compared to PE/PE-g-MA/NC-6% that is attributed to its lower nanoclay content. A mixture of the exfoliated and intercalated morphologies of the PE/PE-g-MA/C15-3% (5:1) nanocomposite can be speculated from its TEM micrograph, which shows individually well dispersed and distributed clay layers with a thickness as low as 5 nm as measured by image analysis software. The average clay stacks and ligament thickness for PE/PE-g-MA/C15-3% (5:1) is 140 nm.

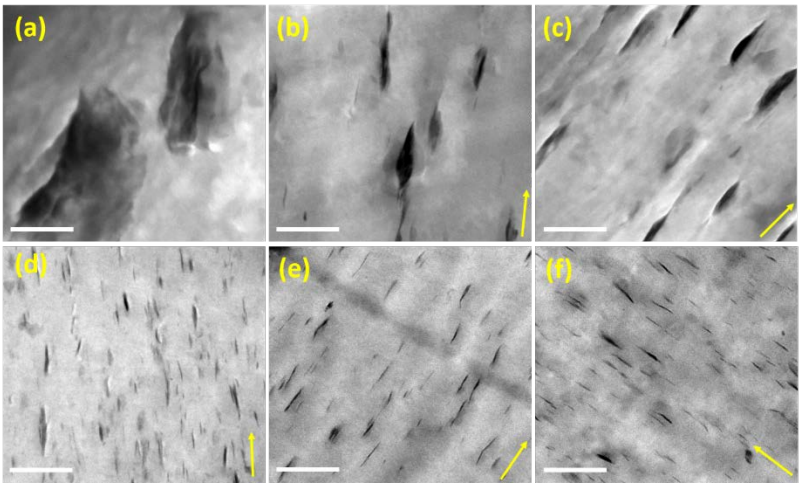

Figure 4.2. TEM micrographs of the nanocomposite films: PE/NC Na+-6% (a), PE/C20-6% (b), PE/C15-6% (c), PE/PE-g-MA/C15-6% (d), PE/PE-g-MA/C15-3% (e) and PE/PE-g-MA/C15-3% (5:1). The scale bars indicate 1 μm and the arrows indicate transverse direction (TD) of the films.

4.4.2 Seal and Peel Properties

Figure 4.3 shows the peel strength of PE/C15 nanocomposite sealants containing 0-10 wt% Cloisite15 nanoclay. The results reveal that the lock seal behavior of PE films is transformed to a peelable behavior through the incorporation of organo-modified C15 nanoclays into PE sealants. It should be noted that, in this study, the temperature range at which peel force falls within 150 to 650 N/m is considered as the peelable heat seal temperature window (ΔT_p). The heat seal initiation temperature (T_i) is the temperature at which a measurable and low level of peel strength is obtained. Addition of 6 wt% nanoclay increases ΔT_p of the nanocomposite sealants to over 10 °C. The

peelability is even more enhanced in the sealants containing 8 and 10 wt% clay so that ΔT_p for PE/C15-10% exceeds 45 °C. In the following sections, nanocomposites with 6 wt% clay are selected as they show balanced peel/seal properties with a potential for further improvements.

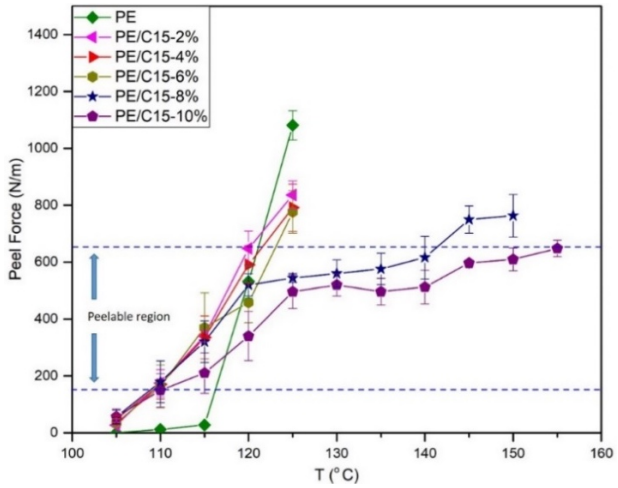

Figure 4.3. Peel strength of PE/C15 sealants with various clay concentrations as a function of temperature.

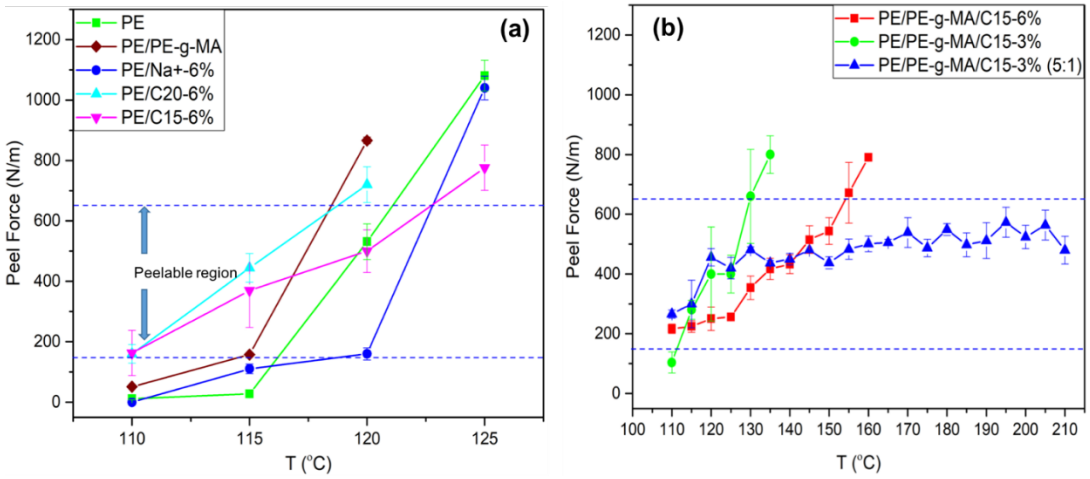

Figure 4.4. Peel force versus temperature of the neat PE sealant and its nanocomposite sealants.

Figure 4.4 shows the peel strength of the different nanocomposites as a function of seal temperature and the results are summarized in Table 4.1. The results show that the T_i of PE blended with 15wt% of PE-g-MA decreases from 120 to 115 °C, which may be due to the lower melting temperature and lower degree of crystallinity of PE-g-MA as compared to PE. The correlation between Ti and T_m is well described in previous studies [10], [11]. It was shown that the T_i of a sealant is at a

temperature around its initiation melting temperature and may be increased by increasing the degree and size of the crystals in the seal layer. PE/Na^+ nanocomposite containing 6 wt% clay shows a T_i of 120 °C similar to neat PE. However, neat PE, PE/PE-g-MA blend and PE/Na^+ nanocomposite sealants show lock seal behaviors beyond their T_i. This means that these sealants retain peelable functionality over a very narrow ΔT_p of less than 5 °C around their T_i only, which makes them practically not suitable for peel applications.

Table 4.1. Thermal, seal and peel properties of the various types of nanocomposites of this study.

Sample	T_m (°C)	X_c (%)	T_i (°C)	ΔT_p (°C)
PE before film casting	110	38	-	-
PE	106.5	11.8	120	Lock seal
PE/PE-g-MA	104	5.7	115	Lock seal
PE/Na+-6%	107.9	25.7	120	Lock seal
PE/C20-6%	108	25.5	110	8
PE/C15-6%	108	26	110	12
PE/C15-10%	108	26	110	45
PE/PE-g-MA/C15-6%	107	16	110	45
PE/PE-g-MA/C15-3%	107	16.2	110	20
PE/PE-g-MA/C15-3% (5:1)	106	14.6	110	Over 100 °C

T_m: melting temperature, X_c: degree of crystallinity, T_i: seal initiation temperature, ΔT_p : peelable heat-seal temperature window.

The incorporation of nanoclay to the sealant layer significantly influence its crystallinity and seal/peel properties as shown in Figure 4.4 and Table 4.1. The melting temperature of PE is not changed regardless of the type of nanoclay and presence of PE-g-MA compatibilizer while the T_i of the PE sealants containing organo-modified nanoclay decreases markedly to less than 110 °C. T_i of the nanocomposites are expected to be similar to that of PE because of the unchanged melting points. The lower T_i of the nanocomposites may be attributed to the higher thermal conductivity of the clay particles which enhances the heat transfer of the nanocomposites (Baniassadi et al., 2011; Chen et al., 2015). It is worth nothing that the temperature of the seal bar of the heat sealing machine is reported as the heat seal temperature here, which is not the accurate temperature of the seal area. The incorporation of nanoclay to the seal layer accelerates the heat transfer from seal

bars to the seal layer and results in a T_i very close to the melting point of the sealant at about 110 °C. The T_i obtained from the nanocomposites are almost at the lower limit of weldability of the films as below these temperatures, the films are not well melted to form a reliable sealant.

The results also indicate that ΔT_p is slightly increased from 8 °C for PE/C20-6% to about 12 °C for PE/C15-6% (Figure 4.4a). Furthermore, a remarkably broader peelable temperature range of 45 °C is achieved for PE/PE-g-MA/C15-6% (Figure 4.4b). By decreasing the nanoclay content from 6 to 3 wt% in PE/PE-g-MA/C15-3%, ΔT_p significantly reduced to 20°C. When the nanoclay content was kept constant at 3wt% but compatibilizer/nanoclay ratio increased from 2 to 5 in the PE/PE-g-MA/C15-3% (5:1) system, an ultra-wide ΔT_p (from 110 to 210 ^oC) is achieved (Figure 4.4b), which implies a temperature-independent peelability behavior.

4.4.3 Peel – seal microstructure relationship

The results presented above imply that the peel performance of the nanocomposite sealants is strongly dependent on the presence of nanoclay and its dispersion and distribution. It is observed that T_i is decreased from 120 °C to as low as 110 °C, which is the lowest possible heat sealing temperature due to the melting temperature of PE. Generally, chain entanglement and co-crystallization in the sealing area are considered as the two main mechanisms to provide anchors to strengthen welding in heat sealing of two polymeric films [10], [11], [54]. At lower heat seal temperatures, short polymer chains can move and penetrate across the seal interface. By increasing the temperature, the movement of longer polymer chains increases and are enabled to move across the seal area and contribute to the welding process. The longer chains form well-ordered and larger crystals, which enhances the density of tie molecules between the crystals and results in a robust seal with lock seal behavior [10], [11]. The incorporation of nanoclay, however, significantly influences the mobility of polymer chains in nanocomposites. Due to the high surface area and well oriented layered structure of the nanoclays in the seal area, the mobility of the polyethylene chains is restricted across the sealant. This restriction most likely affects the movement of the linear long PE molecules rather than that of the short chains. In this way, the reduction of T_i in the nanocomposite sealants can be attributed to the rapid melting of imperfect crystals of short chains due to the enhanced thermal conductivity by nanoclays. These effects are promoted by increasing the clay content and better dispersion and distribution of nanoclay platelets. For example, both

PE/Na^+-6% and PE/C15-6% sealants contain 6 wt% nanoclay, however, the PE/C15-6% system shows a reduced T_i mainly due to the enhanced dispersion and distribution of the nanoclay platelets (see Figure 4.2).

The temperature range of peelability also strongly correlates with the state of dispersion and distribution of nanoclays. The PE/Na^+-6% system does not show intercalation and adequate distribution of nanoclay, which results in a lock sealant. Changing the type of nanoclay to organoclay, i.e. PE/C20-6% or PE/C15-6%, leads to peelable films over a limited temperature window. In the samples containing 6 wt% of organomodified nanoclays, ΔT_p slightly increases to 8 and 12 °C for PE/C20-6% and PE/C15-6%, respectively, which show increases in the basal spacing from 9.4 for unmodified clay to 22 and 24 Å for organomodified clays Cloisite 20 and Cloisite15 respectively. The peel strength of the PE/C15-6% system is slightly lower than that of the PE/C20-6% system over their ΔT_p. This is attributed to the better distribution of the intercalated nanoclay stacks in PE/C15-6% compared to PE/C20-6% (Figure 4.2). Accordingly, when the PE-g-MA is added to the PE/C15-6% system as the compatibilizer, the peel strength markedly decreases and the peelability temperature window is extended to over 45 °C. These results reveal that the enhanced distribution of the intercalated nanoclay stacks in PE/PE-g-MA/C15-6% with an unchanged basal spacing of 24 Å has an important influence on the peel properties. The main difference between the compatibilized and uncompatibilized system is the state of nanoclay distribution. These results indicate that the distribution of nanoclays is the dominant factor influencing the seal properties of the systems. It should be noted that these peel properties are not associated with the addition of the PE-g-MA compatibilizer. The addition of PE-g-MA works against peelability as no peelable film is obtained from the PE/PE-g-MA binary blend containing 15 wt% of the PE-g-MA (see Figure 4.4a). The results show that the ligament thickness of the matrix, i.e. the distance between stacks of nanoclays, is a critical factor in the peelability of the PE/nanoclay nanocomposite films. The quantitative analysis of TEM images in Figure 4.2 confirms that the ligament thickness is directly proportional to the distribution of nanoclays, that is, a better distribution results in a smaller ligament thickness at a given concentration of nanoclay. Similar behavior is observed for the PE-g-MA compatibilized systems. The PE/PE-g-MA/C15-3% system shows a better nanoclay distribution and larger ligament thickness, however, a poor peel functionality was obtained as expected when compared with the PE/PE-g-MA/C15-6% system.

These results suggest that increasing the number of nanoclay stacks and lowering the ligament thickness between stacks are both in favor of peel functionality, i.e. lowering peel force and broadening ΔT_p.

On the other hand, the results show that a semi-exfoliated nanoclay morphology yields into a peelable nanocomposite film with an ultra-wide ΔT_p. As it is illustrated in Figure 4.4, a peelable behavior is obtained for PE/PE-g-MA/C15-3% (5:1) for all the heat seal temperatures used (from 110 to 210 °C), while PE/PE-g-MA/C15-3% system shows a peelable behavior in a limited ΔT_p of about 20 °C. The DSC results presented in Table 4.1 show that no significant change in the crystallinity of the samples containing 3 wt% C15 is observed when the PE-g-MA/nanoclay ratio is increased from 2 to 5. This indicates that the incorporation of PE-g-MA itself as a compatibilizer does not influence the peel performance of the nanocomposites in which no peelability is observed in the PE/PE-g-MA sealant. Thus, a marked peelability behavior for the semi-exfoliated PE/PE-g-MA/C15-3% (5:1) nanocomposite arises from nanoclay microstructure. These results suggest that ligament thickness plays a critical role in the peeling process of the PE nanocomposite films.

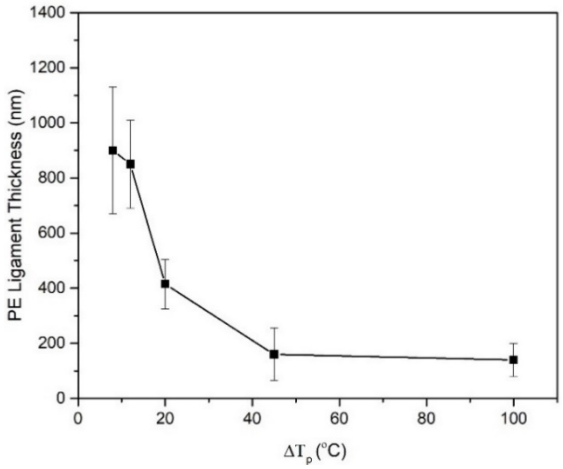

Figure 4.5. Variation of the peelable heat seal temperature range (ΔT_p) with ligament thickness.

Figure 4.5 shows the variation of the ΔT_p as a function of the PE ligament thickness. Since, our results showed identical values for side by side average distance and head to tail average distance of the clay stacks, an average of the side by side distance is reported here as the ligament thickness. As it is seen in Figure 4.5, for PE/C20-6% which has a ΔT_p= 8 °C, the ligament thickness is about 900 nm. A slight enhancement of the ΔT_p of the PE/C15-6% to 12 °C is in line with the small

reduction in the ligament thickness of PE/C15-6% to 850 nm. The ligament thicknesses of the PE/C20-6% and PE/C15-6% have a large error value of about 230 and 160 nm respectively, that indicate a non-uniform distribution of the clay stacks in these nanocomposites. The ligament thickness reduces to 415 nm for PE/PE-g-MA/C15-3% which has a broader ΔT_p of about 20 °C when compared with nanocomposites without compatibilizer. Much smaller ligament thickness of about 160 nm is observed for PE/PE-g-MA/C15-6% that has a ΔT_p of about 45°C. PE/PE-g-MA/C15-6% and PE/PE-g-MA/C15-3% nanocomposites revealed much lower error values (of about 60 nm) that is attributed to the enhanced nanoclay distribution in compatibilized sealant. Ultimately, for the PE/PE-g-MA/C15-3% (5:1) that has an ultra-wide ΔT_p of over 100 °C, the ligament thickness is further reduced to 140 nm with an even lower uncertainty (of about 30 nm).

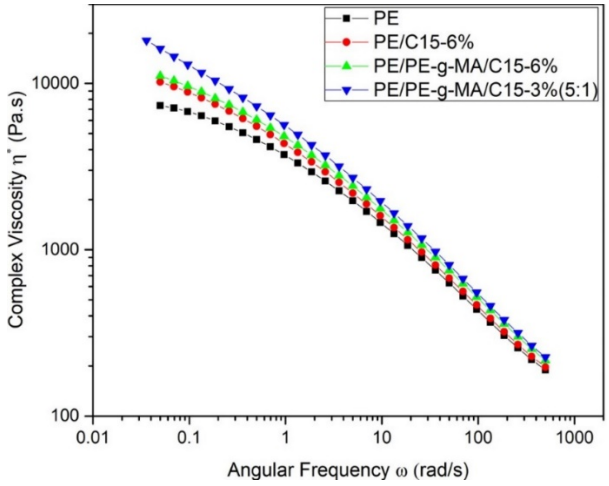

Figure 4.6. Complex viscosity versus angular frequency of the nanocomposites at 190 °C and 10% strain.

These results clearly confirm that the ligament thickness between the clay stacks, as well as the distribution of the nanoclay in the seal area have crucial effects on the peel functionality. Such that, an ultra-wide ΔT_p or thermal-independent peel functionality is achieved when the ligament thickness in the range of 140 nm and nanoclays are well distributed in the seal area. By increasing the heat seal temperature, the chance of the squeeze -out of the seal layer and contribution of the core layer into the seal are increased [55]. For PE/PE-g-MA/C15-3% (5:1) that shows more uniform morphology, good nanoclay platelets distribution and very low ligament thickness,

peelability is retained even at high heat seal temperature (210 °C). This could be due to the significant enhancement of the viscosity of PE/PE-g-MA/C15-3% (5:1) and its solid-like behavior that retards squeeze-out and deterioration of the seal by increasing the sealing temperature. Figure 4.6 shows that the complex viscosity of PE increased following incorporation of organomodified clay. Rheological response at low frequencies reflects the effect of nanoclay structure while at high frequencies it is controlled by the polymer melt [56]. The higher viscosity for PE/PE-g-MA/C15-3% (5:1) system at low frequencies indicates solid-like behavior and the formation of a nanoscale network, which further confirms the partial exfoliation of nanoclays in the polymer matrix [56], [57].

Figure 4.7 shows force versus displacement upon peeling the sealants obtained from T-peel test. The plateau zone of the curves indicates the peeling. PE/PE-g-MA/C15-6%, Figure 4.7a, represents peelable behavior when it is sealed at 120 and 140 °C, but, when it is sealed at 160 °C and above, the seal tears followed by elongation and strain hardening, which is the behavior of lock seals. Figure 4.7b indicates that for PE/PE-g-MA/C15-3% (5:1) with semi-exfoliated morphology, the plateau zones are quite wide and continued until the sealant is completely splits apart, which shows the peelable performance of the sealant. This peel behavior is consistent even by increasing heat seal temperature to 200 °C.

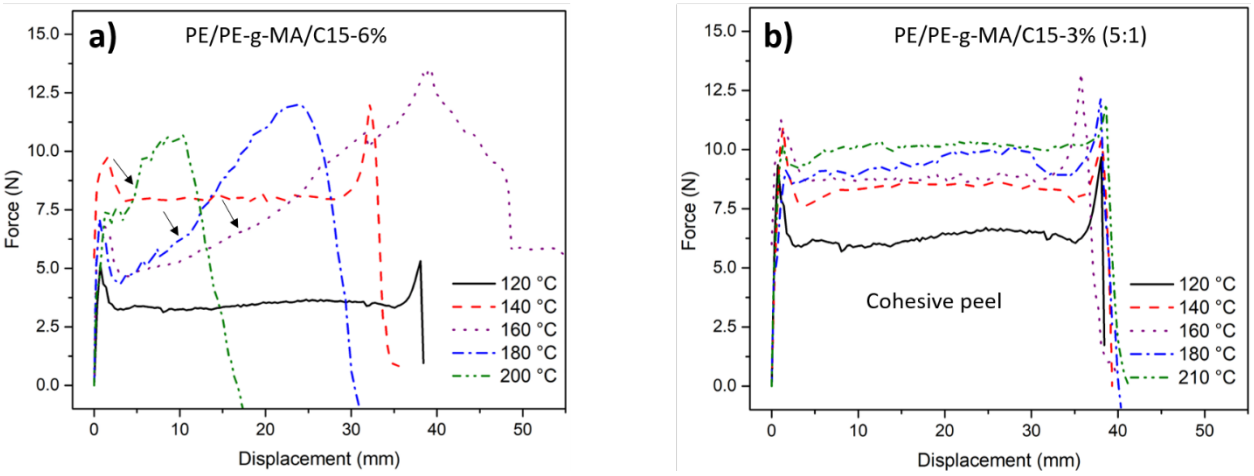

Figure 4.7. Force versus displacement upon peeling the PE/PE-g-MA/C15-3% (5:1) with semi-exfoliated morphology and PE/PE-g-MA/C15-6% with intercalated morphology. The arrows indicate tearing followed by elongation and strain hardening.

4.4.4 Fractured surface analysis

Compositional analysis of the peeled surfaces of the samples sealed on pure PE films at 120 °C was performed using ATR-FTIR spectroscopy and the results are presented in Figure 4.8. In adhesive peels, no residue of the seal is left on the substrate after peeling while the presence of the seal ingredients on the other side indicates cohesive peel failure. The ATR-FTIR spectra show traces of MMT on the PE side of the peeled surface. The intensity of the SiO_X traces increases with nanoclay concentration. These results indicate that a cohesive failure was obtained, in which the fracture path is through the PE/clay nanocomposite interface rather than the sealing interface.

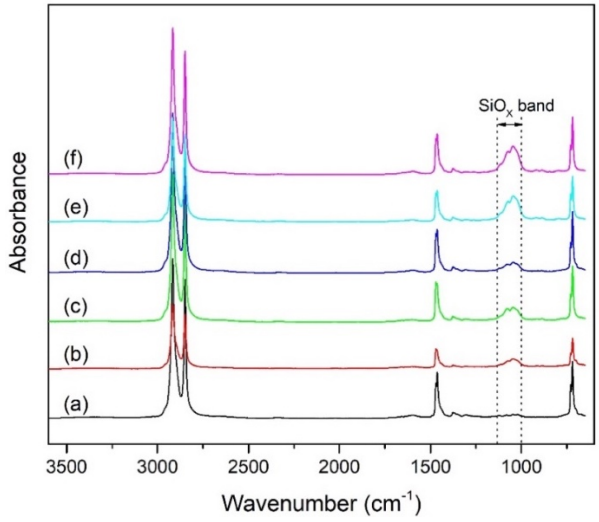

Figure 4.8. ATR-FTIR spectra of a) pure PE, b) PE/C20-6%, c) PE/PE-g-MA/C15-3%, d) PE/PE-g-MA/C15-3% (5:1), e) PE/C15-6%, f) PE/PE-g-MA/C15-6%.

Although the peel force is the most common parameter to represent the adhesion strength, but it does not consider the strains upon peeling. The total energy of peeling, E_G, is constituted by adhesive fracture energy, E_a, and plastic dissipated energy, E_p. The latter is defined as dissipated energy in the peel arm, $E_{d,P}$, and deformation energy of the already peeled seal area, $E_{d,S}$. The incorporation of clay particles in seal layer results in the formation of zones with various adhesion strength which act as potential breaking zones. In order to examine the effect of the seal microstructure on the peel behavior, the adhesive energy which consists of PE adhesion to itself and PE adhesion to clay particles, must be determined by extracting E_{dp} and E_{ds} from total energy. These parameters are determined in Figure 4.9a. The two maxima at the beginning and end of the

curves are attributed to the concave geometry of the seal area due to the flow of the polymer melt to the borders under the pressure of the seal device. This fact results in thickening of the border and thus local increase of the peel force. E_G is total peel energy and is the area under the force-displacement diagram, $E_{d,P}$ is the area under the curve until the point at which the slop is changed. Nase et al. [58] showed that the change of the slop is due to the formation of the crack front and the beginning of the peel process. Based on the theory [59]–[61] and using the mentioned parameters, energy release rate, G_{Ic}, and adhesion energy release rate, G_{aIc}, can be determined using Equations (4.1) and (4.2)

$$G_{Ic} = E_G/WL \quad 4.1$$

$$G_{aIc} = (E_G - E_{dp} - E_{ds})/WL \quad 4.2$$

in which W is the width of the sealant and L is length of the seal.

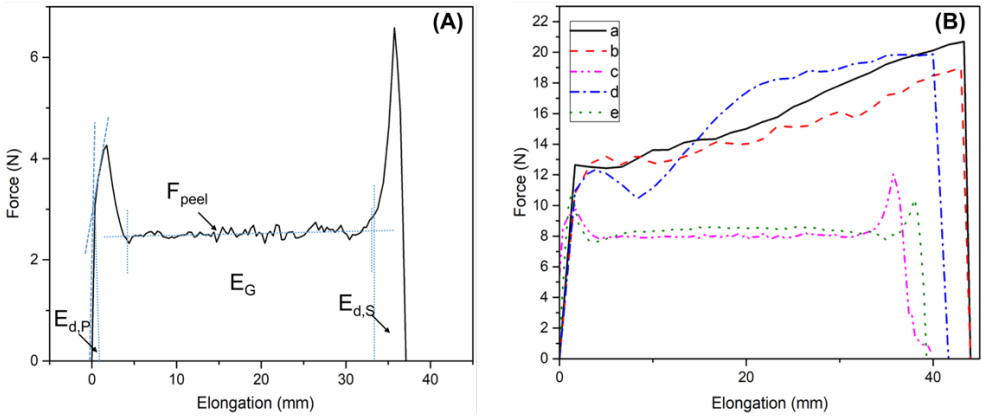

Figure 4.9. Force-displacement diagrams (A) and force-displacement diagram of various nanocomposites of this study (B): PE/C20-6% (a), PE/C15-6% (b), PE/PE-g-MA/C15-6% (c), PE/PE-g-MA/C15-3% (d) and PE/PE-g-MA/C15-3% (5:1) (e).

The force-displacement diagrams of various nanocomposites of this study are presented in Figure 4.9b. It seems that the contribution of the energy dissipation at the peel arm and peeled seal area is significantly reduced for PE/PE-g-MA/C15-6% and PE/PE-g-MA/C15-3% (5:1) in which average PE ligament thickness are 160 and 140 nm respectively. By increase in the PE ligament thickness between the clay stacks in PE/PE-g-MA/C15-3%, PE/C15-6% and PE/C20-6% considerable

strains are observed that imply plastic deformations of the seal upon peeling. Due to immiscibility of PE and clay particles, the welding zones of PE to itself has much higher adhesion force than the PE/clay interface or electrostatically bonded clay-clay interface. Figure 4.10 shows variation of G_{aIc} versus PE ligament thickness at different heat seal temperatures. For different heat seal temperatures, G_{aIc} exponentially increases upon increase in the PE ligament thickness. In addition, the slope of these variations is considerably sensitive at low values of the ligament thickness. Decreasing the G_{aIc} is attributed to the better distribution of the clay particles that results in the reduced contribution of PE-PE adhesive energy and more contribution of the PE-clay or clay-clay interface adhesion energy during peeling process. Decreasing the ligament thickness between the clay stacks to values less than 160 nm apparently results in a network made by regions with low adhesion (PE-clay or clay-clay interfaces) which significantly facilitates crack bridging upon peeling.

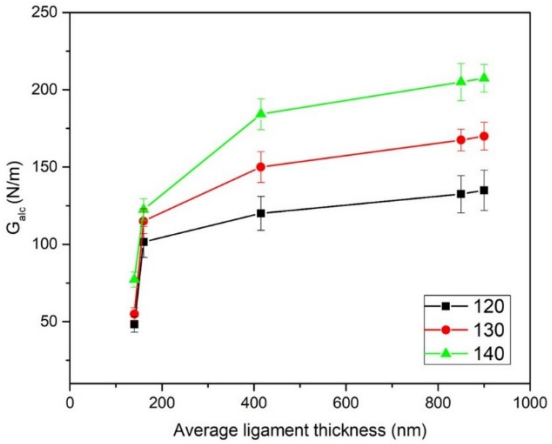

Figure 4.10. Adhesive energy release rate versus average ligament thickness of the sealants sealed at various seal temperatures. The legend denotes heat seal temperature.

To further monitor the peel performance, Figure 4.11 shows SEM images of the peel fractured surface of the various nanocomposite films of this study. These samples were sealed at 120 °C, which is within their peelable region. The rough and fibrillated surface of these peeled samples can be associated with the plastic deformation of the PE matrix. The extent of deformation of the peeled surfaces, that are shown in Figure 4.11, is well in line with the peel forces obtained for these samples (see Figure 4.4), force-displacement diagrams (Figure 4.9b) and adhesion energy release rate data (Figure 4.10). Much intense deformations imply stronger resistance to peeling and

translate into higher peel strength. The peel fractured surface of the PE/Na^+-6% system reveals a less deformed and non-uniform surface, which is consistent with the low peel strength of about 158 N/m at 120 °C. Furthermore, the big agglomerates of unmodified clays are present at the peel fractured surface (Figure 4.11a). By contrast, the PE/C20-6% and PE/C15-6% peel fractured surfaces demonstrate intense plastic deformation of the PE matrix (Figure 4.11b,c). The slightly less and more uniform deformation of PE/C15-6% compared to that of PE/C20-6% agrees with their peel performances. PE/C15-6% shows a peel strength of 458 N/m whereas it is 713 N/m for PE/C20-6%. The peel fractured surface of the sample compatibilized with PE-g-MA, PE/PE-g-MA/C15-3%, has a much smoother fracture surface with the lower peel strength of 400 N/m (Figure 4.11d). By increasing the nanoclay content to 6wt% for PE/PE-g-MA/C15-6%, which has much lower peel strength of about 250 N/m, much smoother and more uniform fractured surface is observed (Figure 4.11e) when compared with other samples. The peeled surface of PE/PE-g-MA/C15-3% (5:1) seems uniform and smooth (Figure 4.11f) but, reveals more deformation when compared with PE/PE-g-MA/C15-6%. It should be because of its peel force (456 N/m) that is higher than that of PE/PE-g-MA/C15-6%. Higher peel force for PE/PE-g-MA/C15-3% (5:1) is attributed to the exfoliation morphology and its less electrostatically bonded clay stacks when compared with the PE/PE-g-MA/C15-6% that need a lower peel force.

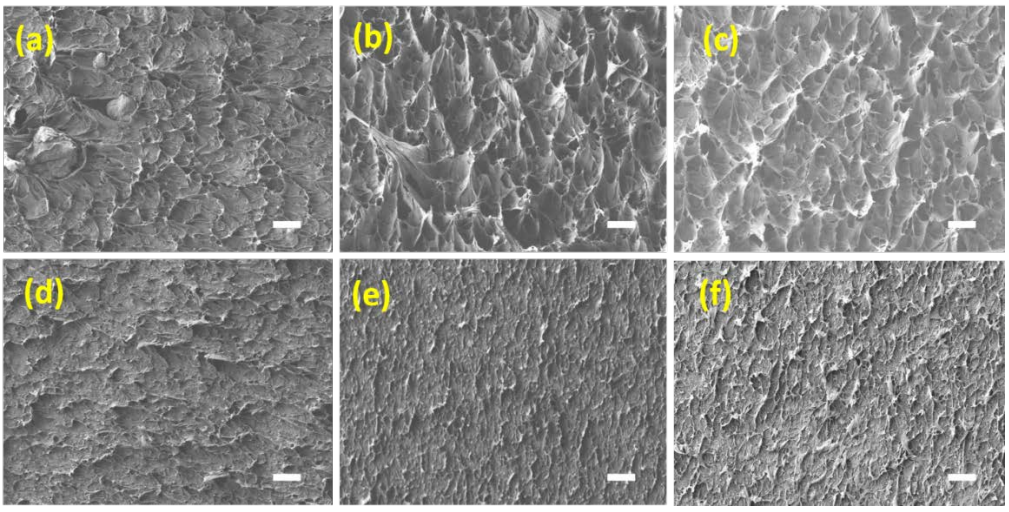

Figure 4.11. SEM micrographs of the peeled surfaces of PE/Na+-6% (a), PE/C20- 6% (b), PE/C15-6% (c), PE/PE-g-MA/C15-3%, (d), PE/PE-g-MA/ C15-6% (e) and PE/PE-g-MA/ C15-3% (5:1) nanocomposite sealants. The scale bars denote 10 µm.

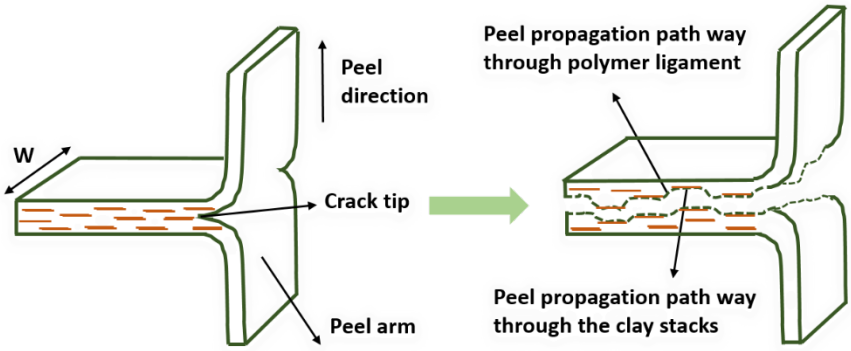

Figure 4.12. Schematic of the peeling a nanocomposite sealant.

4.4.5 Peeling mechanisms

Two main mechanisms are involved in the peeling fracture of sealed films: crack initiation and propagation. Generally, cracks can initiate either at nanoclay/polymer interface or within electrostatically bonded clay layers of nanoclay stacks in polymer/clay nanocomposites under external stress. However, it has been shown that the electrostatically bonded nanoclay layers of clay stacks are most likely to initiate cracks under loading [62]–[64]. The Young's moduli and Poisson's ratios of clay and polymers are significantly different, which results in stress concentration at polymer-clay interface. This idea is confirmed by comparing the peel force of PE/PE-g-MA/C15-6% with that of PE/PE-g-MA/C15-3% (5:1) at various heat seal temperatures. Below 140 °C, PE/PE-g-MA/C15-6%, with an intercalated morphology and more electrostatically bonded clay stacks, reveals lower peel force than PE/PE-g-MA/C15-3% that has semi-exfoliated morphology and more individually clay dispersions. Since, electrostatically clay layers need less peel force for delamination than the polymer-clay interface, the peel force of the PE/PE-g-MA/C15-6% is less than the peel force of the PE/PE-g-MA/C15-3% (5:1). The main question here is: if the electrostatically bonded clay stacks are more likely to initiate crack and need less peel force rather than PE-clay interface, what is the advantage of exfoliated clay morphology over intercalated or even microcomposite? An answer to this question is that although the clay-clay interface needs less peel force than PE-clay interface to be delaminated, but PE-clay interface still needs much less peel force for delamination compared to PE-PE interface. Furthermore, better dispersion of clay stacks results in wider ΔT_p as shown in this study. Over 140 °C due to the

squeeze-out and contribution of the core layer in the seal as discussed before, the peel force of the PE/PE-g-MA/C15-6% is increased.

After cracks are initiated within nanoclay stacks, they transform into rips as further strain constraints are imposed on the seal area by pulling sealed surfaces. Generally, cracks randomly propagate through the weakest points in heterogeneous matrices. In the heterogeneous clay nanocomposite systems studied here, cracks/rips extend from a nanoclay stack to another neighboring nanoclay stack throughout seal area. For this to happen, the ligament matrix between two neighboring stacks must yield and ultimately break. These cracks/rips extend and propagate throughout the seal area and result in the peel fracture of the PE nanocomposites. This proposed mechanism is schematically shown in Figure 4.12. It is worth noting that nanoclay stacks are highly oriented in the direction of the film casting process employed in this study, thus, a crack/rip can either extend end-to-end of stacks in the direction of nanoclay stacks or traverse from a stack to an adjacent stack to propagate throughout the seal area. It is expected that a combination of these two propagation mechanisms occurs in the peeling process of PE nanocomposites. This mechanism justifies the peel properties obtained in this study. It is observed that increasing the distribution state of intercalated nanoclays in the nanocomposite films, either through increasing the nanoclay content or using a compatibilizer, results in a lower peel strength and a wider peelable temperature window. Increasing the state of distribution of nanoclays leads to a smaller average ligament thickness so that cracks/rips can easily propagate from one nanoclay stack to another as a lower force is required to break the matrix. Since the crystallinity of the compatibilized PE/3%clay nanocomposites are similar (Table 4.1), it is thus mainly the distribution of the nanoclay that enhances the peelable heat seal temperature range of the nanocomposite sealants.

4.5 Conclusion

This paper reports on significant improvements in the peelability of PE melt processed films through a novel approach based on the control of the nanoclay dispersion in seal layer. As revealed by ATR-FTIR, a cohesive peel seal is obtained from the samples containing as little as 3 wt% organoclay whereas the sample containing the pristine nanoclay results in a microcomposite with lock seal behavior. The seal/peel results correlate well with the microstructure of nanoclay in the nanocomposite films. Incorporation of the organomodified nanoclay results in decreasing the T_i

into its lower limit (close to the melting point of the matrix). The better the dispersion and distribution of nanoclay are, the lower the peel strength and wider ΔT_p become. The compatibilized PE/PE-g-MA/C15-6% system shows significantly better dispersion and distribution of nanoclay and consequently much broader ΔT_p (45 °C) as compared with the uncompatibilized PE/C15-6% system, which shows relatively narrow ΔT_p (12 °C). The effect of nanoclay distribution on the improvement of peelability becomes more clear by the exfoliation of nanoclay platelets in the PE sealant. The PE/PE-g-MA/C15-3% (5:1) nanocomposite with a semi-exfoliated morphology demonstrates a marked peelable behavior with an ultra-wide ΔT_p of over 100 °C. In contrast, the PE/PE-g-MA/C15-3% system with an intercalated morphology and the same degree of the crystallinity shows a peelable behavior in much narrower ΔT_p of about 20 °C.

The results reveal that the contribution of the plastic deformations, which includes the strains of the peel arm and peeled seal area, decreases by better distribution of nanoclay in the seal layer. PE/PE-g-MA/C15-6% with an intercalated morphology reveals lower peel strength than that of PE/PE-g-MA/C15-3% (5:1), which has partially-exfoliated morphology and consequently less electrostatically bonded clay stacks. The peel fracture analysis of the nanocomposites suggest that cracks are preferentially initiated within the weak electrostatically bonded nanoclay layers rather than at the interface of nanoclays and PE matrix. On the other hand, the better distribution of nanoclay stacks reduces the distance between the stacks and consequently facilitates crack bridge between the regions with low adhesion force (clay-clay and PE-clay interfaces), hence further enhances the capability of initiated crack to propagate throughout the seal area.

4.6 Acknowledgements

The authors gratefully thank Natural Sciences and Engineering Research Council of Canada (NSERC), 3S Pack, Saputo and ProAmpac industrial research chair for their financial support.

4.7 References

[1] R. R. Ahmed, V. Parmar, and M. A. Amin, “Impact of Product Packaging on Consumer’s Buying Behavior,” Eur. J. Sci. Res., vol. 122, no. 2, pp. 125–134, 2014.

[2] A. Ybxoll, R. Janson, S. R. Bradbury, J. Langley, J. Wearn, and S. Hayes, “Openability: Producing design limits for consumer packaging,” Packag. Technol. Sci., vol. 19, no. 4, pp. 219–225, Jul. 2006.

[3] L. Ernesto Mendoza-Navarro, A. Diaz-Diaz, R. Castañeda-Balderas, S. Hunkeler, and R. Noret, “Interfacial failure in adhesive joints: Experiments and predictions,” Int. J. Adhes. Adhes., vol. 44, pp. 36–47, Jul. 2013.

[4] M. Nase, L. Großmann, M. Rennert, B. Langer, and W. Grellmann, “Adhesive properties of heat-sealed EVAc/PE films in dependence on recipe, processing, and sealing parameters,” J. Adhes. Sci. Technol., vol. 28, no. 12, pp. 1149–1166, Jun. 2014.

[5] P. Liewchirakorn, D. Aht-Ong, and W. Chinsirikul, “Practical Approach in Developing Desirable Peel-Seal and Clear Lidding Films Based on Poly(Lactic Acid) and Poly(Butylene Adipate-Co-Terephthalate) Blends,” Packag. Technol. Sci., Jun. 2017.

[6] M. Nase, B. Langer, and W. Grellmann, “Fracture mechanics on polyethylene/polybutene-1 peel films,” Polym. Test., vol. 27, no. 8, pp. 1017–1025, Dec. 2008.

[7] A. Martínez-García, A. Sánchez-Reche, S. Gisbert-Soler, M. D. Landete-Ruiz, R. Torregrosa-Maciá, and J. M. Martín-Martínez, “Durability of corona discharge and low-pressure air plasma-treated ethylene–vinyl acetate copolymers (EVAs),” Int. J. Adhes. Adhes., vol. 28, no. 1–2, pp. 38–46, Jan. 2008.

[8] A. Liebmann, I. Schreib, R. E. Schlözer, and J.-P. Majschak, “Practical Case Studies: Easy Opening for Consumer-Friendly, Peelable Packaging,” J. Adhes. Sci. Technol., vol. 26, no. 20–21, pp. 2437–2448, Jan. 2012.

[9] R. Coles, D. McDowell, and M. Kirwan, Eds., “Plastics in Food Packaging,” in Food Packaging Technology, 2003, p. 174.

[10] C. Mueller, G. Capaccio, A. Hiltner, and E. Baer, “Heat sealing of LLDPE: relationships to melting and interdiffusion,” J. Appl. Polym. Sci., vol. 70, no. 10, pp. 2021–2030, Dec. 1998.

[11] F. C. Stehling and P. Meka, “Heat sealing of semicrystalline polymer films. II. Effect of melting distribution on heat-sealing behavior of polyolefins,” J. Appl. Polym. Sci., vol. 51, no. 1, pp. 105–119, Jan. 1994.

[12] Y. Qiao, Q. Wang, and Y. Men, “Kinetics of Nucleation and Growth of Form II to I Polymorphic Transition in Polybutene-1 as Revealed by Stepwise Annealing,” Macromolecules, vol. 49, no. 14, pp. 5126–5136, Jul. 2016.

[13] M. Yamashita, M. Kato, I. K., H. A., and T. H., “Lamellar crystal thickness transition of melt-crystallized isotactic polybutene-1 observed by small-angle X-ray scattering,” J. Appl. Crystallogr., vol. 40, no. s1, pp. s650–s655, Apr. 2007.

[14] G. Kalay and C. R. Kalay, “Structure and physical property relationships in processed polybutene-1,” J. Appl. Polym. Sci., vol. 88, no. 3, pp. 814–824, Apr. 2003.

[15] J. Hu and K. Tashiro, “Time-Resolved Imaging of the Phase Transition in the Melt-Grown Spherulites of Isotactic Polybutene-1 as Detected by the Two-Dimensional Polarized IR Imaging Technique,” J. Phys. Chem. B, vol. 120, no. 20, pp. 4689–4698, May 2016.

[16] G. Kalay and C. R. Kalay, “Interlocking shish-kebab morphology in polybutene-1,” J. Polym. Sci. Part B Polym. Phys., vol. 40, no. 17, pp. 1828–1834, Sep. 2002.

[17] M. Nase, R. Androsch, B. Langer, H. J. Baumann, and W. Grellmann, “Effect of polymorphism of isotactic polybutene-1 on peel behavior of polyethylene/polybutene-1 peel systems,” J. Appl. Polym. Sci., vol. 107, no. 5, pp. 3111–3118, Mar. 2008.

[18] S. Pavlidou and C. D. Papaspyrides, “A review on polymer–layered silicate nanocomposites,” Prog. Polym. Sci., vol. 33, no. 12, pp. 1119–1198, Dec. 2008.

[19] H. Zou, S. Wu, and J. Shen, “Polymer/Silica Nanocomposites: Preparation, characterization, propertles, and applications,” Chemical Reviews, vol. 108, no. 9. pp. 3893–3957, 2008.

[20] S. Sinha Ray and M. Okamoto, “Polymer/layered silicate nanocomposites: A review from preparation to processing,” Progress in Polymer Science, vol. 28, no. 11. pp. 1539–1641, 2003.

[21] S. Kamel, “Nanotechnology and its applications in lignocellulosic composites, a mini review,” eXPRESS Polym. Lett., vol. 1, no. 9, pp. 546–575, Sep. 2007.

[22] S. D. F. Mihindukulasuriya and L. T. Lim, “Nanotechnology development in food packaging: A review,” Trends Food Sci. Technol., vol. 40, no. 2, pp. 149–167, 2014.

[23] S. Shokoohi and A. Arefazar, “A review on ternary immiscible polymer blends: morphology and effective parameters,” in Polymers for Advanced Technologies, 2009, vol. 20, no. 5, pp. 433–447.

[24] A. Arora and G. W. Padua, “Review: Nanocomposites in food packaging,” Journal of Food Science, vol. 75, no. 1. Blackwell Publishing Inc, pp. R43–R49, Jan-2010.

[25] D. A. Pereira de Abreu, P. Paseiro Losada, I. Angulo, and J. M. Cruz, “Development of new polyolefin films with nanoclays for application in food packaging,” Eur. Polym. J., vol. 43, no. 6, pp. 2229–2243, 2007.

[26] H. M. C. de Azeredo, “Nanocomposites for food packaging applications,” Food Research International, vol. 42, no. 9. pp. 1240–1253, 2009.

[27] J. Weiss, P. Takhistov, and D. J. McClements, “Functional materials in food nanotechnology,” Journal of Food Science, vol. 71, no. 9. Blackwell Publishing Inc, pp. R107–R116, Nov-2006.

[28] S. Sinha Ray and M. Okamoto, “Polymer/layered silicate nanocomposites: a review from preparation to processing,” Prog. Polym. Sci., vol. 28, no. 11, pp. 1539–1641, Nov. 2003.

[29] A. Leszczyńska, J. Njuguna, K. Pielichowski, and J. R. Banerjee, “Polymer/montmorillonite nanocomposites with improved thermal properties,” Thermochim. Acta, vol. 453, no. 2, pp. 75–96, Feb. 2007.

[30] S. K. Sharma and S. K. Nayak, “Surface modified clay/polypropylene (PP) nanocomposites: Effect on physico-mechanical, thermal and morphological properties,” Polym. Degrad. Stab., vol. 94, no. 1, pp. 132–138, 2009.

[31] S. Molinaro et al., “Effect of nanoclay-type and PLA optical purity on the characteristics of PLA-based nanocomposite films,” J. Food Eng., vol. 117, no. 1, pp. 113–123, 2013.

[32] M. Yourdkhani, T. Mousavand, N. Chapleau, and P. Hubert, “Thermal, oxygen barrier and mechanical properties of polylactide-organoclay nanocomposites,” Compos. Sci. Technol., vol. 82, pp. 47–53, 2013.

[33] K. Fukushima, D. Tabuani, M. Arena, M. Gennari, and G. Camino, “Effect of clay type and loading on thermal, mechanical properties and biodegradation of poly(lactic acid) nanocomposites,” React. Funct. Polym., vol. 73, no. 3, pp. 540–549, 2013.

[34] H. Krump, A. S. Luyt, and I. Hudec, “Effect of different modified clays on the thermal and physical properties of polypropylene-montmorillonite nanocomposites,” Mater. Lett., vol. 60, no. 23, pp. 2877–2880, 2006.

[35] S. G. Lei, S. V. Hoa, and M.-T. Ton-That, “Effect of clay types on the processing and properties of polypropylene nanocomposites,” Compos. Sci. Technol., vol. 66, no. 10, pp. 1274–1279, 2006.

[36] K. J. Shah, A. D. Shukla, D. O. Shah, and T. Imae, “Effect of organic modifiers on dispersion of organoclay in polymer nanocomposites to improve mechanical properties,” Polymer, vol. 97, pp. 525–532, 2016.

[37] J.-W. Rhim, S.-I. Hong, and C.-S. Ha, “Tensile, water vapor barrier and antimicrobial properties of PLA/nanoclay composite films,” LWT - Food Sci. Technol., vol. 42, no. 2, pp. 612–617, 2009.

[38] B. Qi, Q. X. Zhang, M. Bannister, and Y.-W. Mai, “Investigation of the mechanical properties of DGEBA-based epoxy resin with nanoclay additives,” Compos. Struct., vol. 75, no. 1, pp. 514–519, 2006.

[39] Y. H. Lee, C. B. Park, M. Sain, M. Kontopoulou, and W. Zheng, “Effects of clay dispersion and content on the rheological, mechanical properties, and flame retardance of HDPE/clay nanocomposites,” J. Appl. Polym. Sci., vol. 105, no. 4, pp. 1993–1999, Aug. 2007.

[40] J.-K. Kim, C. Hu, R. S. C. Woo, and M.-L. Sham, “Moisture barrier characteristics of organoclay–epoxy nanocomposites,” Compos. Sci. Technol., vol. 65, no. 5, pp. 805–813, 2005.

[41] S. G. Jahromi and A. Khodaii, “Effects of nanoclay on rheological properties of bitumen binder,” Constr. Build. Mater., vol. 23, no. 8, pp. 2894–2904, 2009.

[42] T. D. Fernes, D. L. Hunter, and D. R. Paul, “Nylon-6 Nanocomposites from Alkylammonium-Modified Clay: The Role of Alky1 Tails on Exfoliation,” Macromolecules, vol. 37, no. 5, pp. 1793–1798, 2004.

[43] A. Okada and A. Usuki, “Twenty years of polymer-clay nanocomposites,” Macromol. Mater. Eng., vol. 291, no. 12, pp. 1449–1476, Dec. 2006.

[44] M. Kawasumi, N. Hasegawa, M. Kato, A. Usuki, and A. Okada, “Preparation and Mechanical Properties of Polypropylene-Clay Hybrids,” Macromolecules, vol. 30, pp. 6333–6338, 1997.

[45] M. Kato, A. Usuki, and A. Okada, “Synthesis of polypropylene oligomer?clay intercalation compounds,” J. Appl. Polym. Sci., vol. 66, no. 9, pp. 1781–1785, Nov. 1997.

[46] N. Hasegawa, M. Kawasumi, M. Kato, A. Usuki, and A. Okada, “Preparation and mechanical properties of polypropylene-clay hybrids using a maleic anhydride-modified polypropylene oligomer,” J. Appl. Polym. Sci., vol. 67, no. 1, pp. 87–92, Jan. 1998.

[47] E. Jacquelot, E. Espuche, J.-F. Gérard, J. Duchet, and P. Mazabraud, “Morphology and gas barrier properties of polyethylene-based nanocomposites,” J. Polym. Sci. Part B Polym. Phys., vol. 44, no. 2, pp. 431–440, Jan. 2006.

[48] W. Lertwimolnun and B. Vergnes, “Influence of compatibilizer and processing conditions on the dispersion of nanoclay in a polypropylene matrix,” Polymer, vol. 46, no. 10, pp. 3462–3471, Apr. 2005.

[49] L. Chen, S.-C. Wong, and S. Pisharath, “Fracture properties of nanoclay-filled polypropylene,” J. Appl. Polym. Sci., vol. 88, no. 14, pp. 3298–3305, Jun. 2003.

[50] X. Kornmann, “Synthesis of epoxy–clay nanocomposites. Influence of the nature of the curing agent on structure,” Polymer, vol. 42, no. 10, pp. 4493–4499, Feb. 2001.

[51] J. Ma, Z. Qi, and Y. Hu, “Synthesis and characterization of polypropylene/clay nanocomposites,” J. Appl. Polym. Sci., vol. 82, no. 14, pp. 3611–3617, Dec. 2001.

[52] H. Chen et al., “Thermal conductivity of polymer-based composites: Fundamentals and applications,” Progress in Polymer Science, vol. 59, pp. 41–85, 2015.

[53] M. Baniassadi et al., “Mechanical and thermal behavior of nanoclay based polymer nanocomposites using statistical homogenization approach,” Compos. Sci. Technol., vol. 71, no. 16, pp. 1930–1935, 2011.

[54] Z. Najarzadeh and A. Ajji, “Role of molecular architecture in interfacial self-adhesion of polyethylene films,” J. Plast. Film Sheeting, vol. 33, no. 3, pp. 235–261, Jul. 2017.

[55] B. A. Morris and J. M. Scherer, “Modeling and experimental analysis of squeeze flow of sealant during hot bar sealing and methods of preventing squeeze-out,” J. Plast. Film Sheeting, vol. 32, no. 1, pp. 34–55, Jan. 2016.

[56] R. Wagener and T. J. G. Reisinger, “A rheological method to compare the degree of exfoliation of nanocomposites,” Polymer, vol. 44, no. 24, pp. 7513–7518, Nov. 2003.

[57] J. Ren, A. S. Silva, and R. Krishnamoorti, “Linear Viscoelasticity of Disordered Polystyrene−Polyisoprene Block Copolymer Based Layered-Silicate Nanocomposites,” Macromolecules, vol. 33, no. 10, pp. 3739–3746, May 2000.

[58] M. Nase, A. Zankel, B. Langer, H. J. Baumann, W. Grellmann, and P. Poelt, “Investigation of the peel behavior of polyethylene/polybutene-1 peel films using in situ peel tests with environmental scanning electron microscopy,” Polymer, vol. 49, no. 25, pp. 5458–5466, Nov. 2008.

[59] R. S. Rivlin, “The Effective Work of Adhesion,” in Collected Papers of R.S. Rivlin, New York, NY: Springer New York, 1997, pp. 2611–2614.

[60] V. A. Eremeyev and K. Naumenko, “A relationship between effective work of adhesion and peel force for thin hyperelastic films undergoing large deformation,” Mech. Res. Commun., vol. 69, pp. 24–26, Oct. 2015.

[61] E. Breslauer and T. Troczynski, “Determination of the energy dissipated during peel testing,” Mater. Sci. Eng. A, vol. 302, no. 1, pp. 168–180, Apr. 2001.

[62] G.-M. Kim, D.-H. Lee, B. Hoffmann, J. Kressler, and G. Stöppelmann, “Influence of nanofillers on the deformation process in layered silicate/polyamide-12 nanocomposites,” Polymer, vol. 42, no. 3, pp. 1095–1100, 2001.

[63] K. T. Gam, M. Miyamoto, R. Nishimura, and H. J. Sue, “Fracture behavior of core-shell rubber-modified clay-epoxy nanocomposites,” Polym. Eng. Sci., vol. 43, no. 10, pp. 1635–1645, Oct. 2003.

[64] K. Wang, L. Chen, J. Wu, M. L. Toh, C. He, and A. F. Yee, “Epoxy Nanocomposites with Highly Exfoliated Clay: Mechanical Properties and Fracture Mechanisms,” Macromolecules, vol. 38, no. 3, pp. 788–800, Feb. 2005.

CHAPTER 5 ARTICLE 2: EFFECT OF NANOCLAY LOCALIZATION ON THE PEEL PERFORMANCE OF PE BASED BLEND NANOCOMPOSITE SEALANTS [2]

Raziyeh S. Mohammadi, Seyed H. Tabatabaei, Abdellah Ajji

3SPack NSERC-Industry Chair, CREPEC, Chemical Engineering Department, Polytechnique Montreal, C.P. 6079, Succ. Centre-ville, Montreal, QC, H3C 3A7, Canada

5.1 Abstract

Polyethylene (PE) based clay polymer nanocomposites (CPN) are of great importance to generate peelable seals in packaging industry. This study shows the significant effect of organoclay (OC) localization in PE-based blend sealants on their peel properties, for the first time. Two different immiscible blends composed of PE/ethylene-methyl acrylate copolymer (EMA) and PE/ethylene-methyl acrylate-glycidyl methacrylate terpolymer (EMA-GMA) were examined for their potential to generate peelable seals upon addition of organo-modified montmorillonite (OMt). WAXD results and TEM observations reveal that OC is localized at the interface of PE/EMA phases while it is localized within the dispersed EMA-GMA phase in the PE/EMA-GMA blend, which is in agreement with the thermodynamic predictions. The incorporation of 4 phr OC converts the lock seal behavior of the PE/EMA blend seal to a peelable behavior over a wide peelable heat seal temperature range (over 35°C). In contrast, the OC/PE/EMA-GMA nanocomposite sealant, in which OC is mostly located within the EMA-GMA phase, shows lock seal performance similar to the PE/EMA-GMA neat blend.

---

[2] Accepted in *Applied Clay Science*.

5.2 Introduction

Packaging, as an important sector of plastic industry, has a crucial effect on consumer purchase behavior [1] and could be an entire reason for a brand existence [2], [3]. Due to modern life style, easy-open packaging with peelable sealants is increasingly developed for variety of applications [4]–[10]. Monolayer and multilayer films along with a peelable sealant layer provide a good solution to produce user friendly packaging. A peelable sealant can be opened upon peeling either from the interface of the seal layer and its adjacent layer, which is called adhesive peel [11]–[14], or within the seal layer, which is called cohesive peel [15], [16], or combination of both [17]. In an adhesive peel, separation takes place at the interface of two sealed layers and no residue is left on the opposite side. In addition to the poor seal that is provided by adhesive materials, the seal strength of adhesive sealants is more sensitive to the seal parameters i.e. heat seal temperature, pressure and dwell time [14]. A cohesive peel, however, is made by blending two or more immiscible polymers [4], [6] or by incorporation of solid particles in seal area [10]. In this approach, the seal layer is strongly welded to a substrate to provide a reliable seal while peel initiation and propagation upon peeling is controlled by the presence of weak interfaces in the seal layer [16], [18]. Cohesive peelable films provide stronger seals and have received a great deal of attention in the packaging of perishable products. Furthermore, the peel strength can be adjusted through controlling process conditions [19] and seal materials formulation [16], [20] for different applications.

Polyolefins, particularly polyethylene (PE), are the best candidates for the seal layer due to their easy processability, low cost, and low heat seal initiation temperature [21]. Accordingly, blends that are used for cohesive peelable films are usually made of polyolefins such as blends of poly(ethyl methyl acrylate) (PEMA) with propylene co-ethylene copolymer or blends of PE or ionomer with polybutene-1 (PB-1) [18]. Such blends suffer from a narrow peelable heat seal temperature window (ΔT_p) [18] or aging in sealants containing PB-1 [22], [23]. Incorporating organomodified nanoclays in the seal layer is an effective approach to achieve a cohesive peelable sealant with a wide ΔT_p of over 30°C [20]. Nevertheless, it was shown that such a broad ΔT_p is only achieved through well dispersed and distributed organoclay (OC) in the sealant matrix [20]. For PE based sealants, incorporating PE grafted maleic anhydride (PE-g-MA) as well as blending

PE with a functionalized polymer such as PE copolymers and/or terpolymers have been shown to improve the dispersion of the nanoclays in the seal area and consequently increases ΔT_p [20]. Manias et al. [24] showed that blending PE with ethylene vinyl acetate (EVA) is much more effective than PE-g-MA compatibilizer in increasing the dispersion of nanoclay in the PE sealant and broadening ΔT_p.

When solid particles are added to an immiscible binary polymer blend, solid particles either locate at the interface of phases or within one of the components, depending on their interaction or wettability by the blend components. Theoretical predictions and experimental results demonstrate that the morphology and dynamic phase behavior of a polymer blend and thus its properties can be tailored depending on the localization of solid particles in the blend [25]–[32]. In general, the domain size increases when nanoparticles are located in dispersed phase due to an increase in viscosity and breakup suppression [33], [34]. By contrast, the dispersion of solid particles in a polymer matrix can suppress the coalescence due to the barrier effects of solid particles [35] or increase the break-up due to the increase in viscosity of the matrix [33]. Localization of fillers at the interface of a blend components can reduce the domain size through various mechanisms, i.e. the barrier mechanism, change in the viscosity ratio, or compatibilization effect of solid particles [36]–[38]. Nanoparticles can also intercalate in both polymer phases and at the interface and thus result in a strong compatibility between components and reduce the dispersed phase size [39]. Although thermodynamic considerations are the main drivers determining the localization of solid particles in an immiscible multiphase system, this stable equilibrium state dictated by thermodynamics is not always reached [34]. The final localization of solid particles is strongly influenced by kinetic effects including the mixing strategy [40], [41], viscosity ratio [42]–[44], composition [45], mixing time [46]–[48] and shear rate [44], [49], [50]. Due to unfavorable localization dictated by kinetic effects, solid particles migrate from one phase to another phase as soon as they collide with the interface through hydrodynamic forces [42].

It has been shown that various properties of polymer blends such as electrical [51]–[53], thermal [45] and mechanical [45], [54]–[56] properties can be tailored through solid particle localization. To our knowledge, the effect of localization of nanoclay on the peel performance of PE-based blend films has not been reported in the literature. The present work investigates the localization of OC

and its effect on morphology and peel performance of two different PE-based blends composed of OC/PE/EMA and OC/PE/EMA-GMA.

5.3 Experimental

5.3.1 Materials

Low density polyethylene (LDPE) with the trade name of Novapol LF-0219-A was provided by Nova Chemicals. Ethylene-methyl acrylate copolymer (EMA) with the trade name of Elvaloy AC 1224 is a copolymer of ethylene with 24 wt% of methyl acrylate (MA) as comonomer was obtained from DuPont. Ethylene Acrylic ester- Glycidyl Methacrylate terpolymer (EMA-GMA) containing 24 wt% of MA and 8 wt% of Glycidyl Methacrylate (GMA) with commercial name of Lotader AX8900 was purchased from Arkema. EMA and EMA-GMA are commonly used for seal applications due to their thermal and mechanical properties as well as low softening and melting temperatures [57]–[62]. Surface modified Mt with the trade name of Cloisite15 was provided by Byk Company. The organomodifier is dimethyl dihydrogenated tallow in which tallow is approximatly 65% C18, 30% C16, 5% C14 with cation exchange capacity (CEC) of 125 meq/100 g.

5.3.2 Clay polymer nanocomposite film preparation

Two master-batches of OC/EMA-GMA and OC/EMA containing 20 mass% Cloisite15 were prepared using a twin screw extruder (TSE) Leistritz ZSE 18HP, with an L/D ratio of 40 equipped with a separate nanoclay feeder and at a melt temperature of 190°C and rotor speed of 100 rpm. The master batches were then diluted by LDPE to achieve OC/PE/EMA nanocomposites (PE and OC refer to LDPE and Cloisite15 organonoclay respectively) and OC/PE/EMA-GMA containing 4 phr OC with a mass composition of 84/16/4. Blends of PE/EMA and PE/EMA-GMA with a mass composition of 84/16 were also prepared for comparison. Then, the blends and CPN were processed into films and co-extruded with linear low-density PE (LLDPE) and high density PE (HDPE) as support layers through a cast line. In this process, each layer was extruded using a single screw extruder LE20-30 from Labtech at screw speeds of 40, 25, and 60 rpm for the seal layer, LLDPE, and HDPE, respectively. The temperature zones of the extruders were set at

170/180/190/200°C. The molten polymer passed through a 5 layer ABCDA feed block connected to a 12" coat hanger cast die with a die opening of about 500 microns in average. Afterwards, it was stretched in air and directed trough calendar rolls chilled with cold water. The calendar rolls speed and draw ratio were adjusted to obtain uniform films with a thickness of 90 µm consisting in the seal, LLDPE middle and HDPE support layers of 30, 20 and 40 µm respectively.

5.3.3 Contact angle (CA) measurements

CA measurements were carried out using the sessile drop technique with the FDS contact angle system OCA Data Physics TBU 90E at room temperature. CA was measured through placing 2 µl of liquids on films of PE, EMA and EMA-GMA such that three drops in several positions of a sample were tried and for each time the sessile drop CA was stabled over one minute time. For each drop, the average of the right and left angles was used as CA. Then, the surface tensions of polymer components were calculated using contact angle (CA), θ, measurements according to Owens-Wendt equation [63]:

$$\sigma_l(1 + cos\theta) = 2(\sqrt{\sigma_i^d \sigma_l^d} + \sqrt{\sigma_i^p \sigma_l^p}) \qquad 5.1$$

where, σ_l is the surface tension of liquid and σ_i is surface tension of polymer i. σ_l^d and σ_l^p are polar and dispersive portions of the surface tension of the liquid, σ_l, respectively. σ_i^p and σ_i^d are polar and dispersive portions of the surface tension of the polymer, γi, respectively. The average of the CA of the liquids on each polymer film was used in equation 5.1 to calculate the surface tension of the sample. In this work, deionized water and Formamide (FM) were used to measure the contact angle of the polymers with the liquids. Dispersive and polar portions of the surface tension for water are 22.1 and 50.7 mN/m and for FM are 39.5 and 18.7 mN/m respectively [64]. The surface tension of Cloisite15 at room temperature was obtained from literature [65]. The surface tensions of the polymers and the OC at melt process temperature (200°C) were extrapolated based on their surface tension at room temperature and its rate of thermal variation, i.e. $d\sigma/dT$, that was considered -0.067 mN/m.K for LDPE, -0.07 mN/m.K for EMA and EMA-GMA [66] (S Wu, 1982) and -0.1 mN/m.K for organo-modified montmorillonite [67].

The interfacial tension between components i and j were then calculated using the harmonic equation [66]:

$$\sigma_{ij} = \sigma_i + \sigma_j - \frac{4\sigma_i^d \sigma_j^d}{\sigma_i^d + \sigma_j^d} - \frac{4\sigma_i^p \sigma_j^p}{\sigma_i^p + \sigma_j^p} \qquad 5.2$$

where, σ_i and σ_j are surface energies of components i and j, σ_i^d and σ_j^d are their dispersive parts and σ_i^p and σ_j^p their polar parts.

5.3.4 Heat sealing

A heat sealing machine (hot tack/seal tester from LakoTool & Manufacturing IOC, USA) was used to seal the films. Strips of the films with a width of 2.54 cm were sandwiched between acetate films to prevent them from sticking to the hot jaw bars of the sealing machine. The sealing temperatures varied from 110°C, which is around the melting point of LDPE, up to 150°C with an interval of 5°C. The films were heat sealed with a relatively high pressure of 0.5 N/mm^2 and a dwell time of 1 second.

5.3.5 Mechanical tests

T-Peel tests were carried out using a tensile testing machine (Instron E3000) according to ASTM F88 at room temperature. The heat-sealed films were peeled at a peeling rate of 200 mm/min. The plateau of the force-displacement curve is reported as the peel force of each sample. To ensure reproducibility of the data, the average of the peel forces of at least five specimens was reported as the peel force of each sample.

Stress-strain curves were obtained from mechanical tests using Instron E3000 per ASTM D882 and at a cross-head speed of 50 mm/min at room temperature.

5.3.6 Thermal analysis

Thermal properties of the films were analyzed using a DSC instrument Q 2000. Samples of 10-15 mg were weighed and placed in aluminum pans. Samples were heated up from room temperature to 150℃ at a heating rate of 10℃/min during the first cycle to remove the thermal history, and

then, cooled down to 0°C in the second cycle and finally heated up again up to 150°C in the third cycle. The tests were carried out under nitrogen atmosphere to prevent thermal oxidation during the experiments.

5.3.7 Microstructure analysis

Wide angle X-ray diffraction (WAXD) analysis was performed using a Phillips X'pert apparatus with a CuK_a radiation (λ = 1.54 Å) and a scan rate of 0.02°/min over 2θ range of 2-10°. The generator voltage and tube current were set up at 50 kV and 40 mA, respectively, at room temperature. The distance between detector and sample was fixed at 20 cm. 10 layers of each film sample were stacked together, in order to achieve maximum diffraction intensity.

Transmission electron microscopy (TEM) observations were performed to examine the localization of OC in the blends. For this aim, slices of the films were first cut to a thickness of 100 nm at -120°C using an ultracryomicrotome, Leica Microsystem EM-UC7/FC7, equipped with a diamond knife. Then, due to the low contrast between the PE matrix and the dispersed EMA and EMA-GMA phases, the samples were stained using RuO_4 for 90 minutes. Finally, TEM imaging was carried out using JEOL JEM-2100F, Japan, operating at 200 kV. The images were taken in transverse direction-normal direction (TD-ND) surface.

A Field Emission Scanning Electron Microscope (SEM, JSM 7600F, JEOL) operated at a voltage of 2 keV was used to observe the morphology of the films with and without OC. The samples were first embedded in epoxy molds and then were cryomicrotomed using a microtome (Leica RM 2065) equipped with a glass knife and a cryo-chamber (LN21). Then, in order to create contrast between the blend components, the EMA and EMA-GMA phases were extracted using cyclohexane at 50°C for 25 minutes. To remove any trace of epoxy from the microtomed surface, the samples were washed in acetone after solvent extraction and then were well dried in a vacuum oven at 40°C for at least 2 hours. The surfaces of the treated samples were then coated with gold/palladium by plasma vacuum deposition and finally observed using SEM. The images were taken in TD-ND surface.

Image analysis was carried out using SigmaScan Pro 5 equipped with a digitizer table from Wacom and pressure sensitive pen to map the dispersed phase.

5.3.8 Rheological analysis

For rheological analysis, discs of samples with 25 mm diameter and 1 mm thickness were prepared through compression molding at 190°C and 300 kPa under nitrogen atmosphere. The rheological analysis was performed using a stress controlled rheometer (Physica MCR301 from Anton Paar) equipped with 25 mm parallel plate geometry at 1 mm gap between the plates at 190°C under nitrogen atmosphere.

5.4 Results and Discussion

5.4.1 Thermodynamic predictions

The adsorption behavior of a solid particle at polymer- polymer interface is mainly controlled by the wettability of the particle by polymer melts (Fenouillot, Cassagnau, & Majesté, 2009b). At thermodynamic equilibrium, the localization of solid particles in a mixture must be such that to minimize the interfacial energy, ΔG. The wettability parameter, ω, can be used to predict the equilibrium location of solid particles in a mixture of fluids [68]:

$$\omega = \frac{\sigma_{SA} - \sigma_{SB}}{\sigma_{AB}} \qquad 5.3$$

where σ_{SA} is the interfacial tension between filler and phase A, σ_{SB} is the interfacial tension between filler and phase B, and σ_{AB} is the interfacial tension between A and B. If $\omega < -1$ then solid particles are located in phase A, as presented in Figure 5.1a. For $\omega > 1$, the solid particles are predicted to locate in phase B, Figure 5.1b. The solid particles are at the interface of the phases, Figure 5.1c, when $-1 < \omega < 1$. In this work, A, B, and S denote PE, EMA or EMA-GMA, and OC, respectively.

The results of the CA measurements and surface tensions are listed in Table 5.1. The wettability parameter for each blend system was calculated using equation 5.3 according to the interfacial tensions of the components, which are listed in Table 5.2. ω was found to be 0.44 for the OC/PE/EMA and 1.26 for OC/PE/EMA-GMA systems. Thus, the results predict that OC localize at the interface of PE/EMA phases and within the EMA-GMA phase in the PE/EMA-GMA system.

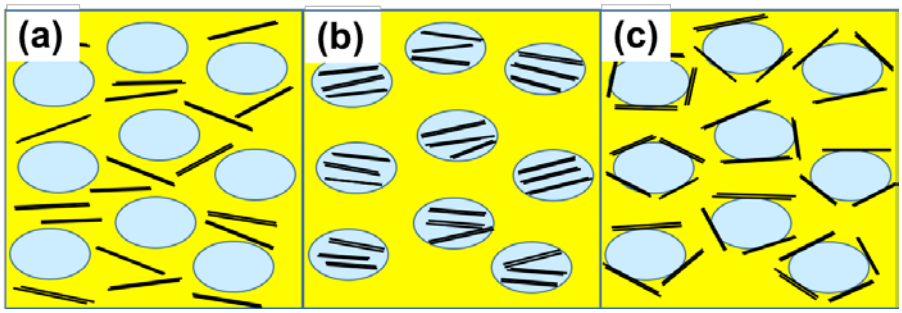

Figure 5.1. Schematic of nanoclay localization in an immiscible polymer blend according to the prediction of the wettability parameter: (a) $\omega < -1$, (b) $\omega > 1$, (c) $-1 < \omega < 1$.

Table 5.1. Contact angles and the corresponding surface tension results at room and process temperatures.

Material	Contact Angle (θ, degree)		Surface tension at 25 °C (mN/m)			Surface tension at 200 °C (mN/m)		
	Water	Formamide	σ^d	σ^p	σ	σ^d	σ^p	σ
LDPE	109.1±1	84.6±2	24.5	0.03	24.53	12.79	0.0156	12.805
EMA	95.3±1	77±1	19.662	2.94	22.6	9	1.345	10.345
EMA-GMA	77±2	58.1±1.5	26	8.3	34.3	16.758	5.292	22.05
Cloisite15	-	-	31.48	11.06	42.54	18.53	6.51	25.04

Table 5.2. Interfacial tensions of the components calculated at process temperature (200°C).

Component		Interfacial tension, σ_{ij} (mN/m)
i	j	
LDPE	EMA	2.02
LDPE	EMA-GMA	5.84
LDPE	OC	7.58
EMA	OC	6.69
EMA-GMA	OC	0.21

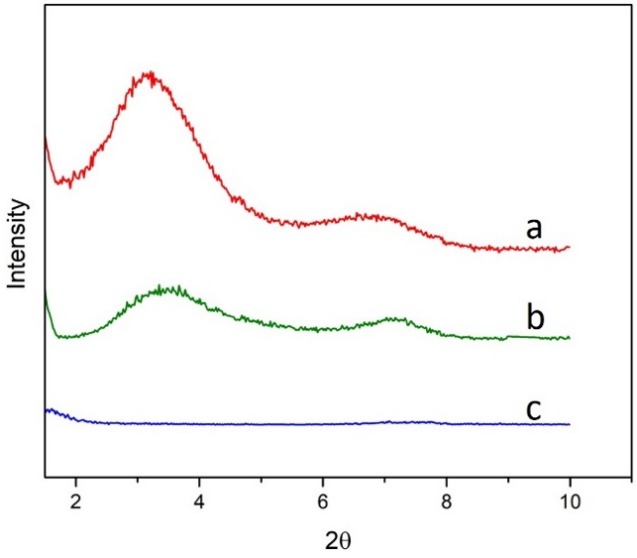

Figure 5.2. WAXD diffraction patterns of (a) OC/PE, (b) OC/PE/EMA, and (c) OC/PE/EMA-GMA sealants.

5.4.2 Microstructure

The WAXD patterns of OC/PE, OC/PE/EMA and OC/PE/EMA-GMA nanocomposite films containing 4 phr OC are presented in Figure 5.2. The OC/PE nanocomposite exhibited two reflections at 2θ = 3.4° and 7.13° associated with the (001) plane with d-value of 26 and 12.3 Å, respectively. The WAXD pattern of OC/PE/EMA was very similar to that of OC/PE and showed two characteristic (001) plane reflections at 2θ = 3.15° and 6.77°, which correspond to d-values of 28 and 13Å, respectively. No characteristic reflection was observed in the WAXD pattern of OC/PE/EMA-GMA that suggests OC basal spacing exceeds 88.2Å, corresponding to 2θ = 1° that was the limit of the WAXD machine. This indicates that the OC interlayer space in the OC/PE/EMA-GMA system was too large to provide layered structure [69]–[71], and thus suggests an exfoliated microstructure. It is worth noting that the EMA-GMA has extremely reactive epoxy groups that can readily interact with the positive charge of the quaternary ammonium or even react with amine groups of modifiers on OC [72], [73]. The reaction/interaction of EMA-GMA with OC can promote the inter-diffusion of the EMA-GMA chains into the OC interlayer spaces and increase the d-spacing. The lower interfacial tension between EMA-GMA and OC at 0.21 mN/m is a proof of higher affinity between EMA-GMA and OC due to these interactions. The WAXD patterns

imply that the OC has similar affinity to PE and EMA phases while possesses more interactions with the EMA-GMA phase.

The TEM images of OC/PE/EMA and OC/PE/EMA-GMA nanocomposites are illustrated in Figure 5.3. The dark phases correspond to the EMA and EMA-GMA phases which were selectively stained as explained in the experimental section. According to Figure 5.3 (a, b and c), OC platelets were mostly located at the interface of PE and EMA. In addition, some clay stacks were observed within the EMA phase which is attributed to the mixing sequence. The OC was first premixed with EMA and then the obtained masterbatch was diluted by PE. Thus, some OC particles are expected to be stuck within the EMA phase because of kinetic effects. These results are in line with the thermodynamic prediction and show that, due to the similar affinity of OC to PE and EMA phases, OC platelets were mainly located at the interface, however, some portion of OC was placed within PE and EMA phases since there was not enough room at the interface for all of the OC particles [39], [74]. In contrast to the OC/PE/EMA system, OC platelets were dominantly located within the EMA-GMA phase in the OC/PE/EMA-GMA system as illustrated in TEM images in Figure 5.3d, e and f. No OC particles were observed neither at the interfaces nor within the PE matrix. These observations are in line with the WAXD results and are also in agreement with the thermodynamic prediction.

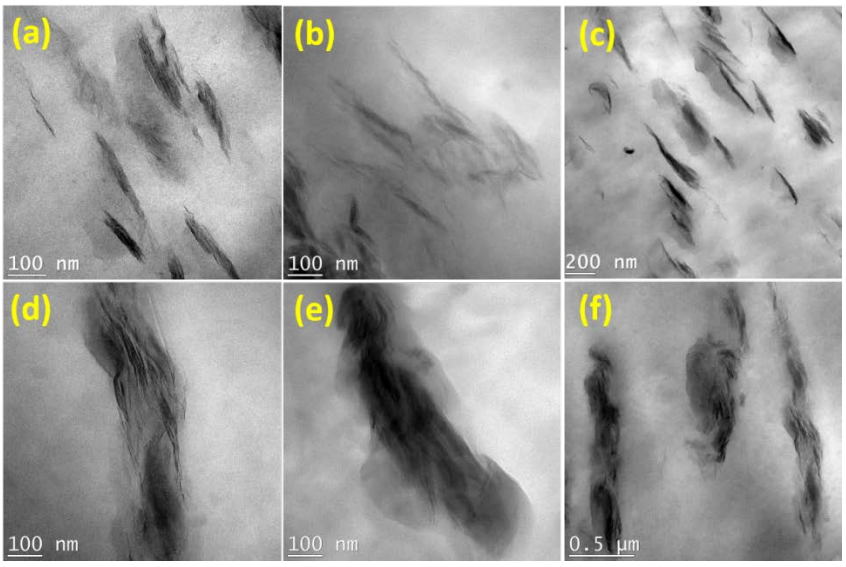

Figure 5.3. TEM micrographs of OC/PE/EMA (a, b, c) and OC/PE/EMA-GMA nanocomposites (d, e, f).

Morphological evolutions of the blends followed by OC incorporation into the blends are illustrated in Figure 5.4. The size of the dispersed EMA phase was slightly reduced from 0.8 to 0.6 µm by OC addition to the PE/EMA system (Figure 5.4a and b). The slight reduction of the EMA dispersed phase size can be atributed to different possible mechanisms such as the suppression of coalescence due to barrier effects of OC at interface, or reduction of the interfacial tension due to the compatibiliation effect of OC at interface. In contrast, the size of the EMA-GMA phase was markedly increased from 0.7 µm in the PE/EMA-GMA blend to 4 µm in the OC/PE/EMA-GMA nanocomposite. This change is significant and suggests either increase in coalescence and/or suppression of break-up of the dispersed EMA-GMA droplets due to the localization of the OC within the EMA-GMA phase. The SEM image of OC/PE/EMA-GMA in Figure 5.4d is in line with the TEM images presented in Figure 5.3(d-f) and corroborates the encapsulation of OC by the EMA-GMA phase as predicted by the thermodynamic model.

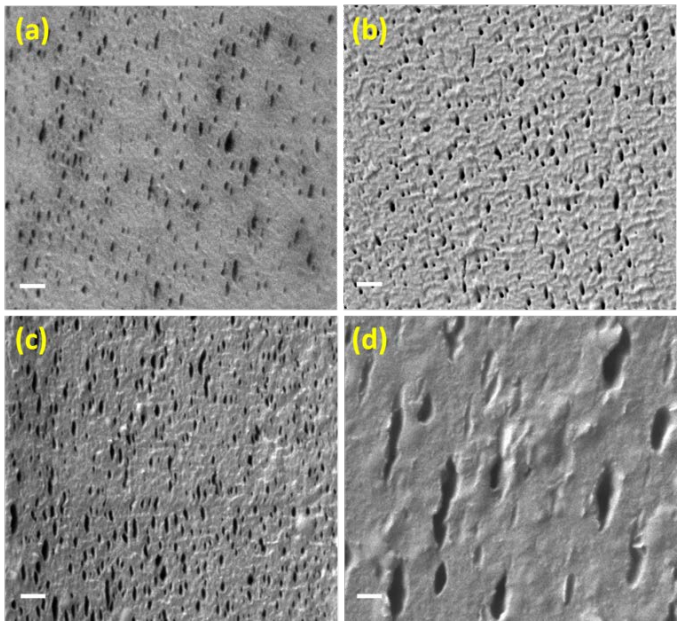

Figure 5.4. SEM micrographs of the PE/EMA (a), OC/PE/EMA (b) PE/EMA-GMA (c) and OC/PE/EMAGMA (d). The scale bars indicate 1 µm.

To further investigate the OC localization in the blends, rheological properties of the blends and CPN were examined. The linear viscoelastic properties of the blends and CPN are shown in Figure 5.5. The complex viscosity and storage modulus of OC/PE/EMA nanocomposite are significantly

higher than those of the PE/EMA blend, particularly at low frequencies (Figure 5.5a,b). These results suggest the formation of a OC network with considerable interactions with the matrix [75], [76]. In contrast, the complex viscosity and storage modulus of the OC/PE/EMA-GMA system did not show any increase when compared with the PE/EMA-GMA blend (Figure 5.5c,d) suggesting poor interaction between OC particles and PE matrix. Thus, these data imply that the OC located at the interface of PE/EMA since the increase in the viscosity and storage modulus are attributed to the interaction of OC with the PE matrix. But, the encapsulated OC in the OC/PE/EMA-GMA system did not interact with the matrix and therefore similar viscoelastic behaviors were obtained for both blend and CPN.

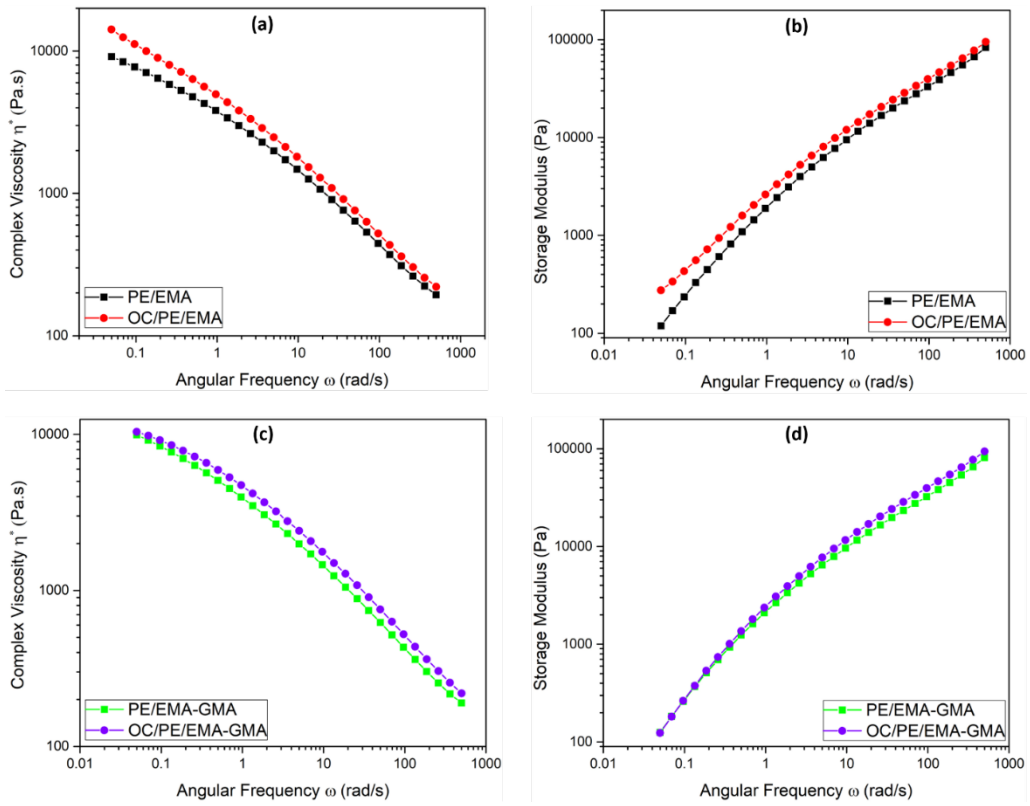

Figure 5.5. Comparison of the complex viscosity and storage modulus of PE/EMA and OC/PE/EMA (a and b) and PE/EMA-GMA and OC/PE/EMA-GMA (c and d).

5.4.3 Peel performance

The peel performance versus temperature of PE/EMA and PE/EMA-GMA blends before and after the incorporation of OC into the blends are illustrated Figure 5.6. Generally, the temperature range

in which the peel force is 150 to 650 N/m is considered as peelable heat seal temperature window (ΔT_p) [77]. Sealants with a peel force higher than 650 N/m yielded and became elongated with no easy peel behavior (that are considered as lock seal), whereas sealants with a peel force less than 150 N/m were not reliably sealed. A lock seal behavior was observed for the PE/EMA blend when the heat seal temperature was increased from 115 to 120°C (and higher) as presented in Figure 5.6a. Due to its very narrow ΔT_p of about 5°C, the PE/EMA blend is practically considered as a lock seal. The lock seal performance of the PE/EMA blend changed to a peelable behavior over a broad ΔT_p of over 35°C upon the incorporation of 4 phr OC to the blend. The PE/EMA-GMA blend showed a ΔT_p of about 5°C similar to that of the PE/EMA blend (see Figure 5.6b). Nevertheless, in contrast to the OC/PE/EMA system that showed a broad ΔT_p of over 35°C, the peelability of the OC/PE/EMA-GMA system was very limited and did not exceed that of the PE/EMA-GMA blend (Figure 5.6b). The peel properties correlate well with the morphology and localization of OC. The results showed that the lock seal behavior of the PE/EMA blend was converted to a peelable behavior upon localization of the OC at the interface of PE/EMA. In contrast, the localization of the OC within the EMA-GMA phase in the PE/EMA-GMA blend resulted in no change in the lock seal behavior of the original blend. These results indicate the importance of the OC localization as a key factor in obtaining peelable films in sealants composed of binary blends for peelable applications.

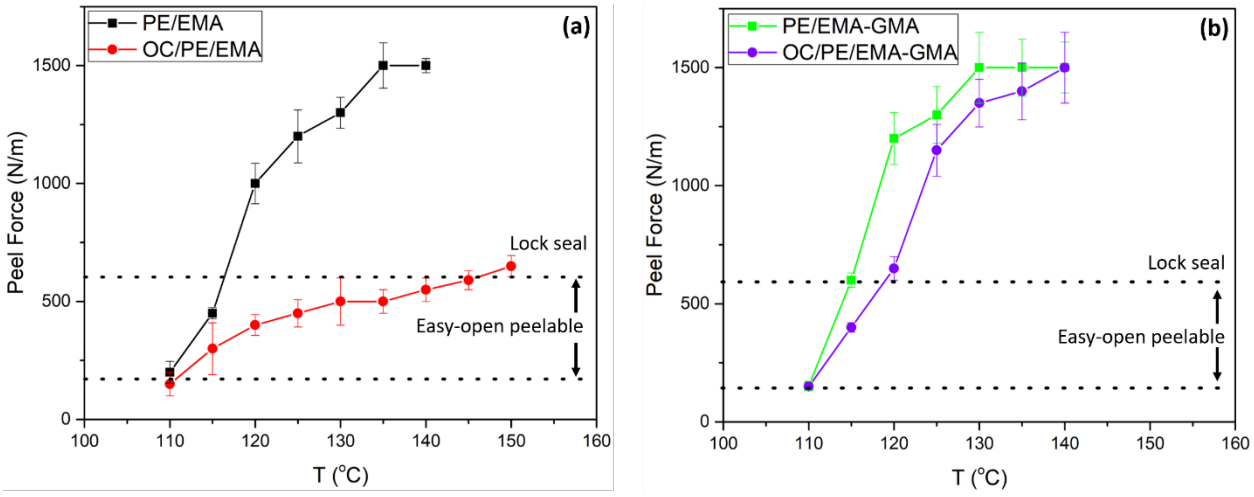

Figure 5.6. Peel performance versus temperature of the PE/EMA and OC/PE/EMA (a) and PE/EMA-GMA and OC/PE/EMA-GMA (b).

In order to determine the peeling behavior of the blends and CPN, they were sealed on a neat PE film at 120°C and then, FTIR were used to examine the surface of PE after peeling the sealant layers. The FTIR spectra of the blends and CPN are presented in Figure 5.7. No trace of carbonyl groups, C=O, C-O related to the polar groups of EMA and EMA-GMA and no trace of chemical bonds of OC was observed on the PE side after being peeled from the PE/EMA and PE/EMA-GMA blends and the OC/PE/EMA-GMA nanocomposite mode (Figure 5.7b, c and d). It should be noted that these samples were partially peeled in an adhesive manner, however, they underwent yielding during the peel experiment due to very high peel strength, which is beyond the range of easy-to-open peel strength (150 to 650 N/m). The OC/PE/EMA nanocomposite, however, leaved traces of EMA and OC on the PE surface after peeling. The stretching vibrations related to C=O and C-O chemical bonds of EMA appeared at 1750 cm^{-1} and 1240 cm^{-1} [78], and a stretching vibration associated with Si-O-Si of OC was detected at 1040 cm^{-1} [79] (Figure 5.7e). These results suggest that only the OC/PE/EMA system demonstrates a cohesive peel behavior and the neat blends and OC/PE/EMA-GMA nanocomposite possess an adhesive peel behavior with a high peel force beyond the easy-to-open peel strength.

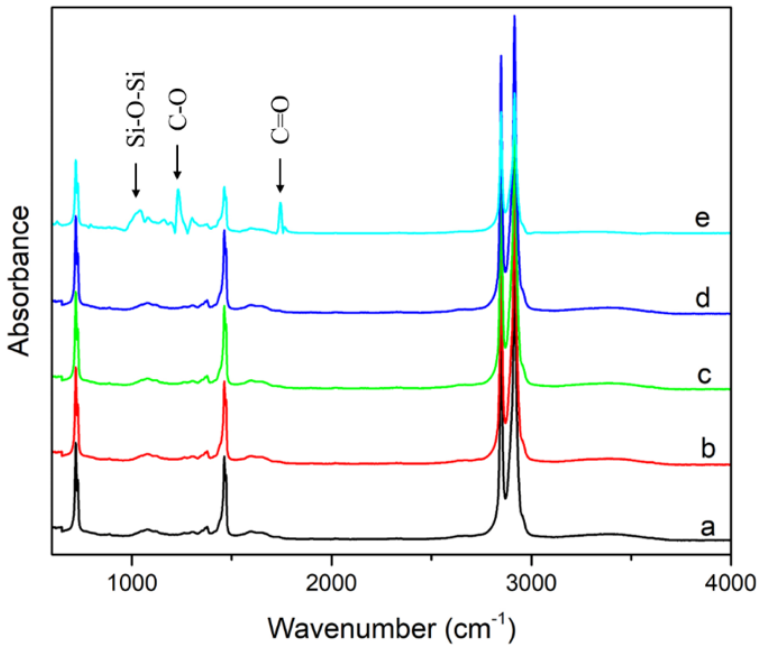

Figure 5.7. FTIR spectra of the neat PE film (a) after being peeled from various substrates: PE/EMA (b), PE/EMA-GMA (c), OC/PE/EMA-GMA (d) and OC/PE/EMA (e).

The lock seals of the PE/EMA and PE/EMA-GMA blend sealants imply that the interface of the blend components is too strong to provide a path way for crack propagation upon peeling. To further examine the adhesion between PE and EMA as well as PE and EMA-GMA, neat films of PE were sealed on EMA and EMA-GMA films. The T-peel test results of these combinations at different heat seal temperatures are illustrated in Figure 5.8. The peel force value which is needed to separate PE film sealed on EMA or EMA-GMA film reflects the interfacial adhesion strength of PE-EMA and PE-(EMA-GMA) interfaces. These values are found to be much higher that the upper limit of the easy-opening peel force (650 N/m). It is worth noting that, due to the high shear field, dynamic mixing, higher melt temperature and long residence time of the melt in the extruder during melt blending, the absolute interfacial adhesion values are expected to be higher in the blends of PE/EMA and PE/EMA-GMA. Thus, a possible way to induce peelability in these systems is either to modify the interface and reduce the interfacial adhesion or to increase the yield strength of sealant to surpass the interfacial adhesion between phases. Indeed, a combination of these two strategies can be used to achieve peelability in blend systems. This is in fact the strategy that has been implemented in the OC/PE/EMA system. The localization of the electrostatically bonded nanoclay platelets at the PE/EMA interface lowers the required stress for initiation and propagation of cracks at the interface due to the much lower delamination stress of OC layers as compared with the high interfacial adhesion of PE/EMA.

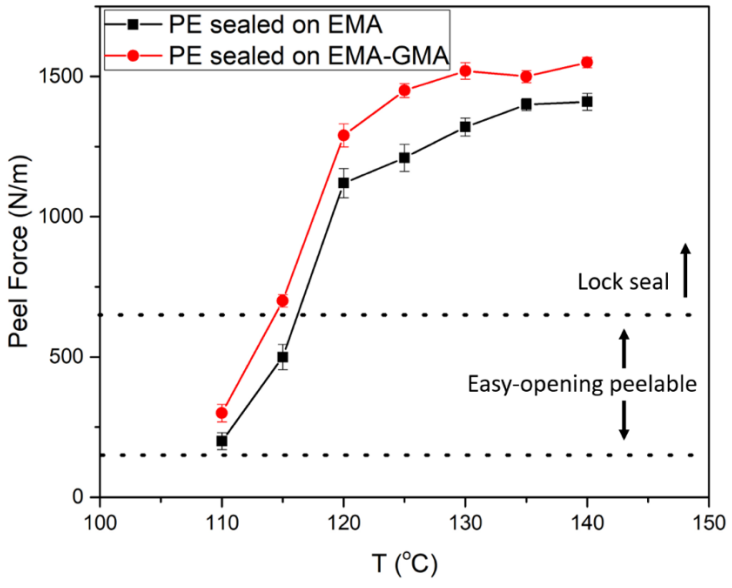

Figure 5.8. Peel force of neat PE film sealed on neat EMA and neat EMA-GMA films.

In order to better understand the peel behavior of a sealant, it is necessary to examine the yield of the sealant since it can significantly affect the peel properties. For a sealant to be peeled in a cohesive manner, the strength of interfacial adhesion between blend components of the sealant must be less than the yield stress of the sealant. But, if the yield stress of the sealant is less than the interfacial adhesion between phases in the sealant, the sealant yields prior to be peeled upon peeling [15]. The yield stress of the blends and CPN sealants are shown in Figure 5.9. The yield stress of the PE/EMA blend was markedly increased from 14.7 MPa to 20 MPa upon the addition of 4 phr OC in the blend (Figure 5.9a). In contrast, the incorporation of the same amount of OC into the PE/EMA-GMA blend only resulted in a marginal enhancement of the yield stress from 15 to 15.7 MPa (Figure 5.9b). The marked enhancement of the yield stress of the OC/PE/EMA system in comparison with the OC/PE/EMA-GMA system is attributed to the different localization of OC in these systems. OC platelets locate at the interface of PE/EMA and resulted in a higher yield strength. Nevertheless, the encapsulation of OC by the EMA-GMA phase caused an effect called filtering effect [55] by which no considerable enhancement in the yield of the CPN compared to the blend was obtained.

The lock seal and/or peel performance of the blends and CPN can be explained based on their yield behavior. Both localization and increase in the yield stress of the seal layer for the OC/PE/EMA systems work in favor of inducing a peelable behavior. First, the localization of the OC at the interface of PE and EMA provides zones which can initiate cracks and propagate throughout the sample when peeling stress is applied. Second, the higher yield of the OC/PE/EMA sealant provides high enough a yield stress compared to the interfacial adhesion between the components and promote peelability. Thus, the higher yield stress of the sealant along with the lower delamination stress for the OC/PE/EMA system converts the lock seal for the blend to a peelable behavior in the CPN. On the other hand, the similar lock seal obtained in the PE/EMA-GMA and OC/PE/EMA-GMA systems can also be explained per their similar yield stress. Since the OC are mainly encapsulated within the EMA-GMA phase and highly interact with EMA-GMA, the yield stress of OC/PE/EMA-GMA is marginally enhanced when compared with PE/EMA-GMA neat blend. For peeling to take place, cracks must pass through the PE and EMA-GMA phases. Considering the fact that the interfacial adhesion between the PE and EMA-GMA phases is high and the yield stress of the OC/PE/EMA-GMA sealant is still similar to that of the PE/EMA-GMA

blend, the OC/PE/EMA-GMA nanocomposite sealant yields upon peeling rather than undergoing a cohesive peel fracture within the sealant. Furthermore, as it was mentioned earlier, the possible interactions between EMA-GMA and OC can also result in the formation of a network between the EMA-GMA chains and OC layers and thus, prevent the delamination of the OC particles and consequently prevent the initiation and propagation of the cracks. Thus, these interactions work against the peelability and further justify the lock seal performance of the OC/PE/EMA-GMA sealants.

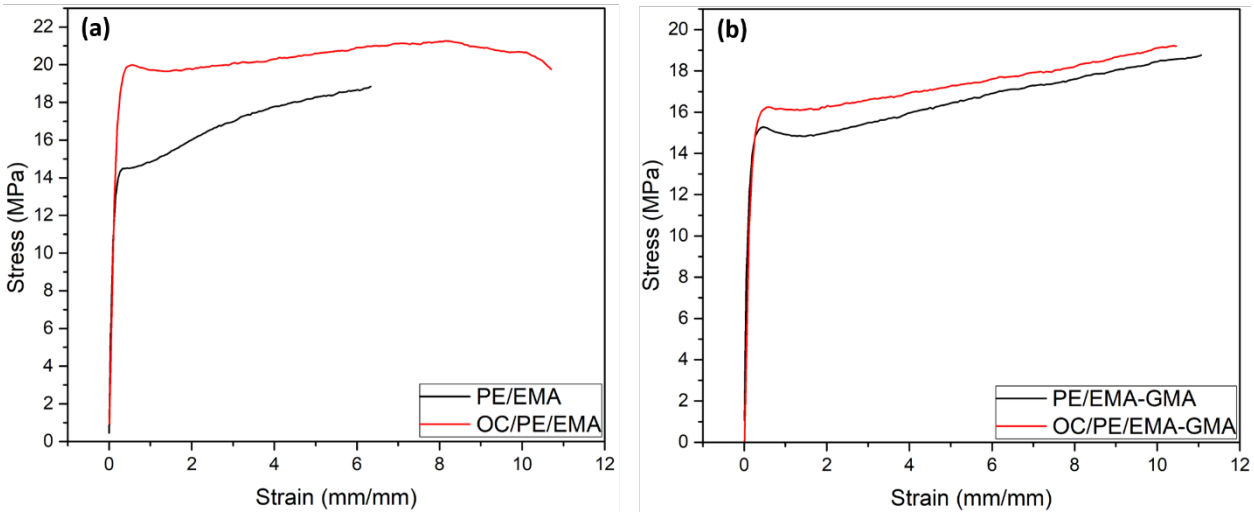

Figure 5.9. Yield behavior of: PE/EMA, OC/PE/EMA (a) and PE/EMA-GMA and OC/PE/EMA-GMA (b).

The lock seal or peel performance of the blends and CPN are better understood by investigating the plastic dissipation energies in peeling process. The force-displacement diagrams of the PE/EMA, PE/EA-GMA blends and their CPN sealants upon peeling at various heat seal temperatures are shown in Figure 5.10a,b. As indicated in Figure 5.10a, the area under the whole curve is the total peel energy, E_t, which consists of adhesive energy, E_a, and plastic energy dissipated in peeling process, E_p. E_a is considered as the energy required to split apart the zones of different adhesive energies i.e. polymer-polymer, polymer-clay and clay-clay interfaces. E_p is dissipated energy at the peel arm, $E_{d,p}$, due to tensile deformation in peeling process and the deformation of the peeled seal, $E_{d,S}$. More details on peel fracture mechanics based on the force-displacement data can be found elsewhere [16]. Due to high immiscibility of polymer and clay

particles, the adhesion energy between polymer ingredients in seal (PE, EMA and EMA-GMA) is expected to be higher than those of the polymer-clay and electrostatically bonded clay-clay layers. High E_p implies that the crack propagation upon peeling is mainly through the zones of high adhesion energy. In contrast, crack propagation through the zones of low adhesion energy such as PE-clay, EMA-clay and clay-clay interfaces results in wide plateau region with relatively low peel force. Based on the force-diagrams the plastic dissipation energy during the peeling process of the blends and their CPN sealed at various seal temperatures were calculated and the results are presented in Figure 5.10c,d. For the PE/EMA sealant, E_p was significantly decreased upon the incorporation of OC in to the blend. While, E_p marginally decreased for OC/PE/EMA-GMA when are compared to PE/EMA-GMA.

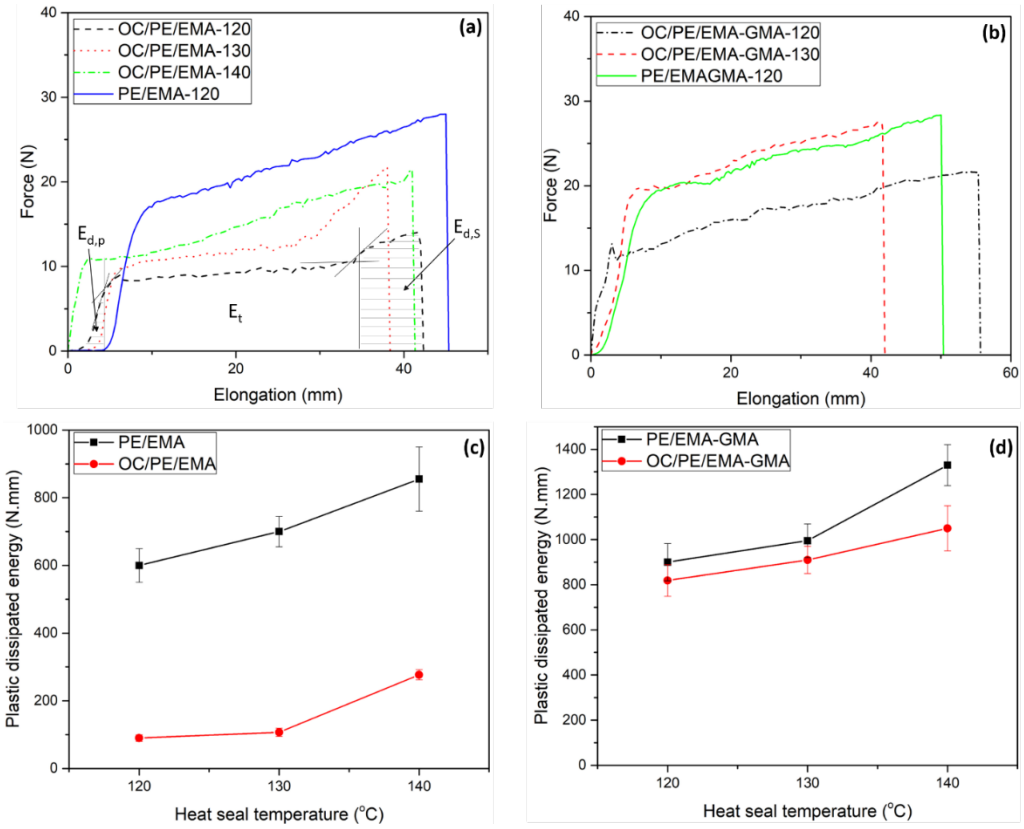

Figure 5.10. Force-displacement diagrams and variation of the peeled seal deformation energy, $E_{d,S}$, versus heat seal temperature of PE/EMA and OC/PE/EMA sealants (a and c), PE/EMA-GMA and OC/PE/EMA-GMA (b and d). The numbers after the nomenclatures of the samples indicate the heat seal temperature.

Furthermore, the analysis of the peel fractured surfaces of the samples in Figure 5.11 confirms the results of the force-displacement experiment. The intense plastic deformations of the peeled surfaces of the PE/EMA, PE/EMA-GMA and OC/PE/EMA-GMA systems sealed at 120°C (Figure 5.11a, b and c) imply a strong peel resistance and a high peel force. While the peeled surfaces of OC/PE/EMA sealed at 120 and 130°C were much smoother and more uniform (Figure 5.11d, e and f). Furthermore, more stretched areas and plastic deformations of the peeled surface of OC/PE/EMA sealed at 140°C (Figure 5.11f) compared to those of the OC/PE/EMA system sealed at 120 and 130°C (Figure 5.11d and e), are attributed to intense molecular chain inter-diffusion across the seal area at high heat seal temperatures. This is an indication of a transition from peelable to lock seal behavior for the OC/PE/EMA system sealed at temperatures over 140°C. Thus, it can be deduced that crack bridging was significantly facilitated in OC/PE/EMA in which clay particles were available in all the seal area, particularly at the interface of the blend components. While, in OC/PE/EMA-GMA crack propagation was not promoted compared to PE/EMA-GMA due to well filtration of the clay particles with EMA-GMA phase.

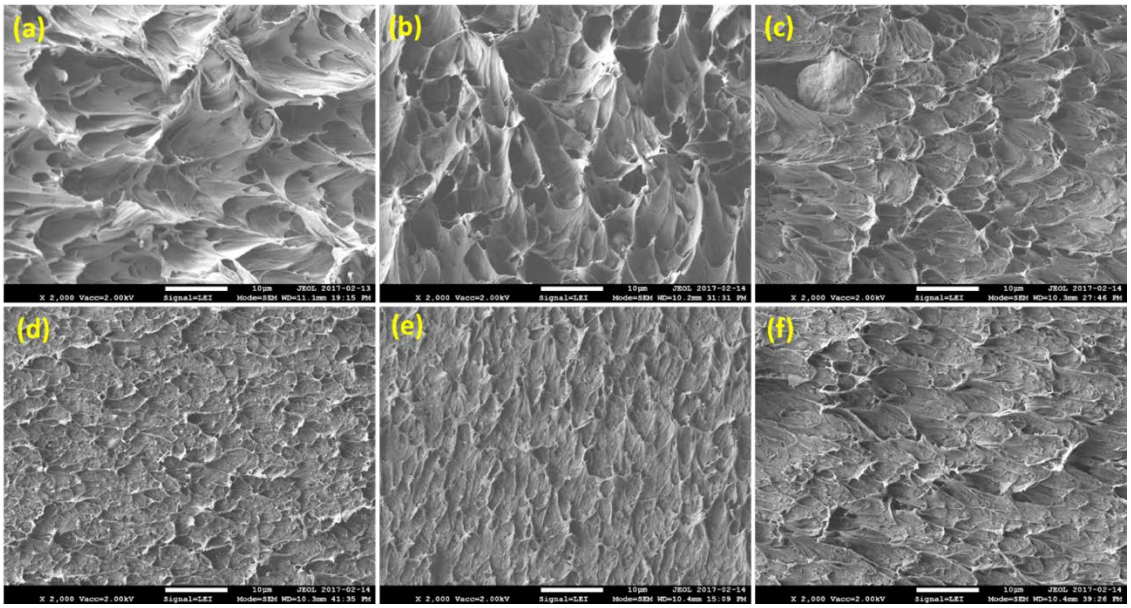

Figure 5.11. SEM micrographs of the peeled surfaces of PE/EMA (a), PE/EMA-GMA (b), OC/PE/EMA-GMA (c) and OC/PE/EMA sealed at 120 °C (d), OC/PE/EMA sealed at 130 °C (e) and OC/PE/EMA sealed at 140 °C.

The proposed mechanisms based on the peel behavior analysis of the CPN are schematically illustrated in Figure 5.12. For OC/PE/EMA in which OC is mainly located at the blend interface, peeling is assisted by the presence of the low adhesion zones, i.e. polymer-clay and clay-clay interfaces in crack propagation path way. Consequently, the sealant is cohesively split apart within the seal area. In contrast, during the peeling of OC/PE/EMA-GMA in which OC is well filtered by the EMA-GMA phase, the crack propagation is suppressed and the sealant was broken after deformation and elongation of seal layer.

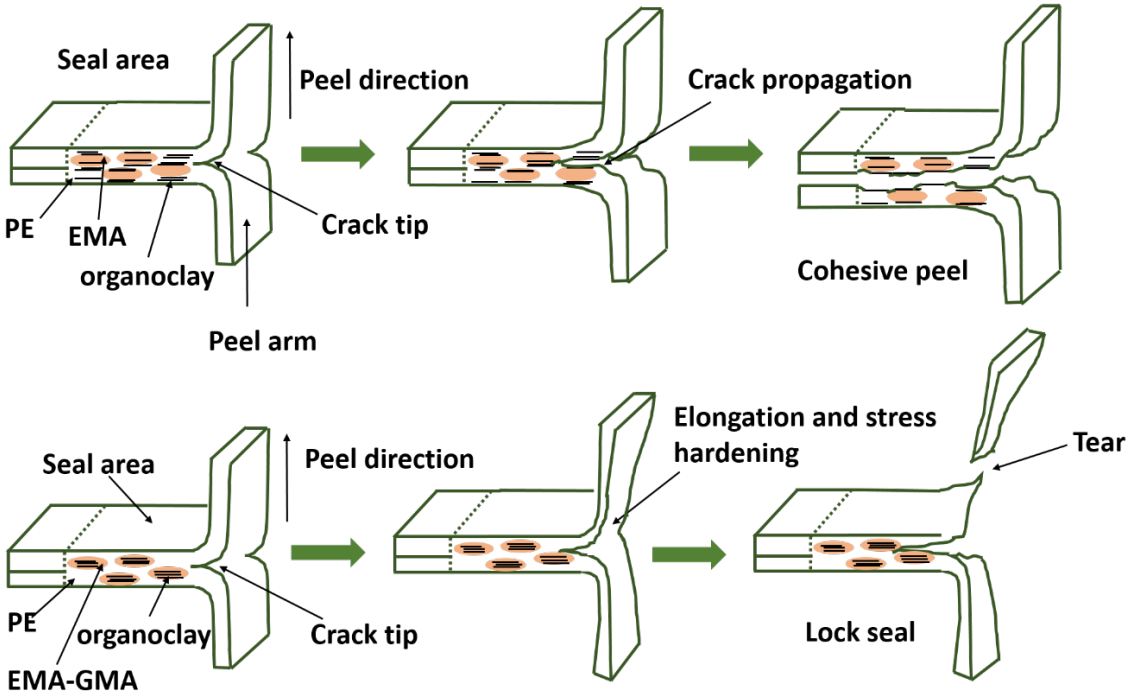

Figure 5.12. Schematic of peel behavior of OC/PE/EMA and OC/PE/EMA-GMA sealants.

5.5 Conclusion

The results obtained from this work indicate that the peel performance of PE-based blend sealants can be controlled through the localization of OC in the blends. It is particularly shown that when 4 phr OC is added to the PE/EMA 84/16 mass% binary blend, they mainly tend to localize at the interface of the PE and EMA phases and convert the lock seal behavior of the PE/EMA blend to a peelable behavior with a wide peelable heat seal temperature window of more than 35°C. The addition of OC to the PE/EMA blend sealant also increases the yield stress of the sealant, which

works in favor of the peeling process by surpassing the impeding interfacial adhesion. In contrast, the same amount of OC is incorporated into the PE/EMA-GMA 84/16 mass% binary blend, the EMA-GMA phase encapsulates the OC through which the lock seal behavior of the PE/EMA-GMA blend is retained in the OC/PE/EMA-GMA sealant. Based on the results of this study, localization of the OC at the interface, suppress the plastic deformation of the peeled seal via conducting the peel propagation path way through regions with low adhesion energy i.e. polymer-clay and electrostatically bonded clay-clay layers. This mechanism is absent in the OC/PE/EMA-GMA system as the localization of the OC within the highly interactive EMA-GMA phase prevents nanoclay platelets to act as crack initiators upon peeling. In addition, the yield stress of the OC/PE/EMA-GMA sealant is not high enough to exceed the interfacial adhesion between the PE and EMA-GMA phases and generate cohesive peeling.

5.6 Acknowledgements

The authors acknowledge the financial support from the Natural Sciences and Engineering Research Council of Canada (NSERC) and industrial partner ProAmpac for the 3S Pack NSERC-Industrial research chair that supported this work.

5.7 References

[1] R. R. Ahmed, V. Parmar, and M. A. Amin, “Impact of Product Packaging on Consumer’s Buying Behavior,” Eur. J. Sci. Res., vol. 122, no. 2, pp. 125–134, 2014.

[2] M. Gómez, D. Martín-Consuegra, and A. Molina, “The importance of packaging in purchase and usage behaviour,” Int. J. Consum. Stud., vol. 39, no. 3, pp. 203–211, May 2015.

[3] J. H. Han, “Innovations in Food Packaging,” in Innovations in Food Packaging, 2nd ed., J. H. Han, Ed. San Diego, CA: Academic Press, 2005, p. 517.

[4] E. Longo, “Ternary polymer blend, the film containing it, and the easy-to-open package made therewith,” US6476137 B1, 05-Nov-2002.

[5] J. W. Rivett, S. R. Tanny, and D. M. Hahm, “Peelably sealed packaging,” US6630237 B2, 07-Oct-2003.

[6] F. Ursino, “Hermetically Sealable, Easy-Opeanable, Flexible Container of Heat-Shrinklable Thermoplastic Material,” US20090017239 A1, 15-Jan-2009.

[7] O. T. Berbert, “Easy-open packages formed from peelable thermoplastic laminates,” US8147934 B2, 03-Apr-2012.

[8] L. L. Laske, “Easy open flexible container,” US9302835 B2, 05-Apr-2016.

[9] P. Kinigakis, K. Pokusa, G. Albaum, A. Jones, and E. Frederickson, “Peelable composite thermoplastic sealants in packaging films,” US9309027 B2, 12-Apr-2016.

[10] Y. Liang, P. Kinigakis, and F. J. Rossi, “Peelable sealant containing thermoplastic composite blends for packaging applications,” US9533472 B2, 03-Jan-2017.

[11] L. Ernesto Mendoza-Navarro, A. Diaz-Diaz, R. Castañeda-Balderas, S. Hunkeler, and R. Noret, “Interfacial failure in adhesive joints: Experiments and predictions,” Int. J. Adhes. Adhes., vol. 44, pp. 36–47, Jul. 2013.

[12] C. R. Frihart, “Specific adhesion model for bonding hot-melt polyamides to vinyl,” Int. J. Adhes. Adhes., vol. 24, no. 5, pp. 415–422, Oct. 2004.

[13] J. M. Santos, M. R. Ribeiro, M. F. Portela, and J. M. Bordado, “Improved adhesion of polyethylene by copolymerisation of ethylene with polar monomers,” Chem. Eng. Sci., vol. 56, no. 13, pp. 4191–4196, Jul. 2001.

[14] M. Nase, L. Großmann, M. Rennert, B. Langer, and W. Grellmann, “Adhesive properties of heat-sealed EVAc/PE films in dependence on recipe, processing, and sealing parameters,” J. Adhes. Sci. Technol., vol. 28, no. 12, pp. 1149–1166, Jun. 2014.

[15] P. Liewchirakorn, D. Aht-Ong, and W. Chinsirikul, “Practical Approach in Developing Desirable Peel-Seal and Clear Lidding Films Based on Poly(Lactic Acid) and Poly(Butylene Adipate-Co-Terephthalate) Blends,” Packag. Technol. Sci., Jun. 2017.

[16] M. Nase, B. Langer, and W. Grellmann, “Fracture mechanics on polyethylene/polybutene-1 peel films,” Polym. Test., vol. 27, no. 8, pp. 1017–1025, Dec. 2008.

[17] A. Martínez-García, A. Sánchez-Reche, S. Gisbert-Soler, M. D. Landete-Ruiz, R. Torregrosa-Maciá, and J. M. Martín-Martínez, “Durability of corona discharge and low-

pressure air plasma-treated ethylene–vinyl acetate copolymers (EVAs),” Int. J. Adhes. Adhes., vol. 28, no. 1–2, pp. 38–46, Jan. 2008.

[18] A. Liebmann, I. Schreib, R. E. Schlözer, and J.-P. Majschak, “Practical Case Studies: Easy Opening for Consumer-Friendly, Peelable Packaging,” J. Adhes. Sci. Technol., vol. 26, no. 20–21, pp. 2437–2448, Jan. 2012.

[19] M. Nase, B. Langer, and W. Grellmann, “Influence of Processing Conditions On the Peel Behavior of Polyethylene/ Polybutene-1 Peel Systems,” J. Plast. Film Sheeting, vol. 25, no. 1, pp. 61–80, Jan. 2009.

[20] J. Zhang et al., “Tailored Polyethylene Nanocomposite Sealants: Broad-Range Peelable Heat-Seals Through Designed Filler/Polymer Interfaces,” J. Adhes. Sci. Technol., vol. 23, no. 5, pp. 709–737, Jan. 2009.

[21] R. Coles, D. McDowell, and M. Kirwan, Eds., “Plastics in Food Packaging,” in Food Packaging Technology, 2003, p. 174.

[22] M. Nase, R. Androsch, B. Langer, H. J. Baumann, and W. Grellmann, “Effect of polymorphism of isotactic polybutene-1 on peel behavior of polyethylene/polybutene-1 peel systems,” J. Appl. Polym. Sci., vol. 107, no. 5, pp. 3111–3118, Mar. 2008.

[23] M. Nase, R. Androsch, S. Henning, and W. Grellmann, “Influence of the Form II/Form I crystal polymorphism of random copolymers of butene-1 with ethylene or propylene on the peel behavior of peel films,” Polym. Eng. Sci., vol. 55, no. 8, pp. 749–1757, Aug. 2015.

[24] J. Zhang et al., “Tailored Polyethylene Nanocomposite Sealants: Broad-Range Peelable Heat-Seals Through Designed Filler/Polymer Interfaces,” J. Adhes. Sci. Technol., vol. 23, no. 5, pp. 709–737, 2009.

[25] M. Si et al., “Compatibilizing Bulk Polymer Blends by Using Organoclays Compatibilizing Bulk Polymer Blends by Using Organoclays,” Macromolecules, vol. 39, no. 14, pp. 4793–4801, Jul. 2006.

[26] Y. Yoo, L. Cui, P. J. Yoon, and D. R. Paul, “Morphology and mechanical properties of rubber toughened amorphous polyamide/MMT nanocomposites,” Macromolecules, vol. 43, no. 2, pp. 615–624, Jan. 2010.

[27] S. H. Lee, M. Bailly, and M. Kontopoulou, “Morphology and properties of poly(propylene)/ethylene-octene copolymer blends containing nanosilica,” Macromol. Mater. Eng., vol. 297, no. 1, pp. 95–103, Jan. 2012.

[28] M. R. Aghjeh, V. Asadi, P. Mehdijabbar, H. A. Khonakdar, and S. H. Jafari, “Application of linear rheology in determination of nanoclay localization in PLA/EVA/Clay nanocomposites: Correlation with microstructure and thermal properties,” Compos. Part B Eng., vol. 86, pp. 273–284, 2016.

[29] S. Thankappan Nair, P. P. Vijayan, P. Xavier, S. Bose, S. C. George, and S. Thomas, “Selective localisation of multi walled carbon nanotubes in polypropylene/natural rubber blends to reduce the percolation threshold,” Compos. Sci. Technol., vol. 116, pp. 9–17, 2015.

[30] Z. Ali et al., “Dynamics of migration and phase selective localization of nanoclay in HNBR/ENR blends,” J. Appl. Polym. Sci., vol. 133, no. 41, Nov. 2016.

[31] L. T. Vo and E. P. Giannelis, “Compatibilizing poly(vinylidene fluoride)/nylon-6 blends with nanoclay,” Macromolecules, vol. 40, no. 23, pp. 8271–8276, Nov. 2007.

[32] R. Grande and L. A. Pessan, “Effects of nanoclay addition on phase morphology and stability of polycarbonate/styrene-acrylonitrile blends,” Appl. Clay Sci., vol. 140, pp. 112–118, May 2017.

[33] J. S. Hong, H. Namkung, K. H. Ahn, S. J. Lee, and C. Kim, “The role of organically modified layered silicate in the breakup and coalescence of droplets in PBT/PE blends,” Polymer, vol. 47, no. 11, pp. 3967–3975, May 2006.

[34] A. Dasari, Z. Z. Yu, and Y. W. Mai, “Effect of blending sequence on microstructure of ternary nanocomposites,” Polymer, vol. 46, no. 16, pp. 5986–5991, 2005.

[35] B. B. Khatua, D. J. Lee, H. Y. Kim, and J. K. Kim, “Effect of Organoclay Platelets on Morphology of Nylon-6 and Poly(ethylene- ran -propylene) Rubber Blends,” Macromolecules, vol. 37, no. 7, pp. 2454–2459, Apr. 2004.

[36] M. Trifkovic, A. T. Hedegaard, M. Sheikhzadeh, S. Huang, and C. W. Macosko, “Stabilization of PE/PEO Cocontinuous Blends by Interfacial Nanoclays,” Macromolecules, vol. 48, no. 13, pp. 4631–4644, Jul. 2015.

[37] Z. Martín, I. Jiménez, M. A. Gómez, H. Ade, and D. A. Kilcoyne, “Interfacial Interactions in PP/MMT/SEBS Nanocomposites,” Macromolecules, vol. 43, no. 1, pp. 448–453, Jan. 2010.

[38] A. Ammar, A. Elzatahry, M. Al-Maadeed, A. M. Alenizi, A. F. Huq, and A. Karim, “Nanoclay compatibilization of phase separated polysulfone/polyimide films for oxygen barrier,” Appl. Clay Sci., vol. 137, pp. 123–134, Mar. 2017.

[39] S. Sinha Ray and M. Bousmina, “Compatibilization Efficiency of Organoclay in an Immiscible Polycarbonate/Poly(methyl methacrylate) Blend,” Macromol. Rapid Commun., vol. 26, no. 6, pp. 450–455, Mar. 2005.

[40] X. Zhao, J. Zhao, J. P. Cao, X. Wang, M. Chen, and Z. M. Dang, “Tuning the dielectric properties of polystyrene/poly(vinylidene fluoride) blends by selectively localizing carbon black nanoparticles,” J. Phys. Chem. B, vol. 117, no. 8, pp. 2505–2515, Feb. 2013.

[41] M. Nofar, M. C. Heuzey, P. J. Carreau, and M. R. Kamal, “Effects of nanoclay and its localization on the morphology stabilization of PLA/PBAT blends under shear flow,” Polymer, vol. 98, pp. 353–364, 2016.

[42] L. Elias, F. Fenouillot, J.-C. Majesté, G. Martin, and P. Cassagnau, “Migration of nanosilica particles in polymer blends,” J. Polym. Sci. Part B Polym. Phys., vol. 46, no. 18, pp. 1976–1983, Sep. 2008.

[43] L. Elias, F. Fenouillot, J. C. Majesté, P. Alcouffe, and P. Cassagnau, “Immiscible polymer blends stabilized with nano-silica particles: Rheology and effective interfacial tension,” Polymer, vol. 49, no. 20, pp. 4378–4385, Sep. 2008.

[44] E. Jalali Dil and B. D. Favis, “Localization of micro and nano- silica particles in a high interfacial tension poly(lactic acid)/low density polyethylene system,” Polymer, vol. 77, pp. 156–166, Oct. 2015.

[45] V. Ojijo, S. S. Ray, and R. Sadiku, “Effect of nanoclay loading on the thermal and mechanical properties of biodegradable polylactide/poly[(butylene succinate)-co-adipate] blend composites,” ACS Appl. Mater. Interfaces, vol. 4, no. 5, pp. 2395–2405, May 2012.

[46] Z. Y. Xiong, L. Wang, Y. Sun, Z. X. Guo, and J. Yu, “Migration of MWCNTs during melt preparation of ABS/PC/MWCNT conductive composites via PC/MWCNT masterbatch approach,” Polymer, vol. 54, no. 1, pp. 447–455, 2013.

[47] A. Göldel, G. R. Kasaliwal, P. Pötschke, and G. Heinrich, “The kinetics of CNT transfer between immiscible blend phases during melt mixing,” Polymer, vol. 53, no. 2, pp. 411–421, 2012.

[48] F. Gubbels, R. Jerome, E. Vanlathem, R. Deltour, S. Blacher, and F. Brouers, “Kinetic and Thermodynamic Control of the Selective Localization of Carbon Black at the Interface of Immiscible Polymer Blends,” Chem. Mater., vol. 10, no. 7, pp. 1227–1235, 1998.

[49] J. S. Hong, Y. K. Kim, K. H. Ahn, and S. J. Lee, “Shear-induced migration of nanoclay during morphology evolution of PBT/PS blend,” J. Appl. Polym. Sci., vol. 108, no. 1, pp. 565–575, Apr. 2008.

[50] A. Taghizadeh and B. D. Favis, “Carbon nanotubes in blends of polycaprolactone/thermoplastic starch,” Carbohydr. Polym., vol. 98, no. 1, pp. 189–198, Oct. 2013.

[51] X. Zhao, J. Zhao, J. P. Cao, X. Wang, M. Chen, and Z. M. Dang, “Tuning the dielectric properties of polystyrene/poly(vinylidene fluoride) blends by selectively localizing carbon black nanoparticles,” J. Phys. Chem. B, vol. 117, no. 8, pp. 2505–2515, 2013.

[52] C. Zhang, X.-S. Yi, H. Yui, S. Asai, and M. Sumita, “Morphology and Electrical Properties of Short Carbon Fiber-Filled Polymer Blends: High-Density Polyethylene/ Poly (methyl methacrylate),” J Appl Polym Sci, vol. 69, no. 9, pp. 1813–1819, Aug. 1998.

[53] D. Wu, Y. Zhang, M. Zhang, and W. Yu, “Selective localization of multiwalled carbon nanotubes in poly(??-caprolactone)/polylactide blend,” Biomacromolecules, vol. 10, no. 2, pp. 417–424, Feb. 2009.

[54] S. Mallick and B. B. Khatua, “Morphology and properties of nylon6 and high density polyethylene blends in absence and presence of nanoclay,” J. Appl. Polym. Sci., vol. 121, no. 1, pp. 359–368, Jul. 2011.

[55] S. Mallick, A. K. Dhibar, and B. B. Khatua, “Effect of nanoclay on the morphology and properties of poly(methyl methacrylate)/high-density polyethylene blends,” J. Appl. Polym. Sci., vol. 116, no. 2, pp. 1010–1020, 2010.

[56] H. Ebadi-Dehaghani, H. A. Khonakdar, M. Barikani, S. H. Jafari, U. Wagenknecht, and G. Heinrich, “On Localization of Clay Nanoparticles in Polypropylene/poly(Lactic Acid) Blend Nanocomposites: Correlation with Mechanical Properties,” J. Macromol. Sci. Part B, vol. 55, no. 4, pp. 344–360, Apr. 2016.

[57] C. C. Hwo, “Packaging film and sheet capable of forming peelable seals with good optics,” US20050266257 A1, 12-May-1987.

[58] I. H. Lee and K. Hausmann, “Polymer blends for peelable and/or permanent seals,” US 20050266257 A1, 01-Dec-2005.

[59] D. H. Hawes and M. Sasthav, “Tear resistant heat sealable packaging structure,” US7144635 B2, 05-Dec-2006.

[60] T. A. Schell and G. R. Pockat, “Heat-shrinkable packaging films with improved sealing properties and articles made thereof,” US7147930 B2, 12-Dec-2006.

[61] D. Galloway, “Easy peel film structures,” US7314669 B2, 01-Jan-2008.

[62] R. T. Chou, “Blends of ethylene copolymers with high-frequency weldability,” US7879949 B2, 01-Feb-2011.

[63] D. K. Owens and R. C. Wendt, “Estimation of the surface free energy of polymers,” J. Appl. Polym. Sci., vol. 13, no. 8, pp. 1741–1747, Aug. 1969.

[64] R. N. Shimizu and N. R. Demarquette, “Evaluation of surface energy of solid polymers using different models,” J. Appl. Polym. Sci., vol. 76, no. 12, pp. 1831–1845, Jun. 2000.

[65] I. Ghasemi, M. Karrabi, and H. Azizi, “Nanocomposites based on polycarbonate/poly (butylene terephthalate) blends effects of distribution and type of nanoclay on morphological behavior,” J. Vinyl Addit. Technol., vol. 19, no. 3, pp. 203–212, Sep. 2013.

[66] S. Wu, Polymer interface and adhesion. New York: M. Dekker, 1982.

[67] E. Picard, H. Gauthier, J. F. Gérard, and E. Espuche, “Influence of the intercalated cations on the surface energy of montmorillonites: Consequences for the morphology and gas barrier properties of polyethylene/montmorillonites nanocomposites,” J. Colloid Interface Sci., vol. 307, no. 2, pp. 364–376, 2007.

[68] F. Fenouillot, P. Cassagnau, and J.-C. Majesté, “Uneven distribution of nanoparticles in immiscible fluids: Morphology development in polymer blends,” Polymer, vol. 50, no. 6, pp. 1333–1350, Mar. 2009.

[69] S. Pavlidou and C. D. Papaspyrides, “A review on polymer–layered silicate nanocomposites,” Prog. Polym. Sci., vol. 33, no. 12, pp. 1119–1198, Dec. 2008.

[70] X. Kornmann, “Synthesis of epoxy–clay nanocomposites. Influence of the nature of the curing agent on structure,” Polymer, vol. 42, no. 10, pp. 4493–4499, Feb. 2001.

[71] J. Ma, Z. Qi, and Y. Hu, “Synthesis and characterization of polypropylene/clay nanocomposites,” J. Appl. Polym. Sci., vol. 82, no. 14, pp. 3611–3617, Dec. 2001.

[72] B. R. Guduri and A. S. Luyt, “Effect of ethylene glycidyl methacrylate compatibilizer on the structure and mechanical properties of clay nanocomposites modified with ethylene vinyl acetate copolymer,” J. Appl. Polym. Sci., vol. 103, no. 6, pp. 4095–4101, Mar. 2007.

[73] F. I. Coskunses and U. Yilmazer, “Preparation and characterization of low density polyethylene/ethylene methyl acrylate glycidyl methacrylate/organoclay nanocomposites,” J. Appl. Polym. Sci., vol. 120, no. 5, pp. 3087–3097, Jun. 2011.

[74] J. Ville, P. Médéric, J. Huitric, and T. Aubry, “Structural and rheological investigation of interphase in polyethylene/polyamide/nanoclay ternary blends,” Polymer, vol. 53, no. 8, pp. 1733–1740, 2012.

[75] R. Wagener and T. J. G. Reisinger, “A rheological method to compare the degree of exfoliation of nanocomposites,” Polymer, vol. 44, no. 24, pp. 7513–7518, Nov. 2003.

[76] J. Ren, A. S. Silva, and R. Krishnamoorti, “Linear Viscoelasticity of Disordered Polystyrene−Polyisoprene Block Copolymer Based Layered-Silicate Nanocomposites,” Macromolecules, vol. 33, no. 10, pp. 3739–3746, May 2000.

[77] E. Manias, J. Zhang, J. Y. Huh, K. Manokruang, P. Songtipya, and M. M. Jimenez-Gasco, “Polyethylene nanocomposite heat-sealants with a versatile peelable character,” Macromol. Rapid Commun., vol. 30, no. 1, pp. 17–23, Jan. 2009.

[78] A. Albrecht, R. Brüll, T. Macko, P. Sinha, and H. Pasch, “Analysing the chemical composition distribution of ethylene-acrylate copolymers: Comparison of HT-HPLC, CRYSTAF and TREF,” Macromol. Chem. Phys., vol. 209, no. 18, pp. 1909–1919, Sep. 2008.

[79] M. Bora, J. N. Ganguli, and D. K. Dutta, “Thermal and spectroscopic studies on the decomposition of [Ni{di(2-aminoethyl)amine}(2)]- and [Ni(2,2 ’: 6 ’,2 - terpyridine)(2)]-Montmorillonite intercalated composites,” Thermochim. Acta, vol. 346, no. 1–2, pp. 169–175, 2000.

CHAPTER 6 ARTICLE 3: NOVEL POLYETHYLENE/POLYBUTENE-1/CLAY NANOCOMPOSITE PEELABLE SEALANTS WITH VERSATILE PEEL PERFORMANCE[3]

Raziyeh S. Mohammadi, Seyed H. Tabatabaei, Abdellah Ajji

3SPack NSERC-Industry Chair, CREPEC, Chemical Engineering Department, Polytechnique Montreal, C.P. 6079, Succ. Centre-ville, Montreal, QC, H3C 3A7, Canada

6.1 Abstract

This study indicates the significant potential of nanoclays to achieve versatile and consistent peel performance from low density polyethylene (LDPE)/polybutene-1(PB-1)/organoclay nanocomposite sealants. WAXD and TEM results suggest organoclay localization mainly at the interface of the LDPE/PB-1 blend components. A very wide peelable heat seal temperature window (ΔT_p) of over 90 °C is achieved for LDPE nanocomposite sealant containing 5 wt% of PB-1 and 1 phr organoclay while, LDPE sealant containing only 5 wt% of the PB-1 or only 1 phr organoclay exhibit lock seal performance similar to the neat LDPE sealant. Keeping the organoclay content 1 phr, the effectiveness of the organoclay to promote the peelability is reduced by increasing the PB-1 content possibly due to the less coverage of the LDPE/PB-1 interface by the clay particles. This speculation is confirmed through morphological analysis through SEM imaging that indicate substantial morphological changes for the sealant containing 5 wt% of the PB-1 but, moderate morphological changes for the sealants containing 10 and 20 wt% of the PB-1 followed by adding 1 phr organoclay in the sealants. In contrast to the neat LDPE/PB-1 sealants that peel force decreases upon aging time after the heat sealing, the consistent peel performance is achieved followed by incorporation of 1 phr organoclay in the sealants containing 5-20 wt% of PB-1. This

[3] To be submitted after patent application.

consistent peel performance is ascribed to the absence of the metastable form II crystal of the PB-1 after the heat sealing as confirmed by WAXD and FTIR analysis right after the seal.

6.2 Introduction

Polybutene-1 (PB-1) is a commercially interesting polyolefin owing to its superior impact properties, toughness, elastic recovery and creep resistance [1], [2]. Depending on crystallization conditions, PB-1 exhibit various crystalline structures including twined hexagonal form I with 3/1 helix [3], untwined hexagonal form I′ with 3/1 helix [4], twinned tetragonal form II with 11/3 helix [5] and orthorhombic form III with 4/1 helix conformation [6]. Crystals I′ and III are usually obtained from solution and can be converted to crystal form II when dried and heated up to 90 °C [6]. During cooling from melt to ambient temperature, PB-1 forms more kinetically favored crystalline form II. Then, the metastable crystal form II spontaneously converts to crystalline form I, which is more thermodynamically stable [4], [7], [8]. Because of the significantly different melting temperature and density of the crystal forms II and I, the transition of crystalline forms from form II to I results in profound thermal and mechanical changes [9]–[12]. So far, extensive efforts have been made to accelerate form II to form I crystal transition through various methods such as pressure [13], [14], orientation and drawing [15]–[19], incorporation of additives [20], [21] and copolymerization [22]–[25]. Some studies tried to obtain directly form I or I′ under peculiar unusual conditions such as ultrathin films [26], self seeding [27], stereodefects [28] and manipulating the melt temperature [29], [30]. Nevertheless, complicated polymorphism and inconsistent thermal, physical and mechanical properties of PB-1 after melt processing remains a challenging issue that restricts its commercial development.

Packaging is one of the main global industries that has crucial effects on consumer purchase behavior and hence on a brand existence [31], [32]. Recently, due to the modern life style, easy-open packaging with peelable seal are increasingly growing for a vast variety of packaging applications such as merchandise, electrical, food and medical packaging [33], [34]. In contrast to adhesive peels that have a relatively high risk of leakage and are more sensitive to seal parameters, i.e. pressure and temperature [35], cohesive peels are welded to the substrate and minimize the chances of leakage [36]. Blending at least two immiscible polyolefins is the main commercial approach to produce peelable seal with cohesive peel performance [34]. Many of the existing peel

formulations show peelability in a narrow heat seal temperature window. By increasing the heat seal temperature, the peel performance may convert to lock seal followed by intense polymer chain inter-diffusion and increasing crystalline anchors at the weld zone [37], [38]. In addition to the fair ΔT_p, a sufficient mechanical strength of the sealant is necessary to maintain the seal integrity and protect the package, particularly during its journey to the end use. In this regard, blending PE and its counterparts such as ethylene-vinyl acetate copolymer (EVA) with PB-1 is a promising approach to produce cohesive peelable seals owing to the fair tensile and yield strength of PB-1 for seal applications and its adequate immiscibility with PE and PE copolymers [39]. It has been shown that incorporation of at least 10 wt% of PB-1 is required to achieve peelable seal with reasonable ΔT_p [40]. In addition to the densification of PB-1 upon aging, which results in the shrinkage of the sealant after the heat sealing, increasing PB-1 content is not economically favored because of its slightly higher cost when compared with other polyolefins such as PE and polypropylene (PP). Decreasing PB-1 content is more cost effective on one hand and results in less aging of the sealant [41] while peelability is suppressed because of the enhanced interparticle distance on the other hand and thus, insufficient crack bridge upon the peeling process [36].

It was shown that PB-1polymorphism is highly influenced by the presence of clay particles [42], [43]. Clay layers can restrict polymer chains movement to form crystalline structures and hence, disturb the kinetics of the metastable form II formation. Also, clay particles may act as nucleating agent that accelerate crystal transformation from form II to form I. The effect of nanoclay on the polymorphism of PB-1 is expected to be more intense when PB-1 is dimensionally confined such as in ultrathin films or in nanofibrils in which PB-1crystallization is already confined. This study demonstrates a novel approach to generate peelable seals with high performance and ultra-wide ΔT_p through the synergy of organoclay and PB-1 with only 1 phr organoclay and as low as 5 wt% of PB-1 in PE/PB-1/clay nanocomposite sealants. Furthermore, the effect of microstructure of PE/PB-1/organoclay sealants on their peel performance and on the aging of the sealants is discussed.

6.3 Experimental

6.3.1 Materials

Low density polyethylene (LDPE) with the trade name of Novapol LF-0219-A was obtained from Nova chemicals. For the sake of simplicity, PE will be used instead of LDPE throughout the paper. Polybutene-1 (PB-1), PB0300M, with a density of 0.915 $g.cm^{-3}$, melt flow index of 4 g/10 min (190 °C/2.16 kg) and molecular weight of 374 kg/mole was kindly provided by Lyondellbasell. Organomodified montmorillonite clay nanoparticles with the trade name of Cloisite15 was obtained from Byk Company. The organoclay was modified with dimethyl dehydrogenated tallow with approximately 65% C18, 30% C16, 5% C14 with cation exchange capacity (CEC) of 125.

6.3.2 Sample preparation

PE/PB-1 blends containing 5 (PEPB5), 10 (PEPB10) and 20 (PEPB20) wt% PB-1 were prepared using a Leistritz ZSE 18HP twin screw extruder (TSE) with an L/D ratio of 40. A masterbatch of PB-1 containing 20 wt% Cloisite15 was also prepared using the same TSE equipped with a separate nanoclay feeder. The master-batch was then diluted with PE to prepare PE/PB-1/organoclay nanocomposites containing 5 (NPEPB5), 10 (NPEPB10) or 20 (NPEPB20) wt % PB-1 and 1 phr Cloisite15. The screw speed of 100 rpm and a temperature profile of 150/160/170/180/180/190/190/190, from hopper to die, were used for all compounding. The blends and nanocomposites were processed in a separate operation into films using the same TSE equipped with a slit die with a die opening of 500 micron. The extruded films were passed through an air knife and drawn with calendar rolls chilled with cold water. The collection speed and draw ratio were manipulated to achieve films of 70 µm in thickness.

The heat sealing was performed using a hot tack/seal tester from LakoTool & Manufacturing Inc, USA. Strips of the films with 2.54 cm in width were cut to be sealed on themselves. The films were sandwiched between two acetate films in order to prevent their sticking to the hot seal bars. A seal pressure of 0.5 N/mm^2, a dwell time of 1 second and identical seal temperature for upper and lower seal bars were set as the seal parameters. Samples were sealed in at heat seal temperatures ranging from 110 to 200 °C with intervals of 5 °C.

T-peel tests were carried out on a tensile testing machine (Instron E3000) per ASTM F88 to evaluate the peel performance of the heat sealed films. The samples were peeled at ambient temperature with a peeling rate of 200 mm/min. The plateau of the force-displacement curves was reported as the peel force for each sample. To ensure reproducibility of the data, the average peel force of at least 5 specimens of each sample was reported as its peel force.

6.3.3 Characterization

Wide angle X-ray diffraction (WAXD) was performed using a Phillips X'pert apparatus. The anode was copper (Cu) with a K_α wavelength of 1.54 Å and the generator voltage and tube current were set at 50 kV and 40 mA, respectively, at room temperature. The scans were run in a 2θ range of 2-30 ° with a scan rate of 0.02 °/s and 20 cm distance between the sample and detector. In order to maximize the diffraction intensity, several layers of each sample were stacked to make samples with an approximately 2 mm in thickness. The d-spacing of the clay layers was calculated through Bragg's equation: $\lambda = 2d\sin\theta$ in which λ is the wavelength of the x-ray radiation, d is the distance between the clay layers and θ is diffraction peak angle.

Differential scanning calorimetry (DSC) was performed using a DSC instrument Q2000 from TA Instruments. About 15 mg of each sample was placed in an aluminum pan and then heated up from 25 to 150 °C to remove thermal history. Then, it was cooled to 0 °C and finally heated up again to 150 °C. All experiments were performed under nitrogen atmosphere with a scan rate of 10 °C/min. The heat of fusion (ΔH_m) of the samples was measured using TA Universal Analysis software to calculate the degree of crystallinity according to equation (6.1) in which X_c is degree of crystallinity, x is the weight fraction of LDPE and $\Delta H_{m,100}$ is the enthalpy of 100% crystal of LDPE and is reported to be 298 J/g [44].

$$X_c = \Delta H_m / x \Delta H_{m,100} \qquad 6.1$$

Scanning electron microscopy (SEM) was performed using a Field Emission SEM (JSM 7600TFE, JEOL) operated at a voltage of 2 kV. Films were embedded in an epoxy mold in machine and transvers directions (MD and TD) and then cryo-microtomed using a glass knife at -150 °C. The cryo-microtomed samples were then treated using cyclohexane at 60 °C at 15 minutes to extract

the dispersed PB-1 phase and create contrast between phases for SEM imaging. The cryo-microtomed samples were gold/palladium coated under plasma vacuum deposition before SEM imaging.

Transmission electron microscopy (TEM) was carried out on a TEM (JEOL JEM-2100F, Japan, operating at 200 kV) to observe nanoclay localization in the blends. The film samples were first embedded in an epoxy mold, then small sections of samples with a thickness of about 70 nm were cut using a diamond knife at -120 °C using a Leica Microsystem EM-UC7 ultramicrotome unit equipped with EM FC7 cryochamber. All observations were performed in MD direction.

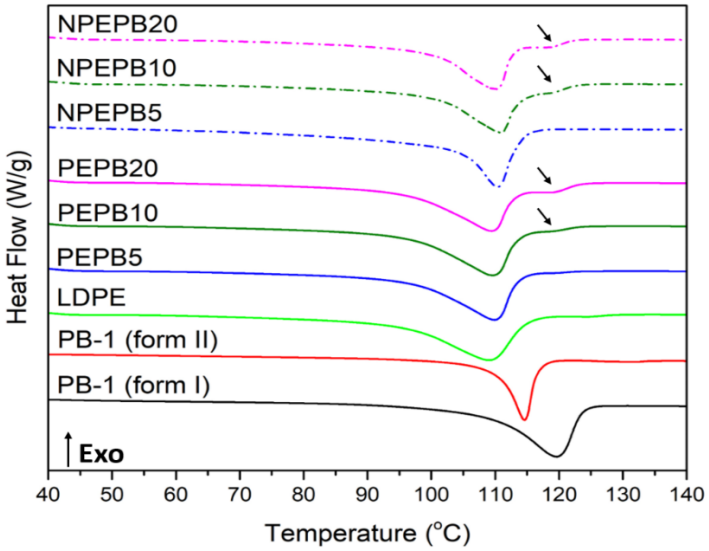

Figure 6.1. DSC micrograms of the neat PE, PB-1 polymers and their blends and nanocomposites. The arrows indicate endotherm corresponding to the crystal form I of PB-1.

6.4 Results and discussion

Figure 6.1 shows the DSC curves of neat PB-1, PE, their blends and nanocomposites. PB-1 in the first heating cycle exhibits an endotherm peak at 120 °C corresponding to the melting point of crystal form I. In the second heating cycle, the endotherm peak of PB-1 shifts to 115 °C and is attributed to the melting point of the crystal form II. The melting temperature of neat PE is at 110 °C, very close to the melting point of crystal form II of PB-1. Neither change in the melting temperature of PE nor endotherm corresponding to crystal form I is observed in the first heating cycle of PEPB5. However, a shoulder at 120 °C appears in the heating run of PEPB10 and is

attributed to crystal form I of PB-1 in the blend. The intensity of this shoulder increased by increasing PB-1 content to 20 wt% in PEPB20. The trends are the same for the nanocomposite compared to neat blends. There is no peak corresponding to the melting of the PB-1 in NPEPB5 while NPEPB10 and NPEPB20 exhibit small endotherms related to the melting of the crystal form I.

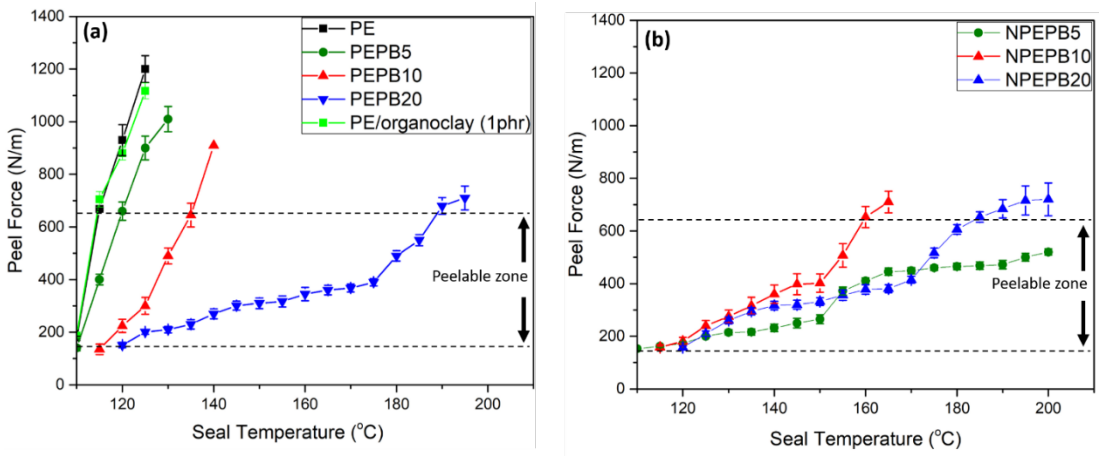

Figure 6.2. Peel force versus seal temperature of the blends (a) and nanocomposites (b).

The peel performances of the LDPE/PB-1 blends and LDPE/PB-1/clay nanocomposites are demonstrated in Figure 6.2. The sealants with a peel force value between the dash lines (150-650 N/m) are considered as the easy-open peelable window [45]. The heat seal initiation temperature (T_i) and ΔT_p obtained from Figure 6.2 are listed in Table 6.1. The T_i of the neat PE film is around 110 °C, very close to its melting temperature. By increasing the heat seal temperature to 115 °C, the peel force of the PE significantly increased beyond 650 N/m with lock seal behavior. Blending PE with 5 wt% of PB-1 slightly enhances its ΔT_p from 5 to 10 °C. ΔT_p is further increased to 20 °C for PEPB10 and 70 °C for PEPB20. In addition, T_i of PEPB10 and PEPB20 increased to 115 and 120 °C respectively. Since T_i depends directly on crystallinity [38], [37], the enhancement of T_i by increasing the PB-1 is attributed to the higher melting point of PB-1 crystals compared to that of PE. Figure 6.2b shows that the peelability of PEPB5 and PEPB10 blends was significantly promoted upon incorporation of 1 phr organoclay to the blends. Surprisingly, the enhancement of ΔT_p for NPEPB5 is much more significant when compared to NPEPB10. Moreover, in contrast to

NPEPB5 and NPEPB10, the peel force of NPEPB20 slightly increased while, its ΔT_p was very similar to its neat blend, PEPB20.

Table 6.1. Seal initiation temperature (Ti) and peelable heat seal temperature (ΔTp) of the blends and nanocomposite sealants of this study.

Sample	T_i	ΔT_p
PE	110	5
PE/organoclay (1 phr)	110	5
PEPB5	110	10
PEPE10	115	20
PEPB20	120	70
NPEPB5	110	90 <
NPEPB10	115	45
NPEPB20	120	70

To better understand these results, the force-displacement curves of the blend sealants were examined against the nanocomposite sealants upon peeling and the results are presented in Figure 6.3. The curves with a wide plateau represent cohesive peel behavior. Sealants with partially cohesive peel behavior show a small plateau and then elongation upon further peeling. The curves without plateau are similar to stress-strain ones and are representative of lock seal performance, as lock seals usually yield and deform until rupture. Figure 6.3a indicates that PEPB5 displays lock seal performance at seal temperatures beyond 120 °C while NPEPB5 is cohesively peeled over all the tested heat seal temperatures from 120 to 200 °C (Figure 6.3b). PEPB10 demonstrates cohesive peel performance when sealed under 130 °C whereas increasing the seal temperature to 135 °C results in a partial peel followed by elongation of the seal (Figure 6.3c). At heat seal temperatures above 140 °C, PEPB10 yields and becomes elongated before being peeled. By contrast, the peelability of NPEPB10 enhances up to the seal temperature of about 160 °C and just yields beyond that seal temperature (Figure 6.3d). The peel performance of PEPB20 blend and NPEPB20 nanocomposite are very similar as displayed in Figure 6.3e and f.

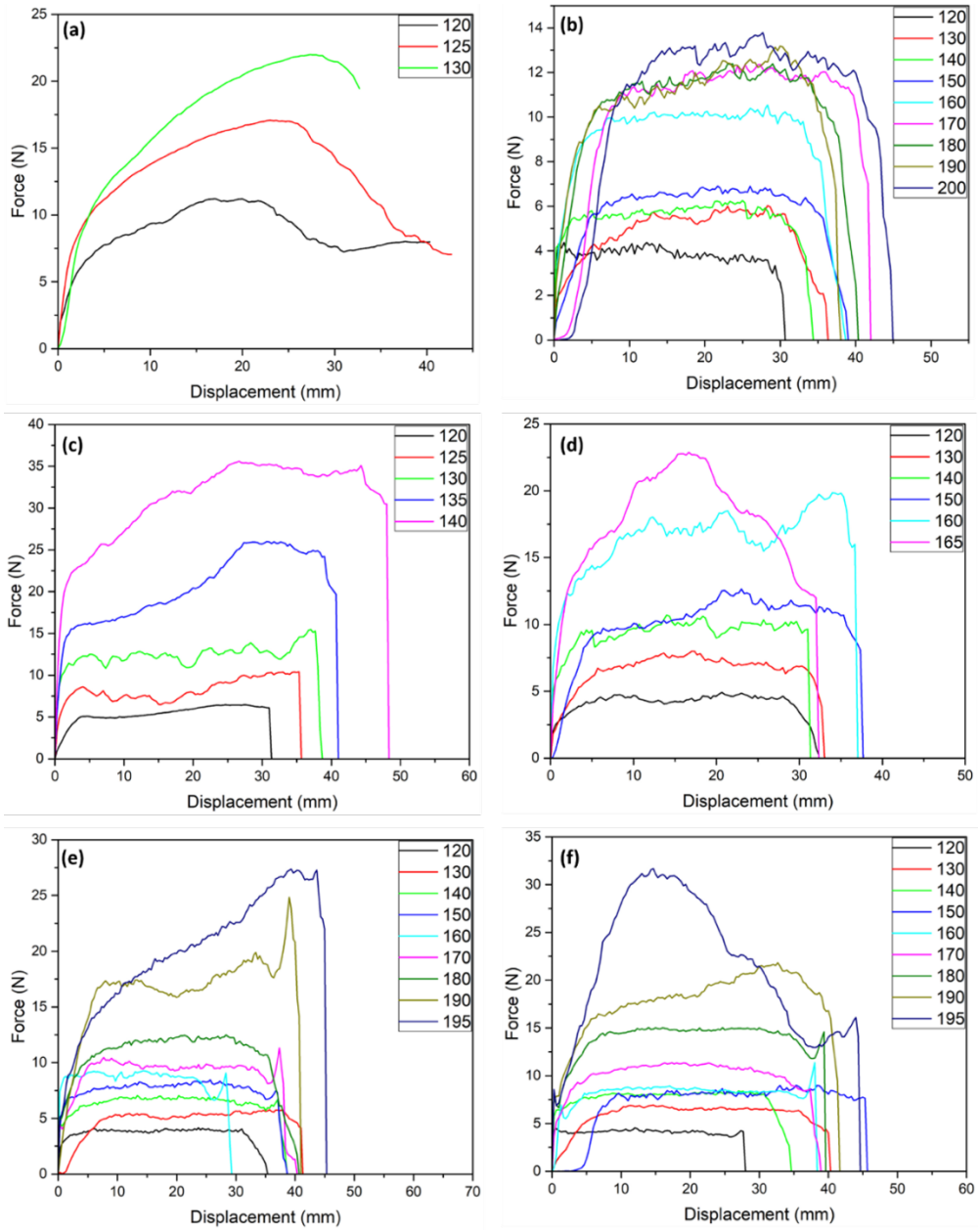

Figure 6.3. Force-displacement curves of PEPB5(a), NPEPB5 (b), PEPB10 (c), NPEPB10 (d), PEPB20 (e) and NPEPB20 (f). The legends indicate the heat seal temperatures.

The peel performance of LDPE/PB-1 blend and nanocomposite sealants can be explained through their yield strengths. For a sealant to be peeled, the yield strength of the sealant should be higher than the adhesion strength of the interfaces inside the seal layer. In this way, the sealant will be peeled through delamination of the interfaces inside the seal upon peeling. By contrast, if the yield

strength of the sealant is less than the interfacial adhesion of the components inside the seal, and or, if the distance between the weak interfaces is not enough for a crack bridge, the sealant yields prior to being peeled. Figure 6.4 shows the stress-strain curves and yield data of the blend and nanocomposite films. By increasing the PB-1 content, the yield strength of the blend sealants increases from 4 to 9 MPa, which works in favor of peelability. Addition of organoclay to the blends, however, increases the yield strength of all nanocomposite films to above 9 MPa regardless of the PB-1 content. The yield strength of PEPB5 is markedly increased from 4 to 10.8 MPa upon the incorporation of 1 phr organoclay that is significantly higher than the increase observed for NPEPB10 and NPEPB20 nanocomposite films when compared to their blends.

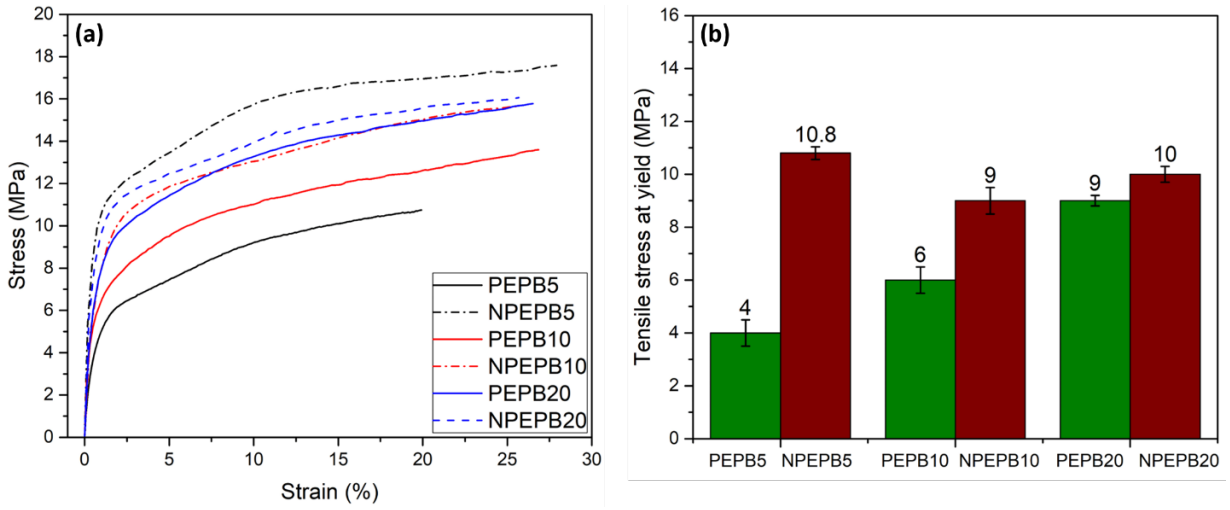

Figure 6.4. Stress-strain curves (a) and yield strength data (b) of LDPE/PB-1 blend and nanocomposite films.

The enhancement of yield strength of the blends upon addition of organoclay to the blends suggests interaction of clay particles with the PE matrix. This interaction is more pronounced in NPEPB5 rather than in NPEPB10 and NPEPB20. This can be due to the higher organoclay/PB-1 ratio and consequently the higher coverage of the interface by clay particles as well as the presence of a portion of clay particles in the PE matrix. The results of the yield behavior are in line with the results of the T-peel test illustrated in Figure 6.2 and Figure 6.3 that show the incorporation of 1 phr organoclay in PEPB5 is significantly effective on its peel performance when compared to PEPB10 and PEPB20.

To better understand the underlying mechanisms of the peel performance, the microstructure of the seal microstructure is examined. Figure 6.5 shows SEM micrographs of the blends in MD and TD. The SEM images were quantified and the results are presented in Figure 6.6. The SEM images indicate that the PB-1 in PEPB5 and PEPB10 have fibrillar structure with an average interparticle distance of 364 and 302 nm, respectively. The morphology of PEPB20 is more sheet like rather than fibril like with an average interparticle distance of 287 nm. Furthermore, it is intuitively clear that the length of the fibrils or sheets increases by increasing PB-1 content. Decreasing the interparticle distance on one hand and increasing the length of the fibrils on the other hand significantly reduces the peel force over a relatively wide ΔT_p of 70 °C for PEPB20 when compared to PEPB5 and PEPB10 (with a narrower ΔT_p of 10 and 20 °C respectively). SEM images of the nanocomposites are shown in Figure 6.7. Compared to the blends, the interparticle distance of dispersed PB-1 phases in the nanocomposites decreased to 160, 260 and 170 nm for NPEPB5, NPEPB10 and NPEPB20, respectively. Also, the SEM images suggest that the length of the fibrils are reduced upon the incorporation of 1 phr organoclay to the blends. This can be attributed to organoclay localization in the blends. Usually, the size of the dispersed phase reduces upon the localization of nanoclay at the interface due to different mechanisms such as compatibilization effect of nanoclay, barrier effect of nanoclay and change in viscosity ratio [46]–[48].

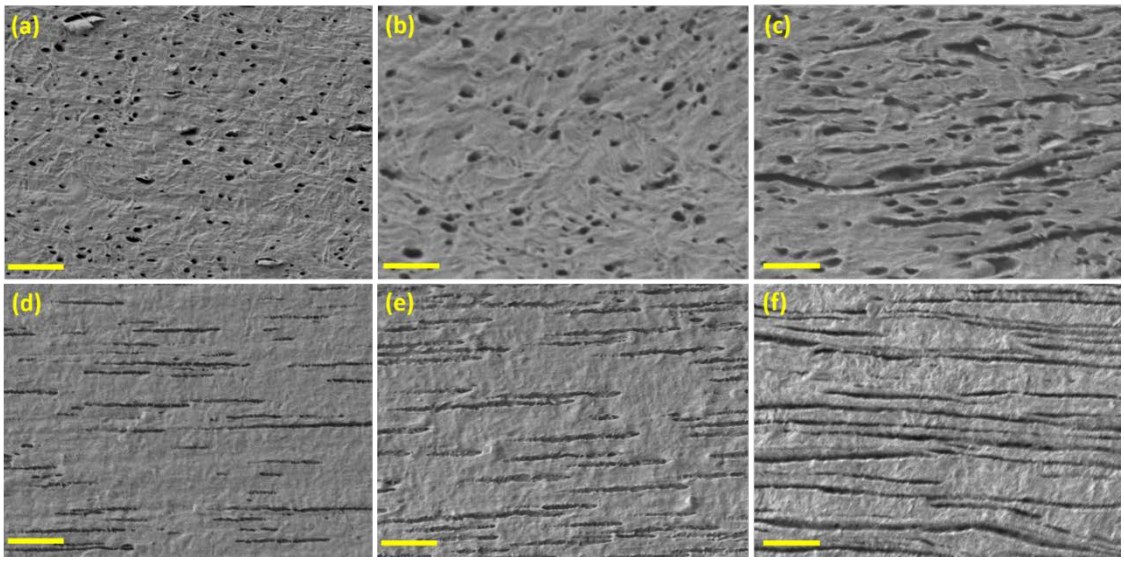

Figure 6.5. SEM images of the PEPB5 (a and d), PEPB10 (b and e) and PEPB20 (c and f) in MD-ND and TD-ND cross section. The scale bars represent 0.5 µm.

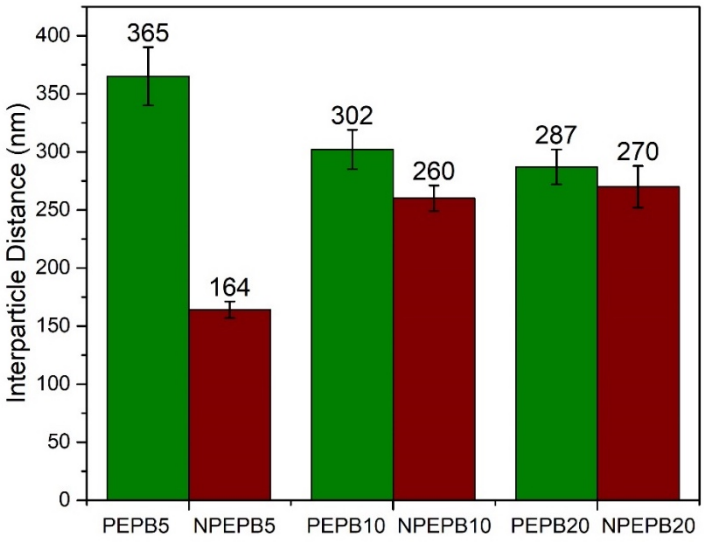

Figure 6.6. Interparticle distance between the dispersed PB-1 phases in the LDPE/PB-1 blends and nanocomposites.

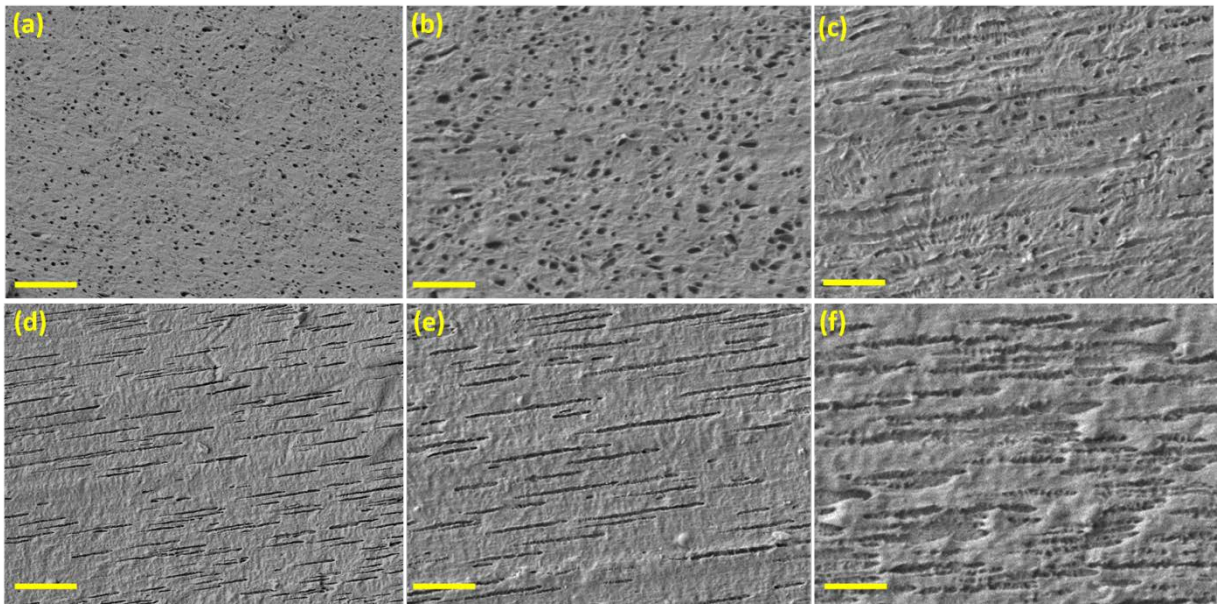

Figure 6.7. SEM images of the NPEPB5 (a and d), NPEPB10 (b and e) and NPEPB20 (c and f) in TD-ND and MD-ND cross section. The scalebars represent 0.5 µm.

Figure 6.8 shows the WAXD pattern for PE and PB-1 containing 1 phr organoclay. The WAXD patterns of both samples are very similar and exhibit two reflections at 2θ = 2.75 and 7.8 ° corresponding to the clay (001) plane with d-spacing of 32.7 and 11.32 Å, respectively. These results suggest very similar affinity of organoclay with PE and PB-1 and thus, the localization of the organoclay at the interface of the LDPE/PB-1 blends is expected. For NPEPB5 and NPEPB10, the (001) plane reflection shifts to higher 2θ = 3.6 and 3.55 which correspond to the clay d-spacing of 24.5 and 24.86 Å respectively suggesting densification of clay layers. This can be due to localization of clay particles at the interface of the blend components. By increasing the PB-1 content to 20 wt% in NPEPB20, the (001) plane reflection slightly moves to lower 2θ = 3.13 corresponding to the d-spacing of 28.2 Å. As the concentration of PB-1 increases, accordingly the interfacial area between components increases which provides much more space for the clay particles and improves their dispersion. These results suggest that an intercalated clay microstructure is achieved in the LDPE/PB-1 nanocomposites and organoclay probably localises preferably at the interface of the PE and PB-1 phases.

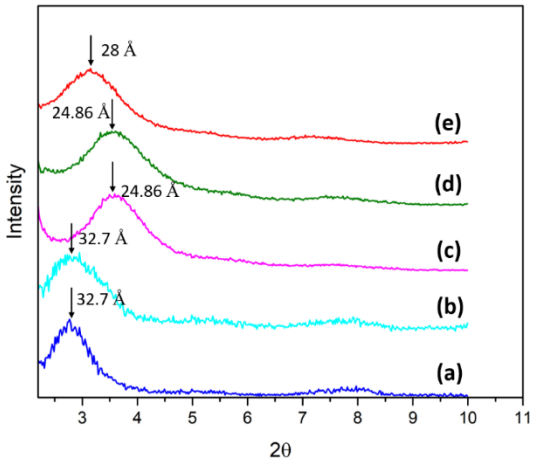

Figure 6.8. WAXD pattern of the neat PE/organoclay (a), PB-1/organoclay (b), NPEPB5 (c), NPEPB10 (d) and NPEPB20 (e).

TEM images taken from TD-ND cross section of the nanocomposites are presented in Figure 6.9. The clay particles are black and gray domains are the dispersed PB-1 phase because of the difference in electronic density with PE. Figure 6.9 imply that organoclays are mainly located at the interface of the PE and PB-1 as predicted through thermodynamic predictions (see tables A1

and A2). Furthermore, a portion of organoclays are observed inside the PB-1 close to the interface. It might be due to the mixing sequence in which organoclays were firstly mixed with PB-1 and then the prepared masterbatches were diluted by PE. The coverage of the blend interfaces by the clay particles increased followed by decreasing the PB-1 content. It is also intuitively deduced that the thickness of the clay stacks reduced followed by increasing the PB-1 content in the nanocomposites. This might be because of the more elongated morphology by increasing the PB-1 content which provide more space for the clay dispersion at the interface.

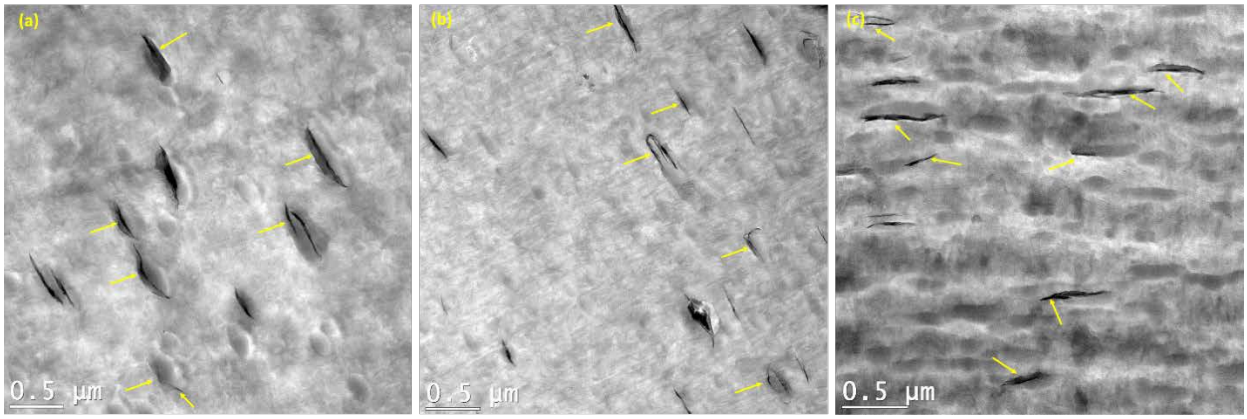

Figure 6.9. TEM images of NPEPB5 (a), NPEPB10 (b) and NPEPB20 (c) in ND-TD cross section. The arrows indicate clay particles at the PE/PB-1 interface.

In order to better understand the peeling mechanism in the LDPE/PB-1 blends and nanocomposites, the fracture surface of the sealants after peeling is examined by SEM imaging as illustrated in Figure 6.10. A non-uniform and highly elongated peel surface indicates a high peel strength and resistance upon peeling. In contrast, a quite uniform and smooth peeled surface with less plastic deformations suggests lower resistance to peeling. Figure 6.10a and b shows the peeled fracture surface of the PEPB5 and NPEPB5 films sealed at 130 and 200 °C respectively. PEPB5 is not peelable at 130 °C while NPEPB5 is cohesively peeled even when sealed at 200 °C. NPEPB10 is peelable until the seal temperature of 160 °C (Figure 6.10c) while it is not easily peelable when sealed at temperatures beyond 160 °C (Figure 6.10d). NPEPB20 indicated easy to open peelable character when sealed up to 190 °C (Figure 6.10e) while its seal strength is significantly increases and the sealant is elongated rather than being peeled when sealed at 195 °C (Figure 6.10f).

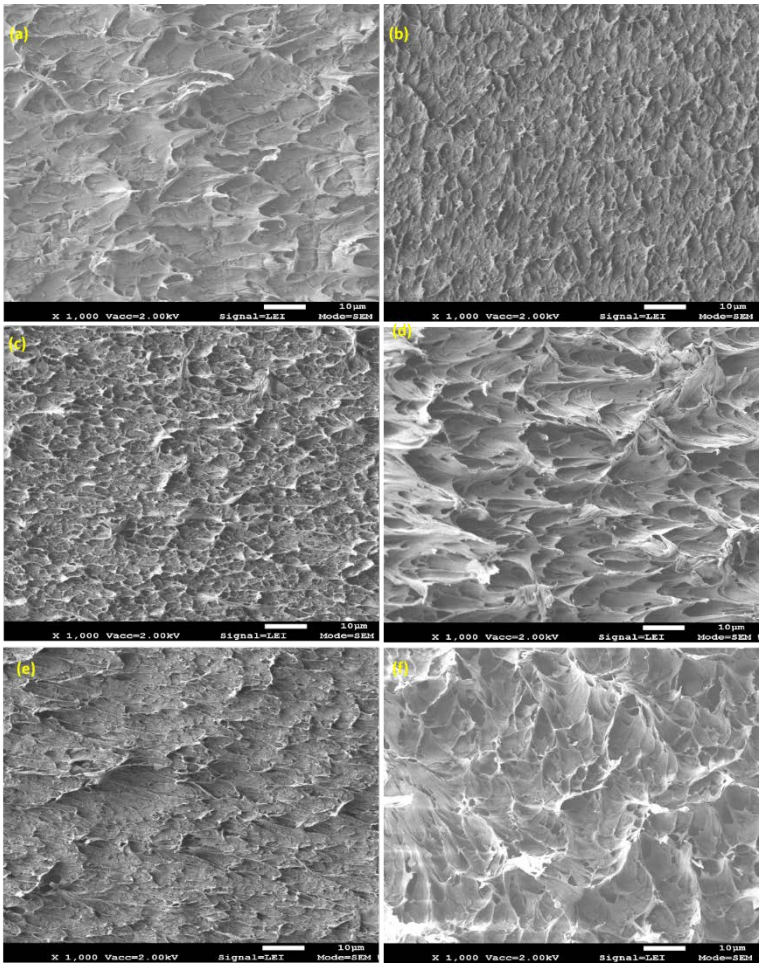

Figure 6.10. peel fractured surface of PEPB5 sealed at 130 (a), NPEPB5 sealed at 200 °C (b), NPEPB10 sealed at 160 °C (c), NPEPB10 sealed at 165 °C (d), NPEPB20 sealed at 180 °C (e) and NPEPB20 sealed at 195 °C.

Based on the mechanical and microstructure analysis of the sealant, it is concluded that the enhancement of the yield strength, reduction of the interparticle distance and the presence of clay particles at the interface as well as in PE matrix in NPEPB5, all work in favor of peelability. On one hand, increasing yield strength surpasses interfacial adhesion in the seal area and, on the other hand, the reduction of dispersed phase size promotes crack bridging in the peeling process, which both promote peelability. However, decreasing PB-1 content is in favor of the peelability of the nanocomposite sealants, possibly due to the higher coverage of the interface by clay particles. The peel force of NPEPB20 is slightly increased when compared with PEPB20. In NPEPB20, the

interparticle distance between the dispersed PB-1 phase is negligibly changed upon addition of 1 phr organoclay when compared with PEPB20, while its sheet like morphology changed to fibril like morphology (see Figure 6.5 and Figure 6.6). This imply that the long sheet and fibril like structures of immiscible PB-1 is more effective in reducing the peel force rather than short fibrils.

As discussed in the introduction section, one of the main drawbacks of LDPE/PB-1 peelable sealants is their seal strength reduction with aging. Figure 6.11a shows the variation of peel force of aged LDPE/PB-1 blends and nanocomposite sealants after heat sealing. The peel force of PEPB5 sealed at 130 °C slightly decreases from 1010 to 936 N/m after 24 hours and remains constant afterwards. PEPB10 has a peel force of 645 N/m when sealed at 135 °C while its peel force decreased to 490 N/m after 72 hours and then remains constant. The peel force of the PEPB20, sealed at 150 °C, decreases from 310 to 195 N/m after 7 days and then remains constant. These results indicate that metastable form II crystals of the PB-1 is generated after the heat sealing of the PE/PB-1 sealants. The metastable form II converts to stable and thermodynamically favored form I upon time aging. Since the density of the form I is more than that of form II, shrinkage of the sealants and suppression of the peel force occur during the form II to form I transition. The results show that, the metastable stable form II to stable form I crystals transition, is completed faster in PEPB5 (24 hours) compared to PEPB10 and PEPB20 that need 72 and 168 hours respectively. This is attributed to the higher amount of form II formation by increasing PB-1 content in the blends. Furthermore, decreasing PB-1 content in the blends results in thinner PB-1 fibrils as discussed earlier. This may disrupt the kinetic of form II crystallization and suppress its formation due to crystallization in a confined environment. The confinement accelerates form II to form I conversion as extensively evidenced in the literature [23], [24], [49]–[51]. Surprisingly, in contrast to the blend sealants, the peel force of the nanocomposite sealants remains constant after heat sealing (Figure 6.11b). This imply that, no form II is formed after the heat seal of the nanocomposites. If there was any form II formation, the peel force would be suppressed due to the form II to form I conversion and shrinkage of the films as will be evidenced below from XRD experiments.

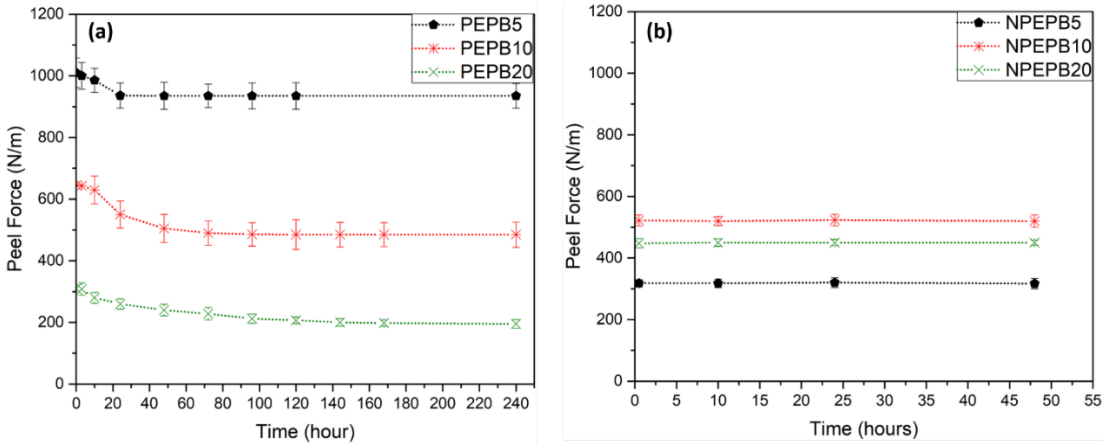

Figure 6.11. variation of the peel force of the blends (a) and nanocomposite sealants (b) of this study.

Formation of form II in LDPE/PB-1 blend sealants and the absence of form II in LDPE/PB-1/organoclay sealants right after the seal is revealed by WAXD patterns as illustrated in Figure 6.12. The reflections at 2θ = 10 corresponds to (110) plane of form I or I′ and the reflections at 2θ = 11.9, 16.9 and 18.2 corresponds to (200), (220) and (213)/(311) planes of crystal form II respectively. Crystal forms I and I′ exhibit similar WAXD reflections but, in contrast to form I′, form I can be obtained only from form II. Presence of the reflection corresponding to form I/I′ might be explained as follows. Due to the very short heat sealing process, 1 second, crystal segregation may happen rather than the complete melting of the crystals. In such a case, the reflection at 2θ = 10° might be ascribed to the residual form I in the sealant. On the other hand, segregation of the crystals results in melt memory effect, because of which similar crystals will grow from the segregated original crystals [30]. Crystal form I′ has the same trigonal crystal structure of the crystal form I but, with many defects. However, crystal form I′ can form from the melt in peculiar condition [26]. Therefore, it can be concluded that the reflection at 2θ = 10 refers to both form I crystal residue from the melt and form I′ which probably grows from the segregated form I crystals. Furthermore, LDPE/PB-1/organoclay nanocomposite sealants exhibit reflections at 2θ = 12.2, 17.2 and 18.8° corresponding to (110), (111) and (201) planes of crystal form III of PB-1 respectively, which are absent in the WAXD patterns of neat LDPE/PB-1 blends. These results show that organoclay effectively prevents aging of the sealants. This is mainly due to the significant effect of organoclay on the polymorphism of the PB-1 phase which will be discussed in

a separate study. It is also worth noting that the absence of form II formation in the sealants containing 10 and 20 wt% of the PB-1, whose dispersed phase size is moderately changed compared to their neat blends, is questionable. This might be due to the better dispersion of the clay particles at the more elongated PB-1 nanofibrils in NPEPB10 and NPEPB20 compared to NPEPB5 (see Figure 6.8) which provide more space for the clay particles to localize at the interface. Furthermore, in this study, organoclay was first mixed with PB-1 then blended with PE. Due to this mixing sequence, a portion of organoclay may remain in PB-1 phase, even in the nanocomposites containing 10 and 20 wt% of PB-1. Ultimately, the presence of clay particles at the interface and inside PB-1 phase may significantly disrupt the kinetic of the form II formation and suppress its formation priority in respect to the form I′. It is worth noting that, the only advantage of the form II formation from the PB-1 melt, is its kinetic which is faster than that of form I′. This confinement in the presence of clay particles is confirmed by the direct formation of form III crystals that can be obtained from the melt only under high stress and confined crystallization conditions (De Rosa et al., 2014).

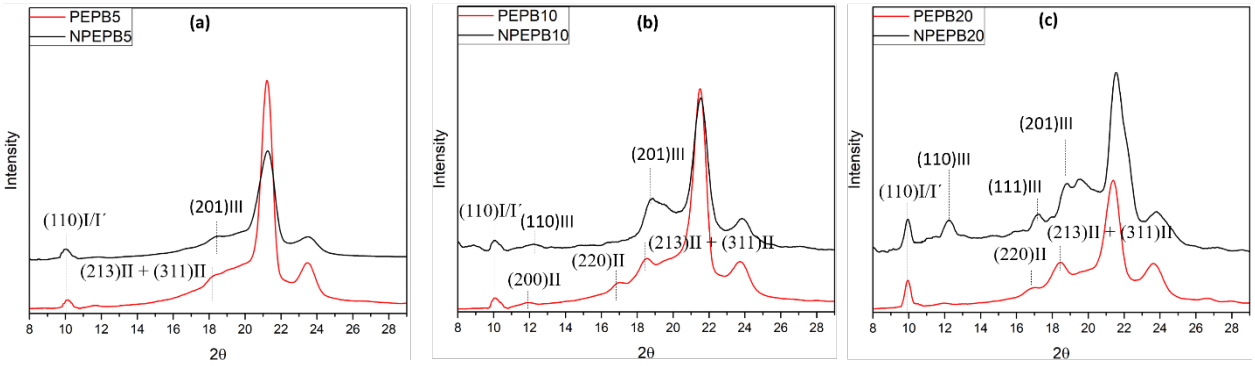

Figure 6.12. WAXD patterns of the blends and nanocomposites sealants of LDPE/PB-1 containing 5 (a), 10 (b) and 20 wt% of PB-1 (c) immediately after the seal.

6.5 Conclusion

In this study, a novel LDPE/PB-1/organoclay nanocomposite with a broad peelable heat seal temperature range is reported for seal/peel applications. Incorporation of 1 phr organoclay or only 5 wt% of PB-1 into the PE sealant results in lock seal performance similar to that of neat PE. While, LDPE/PB-1/organoclay containing the same level of PB-1 and organoclay showed a peelable seal over very broad ΔT_p of 90 °C. The results show that the effectiveness of organoclay to enhance the

peelability is reduced by increasing PB-1 content in the blends, possibly due to less coverage of the interface by clay particles. TEM and WAXD results suggest localization of organoclay at the interface of the blend components. Significant reduction of PB-1 phase size, good distribution of the clay particles in the sealant and significant enhancement of the yield strength of NPEPB5 compared to PEPB5 justify the versatile peel performance of NPEPB5 compared to the lock seal performance of PEPB5. These parameters are moderately enhanced in NPEPB10 and marginally increased in NPEPB20 compared to their neat blends. Furthermore, by incorporation of the clay particles in PEPB20 a portion of the sheet like morphology changed to the fibrillar morphology but, the interparticle distance of PB-1 nanofibrils marginally decreased. The slight increase of the peel force of NPEPB20 compared to PEPB20 suggests the sheet like morphology is more effective to suppress the peel force rather than the fibrillar morphology. Investigating the aging of the peel force of the blends and nanocomposites indicated that, the peel force of the neat blends decreased during 7 days after the heat seal. This reduction was more significant for blends with higher PB-1 content. The reduction of the peel force was attributed to the formation of form II in the blends after heat sealing and that was revealed by WAXD patterns immediately after the heat seal. Surprisingly, the peel force of the nanocomposites remains constant after heat sealing, which suggest the absence of form II formation. WAXD patterns of the nanocomposite sealants right after heat sealing indicate no crystal form II but, direct formation of the stable form I and III that prevent shrinkage and failure of the sealant upon time aging. These results indicate the significant influence of clay particles to suppress the kinetic of form II formation, possibly due to the hindrance of the polymer chain movement.

6.6 Acknowledgements

The authors acknowledge the financial support from the Natural Sciences and Engineering Research Council of Canada (NSERC) and industrial partner ProAmpac for the 3S Pack NSERC-Industrial research chair that supported this work.

6.7 References

[1] L. Luciani, J. Seppälä, and B. Löfgren, “Poly-1-butene: Its preparation, properties and challenges,” Progress in Polymer Science, vol. 13, no. 1. pp. 37–62, Jan-1988.

[2] F. Schemm, V. De Vliet, J. Grasmeder, and F. Cocola, “Basell Polybutene-1: High Performance Polyolefin for Plumbing Appilcations,” 2000.

[3] G. Natta, P. Corradini, and I. W. Bassi, “Crystal structure of isotactic poly-alpha-butene,” Nuovo Cim., vol. 15, no. S1, pp. 52–67, Feb. 1960.

[4] R. L. Miller and V. F. Holland, “On transformations in isotactic polybutene-1,” J. Polym. Sci. Part B Polym. Lett., vol. 2, no. 5, pp. 519–521, May 1964.

[5] Turner-Jones A., “Polybutene-1- Type II Crystalline Form,” J. Polym. Sci. Part B Polym. Lett., vol. 1, no. 8, pp. 455–456, Aug. 1963.

[6] V. F. Holland and R. L. Miller, “Isotactic polybutene-1 single crystals: Morphology,” J. Appl. Phys., vol. 35, no. 11, pp. 3241–3248, Nov. 1964.

[7] R. M. Gohil, M. J. Miles, and J. Petermann, “On the Molecular Mechanism of the Crystal Transformation (Tetragonal-Hexagonal) in Polybutene-1,” J. Macromol. Sci. Part B, vol. 21, no. 2, pp. 189–201, May 1982.

[8] K. W. Chau, Y. C. Yang, and P. H. Geil, “Tetragonal → twinned hexagonal crystal phase transformation in polybutene-1,” J. Mater. Sci., vol. 21, no. 9, pp. 3002–3014, Sep. 1986.

[9] F. Azzurri, A. Flores, G. C. Alfonso, I. Sics, B. S. Hsiao, and F. J. B. Calleja, “Polymorphism of isotactic polybutene-1 as revealed by microindentation hardness. Part II: Correlations to microstructure,” Polymer, vol. 44, no. 5, pp. 1641–1645, Mar. 2003.

[10] G. C. Alfonso, F. Azzurri, and M. Castellano, “Analysis of calorimetric curves detected during the polymorphic transformation of isotactic polybutene-1,” in Journal of Thermal Analysis and Calorimetry, 2001, vol. 66, no. 1, pp. 197–207.

[11] M. L. Di Lorenzo, M. C. Righetti, and B. Wunderlich, “Influence of crystal polymorphism on the three-phase structure and on the thermal properties of isotactic poly(1-butene),” Macromolecules, vol. 42, no. 23, pp. 9312–9320, Dec. 2009.

[12] H. Shao, D. Jiang, M. Zhang, W. Yao, and B. Huang, “Characterization of the polymorphic transformation of poly(1-butene) based on FTIR and mechanical properties,” J. Polym. Res., vol. 19, no. 8, p. 9919, Aug. 2012.

[13] K. -B Hong and J. E. Spruiell, “The effect of certain processing variables on the form ii to form i phase transformation in polybutene-1,” J. Appl. Polym. Sci., vol. 30, no. 8, pp. 3163–3188, Aug. 1985.

[14] C. Nakafuku and T. Miyaki, “Effect of pressure on the melting and crystallization behaviour of isotactic polybutene-1,” Polymer, vol. 24, no. 2, pp. 141–148, Feb. 1983.

[15] G. Kalay and C. R. Kalay, “Interlocking shish-kebab morphology in polybutene-1,” J. Polym. Sci. Part B Polym. Phys., vol. 40, no. 17, pp. 1828–1834, Sep. 2002.

[16] C. H. Choi and J. L. White, “Crystal-crystal transformations in isotactic polybutene-1 oriented filaments and in thick molded rods,” Polym. Eng. Sci., vol. 41, no. 6, pp. 933–939, Jun. 2001.

[17] J. M. Samon, J. M. Schultz, B. S. Hsiao, J. Wu, and S. Khot, “Structure development during melt spinning and subsequent annealing of polybutene-1 fibers,” J. Polym. Sci. Part B Polym. Phys., vol. 38, no. 14, pp. 1872–1882, Jul. 2000.

[18] Y. Liu et al., “Stretch-Induced Crystal–Crystal Transition of Polybutene-1: An in Situ Synchrotron Radiation Wide-Angle X-ray Scattering Study,” Macromolecules, vol. 45, no. 6, pp. 2764–2772, Mar. 2012.

[19] J. Hu and K. Tashiro, “Relation between higher-order structure and crystalline phase transition of oriented isotactic polybutene-1 investigated by temperature-dependent time-resolved simultaneous WAXD/SAXS measurements,” Polymer, vol. 90, pp. 165–177, May 2016.

[20] X. Zhang, X. Zhang, and G. Shi, “The effect of some additives on the Form II to Form I phase transformation in polybutene-1,” Thermochim. Acta, vol. 205, no. C, pp. 245–252, Aug. 1992.

[21] K. Miyazaki, Y. Takahashi, M. Terano, and H. Nakatani, “Additive effects of tripalmitin on morphologies and tensile properties of polybutene-1 and its composite with micro fibrous cellulose,” Polym. Bull., vol. 70, no. 4, pp. 1383–1395, Apr. 2013.

[22] M. Nase, R. Androsch, S. Henning, and W. Grellmann, “Influence of the Form II/Form I crystal polymorphism of random copolymers of butene-1 with ethylene or propylene on the peel behavior of peel films,” Polym. Eng. Sci., vol. 55, no. 8, pp. 749–1757, Aug. 2015.

[23] I. Stolte and R. Androsch, “Kinetics of the melt - Form II phase transition in isotactic random butene-1/ethylene copolymers,” Polymer, vol. 54, no. 26, pp. 7033–7040, Dec. 2013.

[24] I. Stolte, R. Androsch, and M. L. Di Lorenzo, “Spherulite growth rate and fold surface free energy of the form II mesophase in isotactic polybutene-1 and random butene-1/ethylene copolymers,” Colloid Polym. Sci., vol. 292, no. 6, pp. 1479–1485, Jun. 2014.

[25] M. Kaszonyiova, F. Rybnikar, L. Lapcik, and D. Manas, “Effects of beta irradiation, copolymers, and blends on the transformation rate of polybutene-1,” J. Macromol. Sci. Part B Phys., vol. 51, no. 5, pp. 926–945, May 2012.

[26] B. Zhang, D. Yang, and S. Yan, “Direct formation of form I poly(1-butene) single crystals from melt crystallization in ultrathin films,” J. Polym. Sci. Part B Polym. Phys., vol. 40, no. 23, pp. 2641–2645, Dec. 2002.

[27] M. Yamashita and S. Ueno, “Direct melt crystal growth of isotactic polybutene-1 trigonal phase,” in Crystal Research and Technology, 2007, vol. 42, no. 12, pp. 1222–1227.

[28] C. De Rosa et al., “Polymorphic behavior and mechanical properties of isotactic 1-butene-ethylene copolymers from metallocene catalysts,” Macromolecules, vol. 47, no. 13, pp. 4317–4329, Jul. 2014.

[29] Y. Wang, Y. Lu, J. Zhao, Z. Jiang, and Y. Men, “Direct formation of different crystalline forms in butene-1/ethylene copolymer via manipulating melt temperature,” Macromolecules, vol. 47, no. 24, pp. 8653–8662, Dec. 2014.

[30] F. Su et al., “Direct formation of isotactic poly(1-butene) form I crystal from memorized ordered melt,” Macromolecules, vol. 46, no. 18, pp. 7399–7405, Sep. 2013.

[31] R. R. Ahmed, V. Parmar, and M. A. Amin, “Impact of Product Packaging on Consumer’s Buying Behavior,” Eur. J. Sci. Res., vol. 122, no. 2, pp. 125–134, 2014.

[32] M. Gómez, D. Martín-Consuegra, and A. Molina, “The importance of packaging in purchase and usage behaviour,” Int. J. Consum. Stud., vol. 39, no. 3, pp. 203–211, May 2015.

[33] A. Ybxoll, R. Janson, S. R. Bradbury, J. Langley, J. Wearn, and S. Hayes, “Openability: Producing design limits for consumer packaging,” Packag. Technol. Sci., vol. 19, no. 4, pp. 219–225, Jul. 2006.

[34] A. Liebmann, I. Schreib, R. E. Schlözer, and J.-P. Majschak, “Practical Case Studies: Easy Opening for Consumer-Friendly, Peelable Packaging,” J. Adhes. Sci. Technol., vol. 26, no. 20–21, pp. 2437–2448, Jan. 2012.

[35] M. Nase, L. Großmann, M. Rennert, B. Langer, and W. Grellmann, “Adhesive properties of heat-sealed EVAc/PE films in dependence on recipe, processing, and sealing parameters,” J. Adhes. Sci. Technol., vol. 28, no. 12, pp. 1149–1166, Jun. 2014.

[36] M. Nase, B. Langer, and W. Grellmann, “Fracture mechanics on polyethylene/polybutene-1 peel films,” Polym. Test., vol. 27, no. 8, pp. 1017–1025, Dec. 2008.

[37] F. C. Stehling and P. Meka, “Heat sealing of semicrystalline polymer films. II. Effect of melting distribution on heat-sealing behavior of polyolefins,” J. Appl. Polym. Sci., vol. 51, no. 1, pp. 105–119, Jan. 1994.

[38] C. Mueller, G. Capaccio, A. Hiltner, and E. Baer, “Heat sealing of LLDPE: relationships to melting and interdiffusion,” J. Appl. Polym. Sci., vol. 70, no. 10, pp. 2021–2030, Dec. 1998.

[39] C. C. Hwo, “Polybutylene Blends as Easy Open Seal Coats for Flexible Packaging and Lidding,” J. Plast. Film Sheeting, vol. 3, no. 4, pp. 245–260, Oct. 1987.

[40] M. Nase, A. Zankel, B. Langer, H. J. Baumann, W. Grellmann, and P. Poelt, “Investigation of the peel behavior of polyethylene/polybutene-1 peel films using in situ peel tests with environmental scanning electron microscopy,” Polymer, vol. 49, no. 25, pp. 5458–5466, Nov. 2008.

[41] M. Nase, R. Androsch, B. Langer, H. J. Baumann, and W. Grellmann, “Effect of polymorphism of isotactic polybutene-1 on peel behavior of polyethylene/polybutene-1 peel systems,” J. Appl. Polym. Sci., vol. 107, no. 5, pp. 3111–3118, Mar. 2008.

[42] S. D. Wanjale and J. P. Jog, “Poly(1-butene)/clay nanocomposites: Preparation and properties,” J. Polym. Sci. Part B Polym. Phys., vol. 41, no. 10, pp. 1014–1021, May 2003.

[43] S. D. Wanjale and J. P. Jog, “Poly (1-Butene)/Clay Nanocomposites: A Crystallization Study,” J. Macromol. Sci. Part B Phys., vol. 42, no. 6, pp. 1141–1152, Jan. 2006.

[44] F. M. Mirabella and A. Bafna, “Determination of the crystallinity of polyethylene/α-olefin copolymers by thermal analysis: Relationship of the heat of fusion of 100% polyethylene crystal and the density,” J. Polym. Sci. Part B Polym. Phys., vol. 40, no. 15, pp. 1637–1643, Aug. 2002.

[45] E. Manias, J. Zhang, J. Y. Huh, K. Manokruang, P. Songtipya, and M. M. Jimenez-Gasco, “Polyethylene nanocomposite heat-sealants with a versatile peelable character,” Macromol. Rapid Commun., vol. 30, no. 1, pp. 17–23, Jan. 2009.

[46] A. Ammar, A. Elzatahry, M. Al-Maadeed, A. M. Alenizi, A. F. Huq, and A. Karim, “Nanoclay compatibilization of phase separated polysulfone/polyimide films for oxygen barrier,” Appl. Clay Sci., vol. 137, pp. 123–134, Mar. 2017.

[47] Z. Martín, I. Jiménez, M. A. Gómez, H. Ade, and D. A. Kilcoyne, “Interfacial Interactions in PP/MMT/SEBS Nanocomposites,” Macromolecules, vol. 43, no. 1, pp. 448–453, Jan. 2010.

[48] M. Trifkovic, A. T. Hedegaard, M. Sheikhzadeh, S. Huang, and C. W. Macosko, “Stabilization of PE/PEO Cocontinuous Blends by Interfacial Nanoclays,” Macromolecules, vol. 48, no. 13, pp. 4631–4644, Jul. 2015.

[49] G. Strobl, “Strain-Controlled Tensile Deformation Behavior of Isotactic Poly (1- butene) and Its Ethylene Copolymers,” Society, pp. 20036–20036, 2008.

[50] Y. Liu et al., “Stretch-Induced Crystal−Crystal Transition of Polybutene-1: An in Situ Synchrotron Radiation Wide-Angle X-ray Scattering Study.”

[51] J. Baert, P. Van Puyvelde, and F. Langouche, “Flow-induced crystallization of PB-1: From the low shear rate region up to processing rates,” Macromolecules, vol. 39, no. 26, pp. 9215–9222, 2006.

[52] C. De Rosa et al., “Mechanical properties and stress-induced phase transformations of metallocene isotactic poly(1-butene): The influence of stereodefects,” Macromolecules, vol. 47, no. 3, pp. 1053–1064, Feb. 2014.

CHAPTER 7 ARTICLE 4: CONFINED CRYSTALLIZATION OF POLYBUTENE-1 NANOFIBRILS IN LOW DENSITY POLYETHYLENE/ POLYBUTENE-1/ORGANOCLAY NANOCOMPOSITE FILMS[4]

Raziyeh S. Mohammadi,[a] Ali M. Zolali,[b] Seyed H. Tabatabaei,[c] Abdellah Ajji[a]

[a] *3SPack NSERC-Industry Chair, CREPEC, Department of Chemical Engineering, Polytechnique Montreal, C.P. 6079, Succ. Centre-ville, Montreal, QC, H3C 3A7, Canada*

[b] *Microcellular Plastics Manufacturing Laboratory, Department of Mechanical and Industrial Engineering, University of Toronto, Toronto, Ontario M5S 3G8, Canada*

[c] *ProAmpac, 12025 Tricon Road, Cincinnati, OH 45209, USA*

7.1 Abstract

Polybutene-1 (PB-1) is a commercially interesting polymer that its applications are restricted due to its unstable polymorphism after melt treatment. We generated stable PB-1 crystalline structures directly from the melt after heat sealing process through its confinement in low density polyethylene (LDPE)/PB-1 blend and LDPE/PB-1/organoclay nanocomposite films. The particular nanoscale fibrillar morphology of PB-1 in the films is an essential step to provide confined environment for PB-1 crystallization and suppression of the metastable form II crystals of PB-1. Also, the earlier solidification of LDPE matrix, which possesses a significantly higher crystallization temperature than that of PB-1, imposes external stress on the PB-1 nanofibrils. No trace of unstable form II crystals is observed through WAXD and FTIR analysis after the heat sealing of the films containing 1 phr organoclays. This is attributed to organoclays interactions with PB-1 phase that significantly disturb the kinetic of the form II formation. The confined

[4] To be submitted after patent application.

crystallization of PB-1 in the blends and nanocomposite films is further confirmed through anisotropic orientation of PB-1 crystals as examined by polarized-FTIR.

7.2 Introduction

Isotactic polybutene-1 (iPB-1) presents a complex polymorphism based on various helical conformations i.e. 3/1, 11/3 and 4/1 helices characteristics of twined hexagonal form I/untwined hexagonal form I′, twined hexagonal form II and orthorhombic form III crystals respectively [1–4]. Forms I′ and III modifications are usually obtained from solution, but can be converted to crystal form II when dried and heated up to 90 °C [4]. Form II is metastable and is kinetically favored to form during cooling from the melt at ambient pressure. The metastable form II spontaneously converts to form I over about 2 weeks [2,5,6]. Form II to form I conversion is accompanied by profound thermal and mechanical changes due to the significant difference in their melting temperature and density [7–10]. Significant body of literature report form II to form I transition acceleration through various approaches such as pressure [11,12], orientation and drawing [13–17], incorporation of additive [18,19] and copolymerization [20–23]. Moreover, direct formation of form I or I′ under peculiar conditions such as ultrathin films [24], self-seeding [25], stereo defects [26] and manipulating the melt temperature [27] have been reported in literature [27,28]. It has been also reported that incorporation of some stereo irregularity in PB-1 backbone results in direct formation of form III instead of form II [29]. Nevertheless, complex polymorphism of PB-1 remains a challenging task that restricts its applications even though it has superior impact properties, toughness, elastic recovery and creep resistance [30,31]. In this regard, direct formation of stable PB-1 crystals rather than the metastable form II opens up a new avenue toward employing this commercially interesting polymer for some novel applications.

In this work, we examine the direct generation of PB-1 stable form I and form III from heat sealed LDPE/PB-1 blend and LDPE/PB-1/organoclay nanocomposite films containing 5 to 20 wt% of PB-1 and 1 phr organoclay.

7.3 Experimental

Commercial grades low-density polyethylene (LDPE, Novapol LF-0219-A) and polybutene-1 (PB-1, DuPont PB0300M) were melt blended using a twin-screw extruder (TSE) to prepare LDPE/PB-

1 blends containing 5, 10 and 20 wt% of PB-1, which are named as PEPB5, PEPB10 and PEPB20, respectively. To prepare nanocomposites, a masterbatch of PB-1 with 20 wt% of organomodified montmorillonite clay (Cloisite15) was melt-mixed using TSE equipped with a separate nanoclay feeder. The masterbatch was then diluted using the same TSE equipped with slit die to obtain LDPE/PB-1/organoclay films containing 5, 10 and 20 wt% of PB-1 and 1 phr organoclay, which are named as NPEPB5, NPEPB10 and NPEPB20, respectively. The extrudates from the die passed through an air knife and calendar rolls chilled with cold water. The calendar speed was manipulated to achieve films with a thickness of 70 μm.

Strips of the films with 2.54 cm in width were cut and then heat sealed on themselves using a hot tack/seal tester from LakoTool & Manufacturing Inc, USA at a seal pressure of 0.5 N/mm^2, a dwell time of 1 second and a heat seal temperature of 150 °C.

T-peel test was carried out according to ASTM F88 using a tensile testing machine (Instron E3000) to measure the peel force of the sealant films. The heat-sealed films were peeled at a peeling rate of 200 mm/min. The results were plotted in terms of the peel force as a function of displacement. The plateau part of the plot was reported as the peel force of the corresponding specimen. The average plateau force of at least 5 specimens was reported as the peel force of each film.

Crystallographic characteristics of the blends and nanocomposites films have been investigated using Wide angle X-ray diffraction (WAXD) and Fourier Transform Infrared (FTIR) Spectroscopy. The WAXD experiments were performed using a Phillips X'pert apparatus having a copper (Cu) anode with a K_α wavelength of 1.54 Å, a generator voltage of 50 kV, a tube current of 40 mA and a scan rate of 0.02 °/s in a 2θ range of 2-30° at room temperature and 20 cm distance between the sample and detector. FTIR spectroscopy was carried out using a Perkin Elmer 65 FTIR-ATI instrument in a wavelength range of 4000-650 cm^{-1} with a total of 128 scans and 4 cm^{-1} resolution. Polarized FTIR characterizations in machine and transverse directions (MD and TD) were performed using a Spectra-Tech zinc selenide wire grid polarizer from Thermo Electron Corp.

Scanning electron microscopy (SEM) was used to observe and evaluate the morphology of the peeled surface of the films. The specimens were first coated with gold/palladium through plasma vacuum deposition and then SEM observations were carried out using a Field Emission SEM

machine (JSM 7600TFE, JEOL) operated at a voltage of 2 kV. The PB-1 phase is extracted using cyclohexane at 50 °C for 30 minutes.

Differential scanning calorimetry (DSC) was performed using a DSC instrument Q2000 (from TA instruments) to evaluate the thermal properties of the film samples. Specimens of about 15 mg were placed in an aluminum pan and conventional DSC heating and cooling runs were performed from 25 to 150 °C under nitrogen atmosphere at a heating rate of 10 °C/min.

7.4 Results and Discussion

Figure 7.1a and 1b show SEM images of PEPB5 and PEPB10 blend films after being sealed at 150 °C. They show that PB-1 forms small droplets in the TD-ND cross section while elongated structures are observed in the MD-ND cross section in Figure 7.1d and 1e. These results suggest a fibrillar morphology for PB-1 in PEPB5 and PEPB10 blends. SEM images of PEPB20 demonstrate a mixture of droplet and mainly elongated morphology with shorter length in TD-ND cross section (Figure 7.1c) and highly elongated structures in MD-ND cross section (Figure 7.1f) that suggest a mixture of fibrillar and sheet like morphology of PB-1 in PEPB20 film.

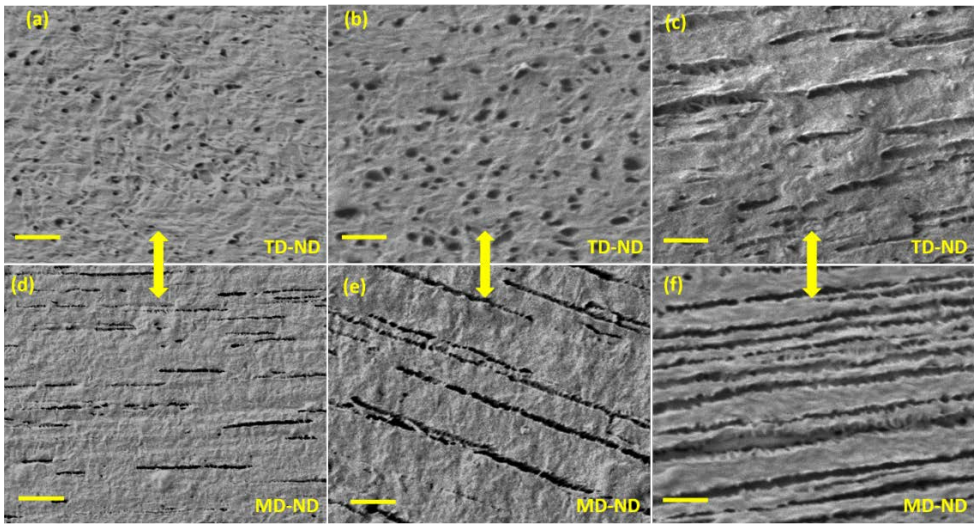

Figure 7.1 The SEM images of PEPB5 (a and d); PEPB10 (b and e) PEPB20 (c and f) in TD-ND (upper images) and MD-ND (lower images) cross sections. The yellow bars indicate 0.5 µm.

SEM images of the nanocomposites presented in Figure 7.2 clearly indicate that the fibrillar morphology is preserved in the nanocomposites, but it can be intuitively deduced that the size of

PB-1 nanofibrils and sheets are reduced upon the incorporation of 1 phr organoclay to the blends. This might be ascribed to the organoclay localization at the interface of the blend components as will be confirmed by the TEM imaged and WAXD patterns.

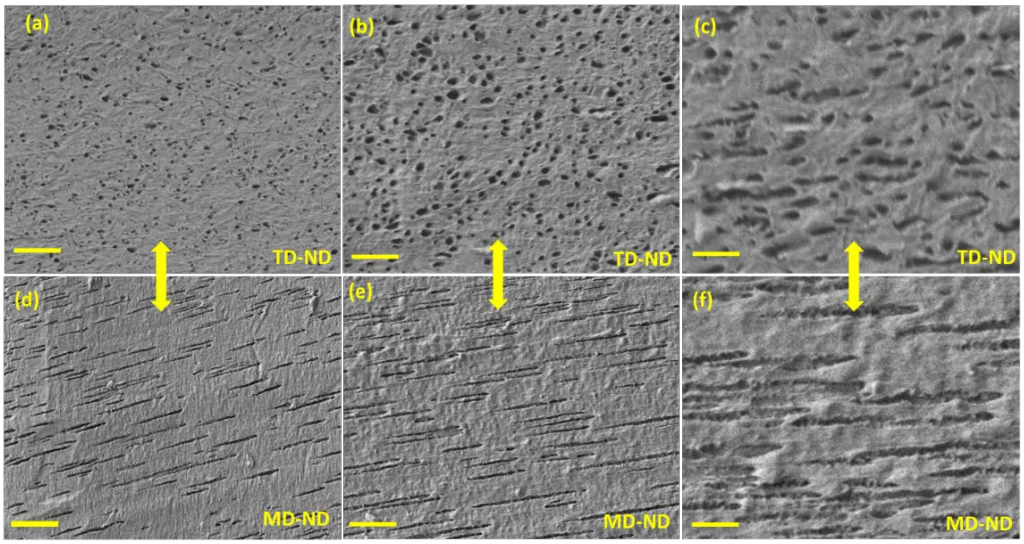

Figure 7.2. The SEM images of NPEPB5 (a and d), NPEPB10 (b and e) and NPEPB20 (c and f) in TD-ND (upper images) and MD-ND (lower images) cross sections. The yellow bars indicate 0.5 µm.

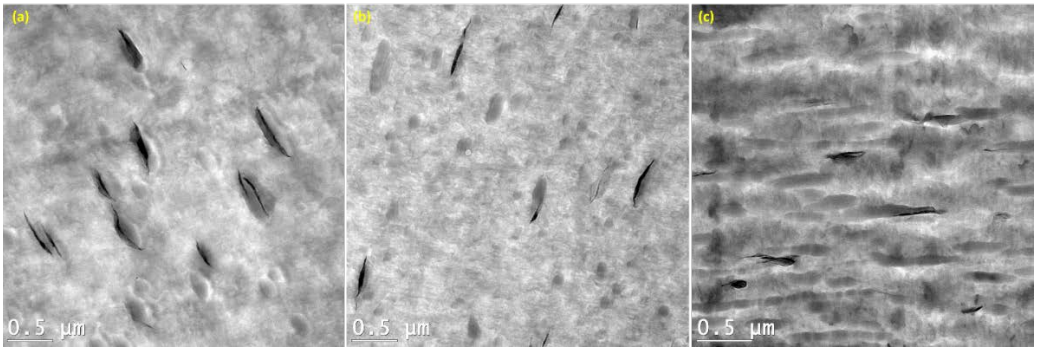

Figure 7.3. TEM images of NPEPB5 (a), NPEPB10 (b) and NPEPB20 (c).

TEM images of the nanocomposites, presented in Figure 7.3, show that organoclay is mainly localized at the interface of phases. The WAXD patterns illustrated in Figure B1 also suggest similar affinity of clay particles with LDPE and PB-1. However, a portion of organoclays are observed inside PB-1 phase, particularly for the NPEPB5 (figure 3a). This might be because of the

insufficient room for organoclay platelets to localize at the interface of the components thus, a portion of them remain in PB-1 that was mixed first with organoclay.

WAXD patterns of all the sealants right after heat sealing (Figure 7.4) exhibit a reflection at 2θ = 10° corresponding to (110) plane of form I or I′. There are reflections at 2θ = 11.9, 16.9, and 18.3° corresponding to (200), (220) and (213) planes respectively of form II in the WAXD pattern of the neat blends. While no reflection corresponding to form II is observed for the nanocomposite sealants. Furthermore, reflections at 2θ = 12.2, 17.2 and 18.8° of form III of PB-1 are detected in WAXD patterns of the nanocomposites, which are absent in the WAXD patters of the neat blends.

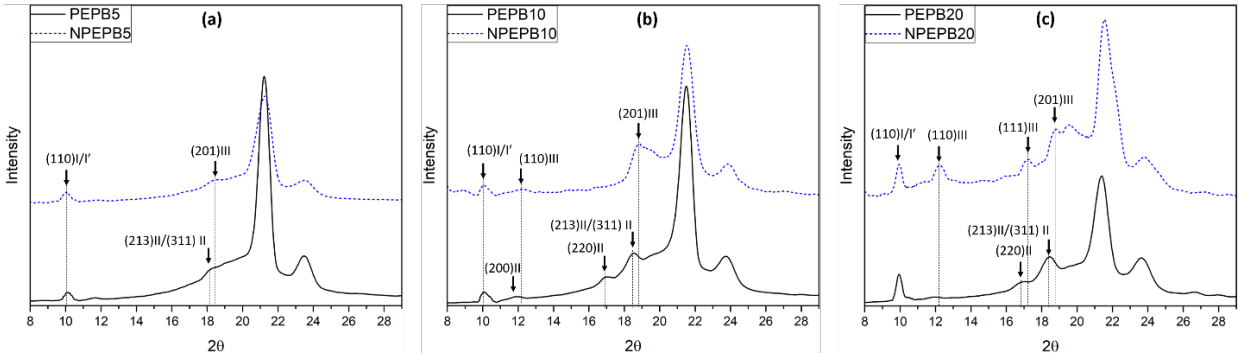

Figure 7.4. WAXD patter of the neat blends and nanocomposites containing 5 (a), 10 (b) and 20 wt% of PB-1 (c) immediately after the seal.

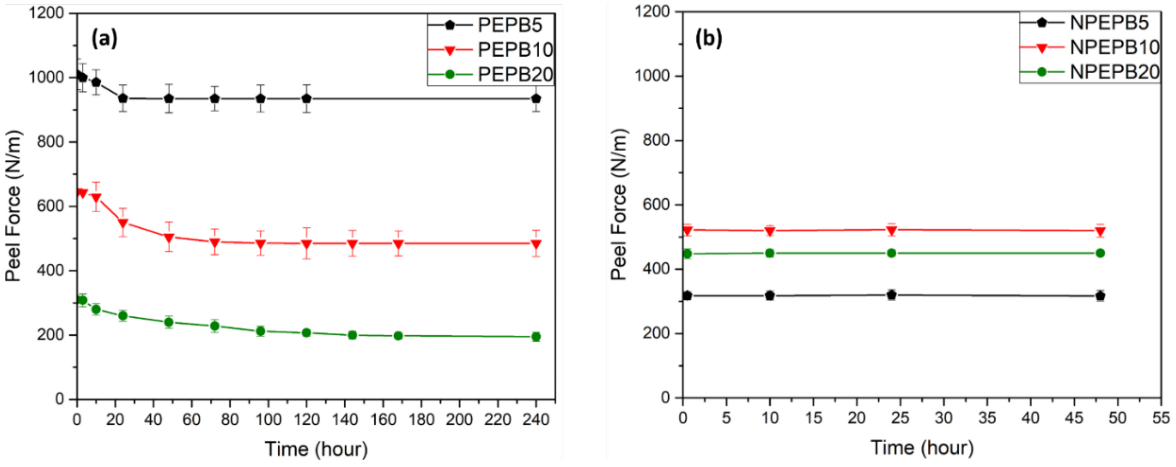

Figure 7.5. Peel force of the blends (a) and nanocomposite sealants (b) right after, 24 hours and 10 days after being heat sealed. PEPB5, PEPB10 and PEPB20 were sealed at 130, 135 and a150 °C. the nanocomposites were sealed at 150 °C.

The absence of form II after heat sealing of PE/PB-1/organoclay films is confirmed by investigating peel performance of the aged films (Figure 7.5). The peel force of the LDPE/PB-1 blends decreased (Figure 7.5a) and is attributed to the shrinkage of the film due to the formation of the form II after the heat seal while, the peel force of the nanocomposite sealants remains constant (Figure 7.5b). The comparison is performed in the first 50 hours after sealing since it is the period in which the most decrease of peel strength is observed for blends films.

The FTIR spectra of the neat blends and nanocomposites films immediately after sealing and 10 days after are presented in Figure 7.6. The vibrations at 905 and 925 cm^{-1} corresponding to CH_2 and CH_3 rocking bands of form II or III and form I respectively [32,33]. Crystal forms II and III exhibit the same vibrations in FTIR spectra. For the neat blends, two vibrations are observed at 905 and 925 cm^{-1} right after the seal (Figure 7.6a). The vibration at 905 cm^{-1} disappeared after 10 days while the intensity of the peak at 925 cm^{-1} is increased, thus the 905 cm^{-1} is assigned to form II because form III is more stable. FTIR spectra of the nanocomposites in Figure 7.6b exhibit two vibrations at 908 and 925 cm^{-1}. The vibration at 908 cm^{-1} is not assigned to organoclay or PE but, since it is very close to 905 cm^{-1}, it might be ascribed to delocalization of the form II or III vibration from 905 to 908 cm^{-1}. FTIR vibrational shift has been reported in literature and is attributed to molecular structural change due to high deformation or environmental confinement effects [34–37]. Since, the intensity of the peak at 908 cm^{-1} remains constant over the time, it is attributed to form III. It is also worth noting that forms I and I′ exhibit similar trigonal crystal structure and similar FTIR vibration at 925 cm^{-1}. In contrast to form I which is only produced from form II, form I′ can be obtained from the melt in peculiar conditions such as from ultrathin films [25]. Therefore, stretching band at 925 $^{-1}$ is attributed to form I′ unless, form I of PB-1 nanofibrils is not completely melted during the short heat sealing time. Thus, the peak at 925 cm^{-1} may be attributed to the residual form I in the seal after heat sealing. Also, if crystal segregation happens rather than complete melting of the sealant, form I′ is most likely produced due to melt memory effect. The melt memory effect and segregation of the crystals result in the recovery of similar crystalline structures from the originally segregated crystals [27,38].

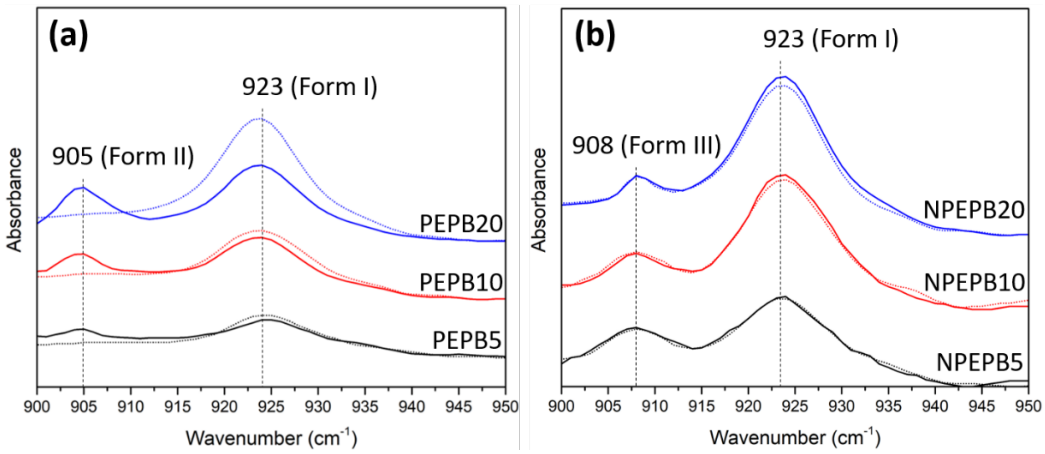

Figure 7.6. FTIR spectra of the PE/PB-1 blends (a) and nanocomposites(b). The solid lines and the dash lines represent the FTIR spectra of the sealants right after and 2 weeks after the heat sealing respectively.

On the other hand, the absence of form II in the nanocomposites films after sealing might be justified as follow. The most probable reason for crystal form II formation from the melt is its faster crystal growth in comparison to form I′ [39]. Therefore, disruption of the crystallization kinetic of form II is likely to suppress its formation priority with respect to the form I′. Furthermore, the experimental results presented by Wang et al. [27] suggest that the minimum lamella thickness for crystal growth is thicker for crystal form II compared to that of form I′ at the same crystallization temperature. Therefore, decreasing the size of PB-1 fibrils, particularly in nanocomposite sealants, may disrupt the kinetics of form II because it needs more space to form rather than form I′. Moreover, the crystallization temperature of LDPE is at 96 ^{o}C, much higher than that of PB-1 at 75 ^{o}C (see Figure B2b). In this case, earlier solidification of LDPE provides external stress which restricts the molecular motion of PB-1 nanofibrils in the blends and disrupts the kinetics of form II crystallization. This confinement is further assisted by the presence of clay particles that further hinder the chain movement during the crystallization process. This confinement is more confirmed through orientation of PB-1 crystals as illustrated in Figure B3. Orientation of PB-1 crystals in the blend and nanocomposite sealants suggest that the size of PB-1 nanofibrils are low enough to feel the confinement otherwise, isotropic orientation would be obtained.

The absence of form II and direct formation of form III in the nanocomposite sealants even by increasing PB-1 content to 20 wt% is questionable and is attributed to the better dispersion of organoclay by increasing PB-1 content which provide more space for organoclay platelets to locate at the interface (See Figure B1). Furthermore, the mixing sequence in which organoclay was first blended with PB-1 and then diluted with LDPE, may cause a portion of the clay nanoparticles to remain in PB-1 fibrils and further suppress form II formation.

7.5 Conclusion

PB-1 forms mainly nanofibrillar structure in LDPE/PB-1 blends and nanocomposite films containing 5 to 20 wt% PB-1. WAXD and FTIR analysis indicate the direct formation of form I or I′ right after the heat seal process. In addition to form I/I′, metastable form II is formed followed by heat sealing of LDPE/PB-1 blend films that decreases the peel force upon aging time. No trace of crystal form II but, crystal form III of PB-1 were detected in the LDPE/PB-1/organoclay films after heat sealing. The absence of form II after the heat sealing of LDPE/PB-1/organoclay films results in their consistent peel performance. The exact mechanism of direct formation of forms I and III and suppression of unstable form II formation is not clear yet, but it can be associated with confined crystallization of nanoscale PB-1 fibrils in glassy LDPE environment. This confinement is speculated to be more intense in the presence of clay nanoparticles at the interface and probably inside PB-1 phase that further hinder the chains movement to form crystalline structures thus, disrupt the kinetic of the unstable form II formation. Anisotropic orientation of PB-1 crystals in the blend and nanocomposite films of this study is a signature that confirms the sufficiently low size of the PB-1 nanofibrils to feel the confinement.

7.6 References

[1] G. Natta, P. Corradini, I.W. Bassi, Crystal structure of isotactic poly-alpha-butene, Nuovo Cim. 15 (1960) 52–67.

[2] R.L. Miller, V.F. Holland, On transformations in isotactic polybutene-1, J. Polym. Sci. Part C Polym. Lett. 2 (1964) 519–521.

[3] A.T. Jones, Polybutene-1 – type II crystalline form, J. Polym. Sci. Part B Polym. Lett. 1 (1963) 455–456.

[4] V.F. Holland, R.L. Miller, Isotactic Polybutene-1 Single Crystals: Morphology, J. Appl. Phys. 35 (1964) 3241–3248.

[5] R.M. Gohil, M.J. Miles, J. Petermann, On the molecular mechanism of the crystal transformation (tetragonal-hexagonal) in polybutene-1, J. Macromol. Sci. Part B. 21 (1982) 189–201.

[6] K.W. Chau, Y.C. Yang, P.H. Geil, Tetragonal → twinned hexagonal crystal phase transformation in polybutene-1, J. Mater. Sci. 21 (1986) 3002–3014.

[7] F. Azzurri, A. Flores, G.C. Alfonso, I. Sics, B.S. Hsiao, F.J.B. Calleja, Polymorphism of isotactic polybutene-1 as revealed by microindentation hardness. Part II: Correlations to microstructure, Polymer. 44 (2003) 1641–1645.

[8] G.C. Alfonso, F. Azzurri, M. Castellano, Analysis of Calorimetric Curves Detected During the Polymorphic Transformation of Isotactic Polybutene-1, J. Therm. Anal. Calorim. 66 (2001) 197–207.

[9] M.L. Di Lorenzo, M.C. Righetti, B. Wunderlich, Influence of Crystal Polymorphism on the Three-Phase Structure and on the Thermal Properties of Isotactic Poly(1-butene), Macromolecules. 42 (2009) 9312–9320.

[10] H. Shao, D. Jiang, M. Zhang, W. Yao, B. Huang, Characterization of the polymorphic transformation of poly(1-butene) based on FTIR and mechanical properties, J. Polym. Res. 19 (2012) 9919.

[11] K.-B. Hong, J.E. Spruiell, The effect of certain processing variables on the form ii to form i phase transformation in polybutene-1, J. Appl. Polym. Sci. 30 (1985) 3163–3188.

[12] C. Nakafuku, T. Miyaki, Effect of pressure on the melting and crystallization behaviour of isotactic polybutene-1, Polymer. 24 (1983) 141–148.

[13] G. Kalay, C.R. Kalay, Interlocking shish-kebab morphology in polybutene-1, J. Polym. Sci. Part B Polym. Phys. 40 (2002) 1828–1834.

[14] C.-H. Choi, J.L. White, Crystal-crystal transformations in isotactic polybutene-1 oriented filaments and in thick molded rods, Polym. Eng. Sci. 41 (2001) 933–939.

[15] J.M. Samon, J.M. Schultz, B.S. Hsiao, J. Wu, S. Khot, Structure development during melt spinning and subsequent annealing of polybutene-1 fibers, J. Polym. Sci. Part B Polym. Phys. 38 (2000) 1872–1882.

[16] Y. Liu, K. Cui, N. Tian, W. Zhou, L. Meng, L. Li, Z. Ma, X. Wang, Stretch-induced crystal-crystal transition of polybutene-1: An in situ synchrotron radiation wide-angle X-ray scattering study, Macromolecules. 45 (2012) 2764–2772.

[17] J. Hu, K. Tashiro, Relation between higher-order structure and crystalline phase transition of oriented isotactic polybutene-1 investigated by temperature-dependent time-resolved simultaneous WAXD/SAXS measurements, Polymer. 90 (2016) 165–177.

[18] X. Zhang, X. Zhang, G. Shi, The effect of some additives on the Form II to Form I phase transformation in polybutene-1, Thermochim. Acta. 205 (1992) 245–252.

[19] K. Miyazaki, Y. Takahashi, M. Terano, H. Nakatani, Additive effects of tripalmitin on morphologies and tensile properties of polybutene-1 and its composite with micro fibrous cellulose, Polym. Bull. 70 (2013) 1383–1395.

[20] M. Nase, R. Androsch, S. Henning, W. Grellmann, Influence of the Form II/Form I crystal polymorphism of random copolymers of butene-1 with ethylene or propylene on the peel behavior of peel films, Polym. Eng. Sci. 55 (2015) 749–1757.

[21] I. Stolte, R. Androsch, Kinetics of the melt - Form II phase transition in isotactic random butene-1/ethylene copolymers, Polymer. 54 (2013) 7033–7040.

[22] I. Stolte, R. Androsch, M.L. Di Lorenzo, Spherulite growth rate and fold surface free energy of the form II mesophase in isotactic polybutene-1 and random butene-1/ethylene copolymers, Colloid Polym. Sci. 292 (2014) 1479–1485.

[23] M. Kaszonyiova, F. Rybnikar, L. Lapcik, D. Manas, Effects of Beta Irradiation, Copolymers, and Blends on the Transformation Rate of Polybutene-1, J. Macromol. Sci. Part B. 51 (2012) 926–945.

[24] B. Zhang, D. Yang, S. Yan, Direct formation of form I poly(1-butene) single crystals from melt crystallization in ultrathin films, J. Polym. Sci. Part B Polym. Phys. 40 (2002) 2641–2645.

[25] M. Yamashita, S. Ueno, Direct melt crystal growth of isotactic polybutene-1 trigonal phase, Cryst. Res. Technol. 42 (2007) 1222–1227.

[26] C. De Rosa, O. Ruiz de Ballesteros, F. Auriemma, R. Di Girolamo, C. Scarica, G. Giusto, S. Esposito, S. Guidotti, I. Camurati, Polymorphic Behavior and Mechanical Properties of Isotactic 1-Butene–Ethylene Copolymers from Metallocene Catalysts, Macromolecules. 47 (2014) 4317–4329.

[27] Y. Wang, Y. Lu, J. Zhao, Z. Jiang, Y. Men, Direct Formation of Different Crystalline Forms in Butene-1/Ethylene Copolymer via Manipulating Melt Temperature, Macromolecules. 47 (2014) 8653–8662.

[28] F. Su, X. Li, W. Zhou, S. Zhu, Y. Ji, Z. Wang, Z. Qi, L. Li, Direct Formation of Isotactic Poly(1-butene) Form I Crystal from Memorized Ordered Melt, Macromolecules. 46 (2013) 7399–7405.

[29] C. De Rosa, F. Auriemma, M. Villani, O.R. de Ballesteros, R. Di Girolamo, O. Tarallo, A. Malafronte, Mechanical Properties and Stress-Induced Phase Transformations of Metallocene Isotactic Poly(1-butene): The Influence of Stereodefects, (2014).

[30] L. Luciani, J. Seppälä, B. Löfgren, Poly-1-butene: Its preparation, properties and challenges, Prog. Polym. Sci. 13 (1988) 37–62.

[31] F. Schemm, V. De Vliet, J. Grasmeder, F. Cocola, " Basell Polybutene-1 : High Performance Polyolefin for Plumbing Appilcations ," (2000).

[32] K.W. Chau, Y.C. Yang, P.H. Geil, Tetragonal → twinned hexagonal crystal phase transformation in polybutene-1, J. Mater. Sci. 21 (1986) 3002–3014.

[33] G. Goldbach, G. Peitscher, Infrared investigations of the polymorphic modifications of polybutene-1, J. Polym. Sci. Part B Polym. Lett. 6 (1968) 783–788.

[34] V.I. Vettegren, I.I. Novak, K.J. Friedland, Overstressed interatomic bonds in stressed polymers, Int. J. Fract. 11 (1975) 789–801.

[35] K. Tashiro, S. Minami, G. Wu, M. Kobayashi, Quasiharmonic treatment of infrared and raman vibrational frequency shifts induced by tensile deformation of polymer chains. II. Application to the polyoxymethylene and isotactic polypropylene single chains and the three-dimensional orthorhombic polyethylene crystal, J. Polym. Sci. Part B Polym. Phys. 30 (1992) 1143–1155.

[36] L.S. Loo, K.K. Gleason, Insights into structure and mechanical behavior of α and γ crystal forms of nylon-6 at low strain by infrared studies, Macromolecules. 36 (2003) 6114–6126.

[37] N. Gierlinger, M. Schwanninger, A. Reinecke, I. Burgert, Molecular changes during tensile deformation of single wood fibers followed by Raman microscopy, Biomacromolecules. 7 (2006) 2077–2081.

[38] L. He, B. Wang, F. Yang, Y. Li, Z. Ma, Featured Crystallization Polymorphism and Memory Effect in Novel Butene-1/1,5-Hexadiene Copolymers Synthesized by Post-Metallocene Hafnium Catalyst, Macromolecules. 49 (2016) 6578–6589.

[39] T. Threlfall, Structural and Thermodynamic Explanations of Ostwald's Rule, (2003).

CHAPTER 8 GENERAL DISCUSSION

This work provides valuable insights for understanding the profound effect of the seal microstructure on the peel-seal performance. In this work, we have used polyolefin based systems as most peelable sealants are composed of polyolefin materials such as LDPE, EMA, etc. mainly due to their excellent processing, low heat seal temperature, low cost. We have examined the morphology and thermal properties of the various polyolefin based blend and nanocomposite sealants and correlated the results to the peel performance of them.

First, we hypothesized that the addition of nanoclay into the seal layer and controlling its dispersion and distribution can play significant role in enhancing the peelability of the LDPE films. To examine this idea, we investigated the potential of different nanoclays in inducing peelability and their effects on the peel performance of lock LDPE sealants through controlling the seal microstructure. The results of this part represent a model system and provide valuable information on the correlation between microstructure and peel performance in nanocomposite sealants. By increasing the nanoclay dispersion in the seal layer, the size of the LDPE ligament thickness between the clay stacks is reduced, thus the crack bridge is facilitated that results in more uniform and smoother peeled fracture surface. Moreover, improving the dispersion and distribution of the nanoclay in PE matrix results in higher yield strength, which is in favor of the peelability. It is known that for a sealant to be cohesively peeled, the yield strength of the sealant must be lower than the interfacial adhesion in seal layers at the weld line. Increasing the interactions of nanoclay and seal material can increase the yield strength of sealants. It also results in increased clay-clay and polymer-clay interfaces, which can be prone to crack initiation and crack propagation upon peeling. The force-displacement diagrams of these systems show a wide plateau indicating an easy peel behavior. The results confirm that reducing the interparticle distance through enhancing the nanoclay dispersion and distribution in the seal area is critical in obtaining peel performance over a wide heat seal temperature window. This can happen either by increasing the nanoclay content or by incorporating compatibilizer to increase the dispersion and distribution of nanoclay. Increasing the nanoclay content may result in thicker clay stacks that are not necessarily well distributed. Much more uniform nanoclay distribution and dispersion at a less clay content can be achieved by the incorporation of a compatibilizer to the seal formulation that results in enhanced

polymer/clay interactions and a shorter interparticle distance. The enhanced PE/clay interactions also increase the yield strength, thus promotes the peel performance. On the other hand, reducing the interparticle distance facilitates crack bridging upon peeling and reduces the crack propagation pass way through the PE ligament, which requires higher peel force to be delaminated compared to clay-clay and polymer-clay interfaces. Accordingly, the ultrawide peelable heat seal temperature was achieved when a semi-exfoliated morphology was generated at 3 wt% of the nanoclay through increasing the compatibilizer content. This is in line with the peeling mechanism proposed in this work.

We were also interested in understanding the peel performance of systems containing two immiscible components in the presence of nanoclay particles. Thus, we proposed two polyolefin-based systems with two different nanoclay localizations: at the interface of phases and within the dispersed phase. Thus, LDPE was chosen as the matrix and two dispersed components, EMA and EMA-GMA, were deliberately selected based on thermodynamic predictions to satisfy the objective. They are both polyolefin copolymers showing different levels of interactions with nanoclay and are usually used in seal formulations to improve the seal properties such as reducing the heat seal initiation temperature. The experimental results were in line with the thermodynamic predictions in which the nanoclay was localized at the interface of LDPE/EMA whereas was encapsulated by the dispersed EMA-GMA phase.

As expected, the peel performance of the LDPE/EMA-GMA/organoclay system was not affected by nanoclay due to the encapsulation of nanoclay particles by the EMA-GMA phase which significantly restricts the ability of clay particle to initiate and propagate cracks throughout the system. Moreover, the viscosity of the dispersed EMA-GMA phase containing nanoclay increases significantly which increases the size of the dispersed phase. Consequently, the interparticle distance significantly increases which works against the peelability, However, the localization of nanoclay at the interface of LDPE/EMA markedly improved the peel performance of the LDPE/EMA/organoclay sealants. The lock seal behavior of the LDPE/EMA blend was converted to a peelable behavior with a broad heat seal temperature range (over 35 °C). The morphology analysis revealed that the localization of nanoclay particles at the interface reduces the dispersed phase size, which can be through different mechanisms such as compatibilization effect of nanoclay and barrier effect reducing the coalescence between the EMA particles. This results in a reduced

interparticle distance and consequently enhanced peelability. Thus, it is deduced that localization of nanoclay within the dispersed phase is not in favor of the peelability whereas localization of nanoclay at the interface promotes the peelability.

Taking advantage of the concepts developed in the first two sections of this research, we proposed that the localization of nanoclay at the interface of a peelable immiscible blend can significantly enhance the peel performance. For this purpose, the LDPE/PB-1 blend was chosen as the thermodynamic model used in this study predicted the interfacial localization of nanoclay. Furthermore, one of the main problems with the peelable LDPE/PB-1 sealants is their inconsistent peel performance due to the aging of PB-1. It was also hypothesized that the incorporation of nanoclay to the LDPE/PB-1 blend can potentially eliminate this issue due to possible interactions of nanoclay with the PB-1 phase. Generally, nanoclays can affect the crystallinity of polymers with two various mechanisms i.e. nucleating effect and barrier effect. Our results showed that the nanoclay particles are mainly localized at the interface of the LDPE/PB-1 blend components. As expected, the peel performance of the LDPE/PB-1/organoclay sealants were significantly enhanced through the localization of nanoclay at the interface. Incorporation of only 1 phr organoclay enhances the peelability of the LDPE/PB-1(5wt%)/organoclay(1phr) sealant over a broad heat seal temperature range of about 100 °C when compared to the LDPE/PB-1(5wt%) and LDPE/organoclay(1phr) sealants, which exhibit a narrow peelable heat seal temperature window of 10 and 5 °C, respectively.

The effectiveness of 1 phr organoclay in promoting the peel functionality is reduced by increasing the PB-1 content. This can be attributed to the higher interfacial area and the less interface coverage by clay particles at the interface. The morphology analysis revealed that PB-1 form nanofibrillar structures in both the blends and nanocomposite sealants. However, the size of the PB-1 nanofibrils are significantly smaller in the nanocomposite sealants (about 60 nm) than those in the blends (above 100 nm). Despite the morphological changes in the LDPE/PB-1/organoclay sealants by increasing the PB-1 content, a consistent peel performance is observed for all the nanocomposites containing 5 to 20 wt% of the PB-1. The consistent peel performance is attributed to the absence of unstable form II crystals and direct formation of stable forms I and III of PB-1 as revealed by WAXD and FTIR experiments right after the sealing process. Although the underlying mechanism of direct formation of stable form I and III are not clear yet, but it can be associated to the confined

crystallization of PB-1 in nanofibrils within the PE matrix. The higher crystallization temperature of LDPE at 96 °C compared to that of PB-1 at 75 °C results in earlier solidification of LDPE imposing external stress on the dispersed PB-1 phase. It is worth noting that, the crystallization of PB-1 is nucleating control and starts from defect points such as contaminations, edge of the imperfect crystals and interface of PB-1 with a second component. The crystallization of PB-1 most likely starts from the LDPE/PB-1 interfaces. In such a case, the presence of nanoclay particles at the interface can significantly affect the kinetic of the PB-1 crystallization. Thus, the presence of organoclay at the interface of the PB-1 phase can hinder the PB-1 chain movement and disrupt the form II formation.

These results are promising for the development of versatile peelable sealants with a broad peel performance. Two of the most important challenges of peelable sealants are addressed in this dissertation. First, the very narrow heat seal peelable window of conventional peelable sealants is significantly extended to ranges over 100 °C. Second, the inconsistent peel force of the most common peelable sealant which is composed of LDPE/PB-1 is converted to a consistent peel behavior over the all seal temperatures. The approaches developed in this study can be used to generate economically viable and functional peelable sealants by significantly reducing the content of the second component to values below 5 wt%.

CHAPTER 9 CONCLUSION AND RECOMMENDATIONS

9.1 Conclusion

In this dissertation, significant potential of the clay nanoparticles to achieve peelable sealants with versatile peel performance from the neat LDPE and LDPE based blends which have poor peelability was demonstrated. It was shown that the dispersion and distribution of the clay nanoparticles are the key factors in controlling the peel performance of the nanocomposite sealants. Examining various types of unmodified and surface modified nanoclays indicated that incorporation of the unmodified nanoclays in the neat LDPE sealant results in microcomposite films, which exhibits lock seal performance similar to the neat LDPE. While, surface modified organoclays results in nanocomposite with notably improved peel performance. These results confirm the advantage of the nanocomposite structure in respect to the microcomposite structure in enhancing the peel performance. Among various surface modified organoclays, the organoclay with higher content of the surface modifier exhibited better dispersion and distribution, thus wider ΔT_p of about 15 °C. Further enhancement of the organoclay dispersion and distribution in the seal area upon the incorporation of the PE-gr-MA in the sealant formulation results in significant enhancement of the ΔT_p to 45 °C. Ultimately, ultrawide ΔT_p of over 100 °C is achieved as a result of the partial exfoliation of the clay particles in the seal area. This significant enhancement of the peelability is attributed to the increase in the mechanical performance and yield strength of the sealant due to the better dispersion and distribution of the nanoclays in the seal area, on one hand, and decrease in the interparticle distance in the seal layer that facilitate the crack bridge upon peeling, on the other hand. Thus, the cracks are initiated upon peeling prior to the yielding of the sealant due to the high yield strength of the nanocomposite sealant. The initiated cracks then propagate through the sealant upon further loading of the sealant because of the well organoclay distribution and reduced interparticle distance.

In the second part of the project, the effect of nanoclay localization on the peel performance of polyethylene-based blends was examined. Thermodynamic predictions, WAXD patterns, TEM and SEM images, rheological and mechanical tests suggest the localization of organoclay particles at the interface of the LDPE/EMA blend whereas its localization inside the dispersed EMA-GMA

phase in the LDPE/EMA-GMA blend. The lock seal performance of the LDPE/EMA blend sealant was converted to a peelable behavior with a broad ΔT_p of over 30 °C upon incorporation of the organoclay at the interface of the LDPE/EMA, while the LDPE/EMA-GMA/organoclay sealant in which organoclays are located within the EMA-GMA phase exhibit lock seal performance similar to the LDPE/EMA-GMA blend sealant. The lock seal performance of the LDPE/EMA and LDPE/EMA-GMA blends is attributed to their low yield strength which is probably lower that the adhesion strength between PE and EMA as well as the adhesion between PE and EMA-GMA. Therefore, the sealants yield upon peeling prior to be peeled. Localization of the clay particles at the interface of the LDPE/EMA blend results in more LDPE/organoclay interactions and a reduced EMA dispersed phase size, which significantly increases the yield strength. In this case, significant enhancement of the yield strength in one hand and the reduced interparticle distance due to decrease in the dispersed phase size on the other hand results in peelability of the sealant. These mechanisms are missing in LDPE/EMA-GMA/organoclay in which organoclays are encapsulated by EMA-GMA phase. In this case there is no interaction between LDPE matrix and organoclays, thus the mechanical properties as well as the yield strength of the sealant are similar to those of the neat LDPE/EMA-GMA sealant. Furthermore, the localization of the organoclay within the EMA-GMA phase suppresses the break-up that increases the interparticle distance and works against peelability.

The results from the third part of the thesis indicate that LDPE/PB-1 containing 5 wt% of the PB-1 and LDPE/organoclay containing 1 phr organoclay demonstrate lock seal performance similar to the neat LDPE. However, LDPE/PB-1/organoclay containing 5 wt% of the PB-1 and 1 phr organoclay represents a peelable seal behavior over a very wide ΔT_p of about 100 °C. This significant enhancement of the peelability is attributed to the organoclay localization at the interface of the LDPE/PB-1 system as revealed by the WAXD patterns and TEM results. The effectiveness of 1 phr organoclay in enhancing the peelability is reduced by increasing the PB-1 content. This might be due to the reduced interfacial coverage of the LDPE/PB-1 interface by 1 phr organoclay by increasing the PB-1 content. On the other hand, the size of the PB-1 nanofibrils is increased by increase in the PB-1 content that results in better dispersion and distribution of the clay particles at the LDPE/PB-1 interface.

In addition to enhancing the peelability, the organoclay incorporation to the LDPE/PB-1 blend significantly affects the aging of the LDPE/PB-1 sealants. The results show that the LDPE/PB-1 sealants containing 5 to 20 wt% of the PB-1 age after the heat sealing process. The reduction of the peel force due to the aging of the PB-1 crystals is increased by increasing the PB-1 content in the blends. In contrast, the peel performance of the nanocomposites containing 5-20 wt% of the PB-1 and 1 phr organoclay is consistent after the heat sealing. The SEM images indicate that PB-1 forms nanofibrils with an average thickness of 100, 190 and 200 nm in the LDPE/PB-1 sealants containing 5, 10 and 20 wt% of PB-1, respectively. Incorporation of the 1 phr organoclay to the LDPE/PB-1 blend significantly reduced the size of the PB-1 fibrils from 100 to 60 nm for the blend containing 5 wt% PB-1. Incorporation of 1 phr organoclay to the LDPE/PB-1 moderately reduced the PB-1 nanofibrillar thickness from 190 to 170 nm and from 200 to 190 nm for the blends containing 10 and 20 w% PB-1, respectively. The FTIR and WAXD patterns indicate the presence of the form I or I′ right after the heat sealing of the LDPE/PB-1 blends and nanocomposite sealants. This might be attributed to the residual form I crystals in the seal area due to the crystal segregation in a quite short sealing time (1 second) rather than the complete melting of the crystals. Also, due to the melt memory effect, if crystal segregation happened, crystal growth and recovery of the segregated crystals may result in the formation of form I′, which has similar crystalline structure to that of the form I. In addition to the forms I and I′, form II is also formed right after the heat sealing of the LDPE/PB-1 sealants due to the partial melting of the PB-1 phase. Nevertheless, no trace of the form II is observed after the heat sealing of the LDPE/PB-1/organoclay sealants. This is attributed to the confined crystallization of the PB-1 nanofibrils in the presence of the organoclays which hinders the polymer chain mobility and disrupts the kinetics of the form II formation. Since the crystallization of the PB-1 is nucleating controlled, the formation of the crystals most likely starts from the interface of the PB-1 with PE as well as the interface of the PB-1 and organoclay. In this case, presence of the organoclay at the interface alters the kinetics of the form II formation and suppresses its priority in respect to the form I′ formation. Furthermore, due to the mixing sequence in which nanoclays were first added to the PB-1 phase and then diluted by LDPE, a portion of the clay particles are possibly within the PB-1 phase that further restrict the form II formation. Moreover, the earlier solidification of the LDPE matrix which has a higher

crystallization temperature (95 °C) compared to that of PB-1 (75 °C) further imposes an external stress and confinement to influence the crystallization of the PB-1 phase.

9.2 Recommendations

This work shows the effect of seal microstructure on the peel performance of the nanocomposite sealants in multilayer and monolayer structures. However, the effect of the microstructure on the peel performance might be either less or more profound in different multilayer structures composed of different support layers in terms of the yield strength. It may be interesting to investigate how the effectiveness of organoclay dispersion and distribution in enhancing the peelability is affected by different support layers with various yield strength. Furthermore, the organoclay incorporation to the support layer is also expected to enhance the yield strength compared to the adhesion forces within the sealant composed of polyolefin blends, thus results in enhanced peelability.

In PE/PB-1 blend and nanocomposite sealants, the effect of the various parameters such as process conditions and different concentrations of the organoclay may affect the morphology of the PB-1 nanofibrils, and thus the peelability and the aging of the PB-1. It was shown that the confinement significantly influences the crystallization and aging of the PB-1 phase. However, it is not still completely clear how this confinement influences the direct formation of crystal form I in nanofibrillar PB-1.

BIBLIOGRAPHY

Acierno, D., Di Maio, L., & Ammirati, C. C. (2000). Film casting of polyethylene terephthalate: Experiments and model comparisons. *Polymer Engineering & Science*, *40*, 108–117.

Aithani, D., & Briggs, D. (2009). Peelable Films Containing Nano Particles. Retrieved from https://www.google.com/patents/US20100092793

Aithani, D., Lockhart, H., Auras, R., & Tanprasert, K. (2006). Predicting the Strongest Peelable Seal for "Easy-Open" Packaging Applications. *Journal of Plastic Film and Sheeting*, *22*, 247–263.

Alexandre, M., & Dubois, P. (2000). Polymer-layered silicate nanocomposites: Preparation, properties and uses of a new class of materials. *Materials Science and Engineering R: Reports*, *28*, 1–63.

Anastasiadis, S. H., Chen, J. K., Koberstein, J. T., Sohn, J. E., & Emerson, J. A. (1986). The determination of polymer interfacial tension by drop image processing: Comparison of theory and experiment for the pair, poly(dimethyl siloxane)/polybutndiene. *Polymer Engineering & Science*, *26*, 1410–1418.

Arora, A., & Padua, G. W. (2010, January). Review: Nanocomposites in food packaging. *Journal of Food Science*. Blackwell Publishing Inc.

Azeredo, H. M. C. de. (2009). Nanocomposites for food packaging applications. *Food Research International*.

Azzurri, F., Flores, A., Alfonso, G. C., & Baltá Calleja, F. J. (2002). Polymorphism of Isotactic Poly(1-butene) as Revealed by Microindentation Hardness. 1. Kinetics of the Transformation. *Macromolecules*, *35*, 9069–9073.

Bai, S. L., & Wang, M. (2003). Plastic damage mechanisms of polypropylene/polyamide 6/polyethelene octene elastomer blends under cyclic tension. *Polymer*, *44*, 6537–6547.

Baniassadi, M., Laachachi, A., Hassouna, F., Addiego, F., Muller, R., Garmestani, H., … Ruch, D. (2011). Mechanical and thermal behavior of nanoclay based polymer nanocomposites using statistical homogenization approach. *Composites Science and Technology*, *71*, 1930–1935.

Barborik, T., & Zatloukal, M. (2015). Effect of viscoelastic stress state at die exit on extrusion film

casting process: Theoretical study. In *AIP Conference Proceedings* (Vol. 1662, p. 30013).

Bourque, R. A., Chung, D. Y.-D., & Diane, R. M. E. (2003). *US7055683 B2*. Retrieved from https://www.google.com/patents/US7055683

Bourry, D., & Favis, B. D. (1998a). Cocontinuity and phase inversion in HDPE/PS blends: Influence of interfacial modification and elasticity. *Journal of Polymer Science Part B-Polymer Physics*, *36*, 1889–1899.

Bourry, D., & Favis, B. D. (1998b). Morphology development in a polyethylene/polystyrene binary blend during twin-screw extrusion. *Polymer*, *39*, 1851–1856.

Chen, H., Ginzburg, V. V., Yang, J., Yang, Y., Liu, W., Huang, Y., … Chen, B. (2015). Thermal conductivity of polymer-based composites: Fundamentals and applications. *Progress in Polymer Science*, pp. 41–85.

Chikhalikar, K., Banik, S., Azad, L. B., Jadhav, K., Mahajan, S., Ahmad, Z., … Lele, A. (2015). Extrusion film casting of long chain branched polypropylene. *Polymer Engineering and Science*, *55*, 1977–1987.

Clarke, J., Clarke, B., Freakley, P. K., & Sutherland, I. (2001). Compatibilising effect of carbon black on morphology of NR–NBR blends. *Plastics, Rubber and Composites*, *30*, 39–44.

Coles, R., McDowell, D., & Kirwan, M. (Eds.). (2003). Plastics in Food Packaging. In *Food Packaging Technology* (p. 174).

De Rosa, C., Auriemma, F., Villani, M., Ruiz De Ballesteros, O., Di Girolamo, R., Tarallo, O., & Malafronte, A. (2014). Mechanical properties and stress-induced phase transformations of metallocene isotactic poly(1-butene): The influence of stereodefects. *Macromolecules*, *47*, 1053–1064.

Dee, G. T., & Sauer, B. B. (1992). The molecular weight and temperature dependence of polymer surface tension: Comparison of experiment with interface gradient theory. *Journal of Colloid And Interface Science*, *152*, 85–103.

Dell'Erba, R., Groeninckx, G., Maglio, G., Malinconico, M., & Migliozzi, A. (2001). Immiscible polymer blends of semicrystalline biocompatible components: Thermal properties and phase

morphology analysis of PLLA/PCL blends. *Polymer*, *42*, 7831–7840.

Elias, L., Fenouillot, F., Majesté, J. C., Alcouffe, P., & Cassagnau, P. (2008). Immiscible polymer blends stabilized with nano-silica particles: Rheology and effective interfacial tension. *Polymer*, *49*, 4378–4385.

Elias, L., Fenouillot, F., Majesté, J. C., Martin, G., & Cassagnau, P. (2008). Migration of nanosilica particles in polymer blends. *Journal of Polymer Science, Part B: Polymer Physics*, *46*, 1976–1983.

Ernesto Mendoza-Navarro, L., Diaz-Diaz, A., Castañeda-Balderas, R., Hunkeler, S., & Noret, R. (2013). Interfacial failure in adhesive joints: Experiments and predictions. *International Journal of Adhesion and Adhesives*, *44*, 36–47.

Everaert, V., Aerts, L., & Groeninckx, G. (1999). Phase morphology development in immiscible PP/(PS/PPE) blends influence of the melt-viscosity ratio and blend composition. *Polymer*, *40*, 6627–6644.

Everaert, V., Groeninckx, G., Pionteck, J., Favis, B. D., Aerts, L., Moldenaers, P., & Mewis, J. (2000). Miscible PS/PPE compounds: an alternative for blend phase morphology studies? Influence of the PPE content on the surface tension of PS/PPE and on the interfacial tension in PP/(PS/PPE) and POM/(PS/PPE) blends. *Polymer*, *41*, 1011–1025.

Farley, J. M., & Meka, P. (1994). Heat sealing of semicrystalline polymer films. III. Effect of corona discharge treatment of LLDPE. *Journal of Applied Polymer Science*, *51*, 121–131.

Favis, B. D. (1990). The effect of processing parameters on the morphology of an immiscible binary blend. *Journal of Applied Polymer Science*, *39*, 285–300.

Favis, B. D. (2000). Factors influencing the morphology of immiscible polymer blends in melt processing. In D. R. Paul & C. B. Bucknall (Eds.), *Polymer Blends Volume 1: Formulation* (pp. 501–538). New York: John Wiley & Sons.

Favis, B. D., & Chalifoux, J. P. (1987). The effect of viscosity ratio on the morphology of polypropylene/polycarbonate blends during processing. *Polymer Engineering & Science*, *27*, 1591–1600.

Fenouillot, F., Cassagnau, P., & Majesté, J.-C. (2009a). Uneven distribution of nanoparticles in immiscible fluids: Morphology development in polymer blends. *Polymer*, *50*, 1333–1350.

Fenouillot, F., Cassagnau, P., & Majesté, J.-C. (2009b). Uneven distribution of nanoparticles in immiscible fluids: Morphology development in polymer blends. *Polymer*, *50*, 1333–1350.

Fenouillot, F., Cassagnau, P., & Majesté, J. C. (2009c). Uneven distribution of nanoparticles in immiscible fluids: Morphology development in polymer blends. *Polymer*, *50*, 1333–1350.

Fereydoon, M., Tabatabaei, S. H., & Ajji, A. (2014). Rheological, crystal structure, barrier, and mechanical properties of PA6 and MXD6 nanocomposite films. *Polymer Engineering & Science*, *54*, 2617–2631.

Fortelný, I., Černá, Z., Binko, J., & Kovář, J. (1993a). Anomalous dependence of the size of droplets of disperse phase on intensity of mixing. *Journal of Applied Polymer Science*, *48*, 1731–1737.

Fortelný, I., Černá, Z., Binko, J., & Kovář, J. (1993b). Anomalous dependence of the size of droplets of disperse phase on intensity of mixing. *Journal of Applied Polymer Science*, *48*, 1731–1737.

Fu, J., & Naguib, H. E. (2006). Effect of Nanoclay on the Mechanical Properties of PMMA/Clay Nanocomposite Foams. *Journal of Cellular Plastics*, *42*, 325–342.

Fukushima, K., Tabuani, D., Arena, M., Gennari, M., & Camino, G. (2013). Effect of clay type and loading on thermal, mechanical properties and biodegradation of poly(lactic acid) nanocomposites. *Reactive and Functional Polymers*, *73*, 540–549.

Gabriele, M., Pasquino, R., & Grizzuti, N. (2011). Effects of viscosity-controlled interfacial mobility on the coalescence of immiscible polymer blends. *Macromolecular Materials and Engineering*, *296*, 263–269.

García-Morales, M., Partal, P., Navarro, F. J., & Gallegos, C. (2006). Effect of waste polymer addition on the rheology of modified bitumen. *Fuel*, *85*, 936–943.

Girifalco, L. A., & Good, R. J. (1957). A Theory for the Estimation of Surface and Interfacial Energies. I. Derivation and Application to Interfacial Tension. *The Journal of Physical*

Chemistry, *61*, 904–909.

Gómez, M., Martín-Consuegra, D., & Molina, A. (2015). The importance of packaging in purchase and usage behaviour. *International Journal of Consumer Studies*, *39*, 203–211.

Grace, H. P. (1982). Dispersion phenomena in high viscosity immiscible fluid systems and application of static mixers as dispersion devices in such systems. *Chemical Engineering Communications*, *14*, 225–277.

Guggenheim, E. A. (1945). The Principle of Corresponding States. *The Journal of Chemical Physics*, *13*, 253–261.

Hajir Bahrami, S., & Mirzaie, Z. (2011). Polypropylene/Modified Nanoclay Composite-Processing and Dyeability Properties. *World Applied Sciences Journal*, *13*, 493–501.

Han, J. H. (2005). Innovations in Food Packaging. In J. H. Han (Ed.), *Innovations in Food Packaging* (2nd ed., p. 517). San Diego, CA: Academic Press.

Harkins, W. D. (1941). A General Thermodynamic Theory of the Spreading of Liquids to Form Duplex Films and of Liquids or Solids to Form Monolayers. *The Journal of Chemical Physics*, *9*, 552.

Heino, M. T., Hietaoja, P. T., Vainio, T. P., & Seppälä, J. V. (1994). Effect of viscosity ratio and processing conditions on the morphology of blends of liquid crystalline polymer and polypropylene. *Journal of Applied Polymer Science*, *51*, 259–270.

Heshmati, V., Zolali, A. M., & Favis, B. D. (2017). Morphology development in poly (lactic acid)/polyamide11 biobased blends: Chain mobility and interfacial interactions. *Polymer*, *120*, 197–208.

Holland, V. F., & Miller, R. L. (1964). Isotactic polybutene-1 single crystals: Morphology. *Journal of Applied Physics*, *35*, 3241–3248.

Hwo, C. C. (1987). Polybutylene Blends as Easy Open Seal Coats for Flexible Packaging and Lidding. *Journal of Plastic Film & Sheeting*, *3*, 245–260.

Idiyatullina, G. K., Vol'fson, S. I., Sabirov, R. K., & Yarullin, R. S. (2012). Effect of the montmorillonite cloisite 15A on the structure and properties of poly(1-butene). *Polymer*

Science Series A, *54*, 493–498.

Iwasaki, T., Takarada, W., & Kikutani, T. (2016). Influence of processing conditions on heat sealing behavior and resultant heat seal strength for peelable heat sealing of multilayered polyethylene films. *Journal of Polymer Engineering*, *36*, 909–916.

Jalbert, C., Jeffrey, T., Corporation, G. C., Gallagher, P., Krukonis, V., & Corporation, P. (1993). Molecular Weight Dependence and End-Group Effects on the Surface Tension of Poly(dimethylsiloxane). *Macromolecules*, *26*, 3069–3074.

Jlassi, K., Chandran, S., Poothanari, M. A., Benna-Zayani, M., Thomas, S., & Chehimi, M. M. (2016). Clay/Polyaniline Hybrid through Diazonium Chemistry: Conductive Nanofiller with Unusual Effects on Interfacial Properties of Epoxy Nanocomposites. *Langmuir*, *32*, 3514–3524.

Jordens, K., Wilkes, G. L., Janzen, J., Rohlfing, D. C., & Welch, M. B. (2000). The influence of molecular weight and thermal history on the thermal, rheological, and mechanical properties of metallocene-catalyzed linear polyethylenes. *Polymer*, *41*, 7175–7192.

Julie W. Gibbons, Alveda J. Williams, Rajen M. Patel, Jeffrey J. Wooster, Enrique Torres, Miguel A. Prieto Goubert, O. B. (2006). Polyolefin based peelable seals. Retrieved from https://www.google.com/patents/US7863383

Kalay, G., & Kalay, C. R. (2002). Interlocking shish-kebab morphology in polybutene-1. *Journal of Polymer Science Part B: Polymer Physics*, *40*, 1828–1834.

Kango, S., Kalia, S., Celli, A., Njuguna, J., Habibi, Y., & Kumar, R. (2013). Surface modification of inorganic nanoparticles for development of organic–inorganic nanocomposites—A review. *Progress in Polymer Science*, *38*, 1232–1261.

Kaszonyiova, M., Rybnikar, F., Lapcik, L., & Manas, D. (2012). Effects of beta irradiation, copolymers, and blends on the transformation rate of polybutene-1. *Journal of Macromolecular Science, Part B: Physics*, *51*, 926–945.

Kaszonyiova M, Rybnikar F, G. P. (2005). Polymorphism of Isotactic Poly(Butene-1). *Journal of Macromolecular Science, Part B: Physics*, *44*, 377–396.

Kiliaris, P., & Papaspyrides, C. D. (2010). Polymer/layered silicate (clay) nanocomposites: An overview of flame retardancy. *Progress in Polymer Science*, *35*, 902–958.

Kim, J.-K., Hu, C., Woo, R. S. C., & Sham, M.-L. (2005). Moisture barrier characteristics of organoclay–epoxy nanocomposites. *Composites Science and Technology*, *65*, 805–813.

Kim, S. W., & Cha, S. H. (2014). Thermal, mechanical, and gas barrier properties of ethylene-vinyl alcohol copolymer-based nanocomposites for food packaging films: Effects of nanoclay loading. *Journal of Applied Polymer Science*, *131*, 40289.

Kinigakis, P., Pokusa, K., Albaum, G., Jones, A., & Frederickson, E. (2016, April 12). *US9309027 B2*. Google Patents. Retrieved from https://www.google.com/patents/US9309027

Krishnamoorti, R., Vaia, R. A., & Giannelis, E. P. (1996). Structure and dynamics of of polymer-layered silicate nanocomposites. *Chem Mater*, *8*, 1728–1734.

Krump, H., Luyt, A. S., & Hudec, I. (2006). Effect of different modified clays on the thermal and physical properties of polypropylene-montmorillonite nanocomposites. *Materials Letters*, *60*, 2877–2880.

Kubo, S., & Kadla, J. F. (2004). Poly(ethylene oxide)/organosolv lignin blends: Relationship between thermal properties, chemical structure, and blend behavior. *Macromolecules*, *37*, 6904–6911.

Lamnawar, K., Vion-Loisel, F., & Maazouz, A. (2010). Rheological, morphological, and heat seal properties of linear low density polyethylene and cyclo olefine copolymer (LLDPE/COC) blends. *Journal of Applied Polymer Science*, *116*, 2015–2022.

LeBaron, P. (1999). Polymer-layered silicate nanocomposites: an overview. *Applied Clay Science*, *15*, 11–29.

Lee, I. H., & Hausmann, K. (2005, December 1). *US 20050266257 A1*. Google Patents. Retrieved from https://www.google.com/patents/US20050266257

Lee, J., & Han, C. (2000). Evolution of polymer blend morphology during compounding in a twin-screw extruder. *Polymer*, *41*, 1799–1815.

Levitt, L., Macosko, C. W., & Pearson, S. D. (1996). Influence of Normal Stress Difference on

Polymer Drop Deformation. *Polymer Engineering & Science*, *36*, 1647–1655.

Liebmann, A., Schreib, I., E. Schlözer, R., & Majschak, J.-P. (2012). Practical Case Studies: Easy Opening for Consumer-Friendly, Peelable Packaging. *Journal of Adhesion Science and Technology*, *26*, 2437–2448.

Liu, Y., Cui, K., Tian, N., Zhou, W., Meng, L., Li, L., … Wang, X. (2012). Stretch-Induced Crystal–Crystal Transition of Polybutene-1: An in Situ Synchrotron Radiation Wide-Angle X-ray Scattering Study. *Macromolecules*, *45*, 2764–2772.

Lyngaae-Jørgensen, J. (1996). Experimental methods for In Situ studies of morphology development during flow: The case of instability of thin films studied by light scattering. *Journal of Macromolecular Science, Part B*, *35*, 357–373.

Ma, H. L., Zhang, H. Bin, Li, X., Zhi, X., Liao, Y. F., & Yu, Z. Z. (2014). The effect of surface chemistry of graphene on cellular structures and electrical properties of polycarbonate nanocomposite foams. *Industrial and Engineering Chemistry Research*, *53*, 4697–4703.

Macosko, C. W., Guégan, P., Khandpur, A. K., Nakayama, A., Marechal, P., & Inoue, T. (1996). Compatibilizers for Melt Blending: Premade Block Copolymers. *Macromolecules*, *29*, 5590–5598.

Majumdar, A., & Kale, D. D. (2001). Properties of films made from ternary blends of metallocene and conventional polyolefins. *Journal of Applied Polymer Science*, *81*, 53–57.

Manias, E., Zhang, J., Huh, J. Y., Manokruang, K., Songtipya, P., & Jimenez-Gasco, M. M. (2009). Polyethylene nanocomposite heat-sealants with a versatile peelable character. *Macromolecular Rapid Communications*, *30*, 17–23.

Martínez-García, A., Sánchez-Reche, A., Gisbert-Soler, S., Landete-Ruiz, M. D., Torregrosa-Maciá, R., & Martín-Martínez, J. M. (2008). Durability of corona discharge and low-pressure air plasma-treated ethylene–vinyl acetate copolymers (EVAs). *International Journal of Adhesion and Adhesives*, *28*, 38–46.

Mazzola, N., Cáceres, C. A., França, M. P., & Canevarolo, S. V. (2012). Correlation between thermal behavior of a sealant and heat sealing of polyolefin films. *Polymer Testing*, *31*, 870–

875.

McNally, T., McShane, P., Nally, G. M., Murphy, W. R., Cook, M., & Miller, A. (2002). Rheology, phase morphology, mechanical, impact and thermal properties of polypropylene/metallocene catalysed ethylene 1-octene copolymer blends. *Polymer*, *43*, 3785–3793.

Meincke, O., Kaempfer, D., Weickmann, H., Friedrich, C., Vathauer, M., & Warth, H. (2004). Mechanical properties and electrical conductivity of carbon-nanotube filled polyamide-6 and its blends with acrylonitrile/butadiene/styrene. *Polymer*, *45*, 739–748.

Meka, P., & Stehling, F. C. (1994). Heat sealing of semicrystalline polymer films. I. Calculation and measurement of interfacial temperatures: Effect of process variables on seal properties. *Journal of Applied Polymer Science*, *51*, 89–103.

Minale, M., Moldenaers, P., & Mewis, J. (1997). Effect of Shear History on the Morphology of Immiscible Polymer Blends. *Macromolecules*, *30*, 5470–5475.

Modesti, M., Lorenzetti, A., Bon, D., & Besco, S. (2006). Thermal behaviour of compatibilised polypropylene nanocomposite: Effect of processing conditions. *Polymer Degradation and Stability*, *91*, 672–680.

Mohammdi, S. R., Ajji, A., & Tabatabaei, S. H. (2015). Peel/seal properties of poly(ethylene methyl acrylate)/polybutene-1 blend films. In *AIP Conference Proceedings* (Vol. 1664, p. 80005).

Molinaro, S., Cruz Romero, M., Boaro, M., Sensidoni, A., Lagazio, C., Morris, M., & Kerry, J. (2013). Effect of nanoclay-type and PLA optical purity on the characteristics of PLA-based nanocomposite films. *Journal of Food Engineering*, *117*, 113–123.

Moreira, A. C. F., Dartora, P. C., & Paulo dos Santos, F. (2017). Polyethylenes in blown films: Effect of molecular structure on sealability and crystallization kinetics. *Polymer Engineering and Science*, *57*, 52–59.

Mueller, C., Capaccio, G., Hiltner, A., & Baer, E. (1998). Heat sealing of LLDPE: relationships to melting and interdiffusion. *Journal of Applied Polymer Science*, *70*, 2021–2030.

Munhoz, T., Fredholm, Y., Rivory, P., Balvay, S., Hartmann, D., da Silva, P., & Chenal, J. M.

(2017). Effect of nanoclay addition on physical, chemical, optical and biological properties of experimental dental resin composites. *Dental Materials*, *33*, 271–279.

Najarzadeh, Z. (2014). *Control and optimization of sealing layer in films*. PhD thesis, École Polytechnique de Montréal.

Nakafuku, C., & Miyaki, T. (1983). Effect of pressure on the melting and crystallization behaviour of isotactic polybutene-1. *Polymer*, *24*, 141–148.

Nase, M., Androsch, R., Langer, B., Baumann, H. J., & Grellmann, W. (2008). Effect of polymorphism of isotactic polybutene-1 on peel behavior of polyethylene/polybutene-1 peel systems. *Journal of Applied Polymer Science*, *107*, 3111–3118.

Nase, M., Großmann, L., Rennert, M., Langer, B., & Grellmann, W. (2014a). Adhesive properties of heat-sealed EVAc/PE films in dependence on recipe, processing, and sealing parameters. *Journal of Adhesion Science and Technology*, *28*, 1149–1166.

Nase, M., Großmann, L., Rennert, M., Langer, B., & Grellmann, W. (2014b). Adhesive properties of heat-sealed EVAc/PE films in dependence on recipe, processing, and sealing parameters. *Journal of Adhesion Science and Technology*, *28*, 1149–1166.

Nase, M., Langer, B., Baumann, H. J., Grellmann, W., Geißler, G., & Kaliske, M. (2009). Evaluation and simulation of the peel behavior of polyethylene/polybutene-1 peel systems. *Journal of Applied Polymer Science*, *111*, 363–370.

Nase, M., Langer, B., & Grellmann, W. (2008). Fracture mechanics on polyethylene/polybutene-1 peel films. *Polymer Testing*, *27*, 1017–1025.

Nase, M., Langer, B., & Grellmann, W. (2009). Influence of Processing Conditions On the Peel Behavior of Polyethylene/ Polybutene-1 Peel Systems. *Journal of Plastic Film and Sheeting*, *25*, 61–80.

Nase, M., Rennert, M., Henning, S., Zankel, A., Naumenko, K., & Grellmann, W. (2017). Fracture mechanics characterisation of peelfilms. In *Springer Series in Materials Science* (Vol. 247, pp. 271–281). Springer, Cham.

Nase, M., Zankel, A., Langer, B., Baumann, H. J., Grellmann, W., & Poelt, P. (2008). Investigation

of the peel behavior of polyethylene/polybutene-1 peel films using in situ peel tests with environmental scanning electron microscopy. *Polymer*, *49*, 5458–5466.

Nofar, M., Heuzey, M. C., Carreau, P. J., & Kamal, M. R. (2016). Effects of nanoclay and its localization on the morphology stabilization of PLA/PBAT blends under shear flow. *Polymer*, *98*, 353–364.

Pavlidou, S., & Papaspyrides, C. D. (2008). A review on polymer–layered silicate nanocomposites. *Progress in Polymer Science*, *33*, 1119–1198.

Planes, E., Marouani, S., & Flandin, L. (2011). Optimizing the heat sealing parameters of multilayers polymeric films. *Journal of Materials Science*, *46*, 5948–5958.

Pol, H., Banik, S., Azad, L. B., Thete, S., Doshi, P., & Lele, A. (2014). Nonisothermal analysis of extrusion film casting process using molecular constitutive equations. *Rheologica Acta*, *53*, 85–101.

Potente, H., Bastian, M., Gehring, A., Stephan, M., & Pötschke, P. (2000). Experimental investigation of the morphology development of polyblends in corotating twin-screw extruders. *Journal of Applied Polymer Science*, *76*, 708–721.

Pötschke, P., & Paul, D. R. (2003). Formation of Co-continuous Structures in Melt-Mixed Immiscible Polymer Blends. *Journal of Macromolecular Science, Part C: Polymer Reviews*, *43*, 87–141.

Qiao, Y., & Men, Y. (2017). Intercrystalline Links Determined Kinetics of Form II to i Polymorphic Transition in Polybutene-1. *Macromolecules*, *50*, 5490–5497.

Qiao, Y., Wang, Q., & Men, Y. (2016). Kinetics of Nucleation and Growth of Form II to I Polymorphic Transition in Polybutene-1 as Revealed by Stepwise Annealing. *Macromolecules*, *49*, 5126–5136.

Ravati, S., Beaulieu, C., Zolali, A. M., & Favis, B. D. (2014). High performance materials based on a self-assembled multiple-percolated ternary blend. *AIChE Journal*, *60*, 3005–3012.

Ravati, S., & Favis, B. D. (2010). Morphological states for a ternary polymer blend demonstrating complete wetting. *Polymer*, *51*, 4547–4561.

Rhim, J.-W., Hong, S.-I., & Ha, C.-S. (2009). Tensile, water vapor barrier and antimicrobial properties of PLA/nanoclay composite films. *LWT - Food Science and Technology*, *42*, 612–617.

Rivett, J. W., Tanny, S. R., & Hahm, D. M. (2003, October 7). *US6630237 B2*. Google Patents. Retrieved from https://www.google.com/patents/US6630237

Rizvi, A., & Park, C. B. (2014). Dispersed polypropylene fibrils improve the foaming ability of a polyethylene matrix. *Polymer (United Kingdom)*, *55*, 4199–4205.

Rizvi, A., Park, C. B., & Favis, B. D. (2015). Tuning viscoelastic and crystallization properties of polypropylene containing in-situ generated high aspect ratio polyethylene terephthalate fibrils. *Polymer*, *68*, 83–91.

Robertson, G. L. (2013). *Food Packaging: Principles and Practice* (Third). CRC press.

Rokade, D., Azad, L. B., Poddar, S., Mishra, S., Pol, H. V., & Shukla, R. (2017). Controlling Necking in Extrusion Film Casting Using Polymer Nanocomposites. *Journal of Macromolecular Science, Part B: Physics*, *56*, 213–233.

Samon, J. M., Schultz, J. M., Hsiao, B. S., Wu, J., & Khot, S. (2000). Structure development during melt spinning and subsequent annealing of polybutene-1 fibers. *Journal of Polymer Science, Part B: Polymer Physics*, *38*, 1872–1882.

Santos, J. M., Ribeiro, M. R., Portela, M. F., & Bordado, J. M. (2001). Improved adhesion of polyethylene by copolymerisation of ethylene with polar monomers. *Chemical Engineering Science*, *56*, 4191–4196.

Sau, M., & Jana, S. C. (2004). A study on the effects of chaotic mixer design and operating conditions on morphology development in immiscible polymer systems. *Polymer Engineering and Science*, *44*, 407–422.

Selke, S., & Culter, J. (2016). *Plastics Packaging (Properties, Processing, Applications, and Regulations)*. Hanser Gardner publications.

Shah, K. J., Shukla, A. D., Shah, D. O., & Imae, T. (2016). Effect of organic modifiers on dispersion of organoclay in polymer nanocomposites to improve mechanical properties. *Polymer*, *97*,

525–532.

Sharma, S. K., & Nayak, S. K. (2009). Surface modified clay/polypropylene (PP) nanocomposites: Effect on physico-mechanical, thermal and morphological properties. *Polymer Degradation and Stability*, *94*, 132–138.

Shieh, Y. T., Lee, M. S., & Chen, S. A. (2001). Crystallization behavior, crystal transformation, and morphology of polypropylene/polybutene-1 blends. *Polymer*, *42*, 4439–4448.

Sinha Ray, S., & Okamoto, M. (2003a). Polymer/layered silicate nanocomposites: a review from preparation to processing. *Progress in Polymer Science*, *28*, 1539–1641.

Sinha Ray, S., & Okamoto, M. (2003b). Polymer/layered silicate nanocomposites: A review from preparation to processing. *Progress in Polymer Science*.

Sinha Ray, S., Pouliot, S., Bousmina, M., & Utracki, L. A. (2004). Role of organically modified layered silicate as an active interfacial modifier in immiscible polystyrene/polypropylene blends. *Polymer*, *45*, 8403–8413.

Stolte, I., & Androsch, R. (2013). Kinetics of the melt - Form II phase transition in isotactic random butene-1/ethylene copolymers. *Polymer*, *54*, 7033–7040.

Stolte, I., Androsch, R., & Di Lorenzo, M. L. (2014). Spherulite growth rate and fold surface free energy of the form II mesophase in isotactic polybutene-1 and random butene-1/ethylene copolymers. *Colloid and Polymer Science*, *292*, 1479–1485.

Sundararaj, U., & Macosko, C. W. (1995). Drop Breakup and Coalescence in Polymer Blends: The Effects of Concentration and Compatibilization. *Macromolecules*, *28*, 2647–2657.

Taguet, A., Cassagnau, P., & Lopez-Cuesta, J.-M. (2014). Structuration, selective dispersion and compatibilizing effect of (nano)fillers in polymer blends. *Progress in Polymer Science*, *39*, 1526–1563.

Taylor, G. I. (1934). The Formation of Emulsions in Definable Fields of Flow. *Proceedings of the Royal Society A: Mathematical, Physical and Engineering Sciences*, *146*, 501–523.

Tetsuya, T., Ishiaku, U. S., Mizoguchi, M., & Hamada, H. (2005). The effect of heat sealing temperature on the properties of OPP/CPP heat seal. I. Mechanical properties. *Journal of*

Applied Polymer Science, *97*, 753–760.

Theller, H. W. (1989). Heatsealability of flexible web materials in hot-bar sealing applications. *Journal of Plastic Film & Sheeting*, *5*, 66–93.

Tokita, N. (1977). Analysis of Morphology Formation in Elastomer Blends. *Rubber Chemistry and Technology*, *50*, 292–300.

Torza, S., & Mason, S. . G. (1970). Three-phase interactions in shear and electrical fields. *Journal of Colloid and Interface Science*, *33*, 67–83.

Virgilio, N., Desjardins, P., L'Esperance, G., & Favis, B. D. (2009). In Situ Measure of Interfacial Tensions in Ternary and Quaternary Immiscible Polymer Blends Demonstrating Partial Wetting. *Macromolecules*, *42*, 7518–7529.

Wagner Jr., J. R. (2009). *Multilayer Flexible Packaging: Technology and Applications for the Food, Personal Care, and Over-the-Counter Pharmaceutical Industries* (Vol. 3). William Andrew.

Winder, B., Ridgway, K., Nelson, A., & Baldwin, J. (2002). Food and drink packaging: who is complaining and who should be complaining. *Applied Ergonomics*, *33*, 433–438.

Wu, S. (1982). *Polymer interface and adhesion*. New York: M. Dekker.

Wu, S. (1987). Formation of dispersed phase in incompatible polymer blends: Interfacial and rheological effects. *Polymer Engineering & Science*, *27*, 335–343.

Xi, C., Jun, X., & Guo, B. H. (2006). Development of dispersed phase size and its dependence on processing parameters. *Journal of Applied Polymer Science*, *102*, 3201–3211.

Yamashita, M., Kato, M., K., I., A., H., & H., T. (2007). Lamellar crystal thickness transition of melt-crystallized isotactic polybutene-1 observed by small-angle X-ray scattering. *Journal of Applied Crystallography*, *40*, s650–s655.

Yourdkhani, M., Mousavand, T., Chapleau, N., & Hubert, P. (2013). Thermal, oxygen barrier and mechanical properties of polylactide-organoclay nanocomposites. *Composites Science and Technology*, *82*, 47–53.

Yuan, C. S., & Hassan, A. (2007). Effect of bar sealing parameters on OPP/MCPP heat seal

strength. *Express Polymer Letters*, *1*, 773–779.

Zeng, J., Aoyama, M., & Takahashi, H. (2003). Effect of the composition on the phase size in immiscible blends with the viscosity ratio close to unity. *Journal of Applied Polymer Science*, *89*, 1791–1799.

Zhang, J., Manias, E., Polizos, G., Huh, J.-Y., Ophir, A., Songtipya, P., & Jimenez-Gasco, M. del M. (2009). Tailored Polyethylene Nanocomposite Sealants: Broad-Range Peelable Heat-Seals Through Designed Filler/Polymer Interfaces. *Journal of Adhesion Science and Technology*, *23*, 709–737.

Zhang, X., Zhang, X., & Shi, G. (1992). The effect of some additives on the Form II to Form I phase transformation in polybutene-1. *Thermochimica Acta*, *205*, 245–252.

Zhou, P., Yu, W., Zhou, C., Liu, F., Hou, L., & Wang, J. (2007a). Morphology and electrical properties of carbon black filled LLDPE/EMA composites. *Journal of Applied Polymer Science*, *103*, 487–492.

Zhou, P., Yu, W., Zhou, C., Liu, F., Hou, L., & Wang, J. (2007b). Morphology and electrical properties of carbon black filled LLDPE/EMA composites. *Journal of Applied Polymer Science*, *103*, 487–492.

Zolali, A. M., Heshmati, V., & Favis, B. D. (2017). Ultratough Co-Continuous PLA/PA11 by Interfacially Percolated Poly(ether- b -amide). *Macromolecules*, *50*, 264–274.

Zumbrunnen, D. A., & Inamdar, S. (2001). Novel sub-micron highly multi-layered polymer ÿlms formed by continuous sow chaotic mixing. *Chemical Engineering Science*, *56*, 3893–3897.

APPENDIX A – SUPPLEMENTARY INFORMATION FOR ARTICLE 3

A.1. Thermodynamic prediction of organoclay localization in LDPE/PB-1 blend

Contact angle (CA) of LDPE and PB-1 with two different liquids i.e. deionized water and formamide, was measured by the sessile drop technique with the FDS contact angle system OCA Data Physics TBU 90E. CA measurements were performed through placing 3 drops of 2 µl of liquids on several positions films of LDPE and PB-1 and EMA-GMA. Each time the sessile drop CA was stabled over one minute. For each drop, the average of the right and left angles was used as CA. Then, the surface tensions of polymer components were calculated using the calculated CA according to Owens-Wendt equation (A.1) [1]:

$$\sigma_l(1 + cos\theta) = 2(\sqrt{\sigma_i^d \sigma_l^d} + \sqrt{\sigma_i^p \sigma_l^p}) \qquad \text{A.1}$$

where, σ_l is the surface tension of liquid and γ_i is surface tension of polymer i. σ_l^p and σ_l^d are polar and dispersive portions of the surface tension of the liquid, σ_l, respectively. σ_i^p and σ_i^d are polar and dispersive portions of the surface tension of the polymer, σ_i, respectively. σ_l^p and σ_l^d is 50.7 and 22.1 for water and 18.7 and 39.5 for formamide, respectively [2]. The surface tension of Cloisite15 at room temperature was used from literature [3]. The surface tensions of the polymers and the organoclay at 200°C were extrapolated based on their surface tension at room temperature and their rate of thermal variation, i.e. $d\sigma/dT$, that was considered -0.067 mN/m.K for LDPE, -0.06 mN/m.K for PB-1 [4] and -0.1 mN/m.K for organo-modified montmorillonite [5].

Then, the interfacial tensions of the components were calculated using the harmonic equation [4]:

$$\sigma_{ij} = \sigma_i + \sigma_j - \frac{4\sigma_i^d \sigma_j^d}{\sigma_i^d + \sigma_j^d} - \frac{4\sigma_i^p \sigma_j^p}{\sigma_i^p + \sigma_j^p} \qquad \text{A.2}$$

where σ_i and σ_i are surface energies of components i and j, σ_i^d and σ_j^d are their dispersive parts and σ_i^p and σ_j^p their polar parts.

The data of the surface tensions were then used to calculate wettability parameter based on following equation to predict equilibrium localization of organoclay in LDPE/PB-1 blend [6]:

$$\omega = \frac{\sigma_{SA} - \sigma_{SB}}{\sigma_{AB}} \qquad \text{A.3}$$

Tables A1,2 list the data of CA, surface tensions and interfacial tensions of the components. The ω was obtained 0.43 that suggests Cloisite15 localization at the interface of LDPE and PB-1.

Table A1. Contact angles and the corresponding surface tension results at room and process temperatures.

Material	Contact Angle (θ, degree)		Surface tension at 25 °C (mN/m)			Surface tension at 200 °C (mN/m)		
	Water ± 1	Formamide	σ^d	σ^p	σ	σ^d	σ^p	σ
LDPE	109.08 ± 1	84.6 ± 1	24.5	0.03	24.53	12.79	0.0156	12.805
PB-1	121.05 ± 1.5	91 ± 1	26.23	0.3	26.53	15.85	0.18	16.03
Cloisite15	-	-	31.48	11.06	42.54	18.53	6.51	25.04

Table A2. Interfacial tensions of the components at process temperature (200 ℃).

Component		Interfacial tension, σ_{ij} (mN/m)
i	j	
LDPE	PB-1	0.77
LDPE	Cloisite15	7.58
PB-1	Cloisite15	7.25

A.2. References

[1] D. K. Owens and R. C. Wendt, “Estimation of the surface free energy of polymers,” *J. Appl. Polym. Sci.*, vol. 13, no. 8, pp. 1741–1747, Aug. 1969.

[2] R. N. Shimizu and N. R. Demarquette, “Evaluation of surface energy of solid polymers using different models,” *J. Appl. Polym. Sci.*, vol. 76, no. 12, pp. 1831–1845, Jun. 2000.

[3] I. Ghasemi, M. Karrabi, and H. Azizi, “Nanocomposites based on polycarbonate/poly (butylene terephthalate) blends effects of distribution and type of nanoclay on morphological behavior,” *J. Vinyl Addit. Technol.*, vol. 19, no. 3, pp. 203–212, Sep. 2013.

[4] S. Wu, *Polymer interface and adhesion*. New York: M. Dekker, 1982.

[5] E. Picard, H. Gauthier, J. F. Gérard, and E. Espuche, “Influence of the intercalated cations on the surface energy of montmorillonites: Consequences for the morphology and gas barrier properties of polyethylene/montmorillonites nanocomposites,” *J. Colloid Interface Sci.*, vol. 307, no. 2, pp. 364–376, 2007.

[6] F. Fenouillot, P. Cassagnau, and J.-C. Majesté, “Uneven distribution of nanoparticles in immiscible fluids: Morphology development in polymer blends,” *Polymer*, vol. 50, no. 6, pp. 1333–1350, Mar. 2009.

APPENDIX B – SUPPLEMENTARY INFORMATION FOR ARTICLE 4

The WAXD patterns of the neat Cloisite15, LDPE and PB-1 containing 1 phr Cloisite15 are illustrated in *Figure B*1. Cloisite15 indicate three reflections at 2θ = 2.8, 5.2 and 7.5° correspond to (001) plane d-spacing of 31.5, 17 and 11.7 Å respectively. The LDPE/Cloisite15 and PB-1/ Cloisite15 exhibit one reflection at 2θ = 2.75° with significantly lower intensity when compared to that of the neat Cloisite15 that suggest intercalation of the LDPE and PB-1 in the clay galleries. The similarity of the WAXD pattern of the organoclay in PE/Cloisite15 and PB-1/Cloisite15 suggests similar affinity of the organoclay with LDPE and PB-1. Compared to the LDPE/Cloisite15 and PB-1/Cloisite15, the (001) plane reflection shifts to higher 2θ of 3.6, 3.55 and 3.13° corresponds to the d-spacing of 24.5, 24.86 and 28.2 Å for NPEPB5 and NPEPB10 and NPEPB20 respectively. This suggests densification of the clay galleries at the interface of the PE/PB-1 blends. Comparison the WAXD patterns of the nanocomposite films indicate that the (001) plane reflection shifts to lower 2θ by increasing the PB-1 content in the nanocomposites. It is attributed to the longer PB-1 fibrils by increasing the PB-1 content in the nanocomposites which provided more space for clay particles at the interface thus, the clay particles which tend to localize at the interface will be better disperse in the nanocomposites with higher elongated morphology.

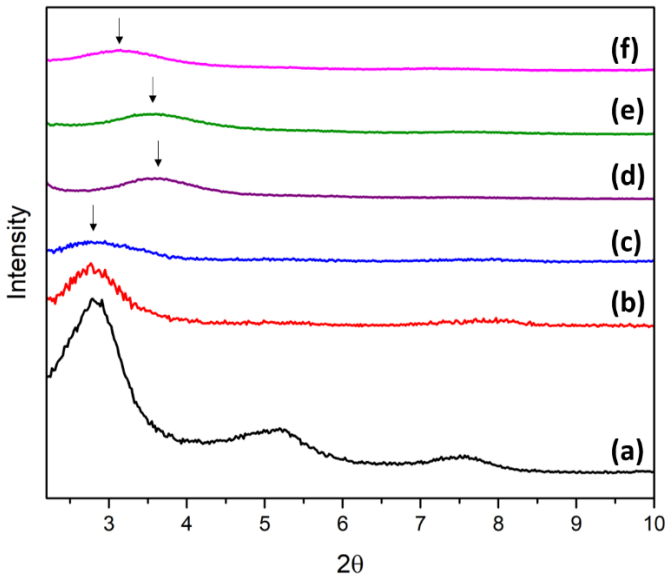

Figure B1. WAXD pattern of the neat Cloisite15 (a), LDPE/Cloisite15 (1 phr) (b) and PB-1/Cloisite15 (1 phr) (c), NPEPB5 (d), NPEPB10 (e) and NPEPB20 (f).

The DSC curves of the LDPE, PB-1 and their blends and nanocomposites are illustrated in Figure *B*2. The LDPE exhibits an endotherm at 110 °C (Figure *B*2a) and an exotherm corresponding to the crystallization temperature at 96 °C (Figure *B*2b). PB-1, in the first heating run indicates a melting peak at 120 °C corresponds to the melting point of the crystal form II (Figure *B*2a). The crystallization temperature of the PB-1 is 75 °C significantly lower than that of LDPE (Figure *B*2b). Figure *B*2a indicates that, in the second heating run PB-1 exhibits an endotherm at 115 °C corresponds to the melting point of the crystal form II. No endotherm corresponding to the PB-1 crystals are observed in PEPB5 and NPEPB5 while, a shoulder at 120 °C corresponds to the melting of the PB-1 form I crystal is observed in the first heating cycle of PEPB10, NPEPB10, PEPB20 and NPEPB20. Since, the FTIR and WAXD results (Figures 4 and 6 of the article) indicate the trace of the PB-1 crystals in PEPB5 and NPEPB5, it might be concluded that the PB-1 crystals in PEPB5 and NPEPB5 are too low to be detected through DSC.

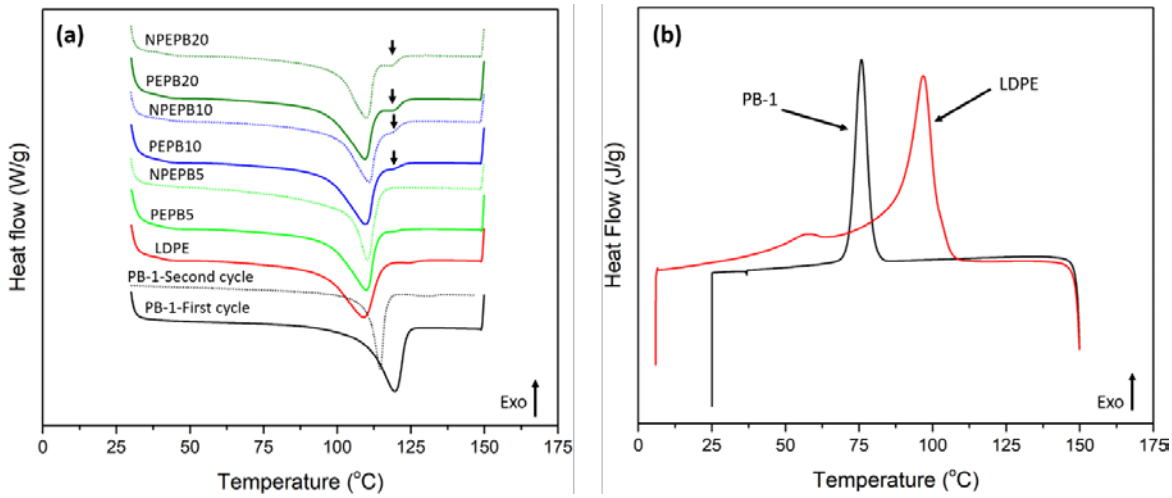

Figure B2. Firs DSC heating run of the blends and nanocomposite films of this study (a) and the crystallization temperatures of LDPE and PB-1 during the DSC cooling cycle (b).

The absence of form II in NPEPB5, is attributed to the crystallization of the PB-1 nanofibrils in a highly confined PB-1 nanofibrils with 60 nm in thickness. By increasing the PB-1 content to 10 and 20 wt% the thickness of the PB-1 fibrils is increased to 170 and 190 nm for NPEPB10 and NPEPB20 respectively very similar to that of their neat blends (190 and 200 nm respectively). Thus, the absence of the form II in NPEPB10 and NPEPB20 is questionable while, form II is

generated after the heat sealing of PEPB10 and PEPB20. Figure B3 indicates the polarized FTIR spectra of the 2 week aged blends and nanocomposite sealants of this study. The IR bond at 925 cm^{-1} corresponds to the CH_3 group which is perpendicular to the chain axis and the bonds at 1026 and 1222 cm^{-1} assigned to the twisting mode of CH_2 units which are parallel to the chain axis [1]–[3]. Figure B3 indicates that for both blends and nanocomposite sealants, the intensity of the bands at 925 cm^{-1} is more intense when the IR beam is parallel to the machine direction (MD) while, the intensities of the bands at 1026 and 1222 are more intense when the beam is in TD perpendicular to the MD. From the polarized FTIR results, it can be deduced that the size of the PB-1 nanofibrils are sufficiently low to feel the confinement otherwise, isotropic orientation of the crystals should be obtained. Figure B3b indicates that the orientation of the clay particles, that is probes by the IR bond of the Si-O-Si group at 1040 cm^{-1} [4], is more intense in NPEPB20 rather than NPEPB10 and NPEPB5. This higher orientation of the clay particles in MD direction of the NPEPB20 is attributed to the better dispersion of the clay at the interface of the PE/PB-1 in NPEPB 20 rather than in NPEPB10 and NPEPB5 as confirmed by WAXD results (See Figure B1). It can be concluded that, less clay coverage at the interface of the blends and nanocomposites with higher PB-1 content will be compensated by more elongated PB-1 morphology in these blends which results in better dispersion of the clay particles at the interface. It is also worth noting that, crystallization of PB-1 is nucleating control process and most likely started from the edge of the PB-1 phase in the heterogenous compounds. Therefore, it is speculated that the presence of the clay particles at the interface of the PE/PB-1 significantly hinders the chain movement hence, disrupt the kinetic of the form II formation and suppress its priority in respect to the form I′. Moreover, the mixing sequence in which organoclays were firstly mixed with PB-1 and then diluted with LDPE, may cause a portion of the clay particles to remain in PB-1 phase. This will further disrupt the kinetic of the form II formation and suppress its priority in respect to the form I′ formation.

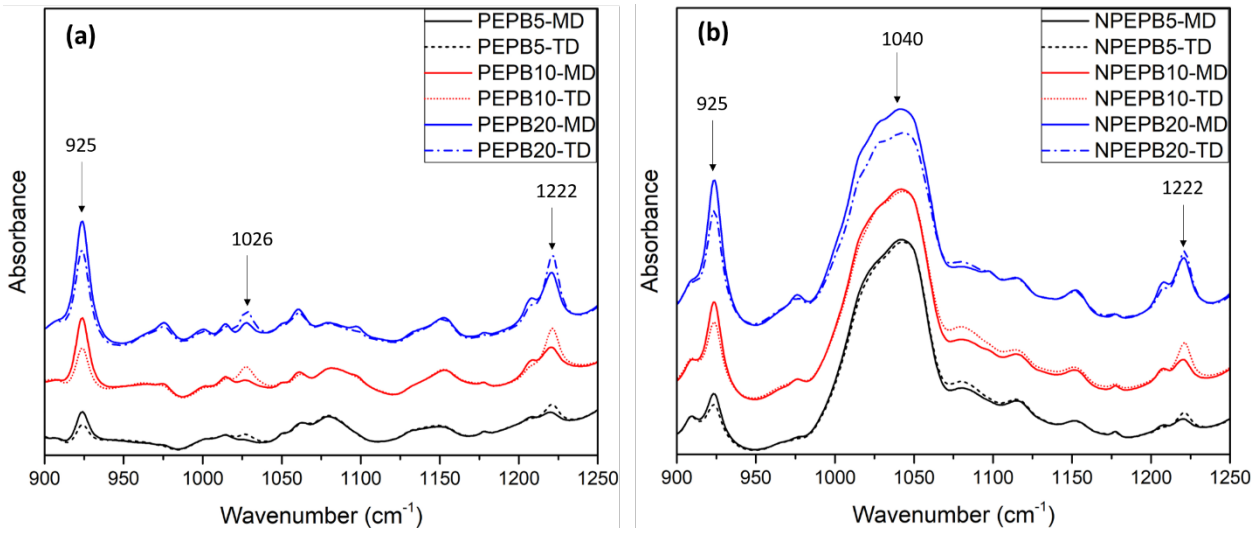

Figure B3. Polarized FTIR spectra of the LDPE/PB-1 blend sealants (a) and LDPE/PB-1/organoclay nanocomposite sealants (b) 2 weeks after the heat seal.

B.1. References

[1] K. Holland-Moritz and E. Sausen, “Vibrational spectra and normal coordinate analysis of isotactic poly(alkyl ethylene)s. I. Modification I of poly(ethyl ethylene) and its deuterated derivatives,” *J. Polym. Sci. Polym. Phys. Ed.*, vol. 17, no. 1, pp. 1–23, Jan. 1979.

[2] M. Ukita, “The Vibrational Spectra and Vibrational Assignments of Isotactic Polybutene-1,” *Bull. Chem. Soc. Jpn.*, vol. 39, no. 4, pp. 742–749, Apr. 1966.

[3] J. P. Luongo and R. Salovey, “Infrared characterization of polymorphism in polybutene-1,” *J. Polym. Sci. Part A-2 Polym. Phys.*, vol. 4, no. 6, pp. 997–1008, Dec. 1966.

[4] M. Bora, J. N. Ganguli, and D. K. Dutta, “Thermal and spectroscopic studies on the decomposition of [Ni{di(2-aminoethyl)amine}(2)]- and [Ni(2,2 ’: 6 ’,2 - terpyridine)(2)]-Montmorillonite intercalated composites,” *Thermochim. Acta*, vol. 346, no. 1–2, pp. 169–175, 2000.